รายงานวิจัยฉบับสมบูรณ์

สมบัติพิเศษขั้นสูงของแบคทีเรียเซลลูโลสแม่เหล็กคอมโพสิต

Advanced Functional Properties of Magnetic Bacterial Cellulose Composites

โดย รศ.ดร. สุปรีดิ์ พินิจสุนทร

กุมภาพันธ์ พ.ศ. 2562

สัญญาเลขที่ RSA5980014

รายงานวิจัยฉบับสมบูรณ์

โครงการ: สมบัติพิเศษขั้นสูงของแบคทีเรียเซลลูโลสแม่เหล็กคอมโพสิต

Project: Advanced Functional Properties of Magnetic Bacterial Cellulose Composites

ผู้วิจัย รศ.ดร. สุปรีดิ์ พินิจสุนทร
สังกัด สาขาวิชาฟิสิกส์ คณะวิทยาศาสตร์ มหาวิทยาลัยขอนแก่น

สนับสนุนโดยสำนักงานกองทุนสนับสนุนการวิจัย

บทคัดย่อ

รหัสโครงการ: RSA5980014

ชื่อโครงการ: สมบัติพิเศษขั้นสูงของแบคทีเรียเซลลูโลสแม่เหล็กคอมโพสิต

ชื่อนักวิจัย: รศ.ดร. สุปรีดิ์ พินิจสุนทร มหาวิทยาลัยขอนแก่น

อีเมล: psupree@kku.ac.th

ระยะเวลาโครงการ: 3 ปี

ในงานวิจัยนี้ได้ทำการสังเคราะห์นาโนเซลลูโลสจากแบคทีเรียได้แผ่นแบคทีเรียเซลลูโลส (BC) ที่มีลักษณะเหมือนวุ้นขาวใส ซึ่งสามารถนำไปทำแห้งด้วยกระบวนการ freeze dry หรือการอบแห้งได้แผ่นแบคทีเรียเซลลูโลสที่ได้มีความเป็นผลึกสูง ประกอบไปด้วยเส้นใยนาโนขนาดน้อยกว่า 100 นาโนเมตร ถักทอกันเป็นโครงข่าย 3 มิติ เมื่อนำมาสังเคราะห์อนุภาคแม่เหล็กนาโนชนิดต่างๆใส่เข้าไปในโครงสร้างแบคทีเรียเซลลูโลส ได้วัสดุคอมโพสิตระหว่างแบคทีเรียเซลลูโลสกับอนุภาคแม่เหล็ก ทำการวิเคราะห์วัสดุด้วยเทคนิคต่างๆได้แก่ TG/DTA, FTIR, XRD, SAXS, UV-Vis, SEM, TEM, EDS, VSM

ผลการทดลองพบว่า วัสดุคอมโพสิต BC ที่ใส่อนุภาคแม่เหล็กโคบอลต์เฟอไรต์ที่ผ่านการทำแห้งด้วยการอบแห้ง จะได้ค่าแม่เหล็กอิ่มตัวสูงที่สุด ส่วนวัสดุคอมโพสิตของแบคทีเรียเซลลูโลสกับอนุภาคแม่เหล็กนาโน Fe_3O_4 ที่เตรียมโดยการจุ่มในสารละลาย ferrofluid พบว่าวิธีนี้เป็นวิธีที่ง่ายและไม่ทำลายโครงสร้างของแผ่น BC อนุภาคของแม่เหล็กนาโนกระจายตัวในโครงสร้าง BC ได้ดี ความแข็งแรงเพิ่มขึ้นหากใส่อนุภาคแม่เหล็กนาโนในปริมาณที่ไม่มากเกินไป แผ่นเมมเบรนแม่เหล็ก BC สามารถตอบสนองกับแม่เหล็กภายนอกได้ดีมากทั้งกับสนามแม่เหล็กแบบทางเดียวหรือเปลี่ยนทิศทาง ส่วนถ้านำแผ่นแม่เหล็ก BC ไปผ่านกระบวนการไพโรไลซิส เส้นใยเซลลูโลสจะเปลี่ยนสภาพกลายเป็นเส้นใยคาร์บอนนาโน ทำให้ได้คอมโพสิตของเส้นใยคาร์บอน (CNF) กับอนุภาคแม่เหล็ก

อีกส่วนหนึ่งของงานวิจัยนี้ ได้ศึกษาการสังเคราะห์กระดาษแม่เหล็กสีขาวจากแบคทีเรียเซลลูโลสคอมโพสิต โดยสังเคราะห์อนุภาคนาโน ZnO ในโครงสร้างของ BC เพื่อให้ได้กระดาษสีขาวและนำมาประกบกับกระดาษแม่เหล็ก BC ผลปรากฏว่าวัดค่าความขาวไปมากกว่า 80% ผลการวัดค่าความแข็งแรงและความต้านแรงฉีก พบว่า กระดาษแม่เหล็กสีขาวจากคอมโพสิตของ BC มีค่าที่ค่อนข้างสูง และยังสามารถตอบสนองกับสนามแม่เหล็กจากภายนอกได้ดี

ในส่วนสุดท้าย ได้ทำการสังเคราะห์อนุภาคแม่เหล็กนาโนของโคบอลต์เหล็กแพลทตินัม ($Co_{1-x}Fe_xPt$) ด้วยวิธีโพลิออล จากนั้นเผาเพื่อให้วัสดุเปลี่ยนเฟสเป็นเฟสแม่เหล็กแรงตามที่ต้องการ พบว่าสามารถสังเคราะห์อนุภาคนาโน ($Co_{1-x}Fe_xPt$) ได้เฟสบริสุทธิ์ มีขนาดเล็กประมาณ 2-3 nm แต่เมื่อเผาแล้วจะเกิดการเปลี่ยนเฟสเป็นเฟสแม่เหล็กแข็ง และขนาดของอนุภาคใหญ่ขึ้นมาก การปรับเปลี่ยนอัตราส่วน Co กับ Fe พบว่าทำให้สมบัติทางแม่เหล็กเปลี่ยนไป โดยมีค่าแมกนีไตเซชันอิ่มตัวสูงที่สุดที่ $x = 0.50$ แต่มีค่าโคเออร์ซิวิตีสูงสุดที่ $x = 0$ หรือ 1

คำหลัก: แบคทีเรียเซลลูโลส; คอมโพสิต; อนุภาคนาโน; สมบัติแม่เหล็ก; วัสดุพิเศษขั้นสูง;

Abstract

Project Code: RSA5980014

Project Title: Advanced Functional Properties of Magnetic Bacterial Cellulose Composites

Investigator: Assoc. Prof. Supree Pinitsoontorn Khon Kaen University

E-mail Address: psupree@kku.ac.th

Project Period: 3 years

In this project, nanocellulose from bacteria has been synthesized. The obtained bacterial cellulose (BC) showed a hydrogel characteristic in which the water could be evaporized by freeze-drying or oven-drying. The BC membrane is highly crystalline, consisting of nanofibrils with average diameter less than 100 nm in three-dimensional structure. The different kinds of magnetic nanoparticles have been incorporated into the BC nanostructure. The fabricated BC/nanoparticle composites were characterized with several techniques, such as TG/DTA, FTIR, XRD, SAXS, UV-Vis, SEM, TEM, EDS, VSM.

The study showed that the BC composite with cobalt ferrite after oven drying showed the highest saturation magnetization. On the other hand, the BC/Fe_3O_4 nanoparticle composites were prepared by simply immersing BC in the ferrofluid solution. This simple method was proved to maintained the structure of BC and sustained the homogeneous distribution of Fe_3O_4 nanoparticles. The strength was improved for the optimized nanoparticle concentration. The magnetic BC showed good response with a static or an alternating magnetic field. Some portions of BC composites were pyrolyzed to change the cellulose nanofibers into carbon nanofiber. The composites of carbon nanofiber (CNF) and magnetic nanoparticles were achieved.

The other section of this project studied the fabrication of white magnetic paper from BC nanocomposites. By synthesizing ZnO nanoparticles in the structure of BC, and then sandwiched with magnetic BC paper, the white magnetic paper was successfully obtained. The whiteness of over 80% was observed. The excellent tensile and tearing strength of the white magnetic paper from BC was measured. In addition, the paper showed a good response with an applied field.

Lastly, the ($Co_{1-x}Fe_xPt$) magnetic nanoparticles were synthesized by a polyol method, with the average particle size of 2-3 nm. After annealing, the desired phase was obtained but the particle size increased significantly. The ratio of Co:Fe had a strong effect on magnetic properties. The highest magnetization was obtained at x = 0.50 but the highest coercivity was found at x = 0 or 1. the final single phase. After

Keywords: bacterial cellulose; composite; nanoparticle; magnetic property; functional material;

1. บทนำ

แบคทีเรียเซลลูโลส (bacterial cellulose, BC) เป็นวัสดุธรรมชาติที่น่าสนใจมาก เพราะมีสมบัติเด่นหลายอย่าง เช่น สมบัติเชิงกลที่ดี ความมีรูพรุนสูง ดูดซับน้ำได้มาก ขึ้นรูปได้ง่าย ย่อยสลายตามธรรมชาติได้ และไม่มีความเป็นพิษ [1-5] ดังนั้นจึงมีงานวิจัยจำนวนมากที่ศึกษาเกี่ยวกับ BC โดยส่วนมากจะศึกษาการสังเคราะห์ทางชีวภาพเพื่อให้มีราคาถูกลง และสามารถนำไปใช้งานไปในหลายสาขาเช่น ด้านสิ่งทอ ด้านวัสดุเสริมแรง หรือด้านที่เกี่ยวข้องกับทางการแพทย์ อย่างไรก็ตามยังมีสมบัติพิเศษอื่นๆที่น่าสนใจอีกมากสำหรับแบคทีเรียเซลลูโลส

แบคทีเรียเซลลูโลส (BC) ด้วยตัวมันเองยังขาดสมบัติอีกหลายๆด้าน แต่การทำให้เป็นวัสดุผสมหรือคอมโพสิตสามารถเพิ่มสมบัติได้อีกมาก ด้วยการที่ BC มีพื้นที่ผิวสูงและมีหมู่ไฮดรอกซิลจำนวนมาก ทำให้อะตอมหรือโมเลกุลของสารอื่นๆสามารถยึดเกาะได้ดี ทำให้สามารถสังเคราะห์วัสดุคอมโพสิตจาก BC ที่มีสมบัติที่น่าสนใจอื่นๆ เช่น ตัวเร่งปฏิกิริยา สมบัตเชิงแสงและไฟฟ้า หรือสมบัติทางแม่เหล็ก เป็นต้น

เมื่อไม่นานมานี้ วัสดุผสมระหว่างเส้นใยนาโนจาก BC และอนุภาคแม่เหล็กนาโน ได้รับความสนใจเป็นอย่างมาก เพราะสามารถนำไปใช้งานได้ในผลิตภัณฑ์หลายอย่างเช่น แอคชูเอเตอร์ [6, 7], การปรินท์เชิงแม่เหล็ก [6, 8], เซนเซอร์ทางแม่เหล็ก [6, 8, 9], การป้องกันสนามแม่เหล็กไฟฟ้า [6, 8, 10, 11], การเก็บข้อมูล [6, 8, 9, 12], การป้องกันการโจรกรรม [6], สิ่งทอ [9], ตัวกรองทางแม่เหล็ก [7, 9], การดูดซับโลหะหนัก [10, 13, 14] นอกจากนี้ การเติมอนุภาคแม่เหล็กนาโนลงใน BC ยังมีข้อได้เปรียบหลายประการเมื่อเทียบกับเซลลูโลสแม่เหล็กชนิดอื่นๆ เพราะ BC ให้ความแข็งแรง ค่ามอดูลัส ที่สูงกว่ามาก ทำให้สามารถได้แผ่นเมมเบรนแม่เหล็กที่ทั้งมีความแข็งแรงและยืดหยุ่นได้ดี การที่ BC มีรูพรุนระดับนาโนเป็นจำนวนมากและมีพื้นที่ผิวสูงทำให้สามารถเติมอนุภาคชนิดอื่นเพื่อเพิ่มสมบัติต่างๆได้อีก และสุดท้าย BC มีน้ำหนักเบาและอุ้มน้ำได้ดี จึงมีประโยชน์กับการใช้งานที่หลากหลาย

ในรายงานงานวิจัยที่ผ่านๆมา วัสดุคอมโพสิตระหว่าง BC และอนุภาคแม่เหล็กนาโน มีการรายงานมาแล้วบ้างพอสมควร แต่ส่วนใหญ่จะใช้อนุภาคแม่เหล็กชนิดอ่อน ได้แก่ Fe_3O_4 [6, 9, 11, 12, 14] ซึ่งวัสดุชนิดนี้ให้สมบัติแม่เหล็กอ่อน ประกอบกับการที่มีขนาดระดับนาโนจึงได้สมบัติแม่เหล็กเป็นแบบ superparamagnetic หมายความว่าไม่มีฮีสเตอรีซิสลูป ซึ่งน่าสนใจสำหรับงานวิจัยบางประเภท อย่างไรก็ตามวัสดุแม่เหล็กชนิดอื่นๆ ก็เป็นที่น่าสนใจเช่นเดียวกัน แต่ยังมีรายงานวิจัยที่เกี่ยวข้องกับการใส่วัสดุแม่เหล็กชนิดอื่นๆเข้าไปในโครงสร้างของ BC อยู่น้อยมาก

วิธีการใส่อนุภาคแม่เหล็กเข้าไปในโครงสร้างของ BC ก็มีความสำคัญไม่แพ้กัน ในงานวิจัยที่ผ่านมีการศึกษาวิธีการดังกล่าวหลายวิธี [9, 12, 13] และศึกษาสมบัติที่เปลี่ยนไปของวัสดุคอมโพสิต เช่น การตอบสนองกับสนามแม่เหล็กภายนอก [8] การดูดซับไอออนของโลหะหนัก [14] และสมบัติเชิงกล [15] เป็นต้น อย่างไรก็ตาม ยังไม่มีการศึกษากลไกการยึดเหนี่ยวระหว่างอนุภาคแม่เหล็กนาโนกับพื้นผิวของเส้นใยนาโนของ BC ความเข้าใจในเรื่องนี้จะช่วยให้สามารถควบคุมการกระจายตัวของอนุภาคแม่เหล็กนาโนได้ดี ซึ่งจะส่งผลโดยตรงกับสมบัติของวัสดุ

การใส่วัสดุนาโนอื่นๆเข้าไปในโครงสร้างเส้นใยนาโนของ BC จะช่วยเพิ่มสมบัติพิเศษหลายๆ ด้าน เช่น เส้นในนาโนจาก BC สามารถมีทั้งสมบัติแม่เหล็กเฟอโรและสมบัติการนำไฟฟ้าได้หากมีการเติมกลุ่มของอนุภาคแม่เหล็กแมกนีไตท์พร้อมๆกับพอลิเมอร์นำไฟฟ้า polyaniline [11] นอกการนี้ การเติมอนุภาคนาโนเงินพร้อมๆกับอนุภาคเหล็กออกไซด์ในแผ่นเมมเบรน BC จะช่วยเพิ่มสมบัติการต้านเชื้อแบคทีเรียได้เป็นอย่างดี [16] ยิ่งไปกว่านั้น พื้นผิวของ BC สามารถดัดแปลงได้ด้วย fluoroalkyl silane (FAS) เพื่อให้เปลี่ยนสภาพจากการชอบน้ำไปเป็นไม่ชอบน้ำ [6]

แนวความคิดที่จะรวมวัสดุหลายๆชนิดเข้าด้วยกันเพื่อให้ได้วัสดุพิเศษขั้นสูงที่มีสมบัติหลายประการไม่ใช่แนวความคิดใหม่ แต่สำหรับวัสดุคอมโพสิตจาก BC ยังมีงานวิจัยในลักษณะนี้ไม่มากนัก และยังมีพื้นที่เหลืออีกมากสำหรับงานวิจัยที่จะเกิดขึ้นได้ในอนาคต

2. วัตถุประสงค์

2.1. เพื่อสังเคราะห์แบคทีเรียเซลลูโลสคอมโพสิตกับอนุภาคแม่เหล็กนาโน

2.2. เพื่อเตรียมอนุภาคแม่เหล็กนาโนชนิดต่างๆเข้าไปในโครงสร้างของแบคทีเรียเซลลูโลสและศึกษาผลของอนุภาคแม่เหล็กชนิดต่างๆต่อโครงสร้าง ลักษณะสัณฐาน การกระจายตัว ลักษณะเฉพาะทางแม่เหล็ก และสมบัติอื่นๆ

2.3. เพื่อศึกษาการยึดเหนี่ยวระหว่างอนุภาคแม่เหล็กนาโนของแบคทีเรียเซลลูโลสโดยใช้กล้องจุลทรรศน์อิเล็กตรอนที่มีกำลังแยกสูงและเทคนิคขั้นสูงอื่นๆ

2.4. เพื่อศึกษาสมบัติฟังก์ชันพิเศษอื่นๆของวัสดุแบคทีเรียเซลลูโลสคอมโพสิตที่สังเคราะห์ได้ ได้แก่ การตอบสนองทางแม่เหล็ก สภาพการนำไฟฟ้า สัมประสิทธิ์การดูดกลืนแสง สมบัติเชิงพื้นผิว

2.5. เพื่อประดิษฐ์วัสดุแม่เหล็กที่มีการเบาและอ่อนตัวได้จากคอมโพสิตของอนุภาคแม่เหล็กนาโนกับแบคทีเรียเซลลูโลส

3. วิธีการทดลอง

3.1. การสังเคราะห์และศึกษาโครงสร้างของแบคทีเรียเซลลูโลส

แบคทีเรียเซลลูโลสได้จากการเลี้ยงเชื้อแบคทีเรีย Glucanobacter xylinum (strain TISTR975) ซึ่งได้มาจาก ศูนย์จุลินทรีย์ สถาบันวิจัยวิทยาศาสตร์และเทคโนโลยีแห่งประเทศไทย เลี้ยงเชื้อแบคทีเรียในอาหารที่มีน้ำตาล D-glucose เป็นส่วนประกอบหลัก ทำการบ่มไว้ที่อุณหภูมิ 30 $^{\circ}$C ภายใต้สภาวะนิ่งเป็นเวลา 5-14 วัน แล้วแต่ความหนาที่ต้องการ หลังจากนั้นทำการเก็บเกี่ยว จะได้แผ่นวุ้นแบคทีเรียเซลลูโลส ซึ่งต้องนำไปต้มเพื่อฆ่าเชื้อแบคทีเรีย และจุ่มในสารละลาย NaOH เพื่อปรับค่า pH จากนั้นล้างทำความสะอาดด้วยน้ำ DI อีกหลายๆรอบจนกว่าจะได้ pH เท่ากับ 7 จะได้แบคทีเรียเซลลูโลสในสภาพชุ่มน้ำในลักษณะวุ้น หากต้องการทำแห้ง สามารถทำได้สองวิธีคือ หนึ่งทำการอบแห้ง (oven dry) ซึ่งจะได้แผ่นแบคทีเรียเซลลูโลสเป็นฟิล์มแบนราบ แต่หากทำแห้งด้วยวิธีแช่เยือกแข็ง (freeze dry) จะทำให้ได้แผ่นแบคทีเรียเซลลูโลสที่มีความฟู และมีรูพรุนสูง

ทำการวิเคราะห์เฟสและโครงสร้างของแบคทีเรียเซลลูโลสด้วยเทคนิค X-ray diffraction (XRD) และส่องกล้อง Scanning Electron Microscope (SEM) รวมทั้งหาค่าสมบัติทางกายภาพอื่นๆ เช่น ความหนาแน่น ขนาด ปริมาณน้ำที่ดูดซับไว้ ฯลฯ

3.2. แบคทีเรียเซลลูโลสคอมโพสิตกับอนุภาคแม่เหล็กนาโนเฟอไรต์

เริ่มต้นจากแผ่นแบคทีเรียเซลลูโลส (BC) ที่เป็นลักษณะวุ้น หรือที่ผ่านการทำแห้งแล้วโดยการ freeze dry นำมาสังเคราะห์เพื่อใส่อนุภาคแม่เหล็กนาโนเฟอไรต์ชนิดต่างๆ ได้แก่ $MO.Fe_2O_4$ (โดย M = Mn, Co, Ni, Cu) วิธีการมีดังนี้ ใช้สารตั้งต้นจาก $MCl_2.nH_2O$ และ $FeCl_3.6H_2O$ ในอัตราส่วน 1:2 ละลายในน้ำ DI จากนั้นจุ่มแผ่นแบคทีเรียเซลลูโลสในสารละลายดังกล่าว ให้ความร้อนไปที่ 90 ^{o}C จากนั้นเติมสารละลาย NaOH ความเข้มข้น 1.2M เพื่อเปลี่ยนไอออนของโลหะให้กลายเป็นอนุภาคนาโนเฟอไรต์ ซึ่งกระบวนการนี้ทำที่ 90 ^{o}C เป็นเวลา 6 ชั่วโมง แล้วล้างด้วยน้ำสะอาดเพื่อกำจัดสารตกค้างที่ไม่ต้องการ

วิเคราะห์เฟสและโครงสร้างของ BC เปล่า และ BC คอมโพสิตด้วยเทคนิค XRD วัดหมู่ฟังก์ชันด้วยเทคนิค Fourier transform infrared (FTIR) spectroscopy วัดสมบัติทางแม่เหล็กด้วยเทคนิค vibrating sample magnetometer (VSM) วัดลักษณะเส้นใยและอนุภาคด้วยเทคนิค SEM

3.3. อนุภาคแม่เหล็กนาโนของโคบอลต์เหล็กแพลทตินัม

อนุภาคแม่เหล็กนาโน $Co_{1-x}Fe_xPt$ (x = 0, 0.25, 0.50, 0.75, 1.0) ถูกสังเคราะห์ขึ้นด้วยกระบวนการโพลิออล เพิ่มต้นด้วยสารตั้งต้น Cobalt (III) acetylacetonate ($Co(acac)_2$), iron acetylacetonate ($Fe(acac)_2$) และ platinum acetylacetonate ($Pt(acac)_2$) โดยชั่งในปริมาณสัดส่วนที่เหมาะสมและละลายในสารละลาย trimethylene glycol (TMEG) เติม NaOH ในปริมาณที่เหมาะสม จากนั้นให้ความร้อนที่ 230 ^{o}C โดยมีการคนอย่างสม่ำเสมอ และรีฟลักซ์ไว้เป็นเวลา 3.5 ชั่วโมง หลังจากรีฟลักซ์เสร็จ ทำให้สารละลายเย็นตัวลง จะเริ่มเห็นการตกตะกอนซึ่งเป็นอนุภาคนาโนของ $Co_{1-x}Fe_xPt$ ทำการแยกอนุภาคนาโนโดยการปั่นเหวี่ยง และล้างด้วยเอทานอลหลายๆรอบเพื่อกำจัดสิ่งเจือปนอื่น ทำการอบอนุภาคที่ได้ในบรรยากาศของก๊าซอาร์กอนที่ 700 ^{o}C เป็นเวลา 2 ชั่วโมง

ทำการวิเคราะห์เฟสและโครงสร้างผลึกด้วยเทคนิค XRD ตรวจสอบลักษณะและขนาดของอนุภาคนาโนด้วยเทคนิค transmission electron microscopy (TEM) ทดสอบสมบัติทางความร้อนด้วยเทคนิค thermogravimetric (TGA) ตรวจสอบองค์ประกอบทางเคมีด้วยเทคนิค energy dispersive X-ray (EDX) และวัดสมบัติทางแม่เหล็กด้วยเทคนิค VSM นอกจากนี้ยังใช้แสงซินโครตรอนในการวิเคราะห์โครงสร้างเฉพาะบริเวณของ Co ด้วยเทคนิค X-ray absorption spectroscopy (XAS)

3.4. เส้นใยคาร์บอนนาโนจากแบคทีเรียเซลลูโลสผสมกับอนุภาคแม่เหล็กนาโน

ในงานวิจัยนี้ เริ่มต้นจาก BC ที่มีขายอยู่ในรูปวุ้นมะพร้าว (ชาวเกาะ) นำมาล้างหลายๆรอบเพื่อกำจัดน้ำตาลหรือสารเจือปนอื่นๆ จากนั้นทำให้บางลงจนมีความหนาเป็น 0.25 cm ก่อนที่จะจุ่มในสารละลายเฟอโรฟรูอิด (สารละลายของอนุภาคนาโน Fe_3O_4) เพื่อให้อนุภาคนาโน Fe_3O_4 แพร่เข้าสู่

โครงสร้างเส้นใยนาโนของ BC ในงานนี้ทำการเปลี่ยนความเข้มข้นของ ferrofluid เป็น 1, 3, 5, 10, และ 20 % โดยปริมาตร เมื่อไว้วุ้นของคอมโพสิตระหว่าง BC กับ Fe_3O_4 แล้ว นำไปทำแห้งแบบ freeze dry

ในขั้นต่อมานำวัสดุคอมโพสิต BC/Fe_3O_4 ไปผ่านกระบวนการไพโรไลซิสโดยอบในบรรยากาศของก๊าซอาร์กอน ใช้อัตราการให้ความร้อนที่ 1 $^{\circ}$C/นาที จากอุณหภูมิห้องถึง 300 $^{\circ}$C จากนั้นเพิ่มอัตราเป็น 2 $^{\circ}$C/นาที จนถึงอุณหภูมิ 600 $^{\circ}$C แล้วแช่ไว้เป็นเวลา 2 ชั่วโมง จะทำให้ BC เปลี่ยนไปเป็นเส้นใยคาร์บอนนาโนที่มีอนุภาคแม่เหล็ก Fe_3O_4 อยู่ในโครงสร้าง

ทำการศึกษาความเสถียรเชิงความร้อนด้วยเทคนิค TGA และหมู่ฟังก์ชันด้วยเทคนิค FTIR ศึกษาโครงสร้างผลึกและเฟสที่ได้ด้วย XRD ศึกษาลักษณะสัณฐานด้วยเทคนิค SEM และ TEM และศึกษาสมบัติแม่เหล็กด้วยเทคนิค VSM

3.5. การศึกษาแผ่นแบคทีเรียเซลลูโลสที่มีความยืดหยุ่นและมีสมบัติแม่เหล็ก

เริ่มต้นด้วยแผ่น BC ที่สังเคราะห์ในตอนแรก นำไปจุ่มในสารละลาย ferrofluid โดยเปลี่ยนความเข้มข้นตั้งแต่ 1, 3, 5, 10, 20 % โดยปริมาตร ในกระบวนการนี้ นำแผ่น BC แช่ในสารละลาย ferrofluid ที่ 80 $^{\circ}$C เป็นเวลา 1 ชั่วโมง โดยมีการคนอย่างต่อเนื่อง ซึ่งจะทำให้แผ่น BC สีขาวเปลี่ยนสีไปเป็นสีดำ แสดงว่าเกิดนาโนคอมโพสิตของ BC/Fe_3O_4

การวิเคราะห์ทำด้วยเทคนิค XRD, SEM, FTIR, TGA, SEM VSM นอกจากนี้ทำการทดสอบสมบัติเชิงกลด้วยเครื่อง universal testing machine (UTM) โดยใช้ความยาวเกจ 20 mm อัตราการดึง 10 mm/นาที

3.6. การสังเคราะห์กระดาษแม่เหล็กสีขาวจากแบคทีเรียเซลลูโลสคอมโพสิต

ในงานนี้ใช้แผ่น BC ที่สังเคราะห์ได้ในตอนต้นมาเตรียมเป็นคอมโพสิตสองชนิดได้แก่ BC/$CoFe_2O_4$ และ BC/ZnO วิธีการมีดังนี้ สำหรับแผ่น BC/$CoFe_2O_4$ เริ่มต้นด้วยการใช้ $CoCl_2.6H_2O$ และ $FeCl_3.6H_2O$ ในอัตราส่วน 1:2 ผสมลงในน้ำ DI จุ่มแผ่น BC ลงในสารละลายดังกล่าว และเพิ่มอุณหภูมิเป็น 60 $^{\circ}$C ทิ้งไว้ 4 ชั่วโมง จากนั้นเติม NaOH แล้วล้างน้ำเปล่าหลายๆครั้งเพื่อปรับ pH ส่วนแผ่นคอมโพสิต BC/ZnO ทำได้โดยละลาย $ZnCl_2$ ในน้ำ DI และแช่แผ่น BC ไว้ 24 ชั่วโมง ก่อนจะเติม NaOH จากนั้นล้างด้วยน้ำสะอาดหลายๆครั้ง

ในการประดิษฐ์กระดาษแม่เหล็กสีขาว นำแผ่น BC/$CoFe_2O_4$ และ BC/ZnO มาประกบกันในลักษณะแซนวิช ในชั้น BC/ZnO อยู่ด้านนอก แล้วนำไปอัดด้วยความร้อนที่ 80 $^{\circ}$C เป็นเวลา 24 ชั่วโมง

วิเคราะห์ด้วยเทคนิค TGA, XRD, SEM, UTM, VSM นอกจากนี้วิเคราะห์การสะท้อนแสงด้วยเทคนิค UV-visible spectrometer ที่ความยาวคลื่น 200 – 800 nm ทดสอบความขาวของกระดาษตามมาตรฐาน ISO 11476:2010 ดัชนีชี้วัดต้านการฉีกขาด ทดสอบตามมาตรฐาน ISO1974:2014

4. ผลการทดลอง

4.1. การสังเคราะห์และศึกษาโครงสร้างของแบคทีเรียเซลลูโลส

- สามารถสังเคราะห์แบคทีเรียเซลลูโลส (bacterial cellulose, BC) จากเชื้อแบคทีเรีย Acetobacter xylinum ได้สำเร็จดังรูป

- BC ที่ได้ จะมีสีเหลืองส้ม (สีของสารละลายกลูโคส) มีความเป็นกรดเนื่องจากปฏิกิริยาของแบคทีเรีย) และมีแบคทีเรียอยู่ จึงต้องทำการล้าง BC ด้วยน้ำเปล่าหลายๆครั้ง และใช้ความร้อนในระหว่างการล้างด้วย เพื่อฆ่าเชื้อแบคทีเรีย และทำให้ BC มีลักษณะใสไม่มีสี จากนั้นล้าง BC ด้วยสารละลาย NaOH แล้วแช่ค้างคืนไว้ และปรับ pH = 7 ด้วยน้ำเปล่า

- เมื่อล้าง ฆ่าเชื้อแบคทีเรีย และปรับ pH ให้เป็นกลางแล้ว BC ที่ได้จะมีลักษณะเหมือนวุ้นขาวใส ดังรูป

- นำไปผ่านกระบวนการ Freeze dry เพื่อไล่น้ำออก ซึ่งจะทำให้ได้เป็นแผ่นเมมเบรนของเส้นใยนาโนเซลลูโลสดังรูป

- เมื่อนำไปทดสอบความเป็นผลึกของ BC ที่ได้ โดยเทคนิค X-ray diffraction (XRD) พบว่าได้ผลดังรูป จะเห็นว่ามีพีคความเป็นผลึกขึ้นหลักๆอยู่ 3 พีค ซึ่งสอดคล้องกับฐานข้อมูลของ BC และตรงกับงานวิจัยอื่นๆก่อนหน้านี้

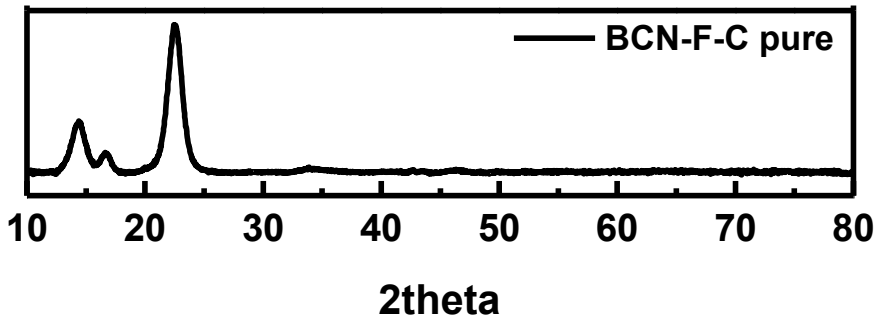

- นำ BC ไปตรวจสอบลักษณะสัณฐานด้วยกล้องจุลทรรศน์อิเล็กตรอน (SEM) พบว่าทั้งที่บริเวณภาคตัดขวางหรือบริเวณผิวหน้าแสดงลักษณะของเส้นใยระดับนาโนที่มีเส้นผ่านศูนย์กลางประมาณ 100 นาโนเมตร ถักทอกันในลักษณะของโครงข่าย 3 มิติ

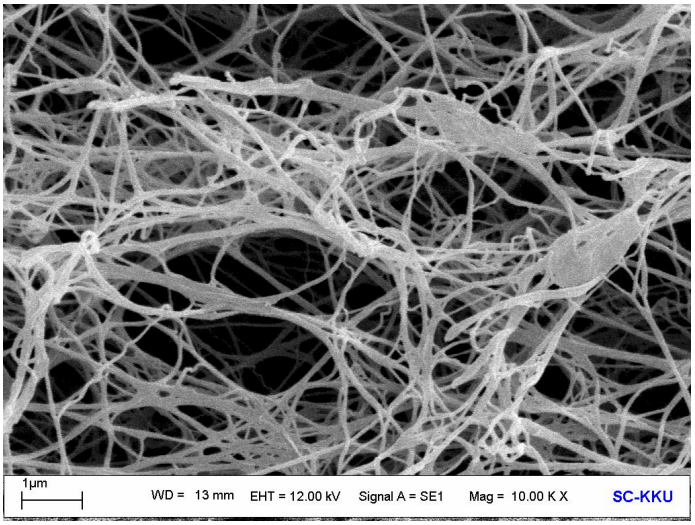

ภาคตัดขวาง

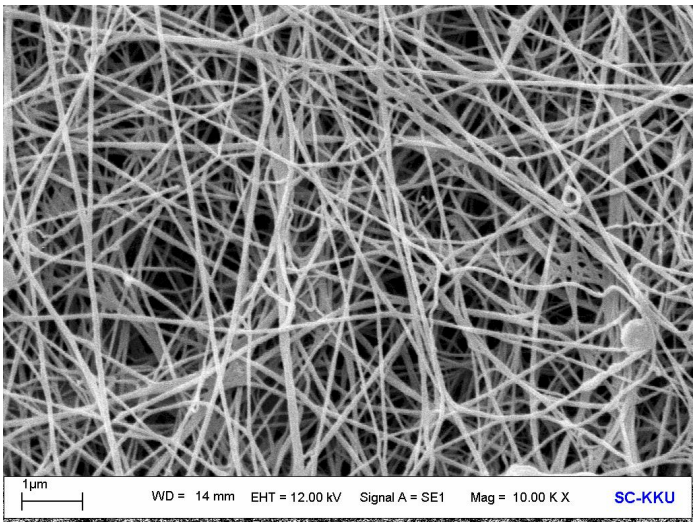

ผิวหน้า

4.2. แบคทีเรียเซลลูโลสคอมโพสิตกับอนุภาคแม่เหล็กนาโนเฟอไรต์

- ได้ทำการสังเคราะห์อนุภาคแม่เหล็กนาโนของเฟอไรต์ชนิดต่างๆ (MFe_2O_4, M = Mn, Co, Ni, และ Cu) ด้วยวิธี co-precipitate ลงในแบคทีเรียเซลลูโลสที่ใช้เป็น template
- ศึกษาเงื่อนของกระบวนการสังเคราะห์และเงื่อนไขให้การทำแห้งแบคทีเรียเซลลูโลส
- ศึกษาลักษณะเฉพาะพร้อมกับสมบัติของวัสดุด้วยเทคนิคต่างๆได้แก่ TG/DTA, FTIR, XRD, SAXS, EDS, VSM,
- ผลการทดลองที่ได้เป็นดังนี้ โดย สัญลักษณ์ตัวย่อ
    - FF หมายถึง แบคทีเรียเซลลูโลสที่ถูกทำแห้งแบบแข็งก่อนกระบวนการสังเคราะห์อนุภาคนาโนเฟอไรต์ หลังจากนั้นทำแห้งแบบแข็งอีกครั้ง
    - FA หมายถึง แบคทีเรียเซลลูโลสที่ถูกทำแห้งแบบแข็งก่อนกระบวนการสังเคราะห์อนุภาคนาโนเฟอไรต์ หลังจากนั้น นำคอมโพสิตที่ได้ไปอบแห้ง
    - NF หมายถึง แบคทีเรียเซลลูโลสที่ไม่ผ่านการทำแห้งก่อนกระบวนการสังเคราะห์อนุภาคนาโนเฟอไรต์ หลังจากนั้นทำแห้งแบบแข็ง
    - NA หมายถึง แบคทีเรียเซลลูโลสที่ไม่ผ่านการทำแห้งก่อนกระบวนการสังเคราะห์อนุภาคนาโนเฟอไรต์ หลังจากนั้น นำคอมโพสิตที่ได้ไปอบแห้ง

- **ผล XRD** พบว่าวัสดุคอมโพสิตเกิดเฟสผลึกผสมระหว่างเฟสของ BC กับเฟสของอนุภาคแม่เหล็กเฟอไรต์ อย่างไรก็ตาม เฉพาะ Co ferrite กับ Mn ferrite เท่านั้น ที่มีการเกิดเฟสของอนุภาคแม่เหล็กที่ชัดเจนในทุกๆเงื่อนไขการเตรียม ซึ่งจะส่งผลดีต่อสมบัติเชิงแม่เหล็ก ส่วน Ni ferrite กับ Cu ferrite นั้นให้พีค XRD ที่ไม่ชัดเจนในทุกเงื่อนไข

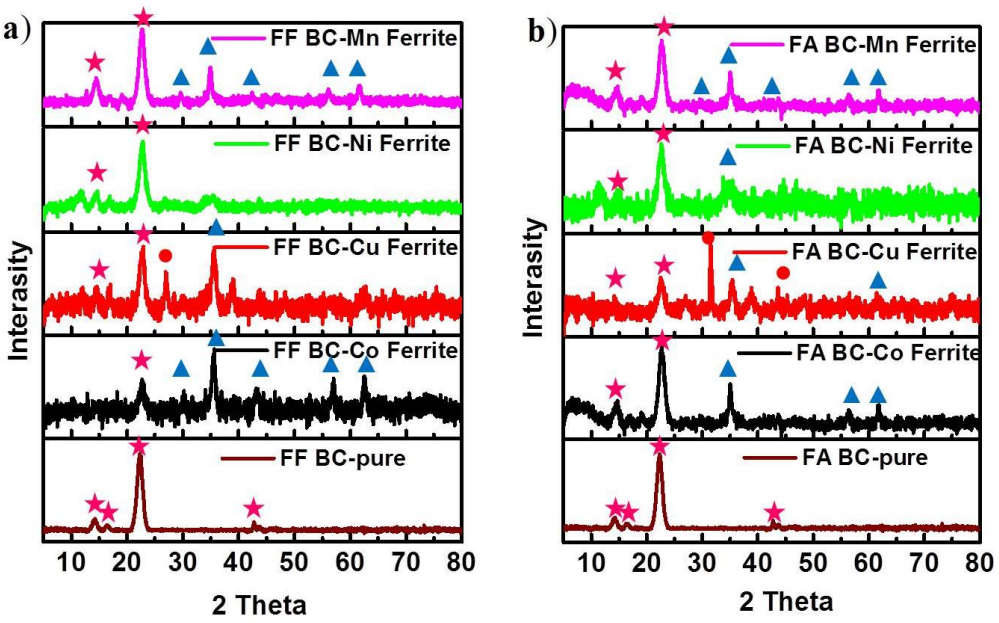

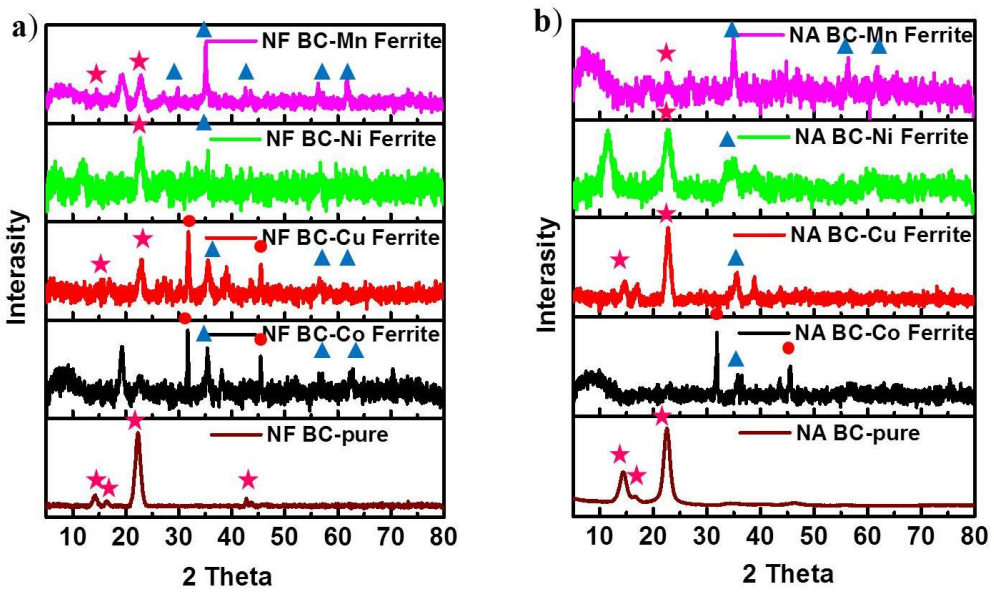

- **ผล FTIR**

ผลการศึกษาด้วยเทคนิค FTIR พบว่า ชิ้นงานทั้งหมดแสดงพีคการดูดกลืนที่ 1055 cm^{-1} และ 3350 cm^{-1} ซึ่งเกี่ยวข้องกับพันธะ C-O-C และ หมู่ –OH ของ BC

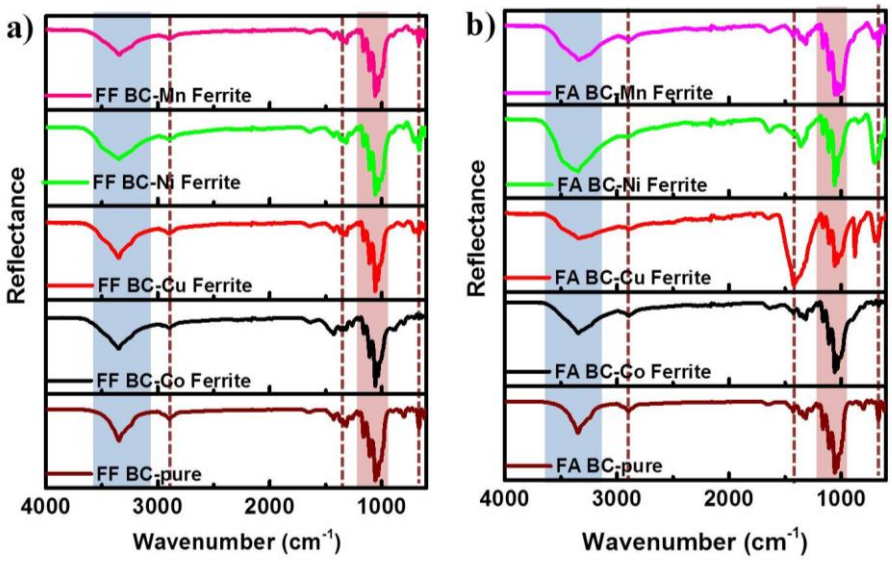

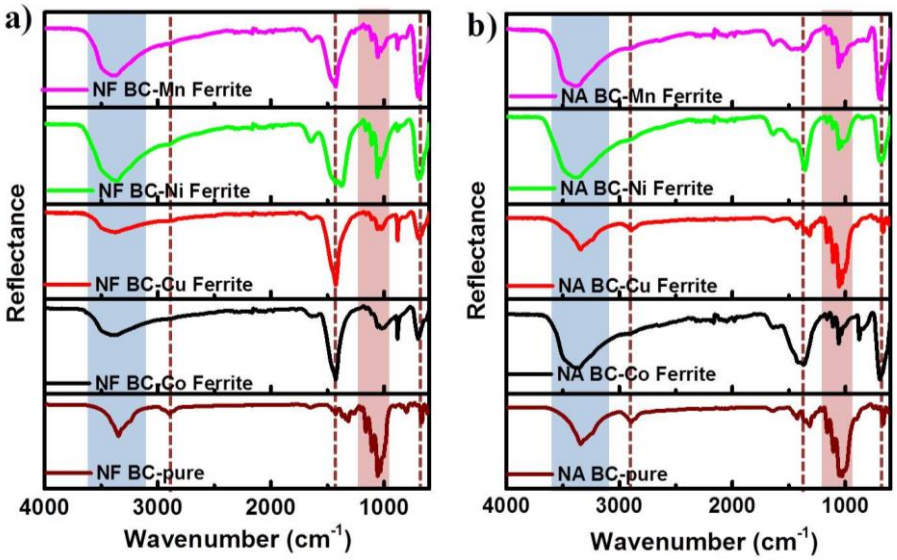

- **ผล VSM**

ผลการศึกษาทางแม่เหล็กพอว่าวัสดุคอมโพสิตที่มีค่าแมกนีไตเซชันสูงที่สุดได้แก่ BC ผสมกับ Co ferrite หรือ Mn ferrite โดยเงื่อนไขการทำแห้งจะส่งผลต่อสมบัติทางแม่เหล็ก วัสดุคอมโพสิตที่ผ่านการทำแห้งด้วยการ freeze dry และ อบ anneal อีกรอบหนึ่ง (ชิ้นงานกลุ่ม FA) จะได้ค่าทางแม่เหล็กที่สูงที่สุด ส่วนวัสดุคอมโพสิตจาก Cu ferrite หรือ Ni ferrite พบว่ามีความเป็นแม่เหล็กอยู่น้อยมาก

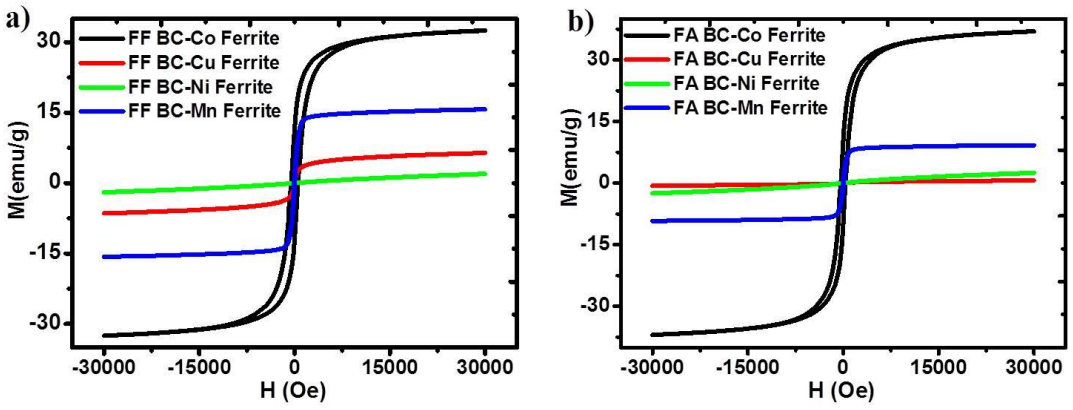

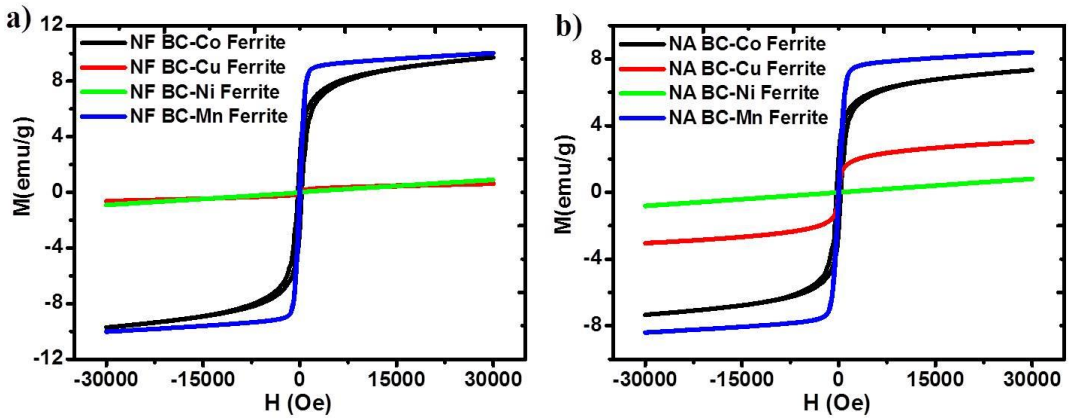

- **ผล SEM**

ผลการวิเคราะห์ด้วยภาพถ่าย SEM พบว่า ชิ้นงานในกลุ่ม FF มีรูปพรุนที่สูงกว่า FA โดยมีขนาดเส้นใยเฉลี่ยอยู่ที่ 100 nm วัสดุคอมโพสิตที่เติม Co ferrite จะสามารถเห็นอนุภาคของ Co ferrite ได้ชัดเจน จึงทำให้สรุปได้ว่าชิ้นงานนี้จึงมีค่าแมกนีไตเซชันที่มากที่สุด

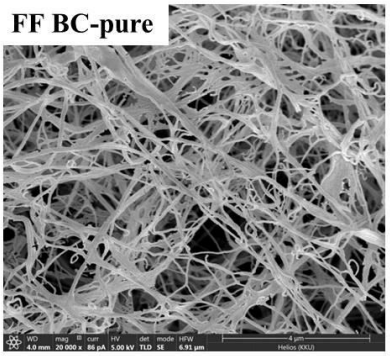

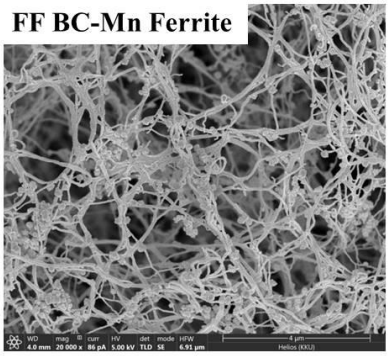

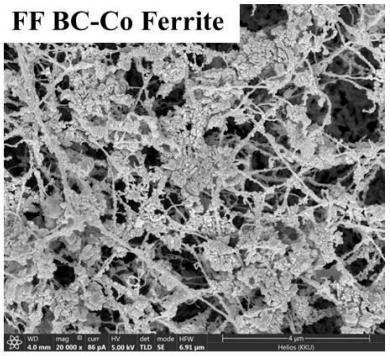

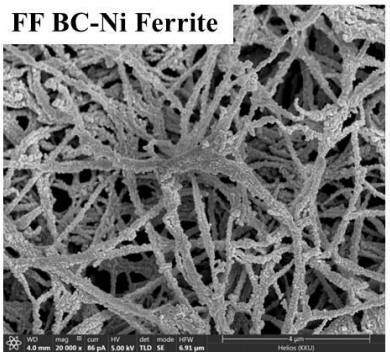

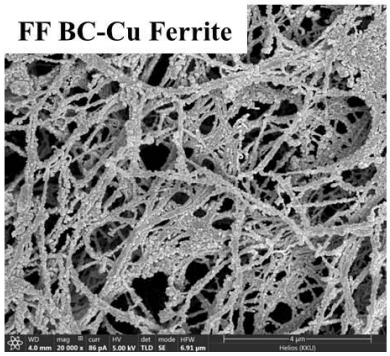

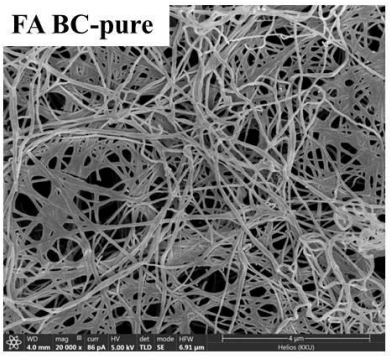

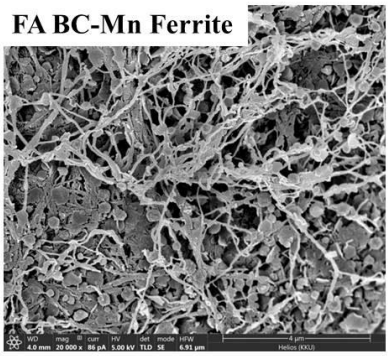

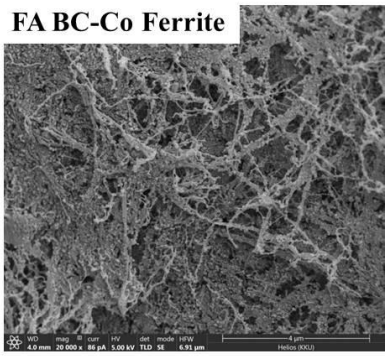

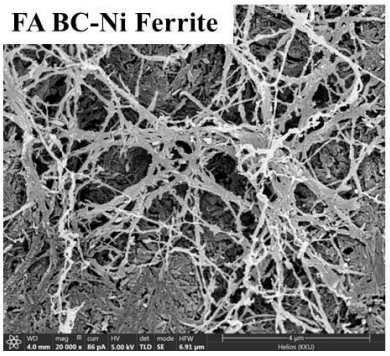

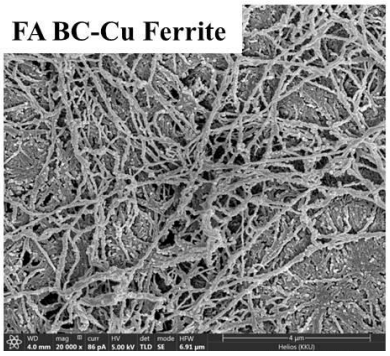

4.3. อนุภาคแม่เหล็กนาโนของโคบอลต์เหล็กแพลทตินัม

- ได้ทำการสังเคราะห์อนุภาคแม่เหล็กนาโนของโคบอลต์เหล็กแพลทตินัม ($Co_{1-x}Fe_xPt$) ด้วยวิธีโพลิออล โดยเปลี่ยนปริมาณของ Co และ Fe จากนั้นเผาเพื่อให้วัสดุเปลี่ยนเฟสเป็นเฟสแม่เหล็กแรงตามที่ต้องการ แล้วทำการวัดลักษณะเฉพาะพร้อมกับสมบัติของวัสดุด้วยเทคนิคต่าง ๆได้แก่ TG/DTA, FTIR, XRD, SAXS, EDS, VSM,
- ผลการทดลองที่ได้ พบว่าสามารถสังเคราะห์อนุภาคนาโน ($Co_{1-x}Fe_xPt$) ได้เฟสบริสุทธิ์ ก่อนการเผา มีขนาดเล็กประมาณ 2-3 nm แต่เมื่อเผาแล้วจะเกิดการเปลี่ยนเฟสเป็นเฟสแม่เหล็กแข็ง และขนาดของอนุภาคใหญ่ขึ้นมาก การปรับเปลี่ยนอัตราส่วน Co กับ Fe พบว่าทำให้สมบัติทางแม่เหล็กเปลี่ยนไป โดยถ้าอัตราส่วน Co:Fe = 0.50:0.50 จะได้ค่าแมกนีไตเซชันอิ่มตัวสูงที่สุด แต่ถ้า Co = 1.00 หรือ Fe = 1.00 จะทำให้ได้ค่า coercivity ที่สูงที่สุด
- ผลการทดลองสรุปได้ดังรูปข้างล่าง

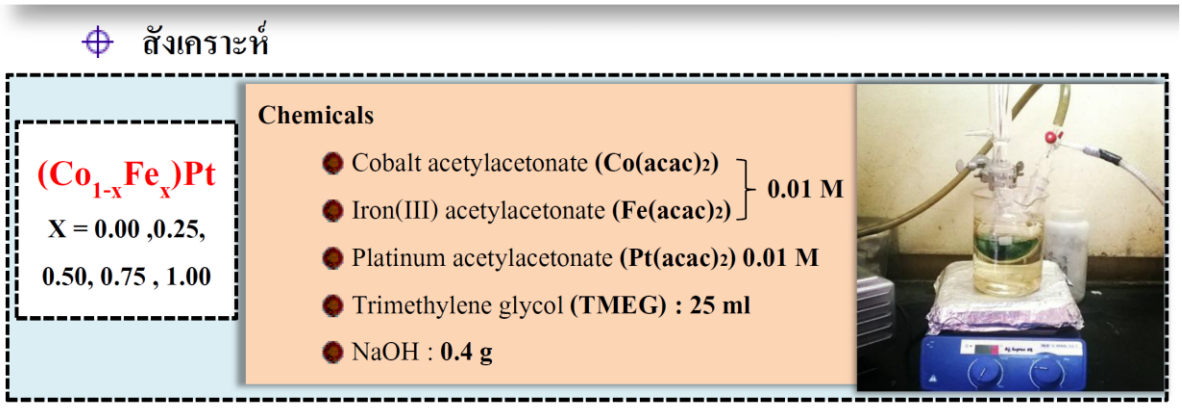

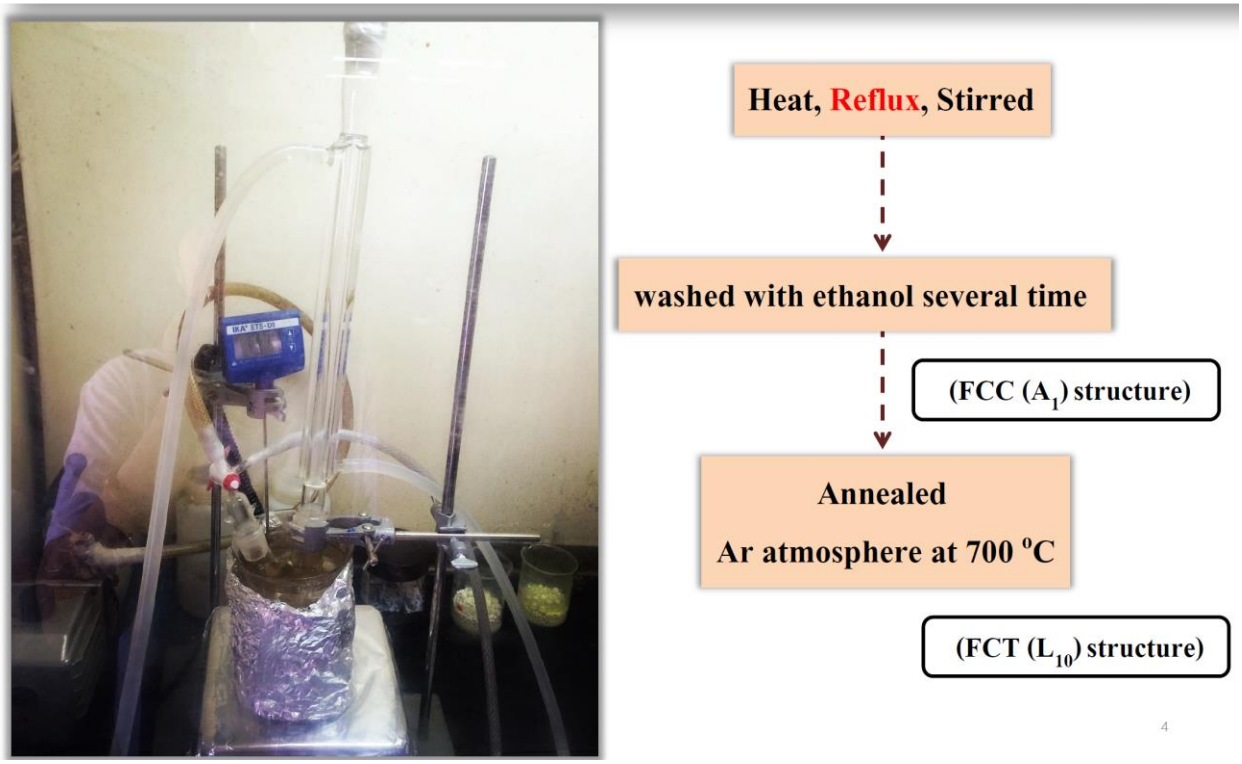

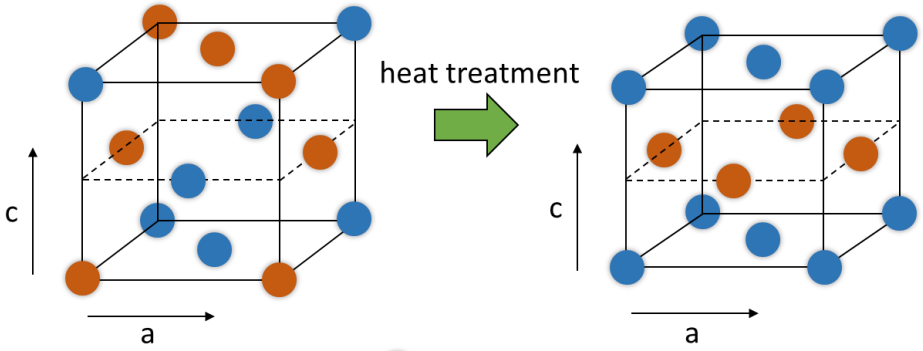

Co (Fe)

Pt

A1 phase
fcc (a = c),
disordered
low K_u

$L1_0$ phase
fct (a ≠ c),
ordered
high K_u

TG-DTA

RT-700 °C

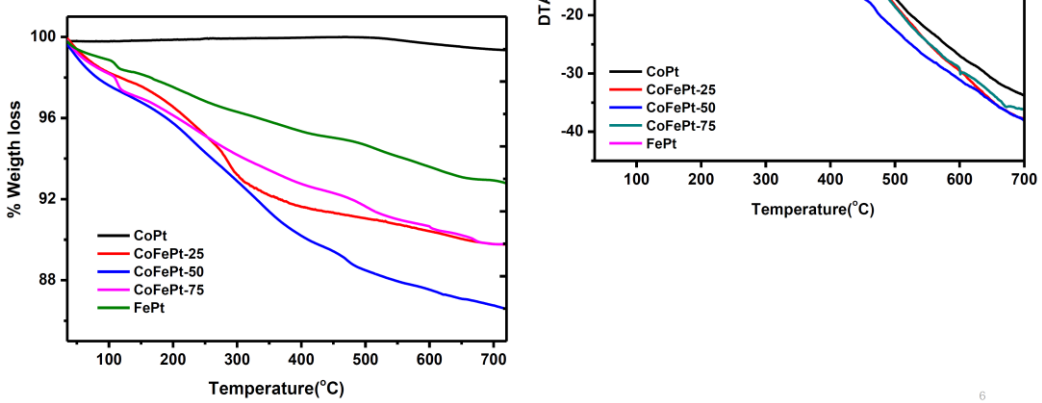

FTIR

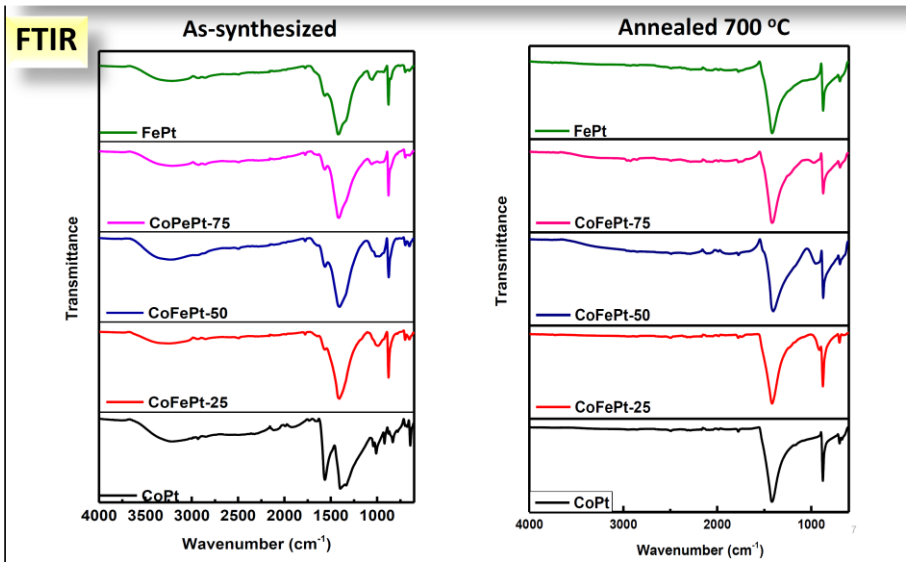

XRD : I

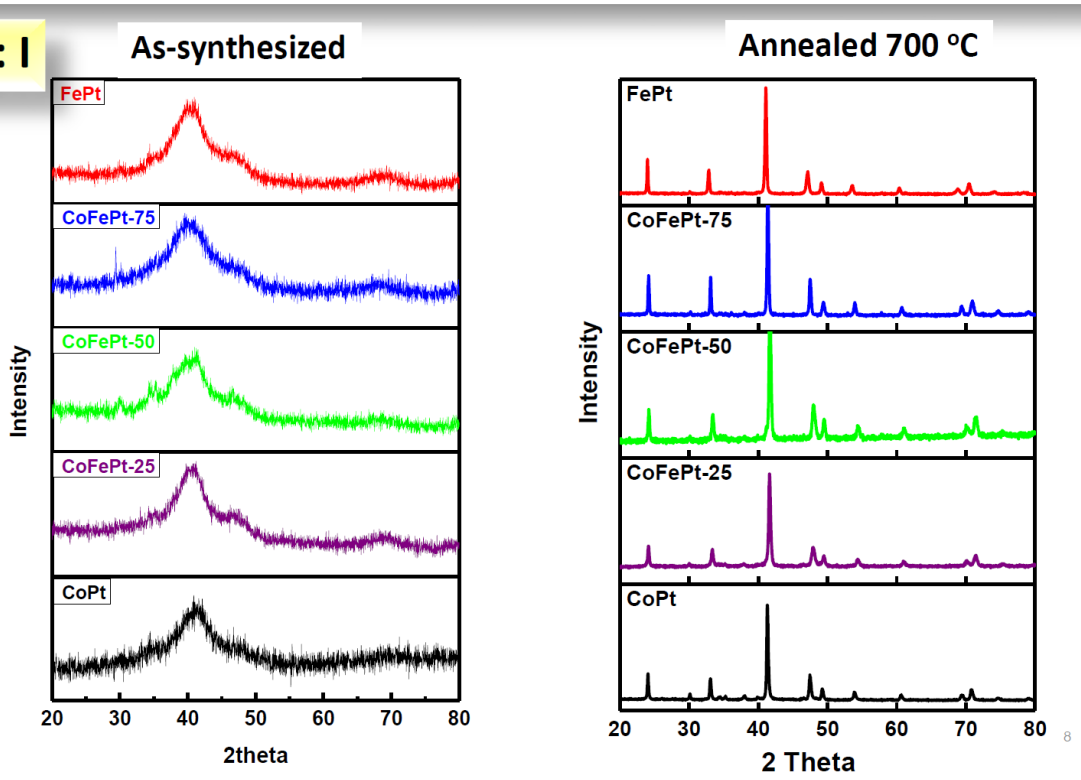

XRD : II

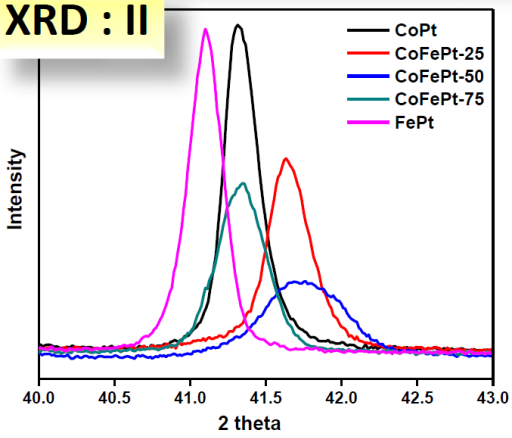

$$2d\sin\theta = n\lambda \quad \text{.....(1)}$$

$$d^2 = \frac{a^2}{h^2+k^2} + \frac{c^2}{l^2} \quad \text{.....(2)}$$

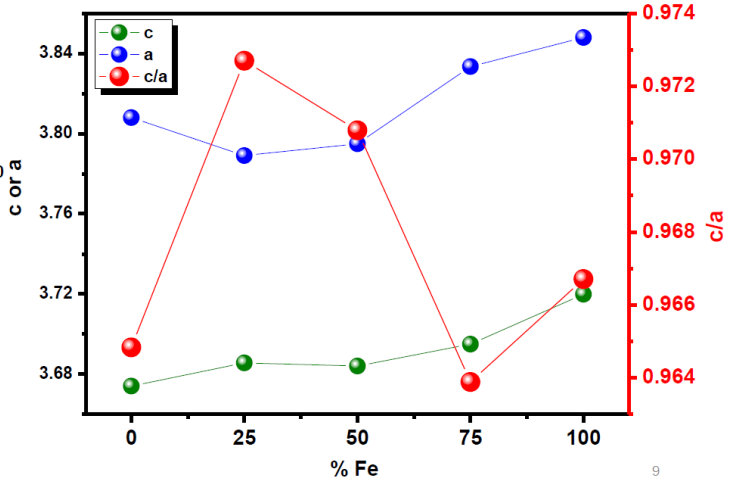

SAXS

Annealed 700 °C

Small-Angle X-ray Scattering (SAXS)

ขนาดรัศมีของอนุภาค

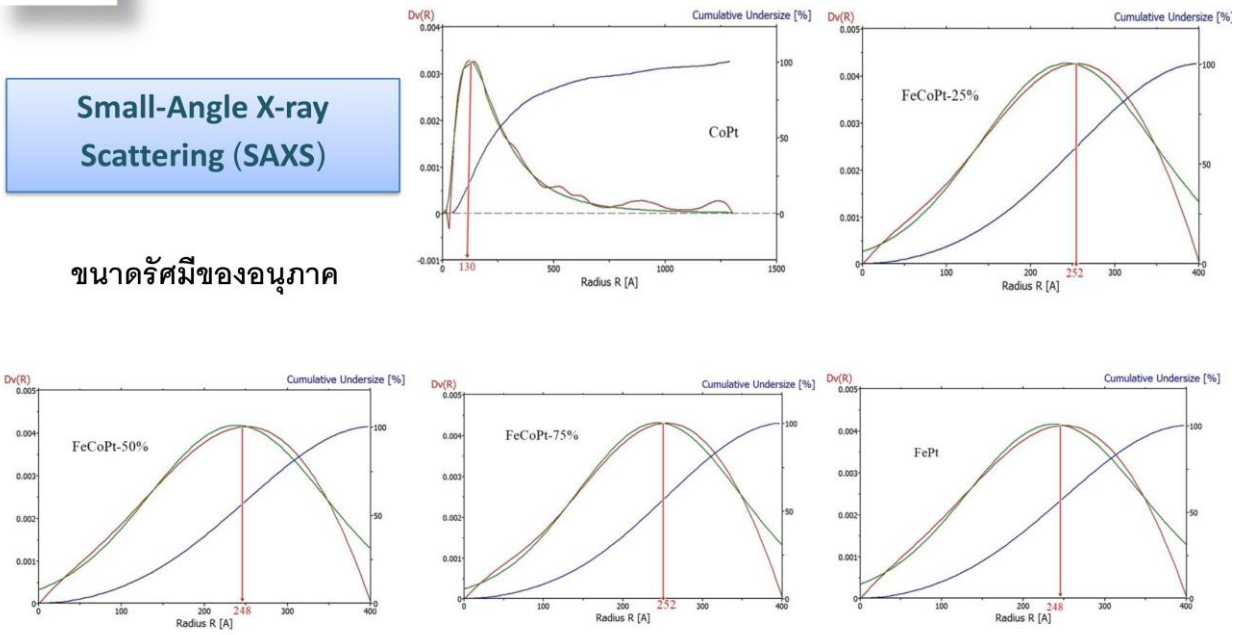

10

EDS

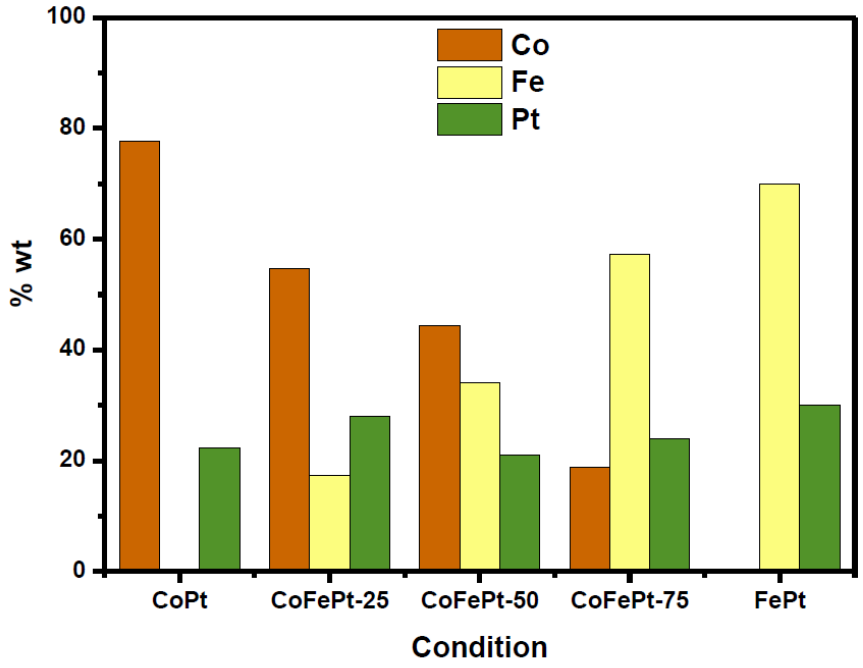

11

VSM : I

M-H 300 K

As-synthesized

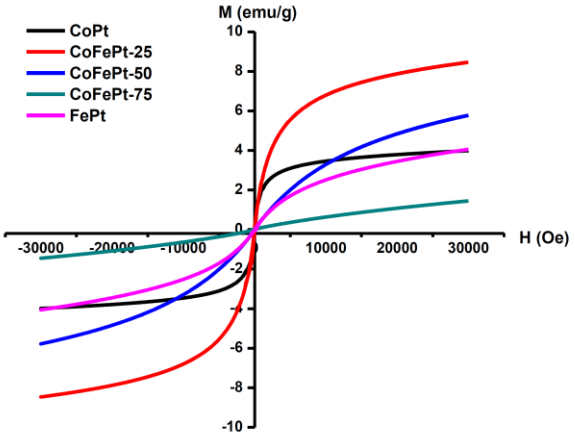

Annealed 700 °C

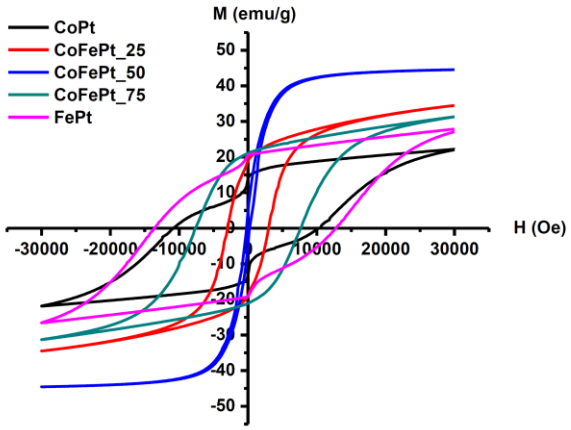

VSM : II

M-H 50 K

As-synthesized

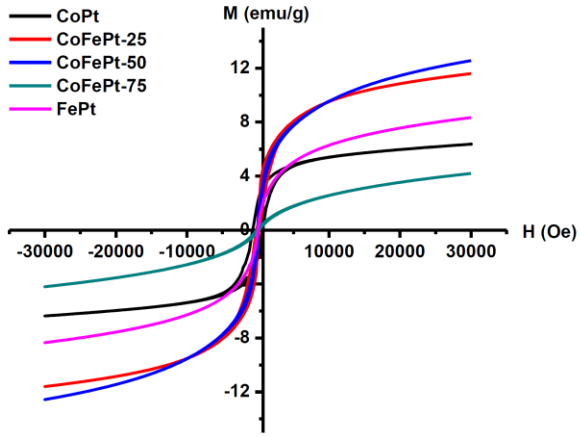

Annealed 700 °C

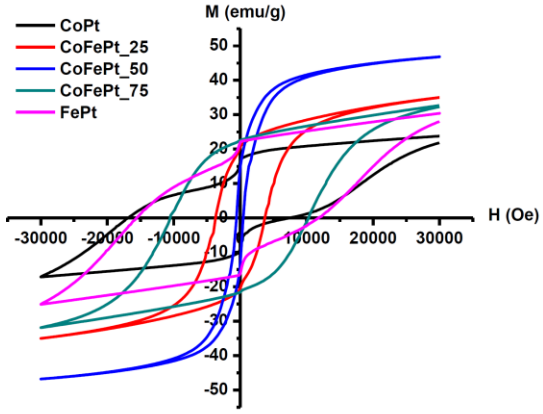

VSM : VI

Annealed 700 °C

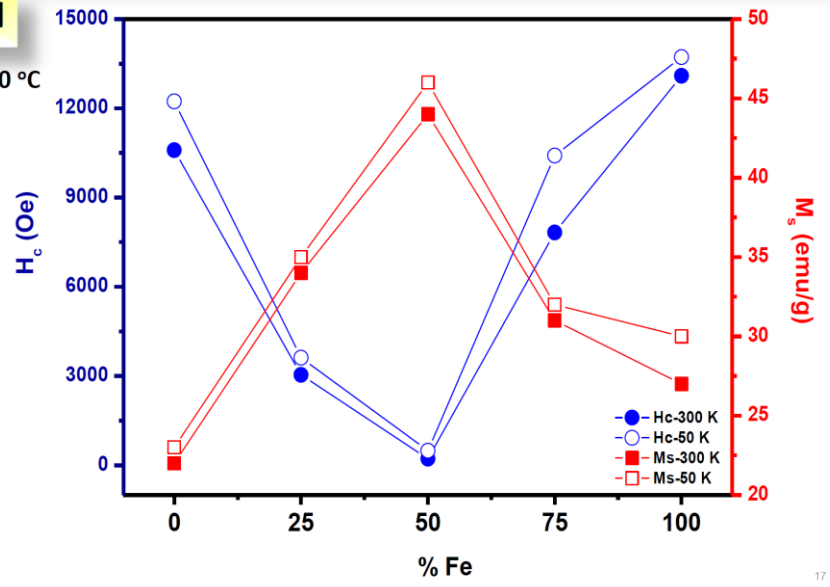

TEM

CoPt NPs As-synthesized

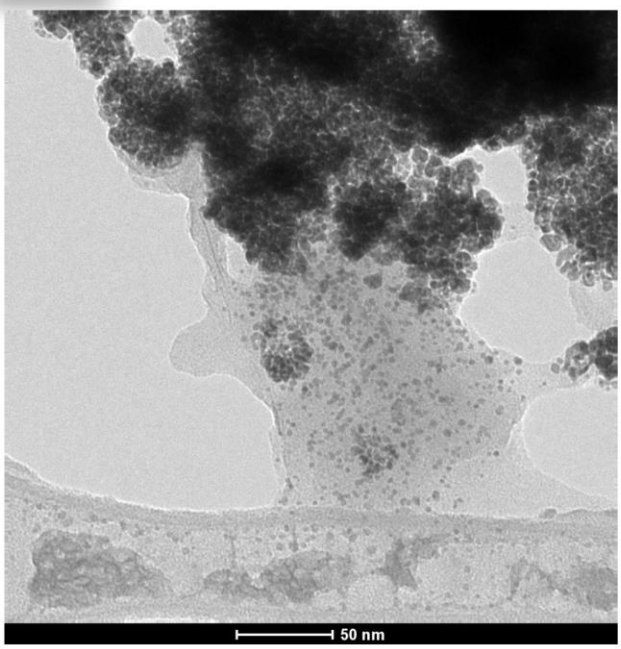

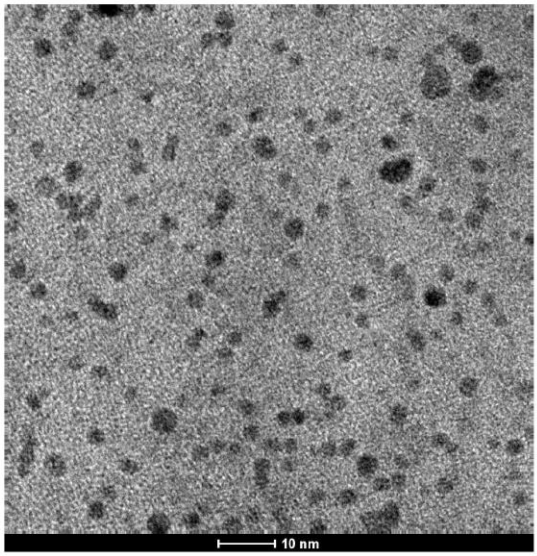

18

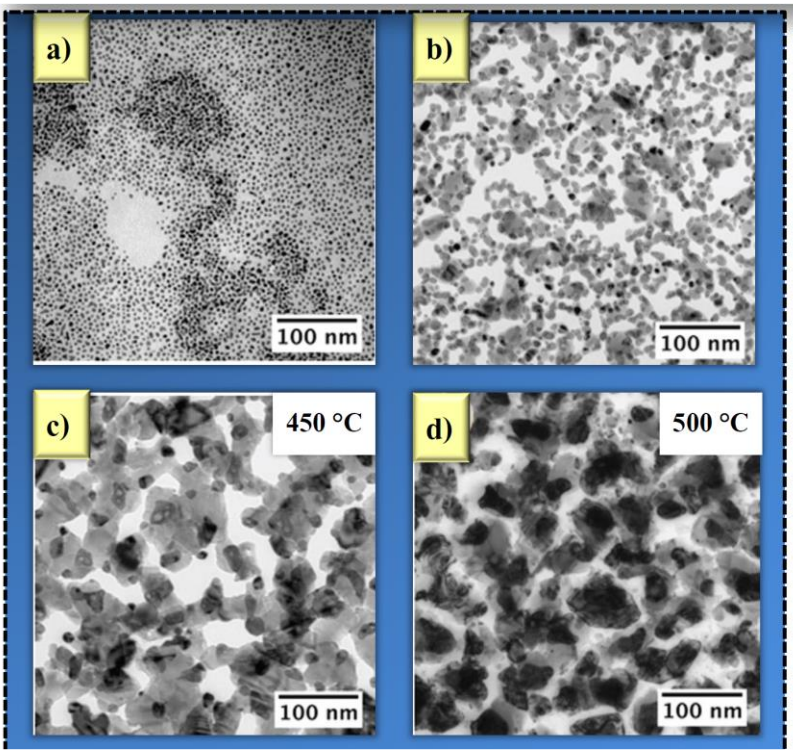

TEM images of CoPt NCs after annealing treatment at 350 °C (a), 400 °C (b), 450 °C (c), 500 °C (d)

20

6

4.4. เส้นใยคาร์บอนนาโนจากแบคทีเรียเซลลูโลสผสมกับอนุภาคแม่เหล็กนาโน

- การเตรียมวัสดุคอมโพสิตของแบคทีเรียเซลลูโลสกับอนุภาคแม่เหล็กนาโน Fe_3O_4 มีขั้นตอนดังรูป กล่าวคือนำแบคทีเรียเซลลูโลสในสถานะไฮโดรเจลจุ่มลงในสารละลาย ferrofluid ที่ประกอบไปด้วยอนุภาค Fe_3O_4 ในน้ำ แช่ทิ้งไว้ที่เวลาและอุณหภูมิที่เหมาะสม จะได้สารประกอบคอมโพสิตตามที่ต้องการ หลังจากนั้นนำไปผ่านกระบวนการไพโรไลซิส เส้นใยเซลลูโลสจะเปลี่ยนสภาพกลายเป็นเส้นใยคาร์บอนนาโน ทำให้ได้คอมโพสิตของเส้นใยคาร์บอนกับอนุภาคแม่เหล็ก

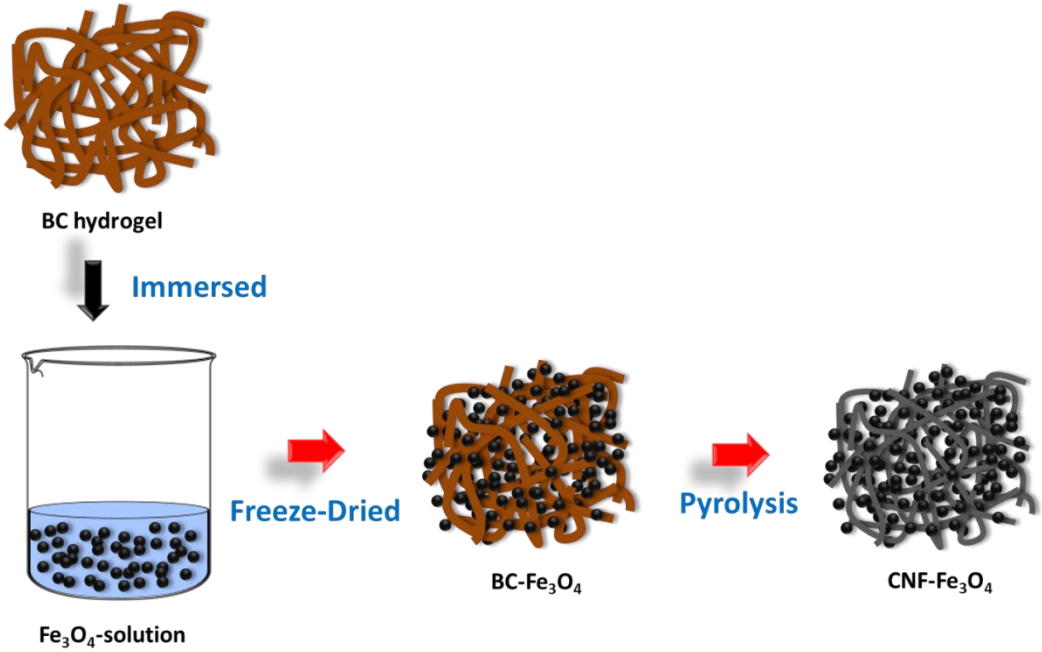

- การศึกษาการเปลี่ยนแปลงทางความร้อนตามปริมาณอนุภาคแม่เหล็กนาโนที่ใส่เข้าไปได้ผลดังรูป ซึ่งจะเห็นได้ว่าเมื่อให้อุณหภูมิสูงกว่า 400 °C จะเกิดการเปลี่ยนแปลงของมวลที่ชัดเจน แสดงว่าเส้นใยเซลลูโลสเกิดการเปลี่ยนเฟสกลายไปเป็นเส้นใยคาร์บอนนาโน

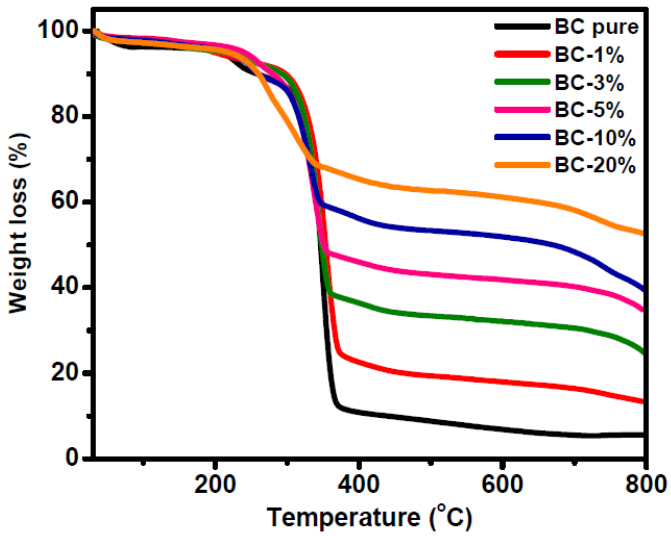

- ผลการทดสอบด้วยเทคนิค FTIR พบว่ามีความแตกต่างอย่างชัดเจนระหว่างแบคทีเรียเซลลูโลส (BC) กับเส้นใยคาร์บอนนาโน (CNF) ดังรูปข้าล่าง ซึ่งจะพบว่าหมู่ฟังก์ชันต่าง ๆที่พบใน BC อาทิเช่น –OH group, C-H stretching, C-O-C หายไป ใน CNF แสดงว่าเกิดการเปลี่ยนเฟสเป็นเส้นใยคาร์บอนนาโน

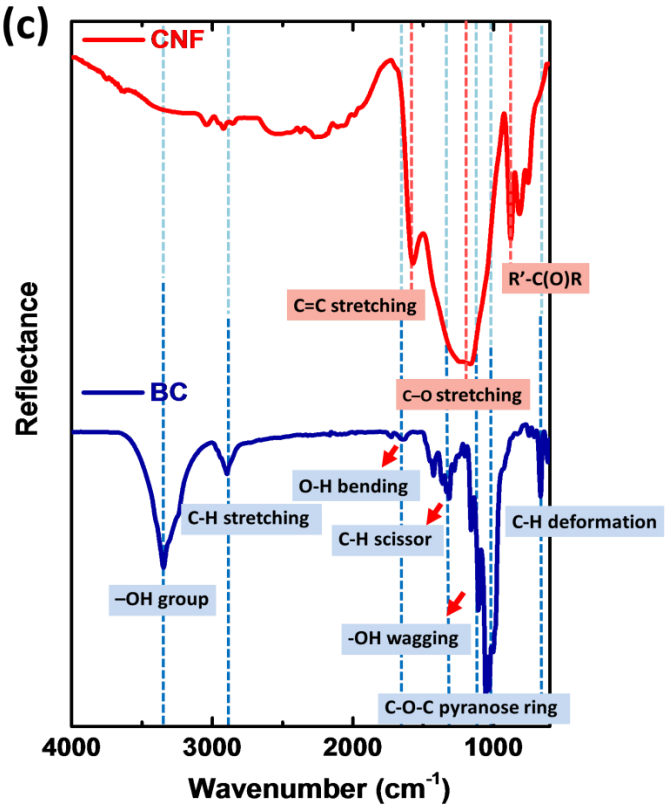

- ผลการทดสอบด้วย XRD พบว่า เมื่อมีการไพโรไลซิส เส้นใยแบคทีเรียเซลลูโลสเกิดการเปลี่ยนเฟสเป็นเส้นใยคาร์บอนนาโน โดยมีกราฟ XRD ที่เปลี่ยนไปอย่างชัดเจน ส่วนปริมาณการเติมอนุภาคแม่เหล็กนาโน ส่งผลให้กราฟ XRD ของเฟส Fe_3O_4 ชัดเจนขึ้น

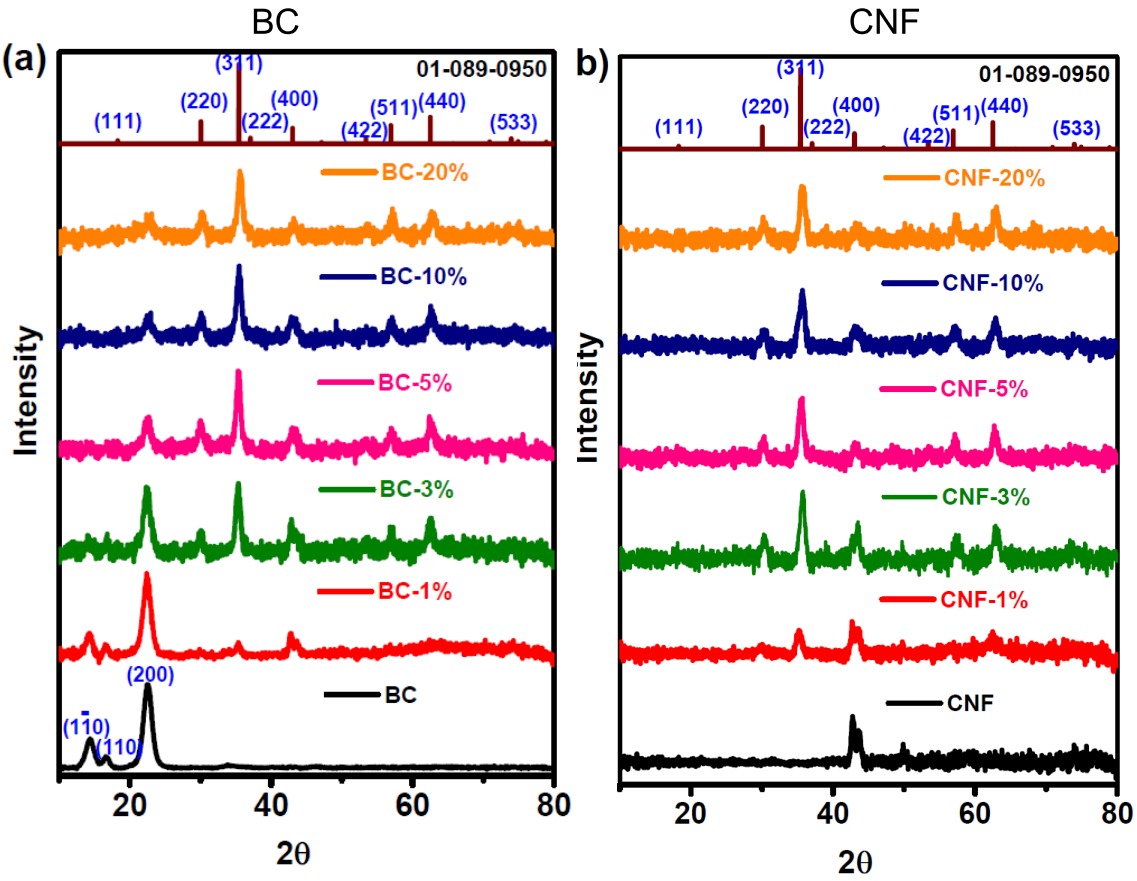

- เมื่อผ่านกระบวนการไพโรไลซิส ถึงแม้ว่า BC จะเปลี่ยนเป็น CNF แต่โครงสร้างเส้นใยนาโน 3 มิติก็ยังอยู่เหมือนเดิม โดยสังเกตได้จากรูป SEM ข้างล่าง อนุภาคแม่เหล็กมีการกระจายตัวที่ดี ยกเว้นที่เติม Fe_3O_4 ในปริมาณมาก (20%) จะได้วัสดุคอมโพสิตที่มีอนุภาคแม่เหล็กกระจุกตัวกัน

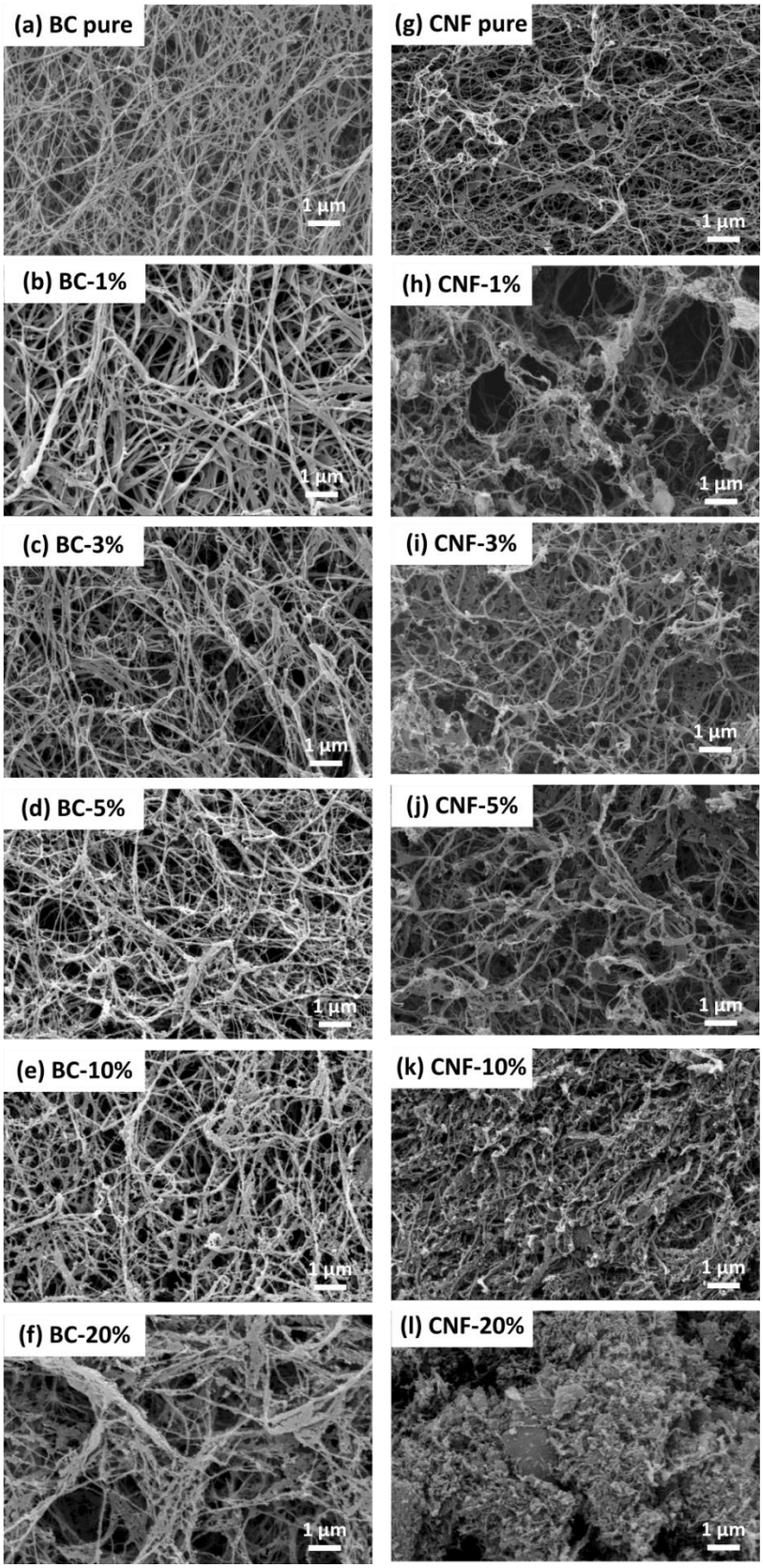

- เมื่อนำไปทดสอบด้วยเทคนิค TEM พบว่าเส้นใยแบคทีเรียเซลลูโลสมีอนุภาคแม่เหล็กกระจายตัวอยู่อย่างสม่ำเสมอ โดยการวิเคราะห์องค์ประกอบของธาตุโดยเทคนิค EDX สามารถยืนยันได้ว่าอนุภาคดังกล่าวเป็นเฟส Fe_3O_4

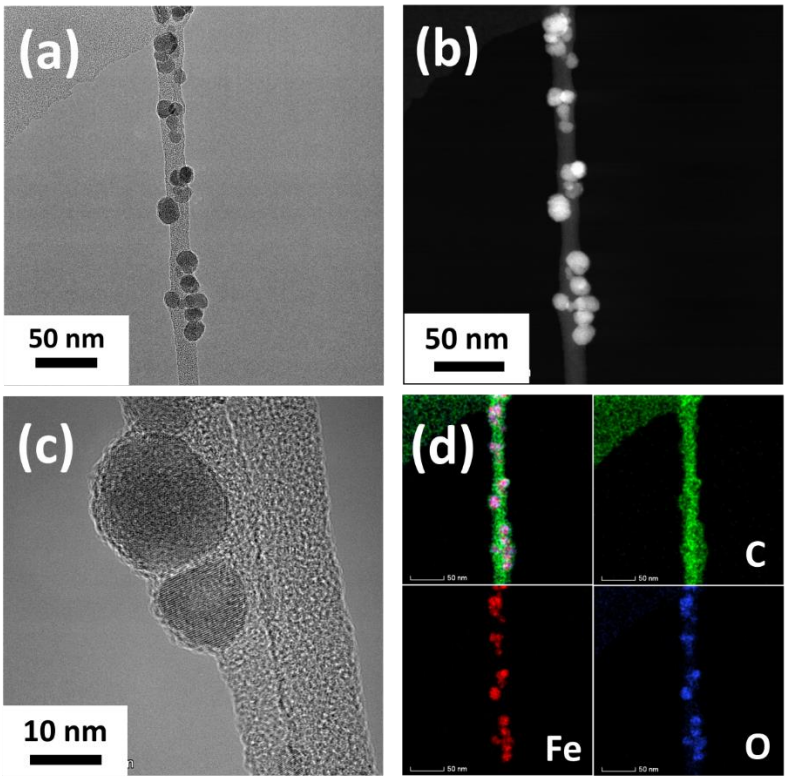

- ภาพถ่าย SEM ของวัสดุคอมโพสิตเส้นใยคาร์บอนนาโน/อนุภาค Fe_3O_4

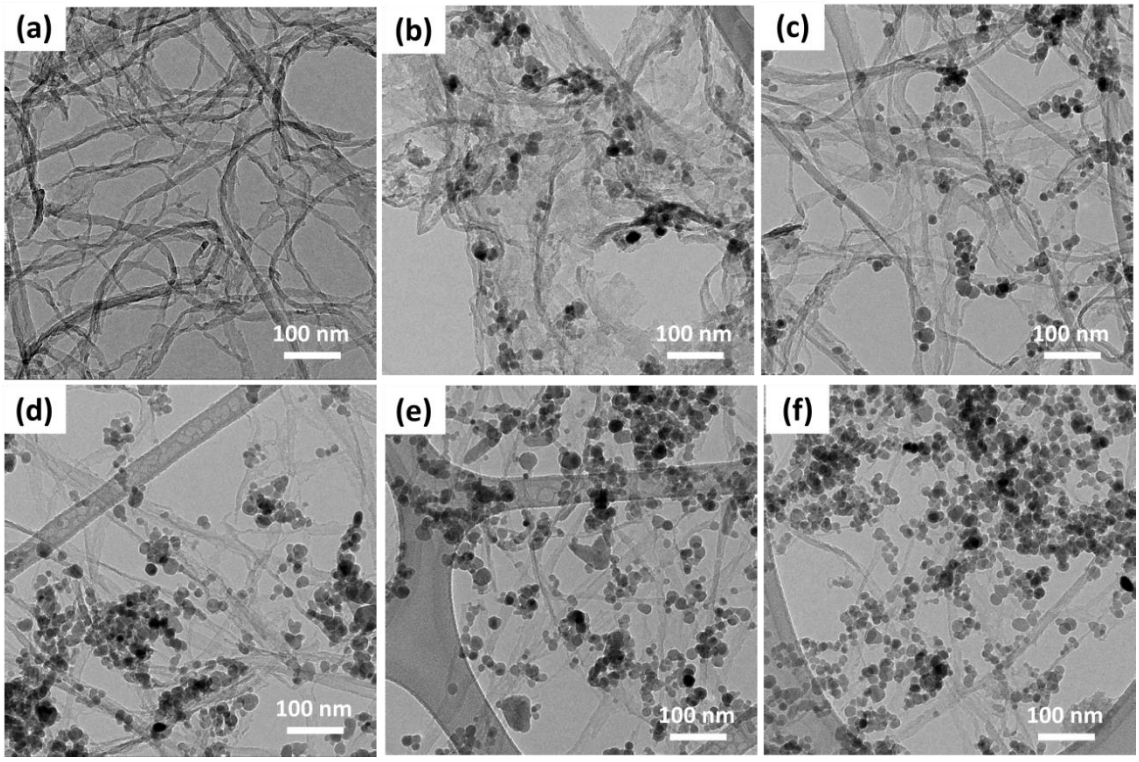

- ผลการวัดสมบัติแม่เหล็กของ BC/Fe_3O_4 และ CNF/Fe_3O_4 จะเห็นได้ว่าค่าแมกนีไตเซชันอิ่ม (M_s) ตัวของวัสดุทั้งสองชนิดเพิ่มขึ้นตามปริมาณแม่เหล็กที่เติมเข้าไป แต่ CNF/Fe_3O_4 มีค่า M_s สูงกว่า BC/Fe_3O_4 มาก

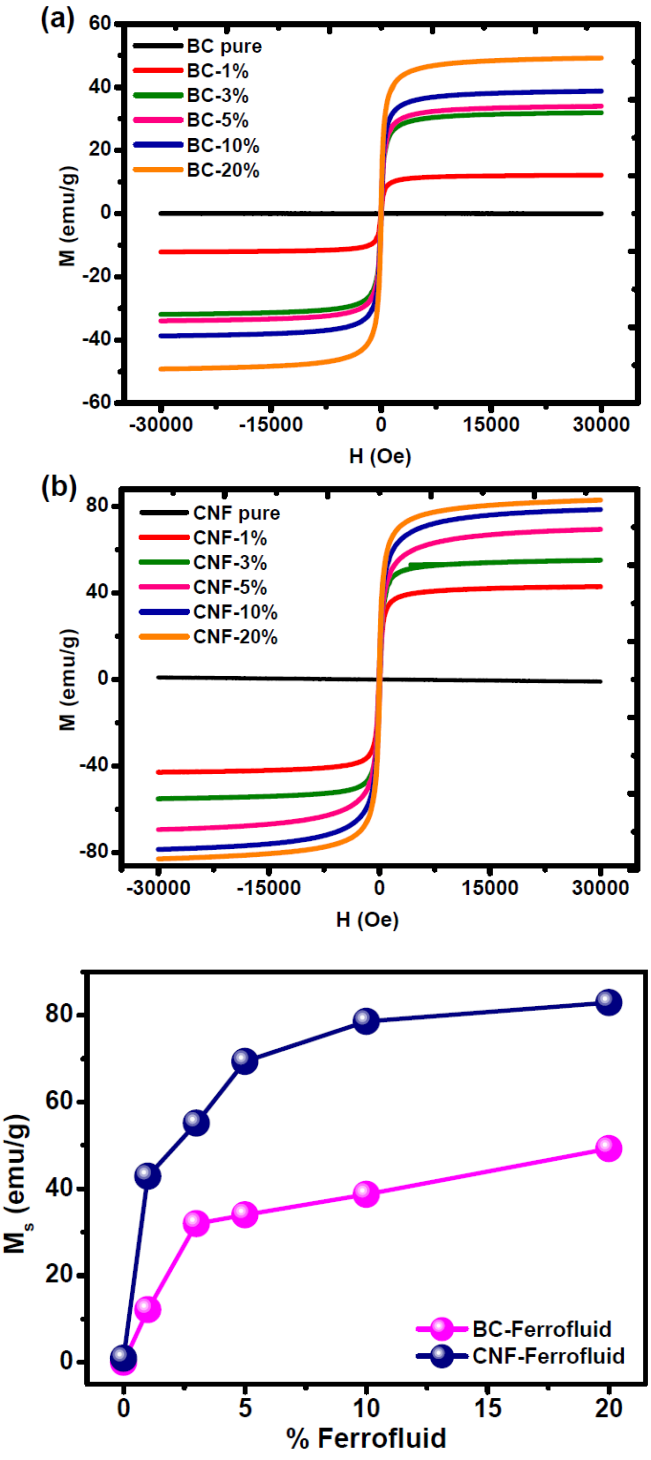

4.5. การศึกษาแผ่นแบคทีเรียเซลลูโลสที่มีความยืดหยุ่นและมีสมบัติแม่เหล็ก (Magnetically responsive and flexible bacterial cellulose membranes)

- ในงานวิจัยส่วนนี้ได้นำเสนอวิธีใหม่ในการสังเคราะห์แผ่นเมมเบรน bacterial cellulose (BC) ซึ่งมีสมบัติแม่เหล็ก membrane ด้วยการจุ่มแผ่น BC ลงในสารละลาย ferrofluid ซึ่งประกอบไปด้วยอนุภาคแม่เหล็กนาโนกระจายตัวอยู่ในสารละลาย เรียกวิธีนี้ว่าวิธี simple diffusion วิธีการนี้ง่ายกว่าวิธีที่ผ่านๆมาและไม่ทำลายโครงสร้างของแผ่น BC นอกจากนี้ยังทดสอบผลของกระบวนการ freeze-dried ต่อวิธีการสังเคราะห์และแผ่นเมมเบรน BC ที่ได้ ซึ่งกระบวนการสังเคราะห์ทั้งหมดในงานวิจัยนี้สรุปได้ดังรูปข้างล่าง

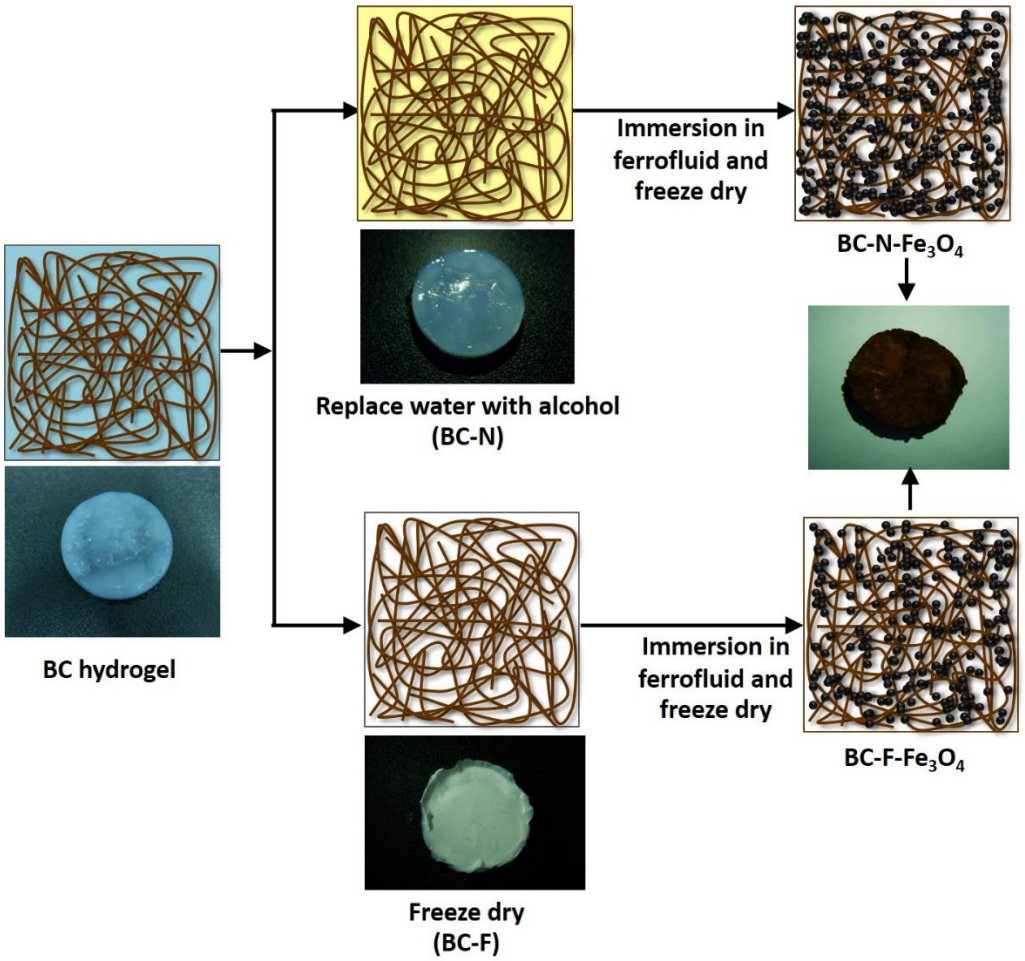

- การวิเคราะห์ด้วยเทคนิค XRD พบว่า ได้เฟสที่เป็นผลึกของ BC และของอนุภาคแม่เหล็กนาโน Fe_3O_4 ซึ่งความสูงของ peak XRD ขึ้นกับปริมาณของ ferrofluid ที่ใส่เข้าไป ส่วนเทคนิค SEM ให้ข้อมูลขนาดของอนุภาคแม่และการกระจายตัวของอนุภาค ซึ่งพบว่าอนุภาคมีขนาดประมาณ 80 – 100 nm และมีการกระจายตัวที่ดี ต่างจากงานวิจัยก่อนหน้านี้ที่จะพบการกระจุกตัวของอนุภาค

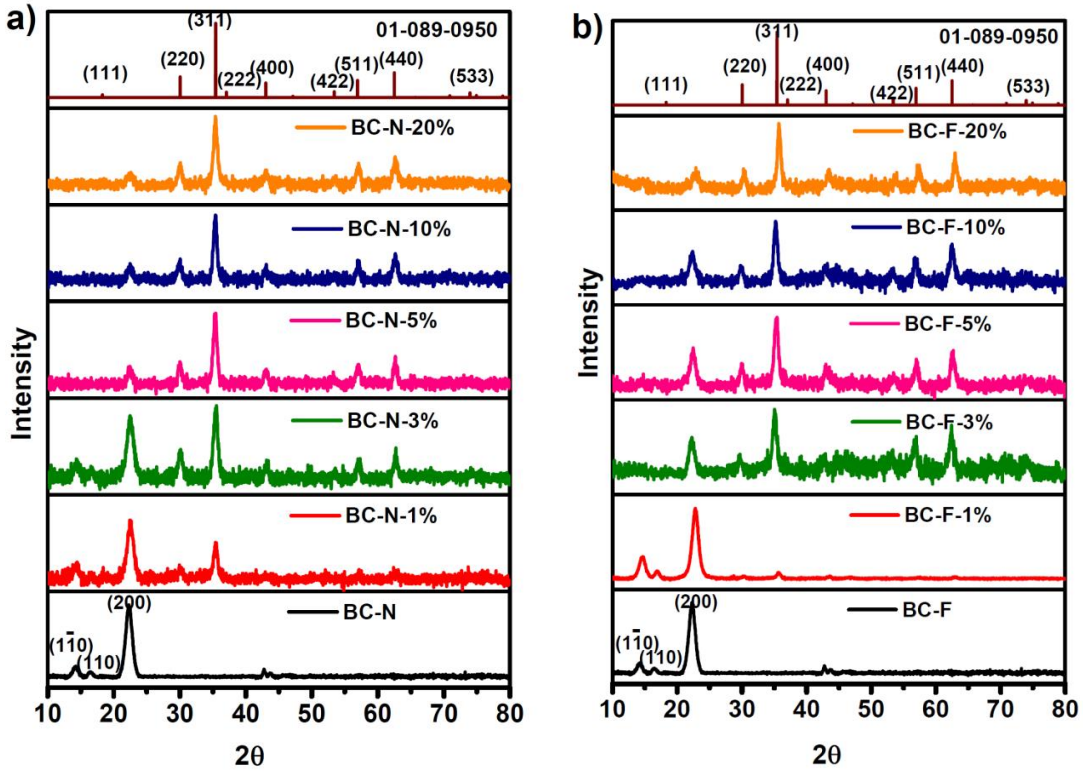

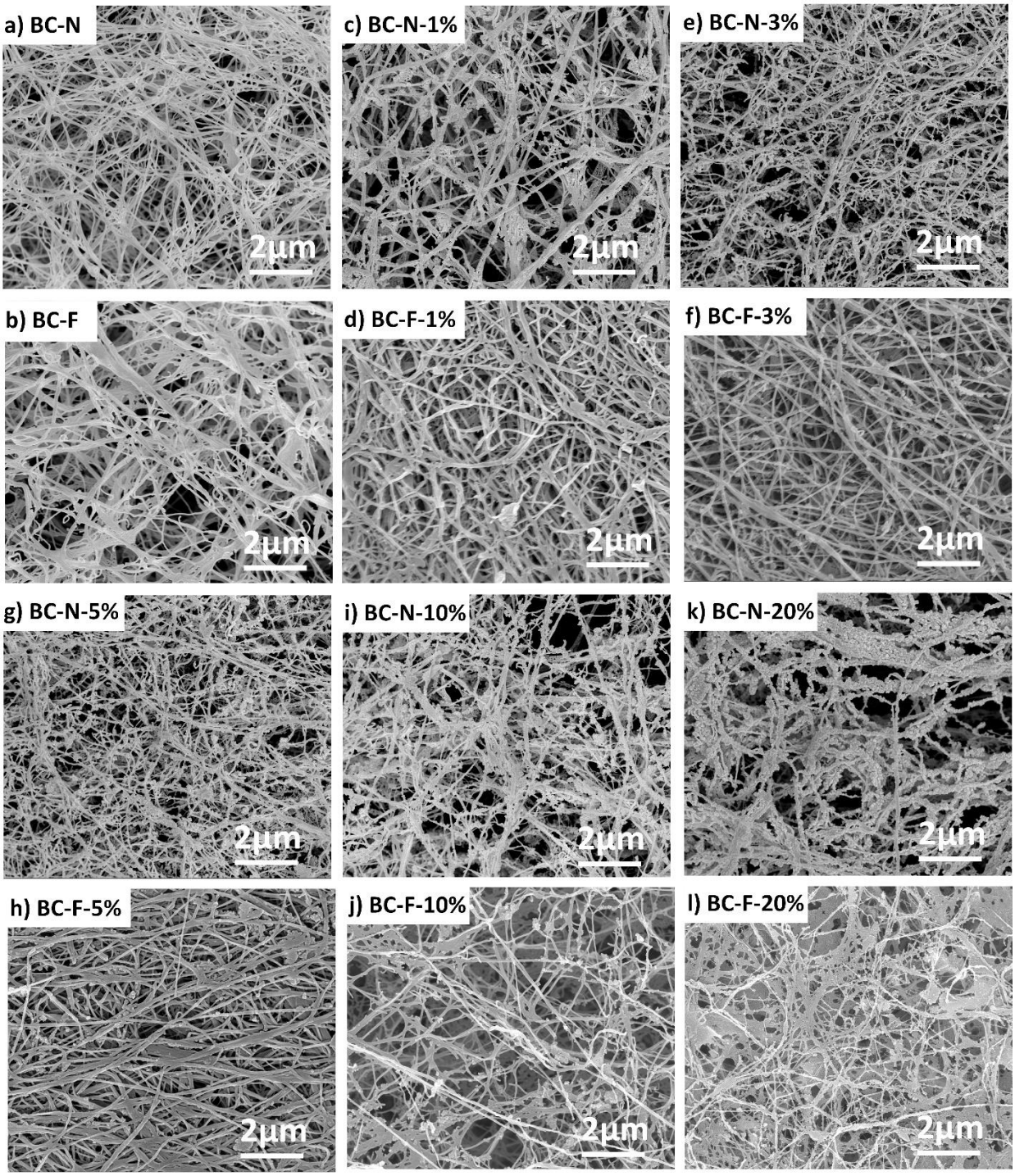
a) BC-N
2μm
c) BC-N-1%
2μm
e) BC-N-3%
2μm
b) BC-F
2μm
d) BC-F-1%
2μm
f) BC-F-3%
2μm
g) BC-N-5%
2μm
i) BC-N-10%
2μm
k) BC-N-20%
2μm
h) BC-F-5%
2μm
j) BC-F-10%
2μm
l) BC-F-20%
2μm

- สาเหตุที่อนุภาคแม่เหล็กนาโนกระจายตัวได้ดีกว่าเทคนิคอื่นๆ คาดว่ามาจากสาเหตุดังนี้ ในวิธีอื่นที่นิยมใช้คือ In situ co-precipitation จะเริ่มต้นจากไอออนของ Fe^{2+} และ Fe^{3+} ซึ่งมีประจุบวก จึงมักจะกระจุกตัวกันที่หมู่ –OH ของ BC แต่วิธี simple diffusion เริ่มต้นด้วยอนุภาคของ Fe_3O_4 ซึ่งเป็นกลางทางไฟฟ้า จึงทำให้อนุภาคสามารถเกาะได้ทุกบริเวณของ BC จึงมีการกระจายตัวอย่างสม่ำเสมอ

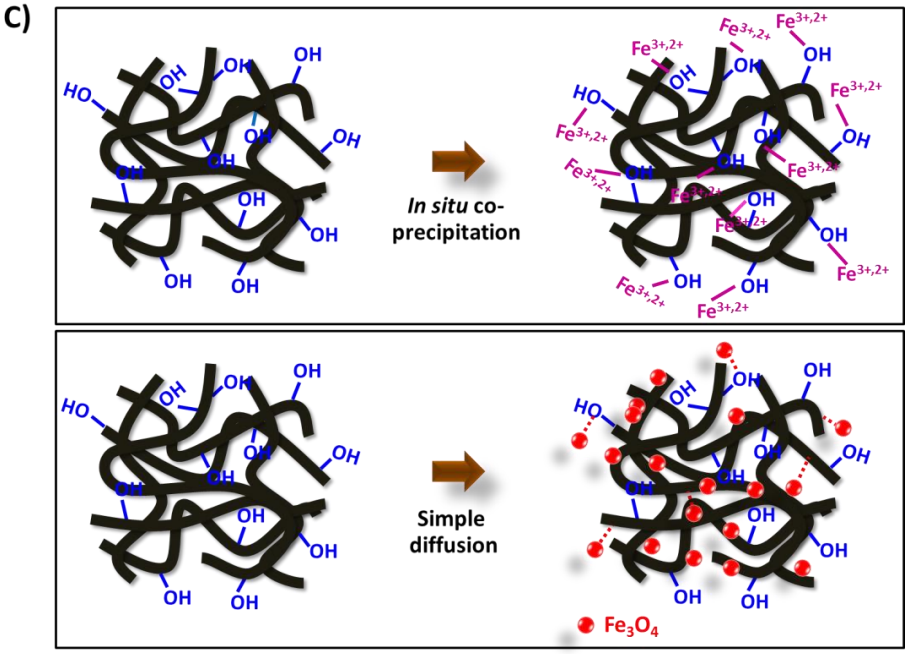

- ผลการทดสอบความแข็งแรงด้วยเทคนิค Tensile test พบว่าความแข็งแรงสามารถเพิ่มขึ้นได้หากใส่อนุภาคแม่เหล็กนาโนในปริมาณที่ไม่มากเกินไป

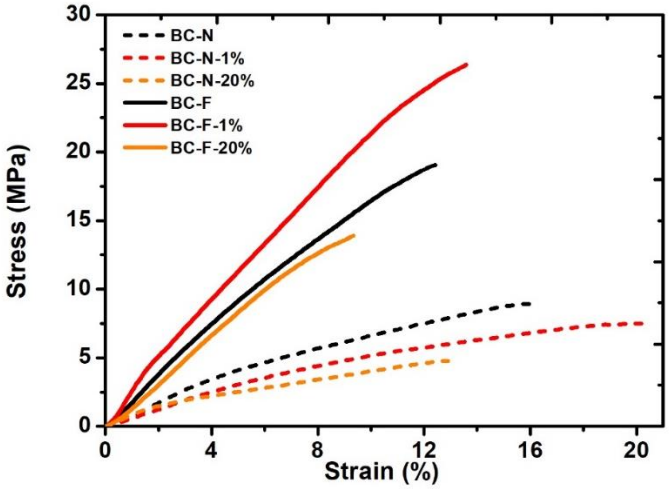

- ผลการทดสอบสมบัติทางแม่เหล็กพบว่าได้สมบัติแม่เหล็กแบบ superparamagnetic มีค่าแม่เหล็กอิ่มตัว (Saturation magnetization, M_s) เพิ่มขึ้นตามปริมาณ ferrofluid ที่ใส่เข้าไป และยังสัมพันธ์กับปริมาณมวลที่หลงเหลือจากการทดสอบด้วยเทคนิค TG-DTA นอกจากนี้ยังพบว่า sample ที่ผ่านการ Freeze-dried (FD) จะมีค่าแม่เหล็กต่ำกว่าที่ไม่ได้ผ่านการ Freeze-dried

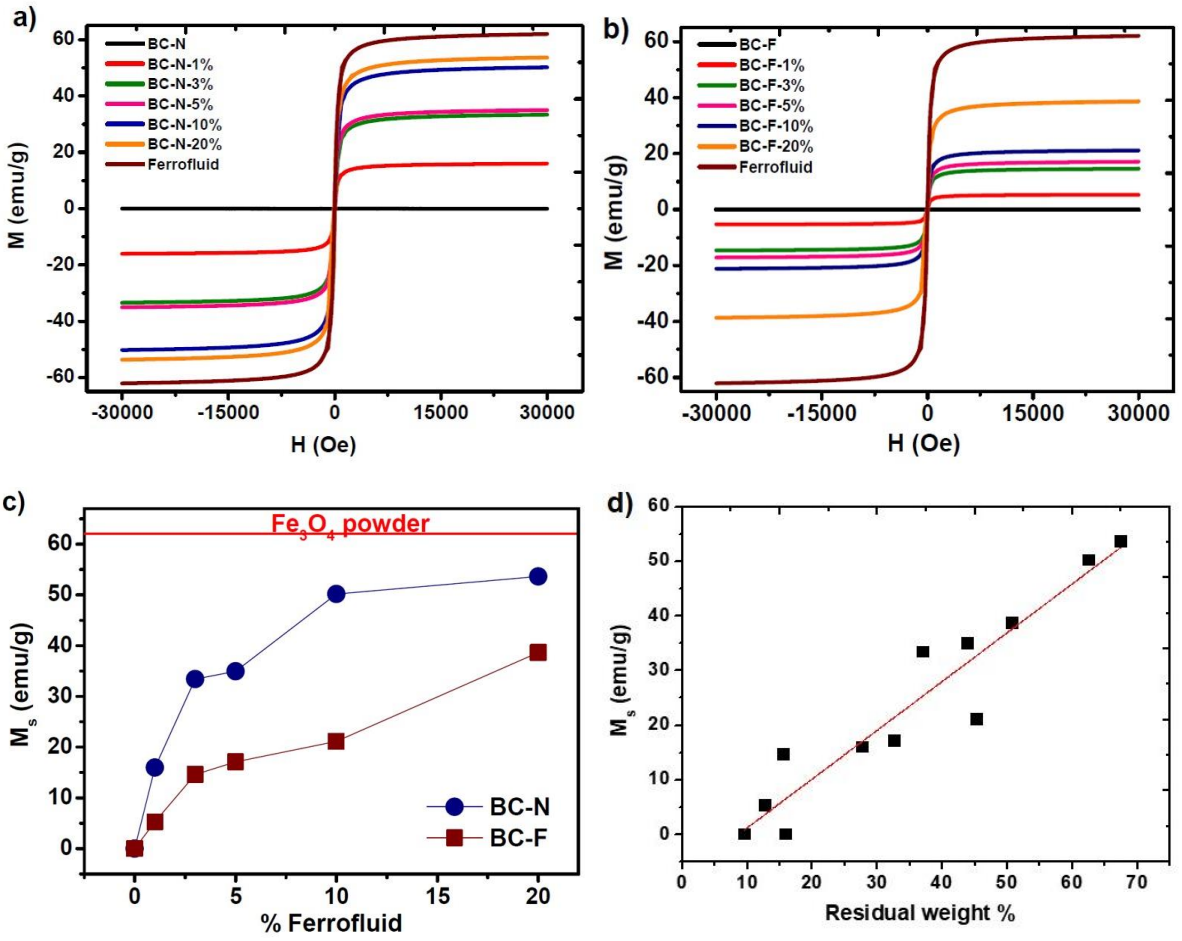

- เมื่อนำแผ่นเมมเบรน BC แม่เหล็กไปทดสอบการตอบสนองกับแม่เหล็กจากภายนอก พบว่าสามารถดูดจับกับแท่งแม่เหล็กถาวรได้ และตอบสนองกับแม่เหล็กภายนอกได้ดีมากทั้งกับสนามแม่เหล็กแบบทางเดียวหรือเปลี่ยนทิศทางตามความถี่

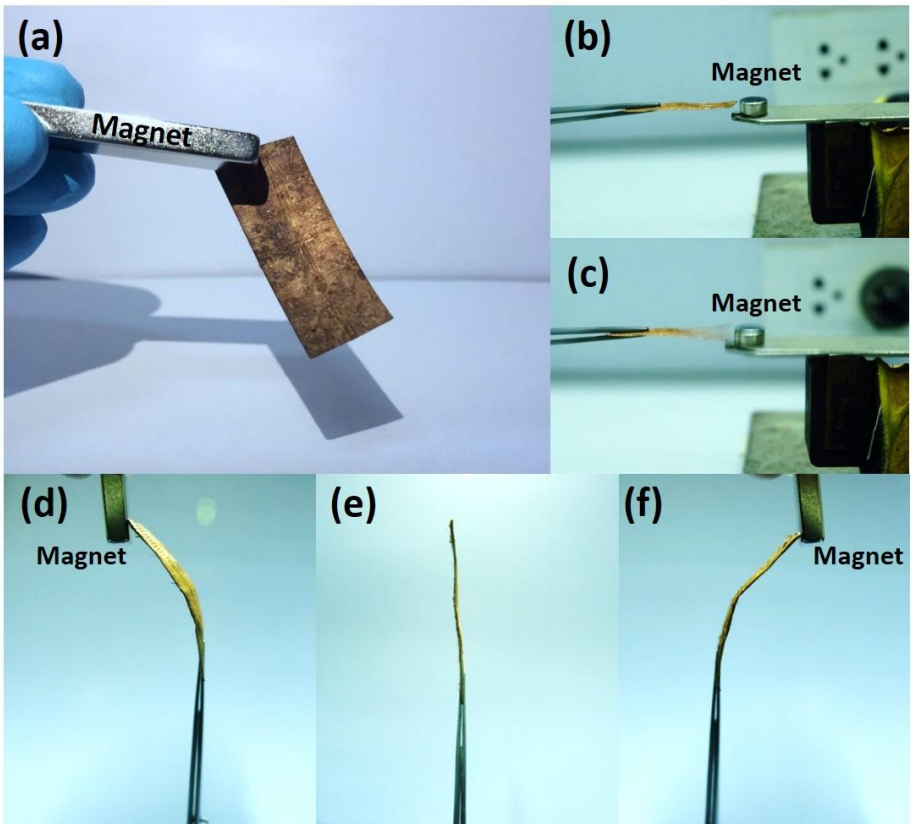

4.6. การสังเคราะห์กระดาษแม่เหล็กสีขาวจากแบคทีเรียเซลลูโลสคอมโพสิต (White magnetic paper based on bacterial cellulose nanocomposite)

- ได้ทำการประดิษฐ์กระดาษแม่เหล็กสีขาวของการคอมโพสิตของแผ่นเมมเบรน BC ในส่วนของกระดาษแม่เหล็กได้สังเคราะห์อนุภาคแม่เหล็กนาโนของโคบอลต์เฟอไรต์ในโครงสร้างของ BC (MBC) ส่วนกระดาษสีขาวได้จากการสังเคราะห์อนุภาคนาโน ZnO ในโครงสร้าง BC (BC) จากนั้นนำแผ่นทั้งสองชนิดมาประกบกันในลักษณะแซนวิช ZBC/MBC/ZBC ก่อนนำไปอบด้วยความร้อน
- ขั้นตอนการสังเคราะห์กระดาษแม่เหล็กสีขาวจาก BC สามารถสรุปได้ดังรูปข้างล่าง

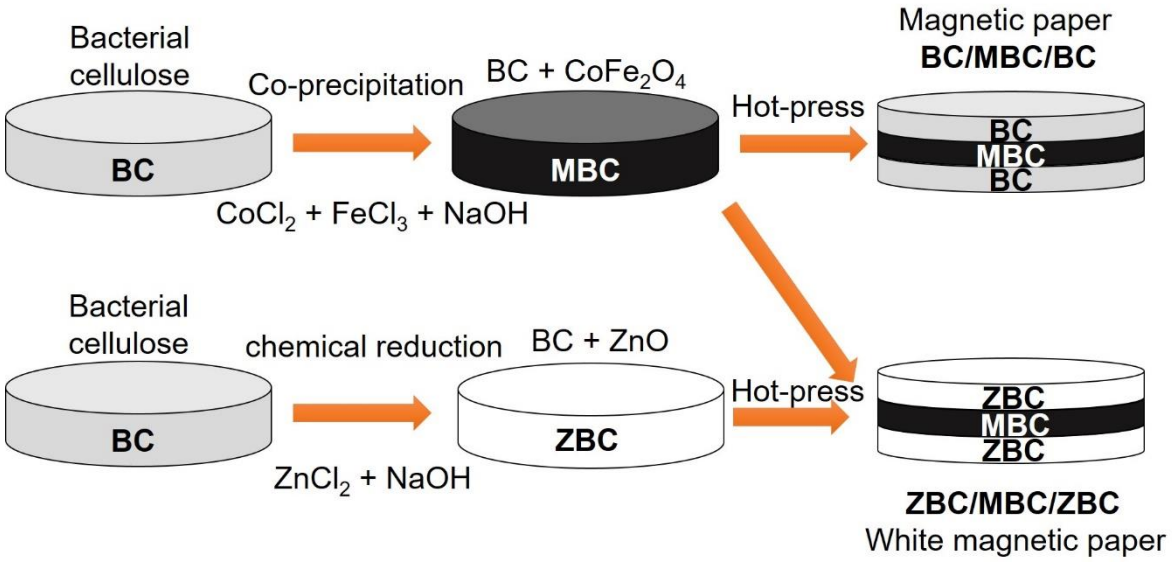

- ชิ้นงานที่สังเคราะห์ได้สังเกตได้ดังรูป

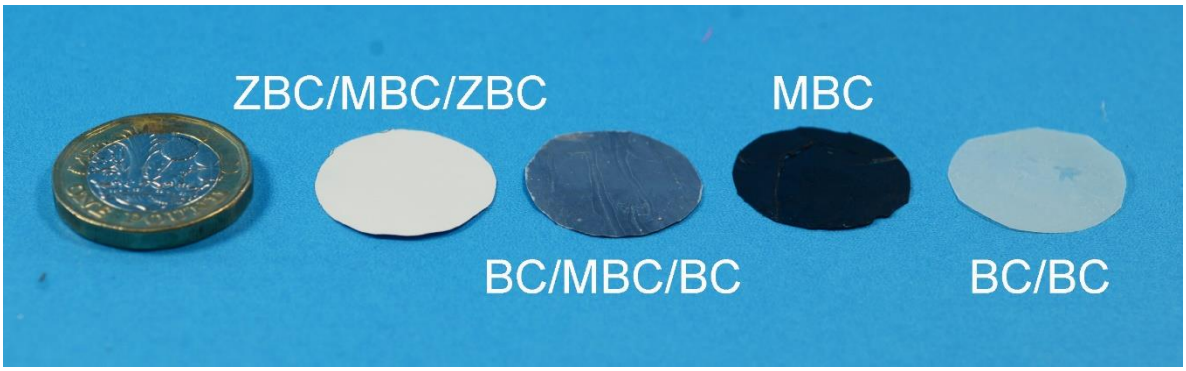

- ผลการวัดความขาวได้ค่า >80% และมีค่าการสะท้อนแสงในช่วงตามองเห็นได้กว่า 70%

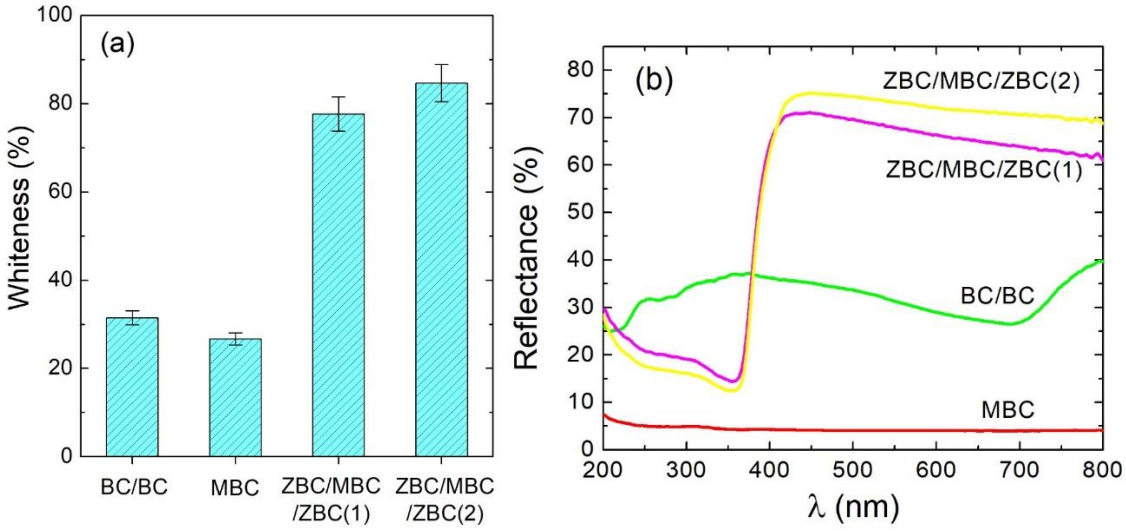

- ผลการวิเคราะห์ด้วย XRD พบการผสมของเฟส BC, $CoFe_2O_4$ และ ZnO

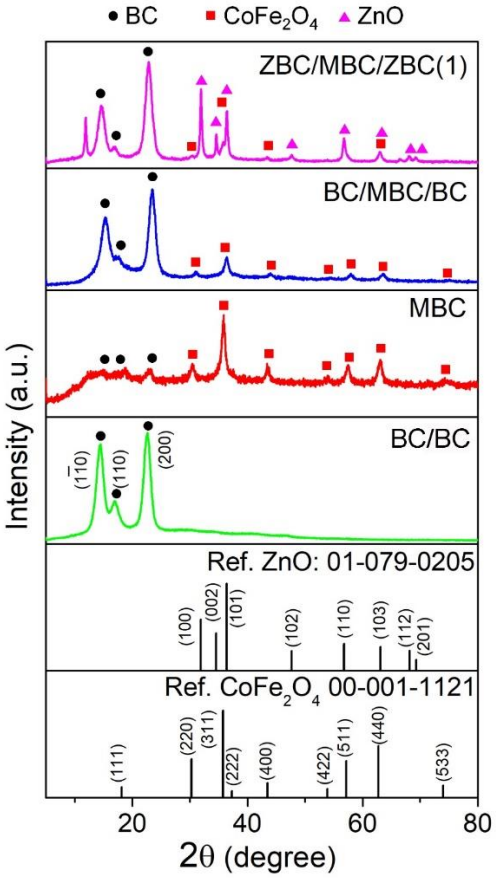

- ภาพถ่าย SEM พบเส้นใยนาโนที่มีเส้นผ่าศูนย์กลางประมาณ 100 nm (a) ส่วนภาพ (b) แสดงอนุภาคนาโนของ $CoFe_2O_4$ ที่เคลือบอยู่บนเส้นใย BC ภาพ (c) และ (d) แสดงภาคตัดขวางของกระดาษแม่เหล็ก BC/MBC/BC และ ZBC/MBC/ZBC ตามลำดับ

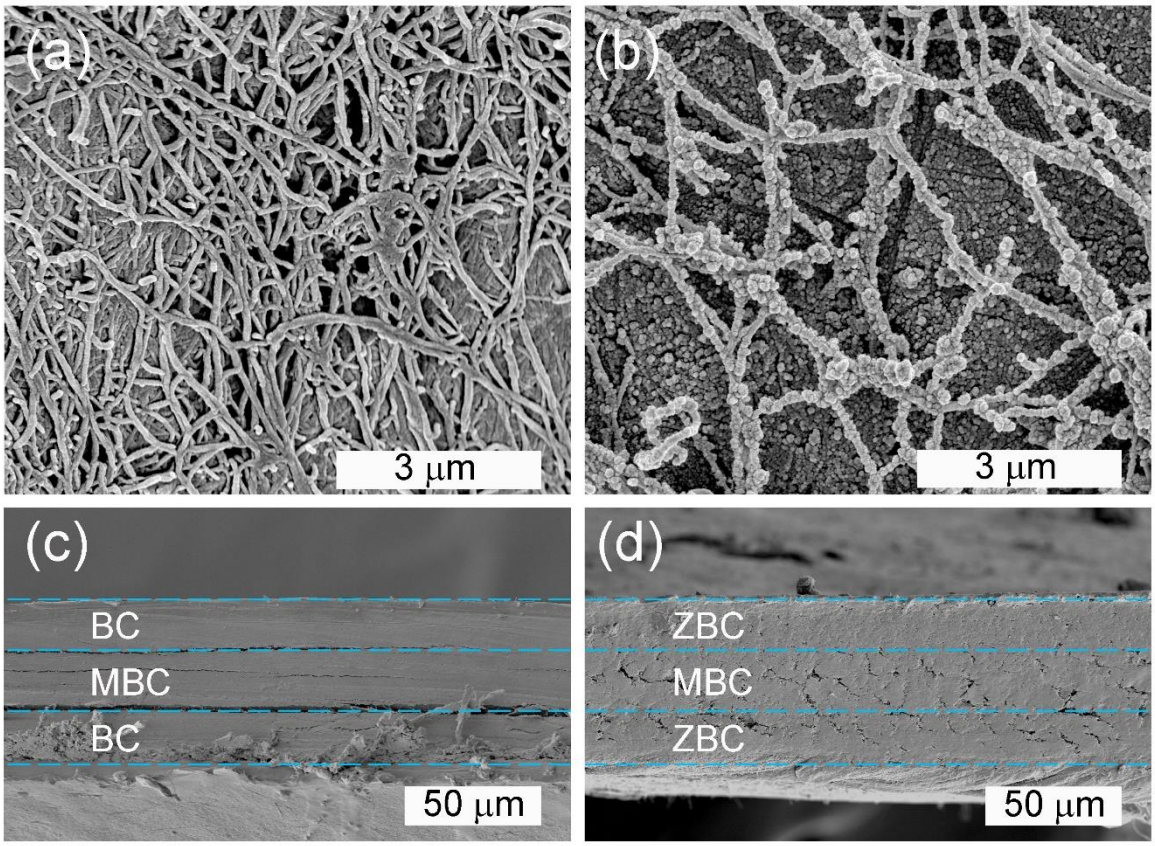

- ผลการวัดค่าความแข็งแรง Tensile index และ ความต้านแรงฉีก Tearing index พบว่า ตัวอย่าง BC/BC มีสมบัติเชิงกลดีที่สุด ตัวอย่าง MBC มีค่าแย่ที่สุด หากทำเป็น composite BC/MBC/BC จะได้ค่าเพิ่มขึ้น แต่ลดลงอีกครั้งเมื่อเติม ZnO

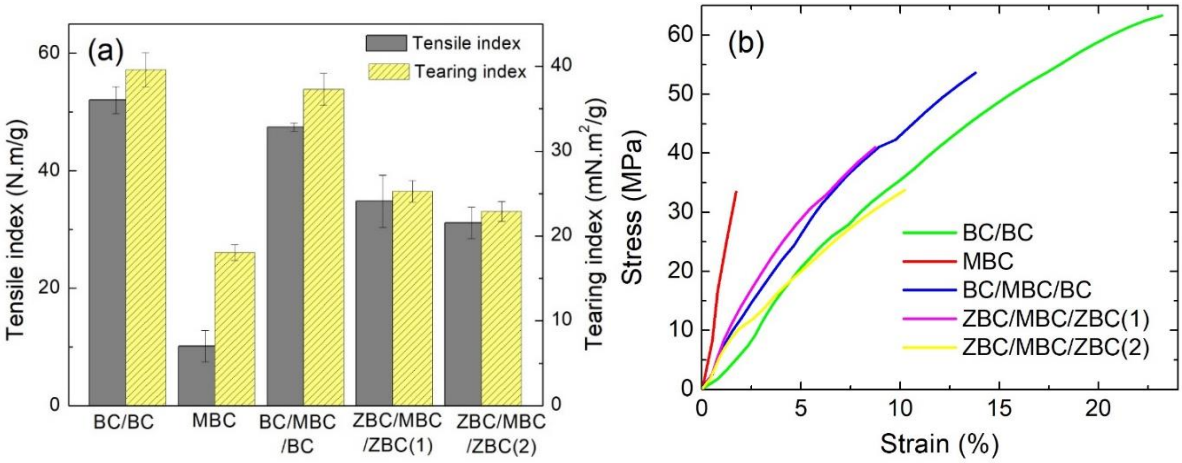

- ผลการวัดสมบัติแม่เหล็กด้วยเทคนิค VSM พบว่าค่าแม่เหล็กมีค่าสูงสุดสำหรับตัวอย่าง MBC และมีค่าลดลงในวัสดุคอมโพสิต BC/MBC/BC และ ZBC/MBC/ZBC ตามลำดับ

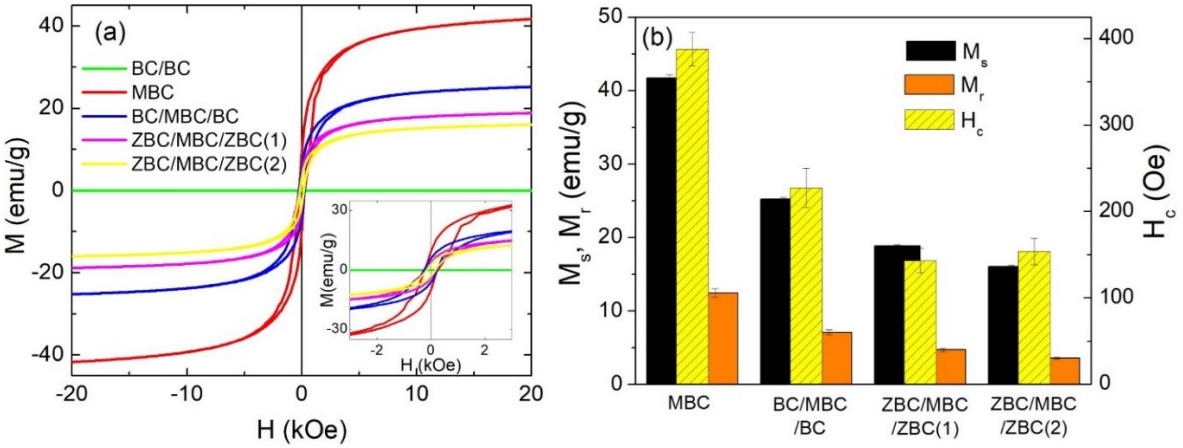

- ผลการทดสอบการตอบสนองกับแม่เหล็กภายนอก พบว่ากระดาษแม่เหล็กสีขาวที่สังเคราะห์ได้ในงานนี้สามารถดึงดูดได้ด้วยแท่งแม่เหล็กถาวร

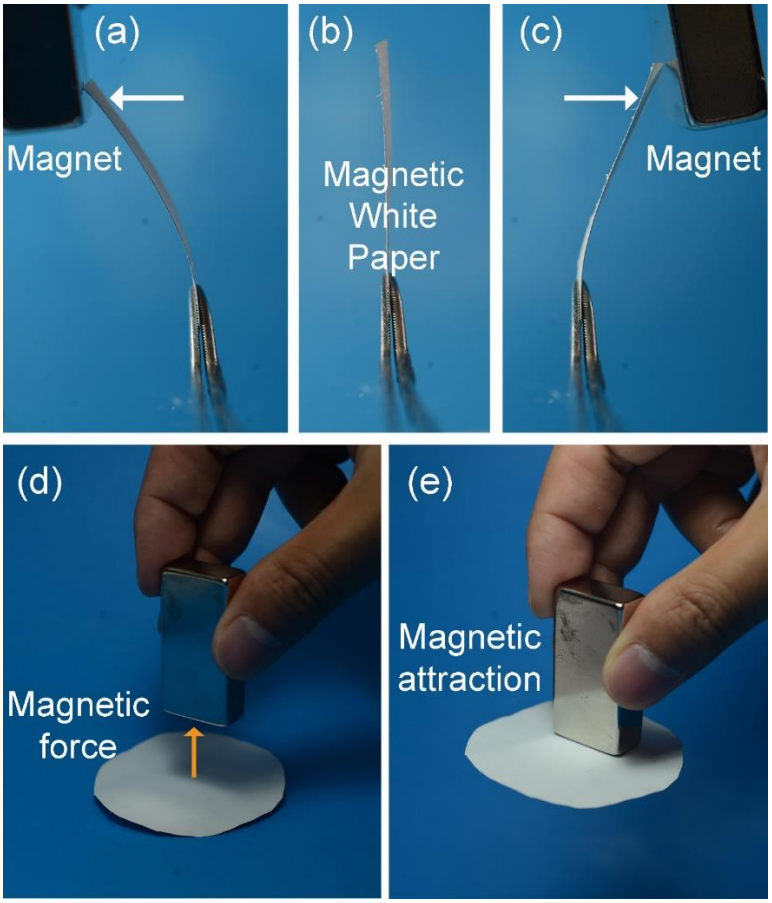

5. สรุปผลการทดลอง

ในงานวิจัยนี้ได้ทำการสังเคราะห์นาโนเซลลูโลสจากแบคทีเรียด้วยกระบวนการการเลี้ยงเชื้อแบคทีเรีย Acetobacter xylinum ได้สำเร็จ ได้แผ่น BC ที่มีลักษณะเหมือนวุ้นขาวใส ซึ่งสามารถนำไปทำแห้งด้วยกระบวนการ freeze dry หรือการอบแห้งได้ แผ่น BC มีความเป็นผลึกสูง ประกอบไปด้วยเส้นใยนาโนขนาดน้อยกว่า 100 นาโนเมตร ถักทอกันเป็นโครงข่าย 3 มิติ จากนั้นนำ BC ที่ได้มาสังเคราะห์อนุภาคแม่เหล็กนาโนชนิดต่างๆใส่เข้าไปในโครงสร้าง ได้แก่อนุภาคแม่เหล็กนาโนเฟอไรต์ ซึ่งสังเคราะห์ด้วยวิธี in-situ co-precipication พร้อมกับศึกษาสมบัติของวัสดุด้วยเทคนิคต่างๆได้แก่ TG/DTA, FTIR, XRD, SAXS, EDS, VSM พบว่าแม่เหล็ก BC ที่ใส่อนุภาคแม่เหล็ก Co-ferrite ขณะเป็นสถานะวุ้นและผ่านการทำแห้งด้วยการอบแห้ง จะได้ค่าแม่เหล็กอิ่มตัวสูงที่สุด

การศึกษาการเตรียมวัสดุคอมโพสิตของแบคทีเรียเซลลูโลสกับอนุภาคแม่เหล็กนาโน Fe_3O_4 โดยจุ่มในสารละลาย ferrofluid ทำให้ได้สารคอมโพสิต BC แม่เหล็กตามที่ต้องการ ซึ่งพบว่าวิธีนี้เป็นวิธีที่ง่ายและไม่ทำลายโครงสร้างของแผ่น BC อนุภาคของแม่เหล็กนาโนกระจายตัวในโครงสร้าง BC ได้ดี ทั้งนี้เนื่องมาจากอนุภาคของ Fe_3O_4 มีความเป็นกลางทางไฟฟ้า จึงสามารถเกาะได้ทุกบริเวณพื้นผิวของ BC จึงมีการกระจายตัวอย่างสม่ำเสมอ ความแข็งแรงเพิ่มขึ้นหากใส่อนุภาคแม่เหล็กนาโนในปริมาณที่ไม่มากเกินไป เมื่อนำแผ่นเมมเบรน BC แม่เหล็กไปทดสอบการตอบสนองกับแม่เหล็กจากภายนอก พบว่าสามารถดูดจับกับแท่งแม่เหล็กถาวรได้ และตอบสนองกับแม่เหล็กภายนอกได้ดีมากทั้งกับสนามแม่เหล็กแบบทางเดียวหรือเปลี่ยนทิศทางตามความถี่ การนำแผ่นแม่เหล็ก BC ไปผ่านกระบวนการไพโรไลซิส เส้นใยเซลลูโลสจะเปลี่ยนสภาพกลายเป็นเส้นใยคาร์บอนนาโน ทำให้ได้คอมโพสิตของเส้นใยคาร์บอน (CNF) กับอนุภาคแม่เหล็ก ค่าแมกนีไตเซชันอิ่ม (M_s) ตัวของ CNF/Fe_3O_4 มีค่าสูงกว่า BC/Fe_3O_4 มาก

ในส่วนหนึ่งของงานวิจัยนี้ ได้ศึกษาการสังเคราะห์กระดาษแม่เหล็กสีขาวจากแบคทีเรียเซลลูโลสคอมโพสิต โดยสังเคราะห์อนุภาคนาโน ZnO ในโครงสร้างของ BC เพื่อให้ได้กระดาษสีขาวและนำมาประกบกับกระดาษแม่เหล็ก BC ซึ่งมีสีดำ ผลปรากฏว่าวัดค่าความขาวไปมากกว่า 80% และมีค่าสะท้อนแสงในช่วงตามองเห็นได้กว่า 70% ผลการวัดค่าความแข็งแรง Tensile index และ ความต้านแรงฉีก Tearing index พบว่า ตัวอย่าง BC/BC มีสมบัติเชิงกลดีที่สุด ตัวอย่าง MBC มีค่าแย่ที่สุด หากทำเป็น composite BC/MBC/BC จะได้ค่าเพิ่มขึ้น แต่ลดลงอีกครั้งเมื่อเติม ZnO ส่วนผลการทดสอบการตอบสนองกับแม่เหล็กภายนอก พบว่ากระดาษแม่เหล็กสีขาวที่สังเคราะห์ได้ในงานนี้สามารถดึงดูดได้ด้วยแท่งแม่เหล็กถาวร

นอกจากนี้ยังได้ทำการสังเคราะห์อนุภาคแม่เหล็กนาโนของโคบอลต์เหล็กแพลทตินัม ($Co_{1-x}Fe_xPt$) ด้วยวิธีโพลิออล โดยเปลี่ยนปริมาณของ Co และ Fe จากนั้นเผาเพื่อให้วัสดุเปลี่ยนเฟสเป็นเฟสแม่เหล็กแรงตามที่ต้องการ แล้วทำการวัดลักษณะเฉพาะพร้อมกับสมบัติของวัสดุด้วยเทคนิคต่างๆ ผลการทดลองที่ได้ พบว่าสามารถสังเคราะห์อนุภาคนาโน ($Co_{1-x}Fe_xPt$) ได้เฟสบริสุทธิ์ ก่อนการเผา มีขนาดเล็กประมาณ 2-3 nm แต่เมื่อเผาแล้วจะเกิดการเปลี่ยนเฟสเป็นเฟสแม่เหล็กแข็ง และขนาดของอนุภาคใหญ่ขึ้นมาก การปรับเปลี่ยนอัตราส่วน Co กับ Fe พบว่าทำให้สมบัติทางแม่เหล็กเปลี่ยนไป

โดยถ้าอัตราส่วน Co:Fe = 0.50:0.50 จะได้ค่าแมกนีไตเซชันอิ่มตัวสูงที่สุด แต่ถ้า Co = 1.00 หรือ Fe = 1.00 จะทำให้ได้ค่า coercivity ที่สูงที่สุด

6. ข้อเสนอแนะสำหรับงานวิจัยในอนาคต

- ศึกษาวัสดุแม่เหล็กประเภทอื่นด้วยเช่นวัสดุแม่เหล็กแข็ง เพื่อให้มีการประยุกต์ใช้งานที่หลากหลายมากยิ่งขึ้น
- ศึกษาการนำไฟฟ้าของวัสดุคอมโพสิต BC หรือเส้นใยคาร์บอนนาโนจาก BC
- ศึกษาแนวทางการนำผลงานวิจัยที่ได้ไปใช้ประโยชน์เชิงพาณิชย์หรือเชิงอุตสาหกรรม เป็นต้น

เอกสารอ้างอิง

[1] Hu WL, Chen SY, Yang JX, Li Z, Wang HP. Functionalized bacterial cellulose derivatives and nanocomposites. Carbohyd Polym. 2014;101:1043-60.

[2] Huang Y, Zhu CL, Yang JZ, Nie Y, Chen CT, Sun DP. Recent advances in bacterial cellulose. Cellulose. 2014;21(1):1-30.

[3] Klemm D, Kramer F, Moritz S, Lindstrom T, Ankerfors M, Gray D, et al. Nanocelluloses: A New Family of Nature-Based Materials. Angewandte Chemie-International Edition. 2011;50(24):5438-66.

[4] Rajwade JM, Paknikar KM, Kumbhar JV. Applications of bacterial cellulose and its composites in biomedicine. Appl Microbiol Biot. 2015;99(6):2491-511.

[5] Shah N, Ul-Islam M, Khattak WA, Park JK. Overview of bacterial cellulose composites: A multipurpose advanced material. Carbohyd Polym. 2013;98(2):1585-98.

[6] Zhang W, Chen SY, Hu WL, Zhou BH, Yang ZH, Yin N, et al. Facile fabrication of flexible magnetic nanohybrid membrane with amphiphobic surface based on bacterial cellulose. Carbohyd Polym. 2011;86(4):1760-7.

[7] Barud HS, Tercjak A, Gutierrez J, Viali WR, Nunes ES, Ribeiro SJL, et al. Biocellulose-based flexible magnetic paper. J Appl Phys. 2015;117(17):17B734.

[8] Vitta S, Drillon M, Derory A. Magnetically responsive bacterial cellulose: Synthesis and magnetic studies. J Appl Phys. 2010;108(5):053905.

[9] Katepetch C, Rujiravanit R. Synthesis of magnetic nanoparticle into bacterial cellulose matrix by ammonia gas-enhancing in situ co-precipitation method. Carbohyd Polym. 2011;86(1):162-70.

[10] Marins JA, Soares BG, Barud HS, Ribeiro SJL. Flexible magnetic membranes based on bacterial cellulose and its evaluation as electromagnetic interference shielding material. Materials Science & Engineering C-Materials for Biological Applications. 2013;33(7):3994-4001.

[11] Park M, Cheng J, Choi J, Kim J, Hyun J. Electromagnetic nanocomposite of bacterial cellulose using magnetite nanoclusters and polyaniline. Colloids and Surfaces B-Biointerfaces. 2013;102:238-42.

[12] Zheng Y, Yang JX, Zheng WL, Wang X, Xiang C, Tang L, et al. Synthesis of flexible magnetic nanohybrid based on bacterial cellulose under ultrasonic irradiation. Materials Science & Engineering C-Materials for Biological Applications. 2013;33(4):2407-12.

[13] Nata IF, Sureshkumar M, Lee CK. One-pot preparation of amine-rich magnetite/bacterial cellulose nanocomposite and its application for arsenate removal. RSC Adv. 2011;1(4):625-31.

[14] Zhu HX, Jia SR, Wan T, Jia YY, Yang HJ, Li J, et al. Biosynthesis of spherical Fe3O4/bacterial cellulose nanocomposites as adsorbents for heavy metal ions. Carbohyd Polym. 2011;86(4):1558-64.

[15] Olsson RT, Samir MASA, Salazar-Alvarez G, Belova L, Strom V, Berglund LA, et al. Making flexible magnetic aerogels and stiff magnetic nanopaper using cellulose nanofibrils as templates. Nat Nanotechnol. 2010;5(8):584-8.

[16] Sureshkumar M, Siswanto DY, Lee CK. Magnetic antimicrobial nanocomposite based on bacterial cellulose and silver nanoparticles. J Mater Chem. 2010;20(33):6948-55.

Output จากโครงการวิจัยที่ได้รับทุนจาก สกว.

1. ผลงานตีพิมพ์ในวารสารวิชาการนานาชาติ (ระบุชื่อผู้แต่ง ชื่อเรื่อง ชื่อวารสาร ปี เล่มที่ เลขที่ และหน้า) หรือผลงานตามที่คาดไว้ในสัญญาโครงการ ประกอบไปด้วย

   1.1. T. Sanasi, S. Pinitsoontorn*, M. Horprathum, P. Eiamchai, C. Chananonnawathorn, W. Hinchreeranun, “Development of WO_3 Nanostructure by Acid Treatment and Annealing”, Journal of Metals, Materials and Minerals, 27 (2017) 6-11. (Scopus)

   1.2. Nipaporn Sriplai, Wiyada Mongkolthanaruk, Supree Pinitsoontorn*, “Synthesis and Magnetic properties of Bacterial Cellulose – Ferrite (MFe2O4, M = Mn, Co, Ni, Cu) Nanocomposites Prepared by Co-Precipitation Method”, Advances in Natural Sciences: Nanoscience and Nanotechnology, 8 (2017) 035005. (IF2015: 1.581).

   1.3. Nipaporn Sriplai, Sireemas Koowattanasuchat, Pinit Kidkhunthod, Narong Chanlek, Stephen J. Eichhorn, Supree Pinitsoontorn*, “Magnetic behavior of novel alloyed L10-phase Co1-xFexPt nanoparticles”, Journal of Alloys and Compounds, 739 (2018) 19-29. (IF2017: 3.779).

   1.4. Nipaporn Sriplai, Wiyada Mongkolthanaruk, Stephen J. Eichhorn, Supree Pinitsoontorn*, “Magnetically responsive and flexible bacterial cellulose membranes”, Carbohydrate Polymers, 192 (2018) 251-262. (IF2017: 5.158).

   1.5. Nipaporn Sriplai, Pornkanok Sirima, Dulayawit Palaporn, Wiyada Mongkolthanaruk, Stephen J. Eichhorn and Supree Pinitsoontorn*, “White magnetic paper based on a bacterial cellulose nanocomposite”, Journal of Materials Chemistry C, 6 (2018) 11427-11435. (IF2017: 5.976).

   1.6. Poramed Wongjom, Supree Pinitsoontorn*, “Investigation of the spin Seebeck effect and anomalous Nernst effect in a bulk carbon material”, Results in Physics, 8 (2018) 1245-1249. (IF2017: 2.147)

   1.7. Suphagrid Wongprakarn, Supree Pinitsoontorn*, Sora-at Tanusilp, Ken Kurosaki, “The effect of YSi_2 nanoinclusion on the thermoelectric properties of p-type SiGe alloy”, Physica Status Solidi A, 214 (2017) 1700235. (IF2017: 1.795).

   1.8. Suphagrid Wongprakarn, Supree Pinitsoontorn*, Sora-at Tanusilp, Ken Kurosaki, “Thermoelectric Properties of Bulk Yttrium Silicide (YSi2) Fabricated by Arc Melting and Spark Plasma Sintering”, Physica Status Solidi A, 215 (2018) 1700769. (IF2017: 1.795).

   1.9. Suphagrid Wongprakarn, Supree Pinitsoontorn*, Sora-at Tanusilp, Ken Kurosaki, “Enhancing thermoelectric properties of p-type SiGe alloy through optimization of carrier

concentration and processing parameters", Materials Science in Semiconductor Processing, 88 (2018) 239-249. (IF2017: 2.593).

1.10. Nattapong Chuewangkam, Supree Pinitsoontorn*, Prinya Chindaprasirt, "Magnetic Cement (Cementitious Magnet)", Cement and Concrete Composites (2019) (under review) (IF2017: 4.66)

2. การนำผลงานวิจัยไปใช้ประโยชน์ (ในเชิงวิชาการ)
   - การนำไปใช้ในการเรียนการสอนในหลักสูตรวัสดุศาสตร์และนาโนเทคโนโลยี ในรายวิชา 301340 วัสดุแม่เหล็ก สำหรับนักศึกษาระดับปริญญาตรี และในรายวิชา 301706 วัสดุแม่เหล็ก สำหรับนักศึกษาระดับบัณฑิตศึกษา
   - มีการต่อยอดผลงานวิจัย โดยได้นำองค์ความรู้ที่ได้จากงานวิจัยนี้พัฒนาต่อไป และมีความร่วมมือกับนักวิจัยอื่นๆทั้งในไทยและต่างประเทศ รวมทั้งผลงานวิจัยที่ได้ตีพิมพ์ผลงานไปแล้วมีการอ้างอิง (citation) เพื่อนำไปใช้ประโยชน์ต่อไป

3. อื่นๆ (เช่น ผลงานตีพิมพ์ในวารสารวิชาการในประเทศ การเสนอผลงานในที่ประชุมวิชาการ หนังสือ การจดสิทธิบัตร)
   3.1. การนำเสนอผลงานแบบโปสเตอร์ในงานประชุมวิชาการ The 4th Southeast Asia Conference on Thermoelectrics 2016, ระหว่างวันที่ 15 ถึง 18 ธันวาคม 2559 ณ โรงแรม Sea Garden เมืองดานัง ประเทศเวียดนาม หัวข้อการนำเสนอ "Electronic structure of iron-doped misfit-layered calcium cobaltite"

   3.2. การนำเสนอผลงาน (Invited Talk) ในงานประชุมวิชาการ NanoThailand 2016, ระหว่างวันที่ 27 ถึง 29 พฤศจิกายน 2559 ณ โรงแรม The Greenery Resort, เขาใหญ่ จ. นครราชสีมา ประเทศไทย หัวข้อการนำเสนอ "Effect of Boron addition on the structure and magnetic properties of CoPt nanoparticles"

   3.3. การนำเสนอผลงาน (Invited Talk) ในงานประชุมวิชาการ 3rd International Conference on Applied Physics and Material Applications (ICAPMA2017), ระหว่างวันที่ 31 พฤษภาคม ถึง 2 มิถุนายน 2560 ณ โรงแรม Garden Cliff Resort and Spa, พัทยา จ.ชลบุรี ประเทศไทย หัวข้อการนำเสนอ "Electrical Conductivity and Compressive Strength of Carbon Fiber Reinforced Fly Ash Geopolymeric Composites"

   3.4. การนำเสนอผลงาน (Invited Talk) ในงานประชุมวิชาการ Thailand-Japan Joint Research Meeting on Nanomaterials and Nanocomposites, ในวันที่ 7 กันยายน 2560 ณ โรงแรม Dusit Thani กรุงเทพฯ ประเทศไทย หัวข้อการนำเสนอ "Development of oxides and and silicides based thermoelectric materials"

3.5. การนำเสนอผลงาน (Oral presentation) ในงานประชุมวิชาการ The Twenty-Fifth Annual International Conference on COMPOSITES/NANO ENGINEERING (ICCE-25), ระหว่างวันที่ 16 ถึง 22 กรกฎาคม 2560 ณ โรงแรม Sheraton Parco de'Medici Rome Hotel, Rome, Italy หัวข้อการนำเสนอ "Characteristics And Magnetic Properties Of Fe3O4 Nanoparticle Dispersions In Bacterial Cellulose And Carbon Nanofiber Scaffoldings"

3.6. การนำเสนอผลงานแบบโปสเตอร์ในงานประชุมวิชาการ The First Materials Research Society of Thailand International Conference (MRS Thailand), ระหว่างวันที่ 31 ตุลาคม ถึง 3 พฤศจิกายน 2017 ณ โรงแรม The Empress Convention Center, เชียงใหม่ ประเทศไทย หัวข้อการนำเสนอ "Fabrication and characterization of 3D carbon nanofiber derived from bacterial cellulose for liquid absorption"

3.7. การนำเสนอผลงาน (Invited Talk) ในงานประชุมวิชาการ 3rd International Conference on Applied Physics and Material Applications (ICAPMA2017), ระหว่างวันที่ 31 พฤษภาคม ถึง 2 มิถุนายน 2560 ณ โรงแรม Garden Cliff Resort and Spa, พัทยา จ.ชลบุรี ประเทศไทย หัวข้อการนำเสนอ "Electrical Conductivity and Compressive Strength of Carbon Fiber Reinforced Fly Ash Geopolymeric Composites"

3.8. การจัดงานประชุมวิชาการ NAF-TRF Workshop on Nanocellulose 2017 ระหว่างวันที่ 11-14 กันยายน 2560 ณ โรงแรม Pullman Hotel จ.ขอนแก่น ประเทศไทย มี Keynote Speaker ได้แก่ Prof. Stephen Eichhorn จาก University of Bristol, UK และ Invited Speaker จากนักวิจัยชั้นนำในประเทศไทยอีก 11 ท่าน มีผู้ร่วมงานทั้งสิ้นกว่า 80 คน

ภาคผนวก

ผลงานตีพิมพ์ในวารสารวิชาการนานาชาติ

1. T. Sanasi, S. Pinitsoontorn*, M. Horprathum, P. Eiamchai, C. Chananonnawathorn, W. Hinchreeranun, “Development of WO_3 Nanostructure by Acid Treatment and Annealing”, Journal of Metals, Materials and Minerals, 27 (2017) 6-11. (Scopus)
2. Nipaporn Sriplai, Wiyada Mongkolthanaruk, Supree Pinitsoontorn*, “Synthesis and Magnetic properties of Bacterial Cellulose – Ferrite (MFe2O4, M = Mn, Co, Ni, Cu) Nanocomposites Prepared by Co-Precipitation Method”, Advances in Natural Sciences: Nanoscience and Nanotechnology, 8 (2017) 035005. (IF2015: 1.581).
3. Nipaporn Sriplai, Sireemas Koowattanasuchat, Pinit Kidkhunthod, Narong Chanlek, Stephen J. Eichhorn, Supree Pinitsoontorn*, “Magnetic behavior of novel alloyed L10-phase Co1-xFexPt nanoparticles”, Journal of Alloys and Compounds, 739 (2018) 19-29. (IF2017: 3.779).
4. Nipaporn Sriplai, Wiyada Mongkolthanaruk, Stephen J. Eichhorn, Supree Pinitsoontorn*, “Magnetically responsive and flexible bacterial cellulose membranes”, Carbohydrate Polymers, 192 (2018) 251-262. (IF2017: 5.158).
5. Nipaporn Sriplai, Pornkanok Sirima, Dulayawit Palaporn, Wiyada Mongkolthanaruk, Stephen J. Eichhorn and Supree Pinitsoontorn*, “White magnetic paper based on a bacterial cellulose nanocomposite”, Journal of Materials Chemistry C, 6 (2018) 11427-11435. (IF2017: 5.976).
6. Poramed Wongjom, Supree Pinitsoontorn*, “Investigation of the spin Seebeck effect and anomalous Nernst effect in a bulk carbon material”, Results in Physics, 8 (2018) 1245-1249. (IF2017: 2.147)
7. Suphagrid Wongprakarn, Supree Pinitsoontorn*, Sora-at Tanusilp, Ken Kurosaki, “The effect of YSi_2 nanoinclusion on the thermoelectric properties of p-type SiGe alloy”, Physica Status Solidi A, 214 (2017) 1700235. (IF2017: 1.795).
8. Suphagrid Wongprakarn, Supree Pinitsoontorn*, Sora-at Tanusilp, Ken Kurosaki, “Thermoelectric Properties of Bulk Yttrium Silicide (YSi2) Fabricated by Arc Melting and Spark Plasma Sintering”, Physica Status Solidi A, 215 (2018) 1700769. (IF2017: 1.795).
9. Suphagrid Wongprakarn, Supree Pinitsoontorn*, Sora-at Tanusilp, Ken Kurosaki, “Enhancing thermoelectric properties of p-type SiGe alloy through optimization of carrier concentration and processing parameters”, Materials Science in Semiconductor Processing, 88 (2018) 239-249. (IF2017: 2.593).
10. Nattapong Chuewangkam, Supree Pinitsoontorn*, Prinya Chindaprasirt, “Magnetic Cement (Cementitious Magnet)”, Cement and Concrete Composites (2019) (under review) (IF2017: 4.66)

Journal of Metals, Materials and Minerals, Vol. 27 No. 2 pp. 6-11, 2017

Development of WO_3 Nanostructure by Acid Treatment and Annealing

T. Sanasi[1], S. Pinitsoontorn[1,*] , M. Horprathum[2], P. Eiamchai[2], C. Chananonnawathorn[2], and W. Hinchreeranun[2]

[1]Integrated Nanotechnology Research Center, Department of Physics, Faculty of Science, Khon Kaen University, Khon Kaen, 40002, Thailand
[2]Optical Thin- Film Laboratory, National Electronics and Computer Technology Center, Pathumthani, 12120, Thailand

Abstract

Tungsten oxide (WO_3) nanostructure is an interesting material for many applications such as batteries, gas sensors, photocatalysts, display utilizing, and smart windows. In this work, we fabricated the WO_3 nanoplates by sputtering, acid treatment and annealing. Firstly, a tungsten film was deposited on a silicon or glass substrate by sputtering. The film was then immersed in nitric acid (HNO_3) at 80°C. The effect of the exposure time, and annealing temperature was investigated. After the acid treatment, the tungsten oxide hydrate or tungstile ($WO_3 \cdot H_2O$) with nanoplate structure was developed. The optical transmittance in the visible range was significantly improved compared to the continuous tungsten film. The size of the nanoplate was found to increase with increasing the immersion time. The tungsten oxide hydrate nanoplates transformed into WO_3 after annealing at ≥ 200°C. Increasing annealing temperature resulted in the decreasing size of the nanoplates. The shape of the nanoplates became more of the rectangular shape with annealing. The optical transmittance of the WO_3 film increased with the annealing temperature up to 400°C.

Keywords: Tungsten oxide; Nanoplates; Acid treatment; Annealing

Introduction

Tungsten oxide (WO_3) nanostructure is an interesting material for many applications such as batteries, gas sensors, photocatalysts, display utilizing, and smart windows[(1-3)]. In order to prepare WO_3 nanostructured thin films, several methods have been used, for instance, chemical vapor deposition[(4)], electron beam deposition [(5)], spray deposition[(6)], and sol-gel spin coating.

Another interesting but simple method for preparing the WO_3 nanostructure is by using acid treatment[(7-10)]. In this method a continuous tungsten film/sheet is immersed in an acid solution for developing the WO_3 nanostructure. In particular, the nanoplate morphology is preferential formed by using this method. The acid treatment method shows several advantages over the other techniques, for example, simple set-up, fast, ability for up-scaling. Generally, nitric acid (HNO_3) was selected in the process due to its potential for oxidizing W film. The W film did not directly transform into WO_3 by acid immersion process but the intermediate phase (tungsten oxide hydrate, $WO_3 \cdot H_2O$) was usually formed. The $WO_3 \cdot H_2O$ phase could be easily transformed into WO_3 nanoplates by heat treatment. Although the previous literatures have reported the synthesis of WO_3 by the acid treatment process and its application in various fields[(7-10)], the detailed study for the effect of acid immersion time and annealing temperature on the morphology of the nanoplates and the optical transmission properties has not been researched. Therefore, the objective of this research is to study such topics in more details.

Experimental methods

Thin tungsten films were deposited on Si wafer or glass substrates by using pulsed DC sputtering under Ar atmosphere at 5 mTorr and the power of 100 Watt for 10 min. After that, to obtain the hydrated tungsten oxide ($WO_3 \cdot H_2O$) nanoplates, the acid treatment process was carried out. The samples were immersed in 1.5

* Corresponding author E-mail: psupree@kku.ac.th

DOI: 10.14456/jmmm.2017.xx

M HNO_3 at 80°C with the various immersion time of 30, 60 and 90 min. As subsequently shown in the next section, the films immersed in the acid for 90 min showed the clear and smooth surface of the $WO_3 \cdot H_2O$ nanoplates. Thus, this sample was chosen for the annealing process at the temperature range of 100–500 °C at the fixed time of 1 h. The annealing process transformed the $WO_3 \cdot H_2O$ to the WO_3 nanostructured film by removing water molecules.

The plan view and cross-section morphology of the films was investigated by using the scanning electron microscope (Hitachi, S4700). The phase and crystalline structure of the films were analyzed by using the X-ray diffraction technique (Rigaku, TTRAX III). The optical transmittance of the $WO_3 \cdot H_2O$ and WO_3 films deposited on glass substrate was measured by using the spectrophotometer (Agilent Cary, 7000).

Results and Discussion

Figure 1 shows the cross-section SEM image of the tungsten film after the deposition on Si wafer. It can be seen that the film is continuous and uniform with very smooth surface over a large scale. The film thickness was estimated to be around 72 nm (the average value from the measurement directly in the SEM image of over 10 locations).

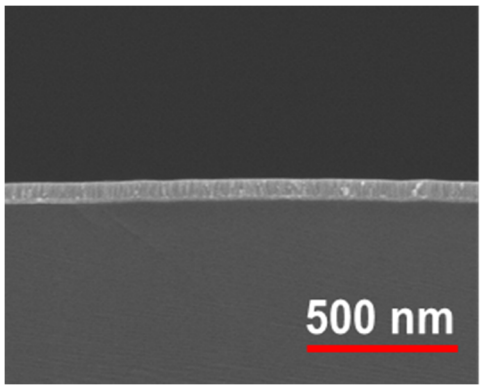

Figure 1. Cross section SEM image of the W film on Si wafer.

Figure 2 shows the plan view and cross section morphology of the films after the acid treatment. It is obvious that the film morphology has changed significantly compared to Figure 1. The HNO_3 acid has transformed the continuous W film into the nanoplate structure of the hydrated tungsten oxide ($WO_3 \cdot H_2O$). The nanoplated films also became thicker (> 400 nm). The thickness of the $WO_3 \cdot H_2O$ film as well as the average size of each nanoplate increased with the acid immersion time as summarized in Figure 3.

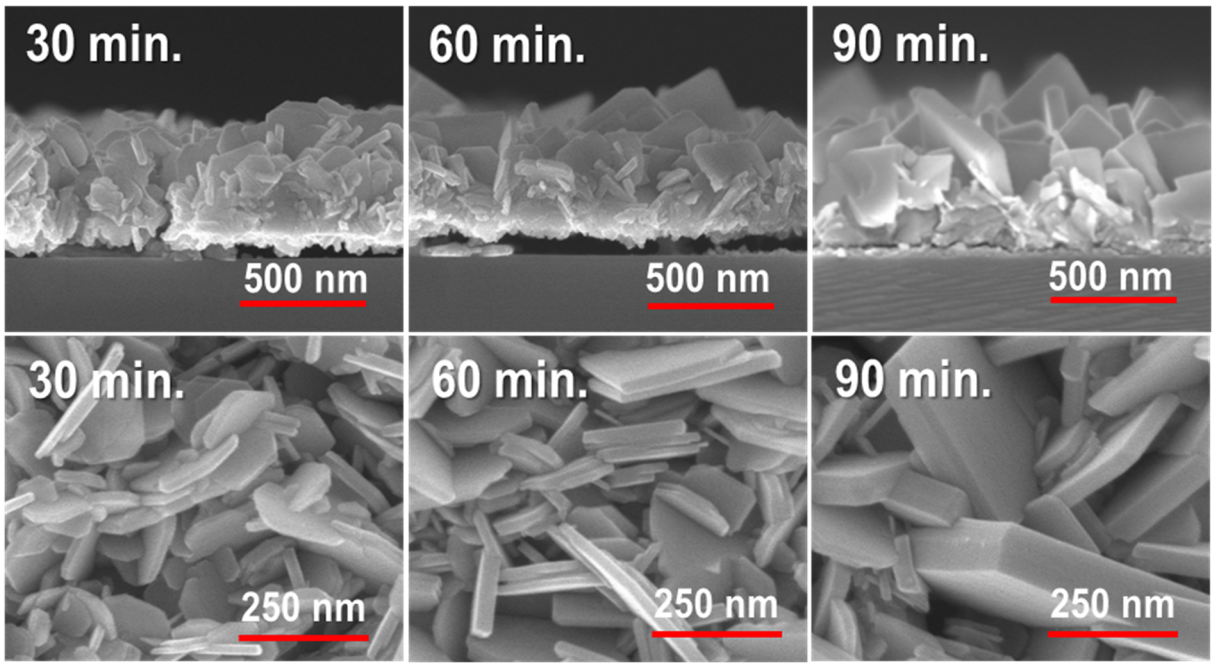

Figure 2. Plan view and cross section images of the $WO_3 \cdot H_2O$ nanoplated films after acid treatment of 30, 60 and 90 min.

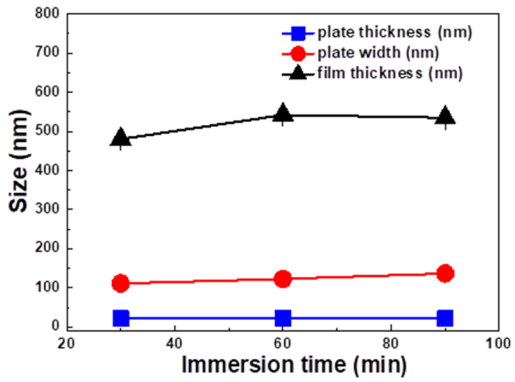

Fig 3. $WO_3 \cdot H_2O$ film thickness and the size of nanoplate as a function of immersion time.

The optical transmission spectra of the W film and the $WO_3 \cdot H_2O$ films are presented in Figure 4(a). There is a significant change in the spectra from the W film to the $WO_3 \cdot H_2O$ films. For the W film, the sample did not allow the light transmission throughout the measurement wavelength range, i.e. the film is mostly opaque for light from 200 to 2,000 nm. On the other hand, the $WO_3 \cdot H_2O$ nanostructured films show some transparencies in the visible and infrared spectra. The change in the optical properties can be explained from the formation of WO_3 in the samples after acid treatment. The introduction of oxygen to the W film change the metallic behavior of the W film into the insulating tungsten oxide films. This in turn also changed the electronic structure of the sample from no band gap (metallic) to wide band gap semiconductor, which did not absorb light in the visible range, and thus became more optically transparent. Figure 4(b) shows the average %transmittance in the visible range. The transmittance increased with acid immersion time. Again this could be explained from the reaction of oxygen with the W film. The longer the acid treatment, the more $WO_3 \cdot H_2O$ nanostructured film was formed.

The optical band gap of the sample as a function of acid immersion time was evaluated according to the equation.

$$(\alpha h\upsilon)^n = A(h\upsilon - E_g) \qquad (1)$$

where α , $h\upsilon$, A and E_g are absorption coefficient, photon energy, relation constant and optical band gap, respectively. By using n = 1/2 for indirect band gap semiconductors, and the extrapolation technique (Figure 5(a)), the optical band gaps as a function of acid immersion time are presented in Fig. 5(b). Obviously, one can see that the optical band gap increases with the longer immersion time as the oxidization of the W film is in a more advanced state.

Since the sample immersed for 90 min showed the clearest and smoothest morphology of the $WO_3 \cdot H_2O$ nanoplate, and the highest optical transmittance in the visible range, we have chosen this sample for the annealing treatment.

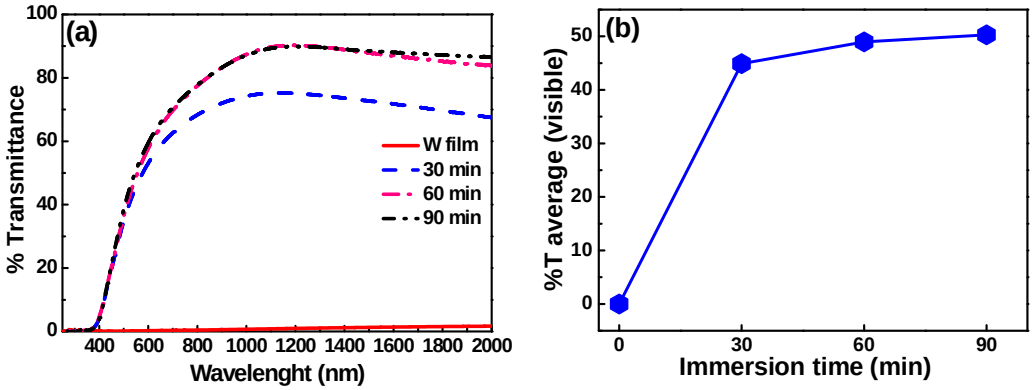

Figure 4. (a) Optical transmission spectra and (b) average transmittance of W film and $WO_3 \cdot H_2O$ films with different immersion time

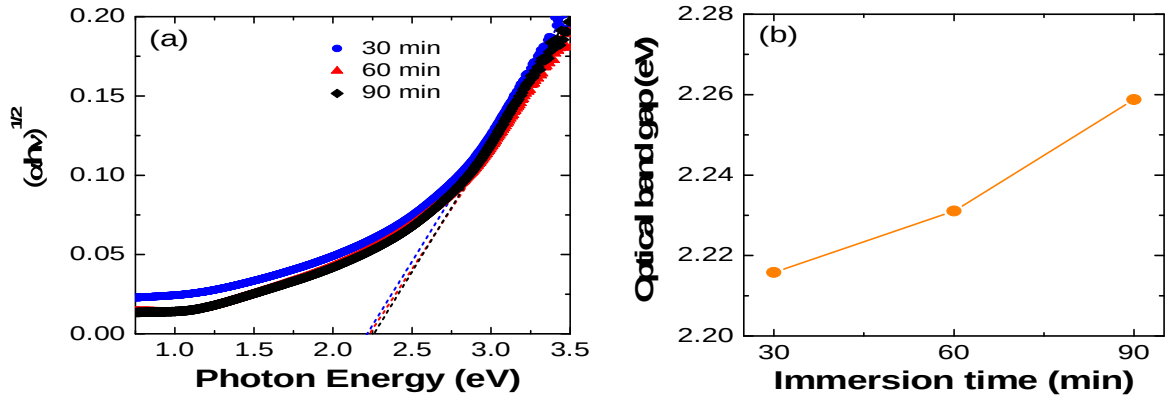

Figure 5. (a) Optical band gap estimation by extrapolation technique, and (b) optical band gap as a function of immersion time.

Figure 6 shows the plan view and cross images of the WO_3 nanostructured films after the heat treatment at 100–500°C. The annealing has no effect of the shape of the nanostructure, i.e. the nanoplate morphology was maintained up to 500°C. However, the thickness of the films was decreased and the width of individual nanoplates was slightly reduced as the annealing temperature increased (Figure 7) as a result of the removal of water molecules.

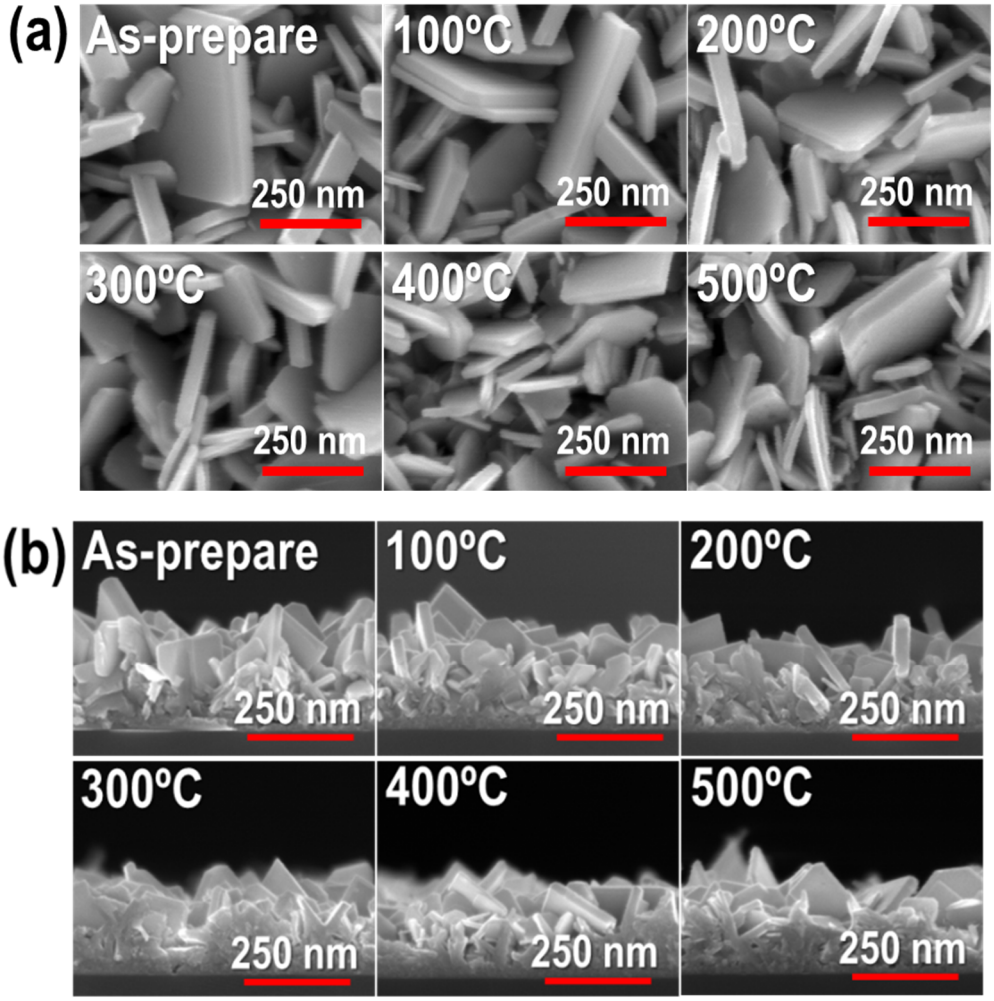

Figure 6. Plan view and cross section images of the W nanoplated films after 1 h annealing at 100–500°C.

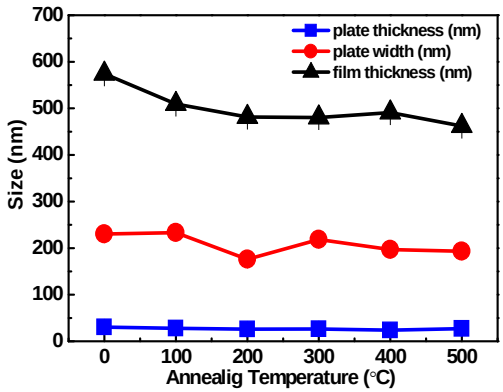

Figure 7. WO_3 film thickness and the size of nanoplate as a function annealing temperature.

The transformation of the $WO_3 \cdot H_2O$ to the WO_3 nanoplated films manifested in the optical transmission measurement. The transmission spectra of the non-annealed and the annealed WO_3 films in the wavelength of 200–2,000 are shown in Figure 8(a). The transmission curves look very similar for every sample. However, when plotted the average %transmittance in the visible range against the annealing temperature, a trend emerged as shown in Figure 8(b). The transmittance has a tendency to increase with annealing temperature. This is probably due to the removal of water molecules, making the more complete WO_3 films, and thus more optical transparent. The exception is for the sample annealed at 500°C where there is a sudden drop in the transmittance. The possible reasons for the sudden change could be from deteriorated and poorly deformed as the glass slide substrate melted. It should be noted that the transparency of all samples were still lower than 55% which could be probably due to a large surface roughness of the film.

The optical band gap of the samples as a function of annealing temperature could be was evaluated using the extrapolation technique according to the equation 1 as explained previously. The results are shown in Figure 9. The optical band gap has a tendency to increase with increasing annealing temperature up to 400°C due to the more complete formation of the WO_3 crystalline phase. At 500°C, a sudden drop in the band gap was found which was due to themelt of the glass slide substrate as discuss earlier.

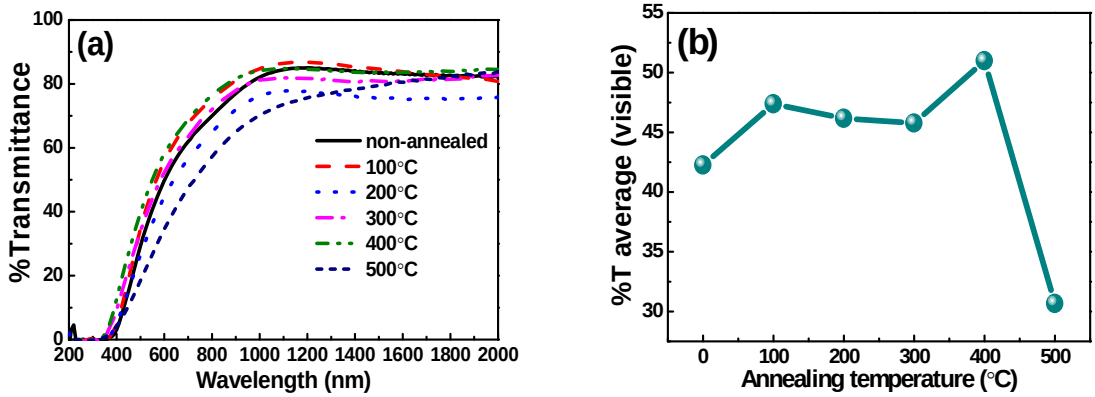

Figure 8. (a) Optical transmission spectra and (b) average transmittance of the $WO_3 \cdot H_2O$ film and WO_3 films with different annealing temperature.

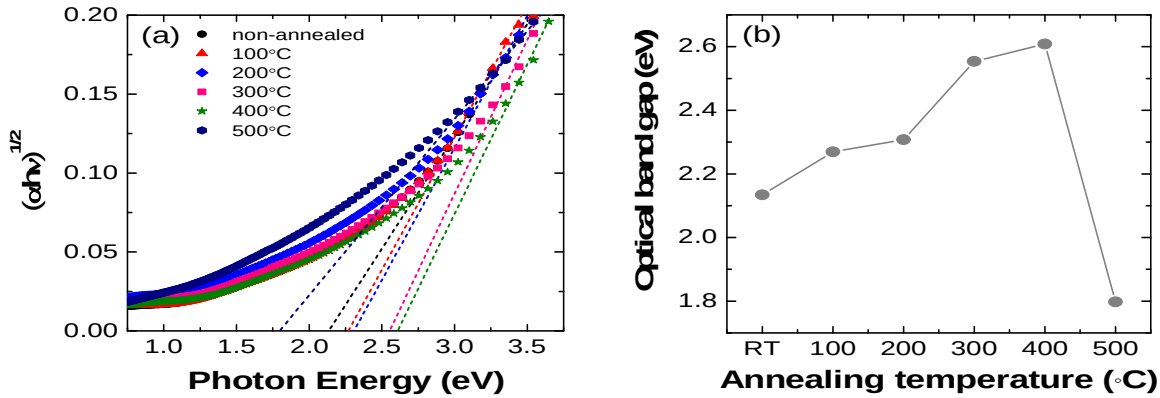

Figure 9. (a) Optical band gap estimation by extrapolation technique, and (b) optical band gap as a function of annealing temperature.

Finally, to verify the phase transformation and the crystallinity of the films in this study, the XRD analysis was carried out as shown in Figure 10. For the acid treated film without annealing, the orthorhombic phase of the $WO_3 \cdot H_2O$ was clearly visible. This confirmed the existence of the water molecules from the acid treatment process. As the annealing temperature increased above 200°C, the phase was transformed to monoclinic phase of the WO_3 film. The residual water molecules were completely eliminated. The crystallinity of the WO_3 was also promoted with higher annealing temperature as observed from the higher monoclinic peak intensities.

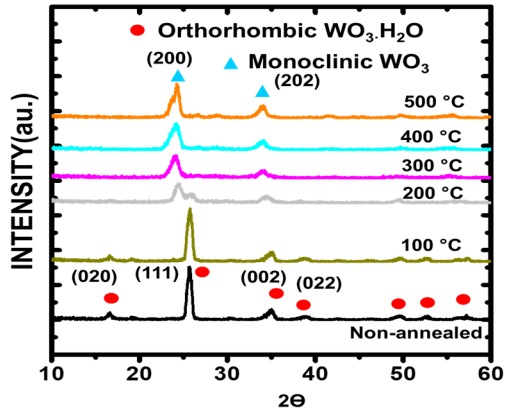

Figure 10. XRD patterns of the $WO_3 \cdot H_2O$ film and WO_3 films with different annealing temperature.

Conclusions

In this research, the WO_3 films with the nanoplate structure were successfully fabricated by the sputtering technique following by acid treatment and annealing. It was found that the $WO_3 \cdot H_2O$ nanostructure film was best formed at the HNO_3 immersion time of 90 min. The $WO_3 \cdot H_2O$ nanostructure film was transformed into the WO_3 film by annealing at temperature of $\geq$ 200°C. The film thickness was decreased as the annealing temperature was higher. The visible optical transmittance increased with the annealing temperature up to 400°C.

Acknowledgements

This work is supported by the Thailand Research Fund (TRF) in cooperation with Khon Kaen University (RSA5980014), and the Nanotechnology Center (NANOTEC), NSTDA, Ministry of Science and Technology, Thailand, through its program of Center of Excellence Network.

References

1. Bignozzi, C.A., et al. (2013). Nanostructured photoelectrodes based on WO_3: applications to photooxidation of aqueous electrolytes. *Chem Soc Rev*. **42(6)**: 2228-46.

2. Horprathum, M., et al. (2013). NO_2-sensing properties of WO_3 nanorods prepared by glancing angle DC magnetron sputtering. *Sensor Actuat B-Chem*. **176**: 685-91.

3. Santato, C., et al. (2001). Crystallographically oriented Mesoporous WO_3 films: Synthesis, characterization, and applications. *J Am Chem Soc*. **123(43)**: 10639-49.

4. Garg, D., et al. (2005). An economic analysis of the deposition of electrochromic WO_3 via sputtering or plasma enhanced chemical vapor deposition. *Mat Sci Eng B-Solid*. **119(3)**: 224-31.

5. Joraid, A.A. (2009). Comparison of electrochromic amorphous and crystalline electron beam deposited WO_3 thin films. *Curr Appl Phys*. **9(1)**: 73-9.

6. Patil, P.S., et al. (2005). Electrochromic properties of spray deposited TiO_2-doped WO_3 thin films. *Appl Surf Sci*. **250(1-4)**: 117-23.

7. Ng, C.Y., et al. (2015). Effect of annealing on acid-treated WO_3 center dot H_2O nanoplates and their electrochromic properties. *Electrochimica Acta*. **178**: 673-81.

8. Li, W.Z., et al. (2012). Platelike WO_3 from hydrothermal RF sputtered tungsten thin films for photoelectrochemical water oxidation. *Materials Letters*. **84**: 41-3.

9. Widenkvist, E., et al. (2008). Synthesis of nanostructured tungsten oxide thin films. *Cryst Growth Des*. **8(10)**: 3750-3.

10. Amano, F., et al. (2011). Facile Preparation of Platelike Tungsten Oxide Thin Film Electrodes with High Photoelectrode Activity. *Acs Appl Mater Inter*. **3(10)**: 4047-52.

Synthesis and magnetic properties of bacterial cellulose—ferrite (MFe_2O_4, M=Mn, Co, Ni, Cu) nanocomposites prepared by co-precipitation method

2017 Adv. Nat. Sci: Nanosci. Nanotechnol. 8 035005

(http://iopscience.iop.org/2043-6262/8/3/035005)

OPEN ACCESS
IOP Publishing
Advances in Natural Sciences: Nanoscience and Nanotechnology
Adv. Nat. Sci.: Nanosci. Nanotechnol. **8** (2017) 035005 (7pp)
https://doi.org/10.1088/2043-6254/aa7229

Synthesis and magnetic properties of bacterial cellulose—ferrite (MFe_2O_4, M = Mn, Co, Ni, Cu) nanocomposites prepared by co-precipitation method*

Nipaporn Sriplai[1], Wiyada Mongkolthanaruk[2] and Supree Pinitsoontorn[3,4]

[1] Materials Science and Nanotechnology Program, Faculty of Science, Khon Kaen University, Khon Kaen 40002, Thailand
[2] Department of Microbiology, Faculty of Science, Khon Kaen University, Khon Kaen 40002, Thailand
[3] Integrated Nanotechnology Research Center, Department of Physics, Faculty of Science, Khon Kaen University, Khon Kaen 40002, Thailand
[4] Nanotec-KKU Center of Excellence on Advanced Nanomaterials for Energy Production and Storage, Khon Kaen University, Khon Kaen 40002, Thailand

E-mail: psupree@kku.ac.th

Received 3 February 2017
Accepted for publication 12 April 2017
Published 17 July 2017

Abstract

The magnetic nanocomposites based on bacterial cellulose (BC) matrix and ferrite (MFe_2O_4, M = Mn, Co, Ni and Cu) nanoparticles (NPs) were fabricated. The never-dried and freeze-dried BC nanofibrils were used as templates and a co-precipitation method was applied for NPs synthesis. The nanocomposites were either freeze-dried or annealed before subjected to characterization. The x-ray diffraction (XRD) and Fourier transform infrared (FTIR) spectroscopy showed that only $MnFe_2O_4$ and $CoFe_2O_4$ NPs could be successfully incorporated in the BC nanostructures. The results also indicated that the BC template should be freeze-dried prior to the co-precipitation process. The magnetic measurement by a vibrating sample magnetometer (VSM) showed that the strongest ferromagnetic signal was found for BC-$CoFe_2O_4$ nanocomposites. The morphological investigation by a scanning electron microscope (SEM) showed the largest volume fraction of NPs in the BC-$CoFe_2O_4$ sample which was complimentary to the magnetic property measurement. Annealing resulted in the collapse of the opened nanostructure of the BC composites.

Keywords: bacterial cellulose, nanocomposite, ferrite, magnetic property
Classificationa numbers: 2.04, 5.02, 5.11

* Invited talk at 5th Thailand International Nanotechnology Conference (Nano Thailand-2016), 27–29 November 2016, Nakhon Ratchasima, Thailand.

1. Introduction

Bacterial cellulose (BC) is a fascinating and renewable natural nanomaterial. It has received substantial interest owing to its unique structural features and favorable properties such as remarkable mechanical properties, porosity, water absorbency, moldability, biodegradability and excellent biological affinity [1–3]. Intensive research and exploration in the past few decades on BC nanomaterials mainly focused on their biosynthetic process to achieve the low-cost preparation and application in a wide range of fields such as paper making, textile industry, reinforcement materials, and medical applications [1–3]. Nevertheless, the investigations of BC in these fields have led to the emergence of more diverse potential applications exploiting the functionality of BC nanomaterials.

The hybrid nanocomposites consisting of BC nanofibers and magnetic nanoparticles (NPs) have attracted attention from many research groups due to their potential novel applications. Generally, cellulosic magnetic composites have a wide range of potential applications, for instance, electronic actuator [4, 5], magnetographic printing [4, 6], magnetic sensor [4, 6, 7], electromagnetic shielding [4, 6, 8, 9], and heavy metal adsorption [8, 10, 11]. Incorporated magnetic NP-BC has several advantages over other magnetic celluloses since BC offers much better mechanical properties. BC shows relative high Young's modulus making it both flexible and stiff membrane. Furthermore, BC-magnetic nanoparticles composites have a potential application as flexible ultra-light weight magnets [12, 13]. A previous research has reported synthesis of magnetic aerogels based on BC-ferrite nanoparticles composite [14]. Unlike other magnetic gels which are brittle in their dry states [13, 15], the BC magnetic aerogels are stiff and flexible making them very useful for practical applications.

Amongst NPs, the magnetite (Fe_3O_4) NP is the most widely used for incorporation in BC hybrid nanocomposites due to its generally excellent magnetic properties [4, 7–9, 11, 16]. However, in some applications other kinds of magnetic NPs may be more appropriate [6, 14, 17, 18]. Very few studies for other types of magnetic NPs in BC were reported. For examples, Olsson *et al* [14] reported the fabrication of magnetic aerogels by incorporating cobalt ferrite ($CoFe_2O_4$) NPs in the BC nanofibril templates. In their method, the freeze-dried BC was immersed in an aqueous $FeSO_4/CoCl_2$ solution before an immersion in $NaOH/KNO_3$ solution. In this process, the precursors were converted into cobalt ferrite in the BC scaffold resulting in highly flexible magnetic membranes. Furthermore, Menchaca-Nal *et al* [18] used BC nanofibril as a template for the synthesis of cobalt ferrite nanutubes by a simple co-precipitation of $FeCl_3{\cdot}6H_2O$ and $CoCl_2{\cdot}6H_2O$. The cobalt ferrite NPs formed into a tube shape (diameter of 200 nm) surrounding the BC nanofibers. In addition, hydrothermally synthesized barium hexaferrite nanoplates were mixed in BC solution and vacuum filtered to produce flexible magnetic papers [17]. The mechanical properties of the papers were improved by treating barium hexaferrite with silane coupling agent. On the other hand, Vitta *et al* [6, 19] reported the magnetically responsive BC based on crystalline metallic Ni NPs. The Ni NPs were infiltrated into the BC structure by a simple aqueous phase salt reduction method. The different drying techniques were also explored which resulted in the BC-based aerogel and xerogel with ferromagnetic behavior.

From the previous paragraph, it can be seen that very few research has been done in this field and more experimental works are still needed. Therefore, in this paper we fabricated BC-ferrites nanocomposites and investigated the phase, microstructure and magnetic properties. Four different types of cubic ferrite (MFe_2O_4 where M = Mn, Co, Ni, Cu) NPs were synthesized using BC (never-dried and freeze-dried states) as the template for NPs nucleation. In order to study the effect of different ferrite types on the morphology and properties, except the difference in the starting materials, other synthesis parameters were kept the same. The post-synthesis treatments (freeze-drying and annealing) of the BC-ferrite nanocomposites were also investigated.

2. Materials and methods

2.1. Chemicals

The chemical used for NPs synthesis were iron (III) chloride hexahydrate ($FeCl_3{\cdot}6H_2O$, reagent grade, Sigma-Aldrich), copper (II) chloride dihydrate ($CuCl_2{\cdot}2H_2O$, grade AR, QRëC), nickel (II) chloride hexahydrate ($NiCl_2{\cdot}6H_2O$, grade AR, QRëC), manganese (II) chloride tetrahydrate ($MnCl_2{\cdot}4H_2O$, grade AR, QRëC), cobalt (II) chloride hexahydrate ($CoCl_2{\cdot}6H_2O$, reagent grade, Ajax Finechem), sodium hydroxide (NaOH, 99%, EMSURE®)

2.2. BC biosynthesis

BC was cultivated using Glucanobacter *xylinum* (strain TISTR 975), supplied from the Microbiological Resources Centre, Thailand Institute of Scientific and Technological Research (TISTR), in D-glucose medium. The procedure was adapted from [7]. After incubating at 30 °C under static culture for 8 d, about 1 cm thick BC hydrogels were obtained. They were boiled in de-ionized (DI) water, and soaked in 0.5 M NaOH for 15 min. The BCs were then soaked in 5 wt% NaOH for 24 h. After that, they were rinsed with DI water several times until pH of 7 was reached. Since water was not easily evaporated from the BC nanostructure, it was called the never-dried BC, which was then used as a template for synthesis of ferrite nanocomposites. Alternatively, the water molecules were replaced with alcohol, and the freeze-drying process was applied. The freeze-dried BC was also used as a template for MFe_2O_4 NP synthesis.

2.3. Synthesis of BC-ferrite nanocomposites

The synthesis procedure was adapted from [18]. Firstly, 0.005 mol of $MCl_2.nH_2O$ (M = Mn, Co, Ni, Cu) and 0.01 mol of $FeCl_3{\cdot}6H_2O$ were dissolved in 100 ml of DI water. Secondly, the freeze-dried BC or never-dried BC were soaked in the prepared solution which was pre-heated to 90 °C. After 3 h, 80 ml of 1.2 M NaOH solution was added to convert the metallic ions into ferrite NPs. The process was kept for 6 h at 90 °C.

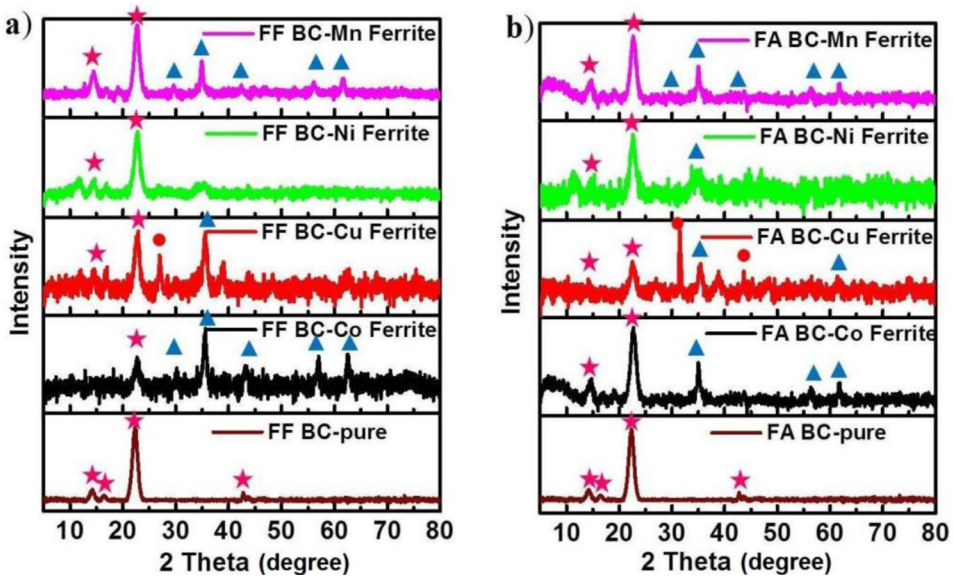

Figure 1. XRD patterns of (a) FF and (b) FA BC-ferrites nanocomposites. ★ for the BC phase, ▲ for the ferrite phase, and ● for the remaining salt.

Lastly, the BC-ferrite composites were rinsed with water several times to remove unwanted materials.

Two drying methods were applied to the BC-ferrite nanocomposites, namely, freeze-drying and oven-annealing. By combining the freeze-dried (F) and never-dried (N) BC templates and the 2 drying techniques (freeze-drying (F) and oven-annealing (~70 °C for 3 d) (A)), there are 4 series of samples, which were termed as FF, FA, NF and NA. The first letter represents the state of the BC template whereas the second letter represents the drying process of the BC-ferrite nanocomposites.

2.4. Characterization techniques

The phases and crystalline structures of pristine BC and BC-ferrite nanocomposites were examined using x-ray diffraction (XRD) with an x-ray diffractometer employing Cu-Kα radiation (PANalytical, Empyrean, USA). The functional groups and formation of NPs in BC nanostructure were investigated by using Fourier transform infrared (FTIR) spectroscopy (Bruker, TENSOR27, Germany). Magnetizations (M) versus magnetic fields (H) were measured using a vibrating sample magnetometer (VSM) option in the VersaLab (Quantum Design, USA) under a maximum field of 30 kOe. The morphologies of BC nanofibrils and the distribution of NPs were observed under a scanning electron microscope (SEM, FEI, Helios, USA).

3. Results and discussion

The phase and crystal structure of BC-ferrites nanocomposites can be seen from the XRD patterns (figures 1 and 2). For the pristine BC, XRD patterns showed three nicely sharp peaks indicating a good crystalline structure of BC, similar to those in literatures [4, 20, 21]. For the BC-ferrite nanocomposites, depending on the types of ferrites and the process of NP impregnation and drying, the XRD patterns varied from one sample to another. In the FF series (figure 1(a)), the strong crystalline peaks can be found for the Co ferrite and Mn ferrite samples. The Cu ferrite nanocomposite showed a peak for the ferrite phase but other unidentified peaks were still visible implying impurity phases. Almost no peak was found for BC-Ni ferrite sample, except a small hump around 35°. Similar results can be observed for the FA series (figure 1(b)), except that the peaks for NaCl salt (by-products) were observed in the Cu and Ni ferrites samples. The XRD results in figure 1 implied that our method for the synthesis of Cu and Ni ferrite NPs in the freeze-dried BC scaffold may not be suitable since the composite phases were not found simultaneously. On the other hand, Mn and Co samples showed the strong crystalline peaks for both BC and ferrite phases, making this method appropriate for fabrication the Mn and Co ferrites-BC nanocomposites.

When the NPs were synthesized in the never-dried BC template, the XRD patterns are shown in figure 2. A number of impurity phases can be found, particularly the NaCl peaks. The peaks for the ferrite phases were not strong, except for the NF BC-Mn ferrite sample. These results indicated that the co-precipitation of ferrite NPs were not very successful using the never-dried BC as a template. Generally, the pristine BC in the never-dried state absorbs significant amount of water [22, 23]. The water molecules are very stable unless they are exacted by force, i.e. under drying process. We hypothesize that, during the NP synthesis, it is difficult for Fe^{3+} and M^{2+} ions to infiltrate through the water barrier to reach the surface of BC nanofibers. Thus, the co-precipitation process for producing ferrite NPs is obstructed. Unlike the co-precipitation process of NPs using the freeze-dried BC template (this work and also in [14, 18]), the metallic ions can easily be adsorbed at the functional groups of BC nanofibrils. It should be noted that although it was carried out in water-based solution, water

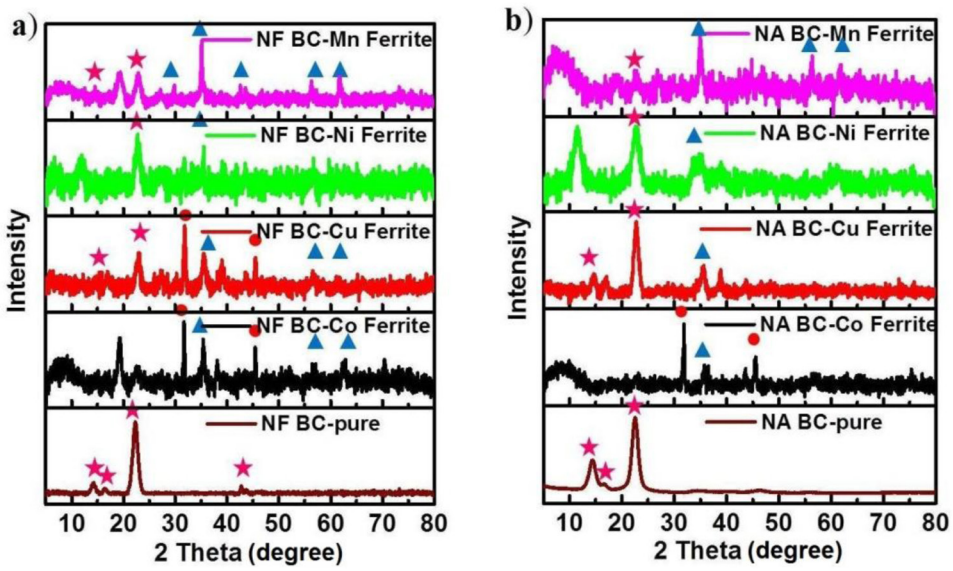

Figure 2. XRD patterns of (a) NF and (b) NA BC-ferrites nanocomposites. ★ for the BC phase, ▲ for the ferrite phase, and ● for the remaining salt.

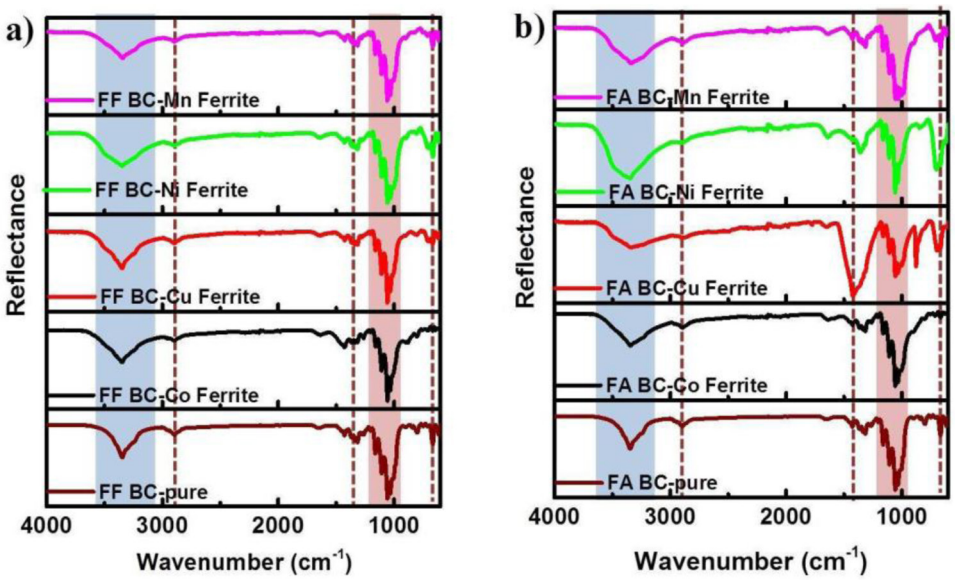

Figure 3. FTIR spectra of (a) FF and (b) FA BC-ferrites nanocomposites.

molecules were not strongly bonded with the freeze-dried BC. It is hence advised that the co-precipitation reaction should not be done using never-dried BC templates.

The presence of the strong NaCl peaks in figure 2 can be explained from the co-precipitation reaction

$$\begin{aligned} &MCl_2 + 2FeCl_3 \rightarrow M^{2+} + 2Fe^{3+} + 8Cl^-, \\ &8NaOH \rightarrow 8Na^+ + 8OH^-, \\ &M^{2+} + Fe^{3+} + 8Cl^- + 8Na^+ + 8OH^- \rightarrow MFe_2O_4 + 4H_2O + 8NaCl. \end{aligned} \quad (1)$$

It can be seen that NaCl is the by-product of the co-precipitation reaction. However, the NaCl peaks were observed only in the samples using the never-dried BC as a template but not in the freeze-dried BC templates. We believed that for the freeze-dried BC, NaCl was mostly washed away easily in the rinsing process. On the other hand, the never-dried BC contained numerous water molecules. NaCl was dissolved in water and trapped in the BC structure which could not be easily removed by rinsing. That is the reason why the large XRD NaCl peaks were found for the never-dried BC template samples.

Another important point from XRD analysis is that though the synthesis process was the same for every sample, only the Mn and Co ferrite-BC composites showed the diffracted peaks for both ferrite and BC phases. It can be concluded that a simple co-precipitation method using chloride salts may not be suitable for preparing Ni and Cu ferrite NPs. In fact, it was reported that the as-synthesized Ni ferrite NP produced from $Ni(NO_3)_2$ and $Fe(NO_3)_3$ did not form the crystalline phase unless a high temperature annealing (>600 °C) was applied [24]. Similarly, previous research showed that

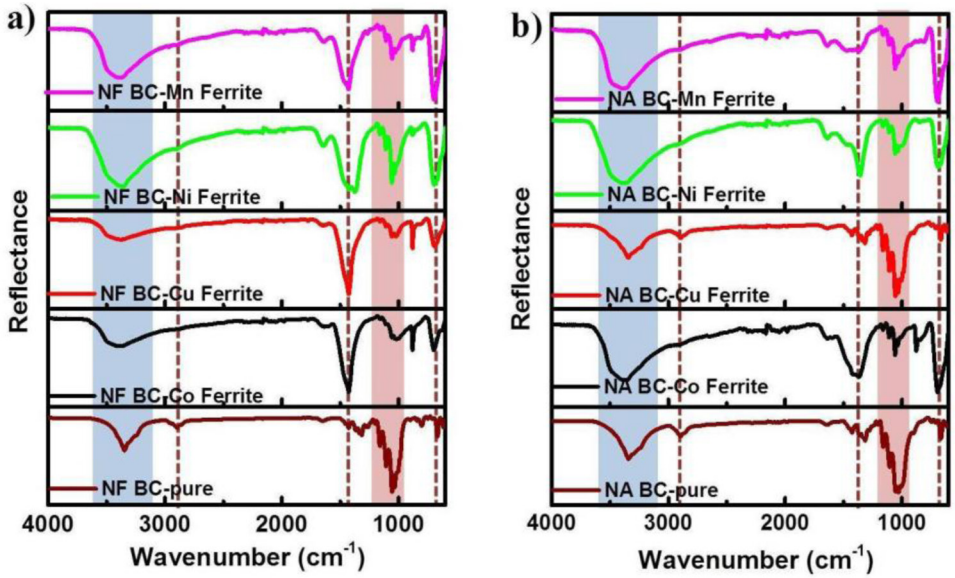

Figure 4. FTIR spectra of (a) NF and (b) NA BC-ferrites nanocomposites.

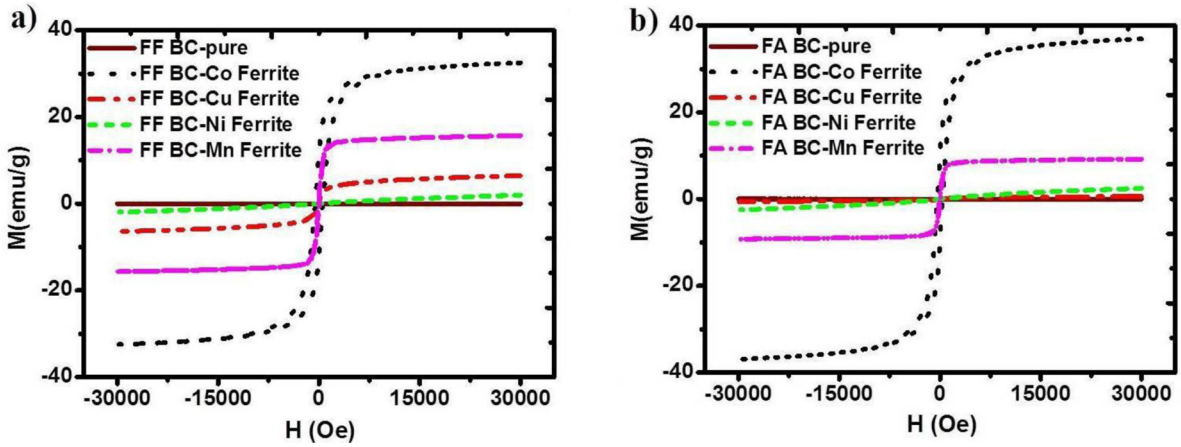

Figure 5. Magnetization (M) versus magnetic field (H) of (a) FF and (b) FA BC-ferrites nanocomposites.

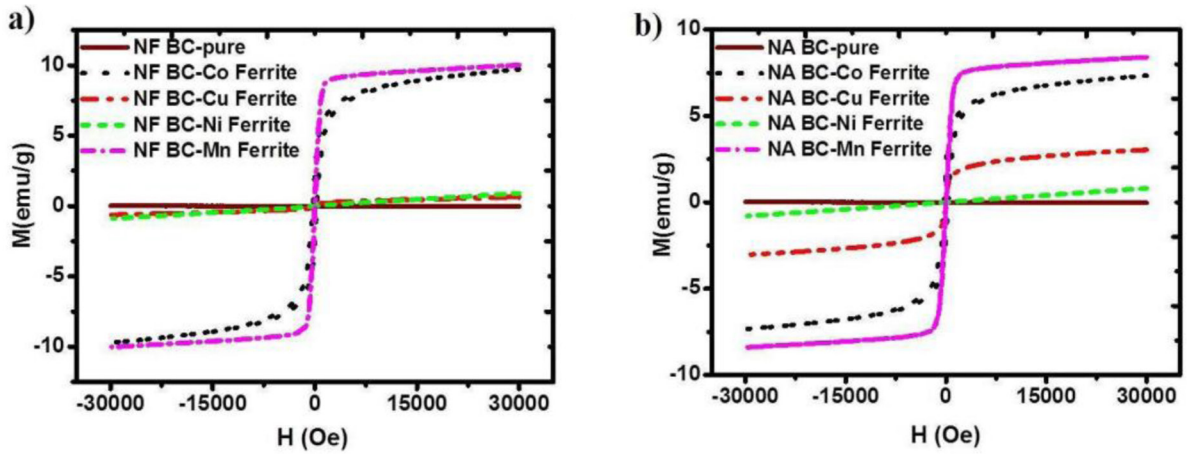

Figure 6. Magnetization (M) versus magnetic field (H) of (a) NF and (b) NA BC-ferrites nanocomposites.

$CuFe_2O_4$ phase, starting from $Cu(CH_3COO)_2$ and $Fe(NO_3)_3$, was obtained only when the NPs were heated above 600 °C [25]. It is thus assumed that the kinetics of forming the Ni and Cu ferrite phases require higher temperature than that of Mn and Co ferrites.

We further investigated the formation of ferrite NPs in BC structure by using FTIR spectra as shown in figures 3 and 4. Every sample in the FF series showed very similar spectra consisting of the main absorption peak at 1055 cm^{-1} and the broad peak at 3350 cm^{-1} which corresponded to the C–O–C

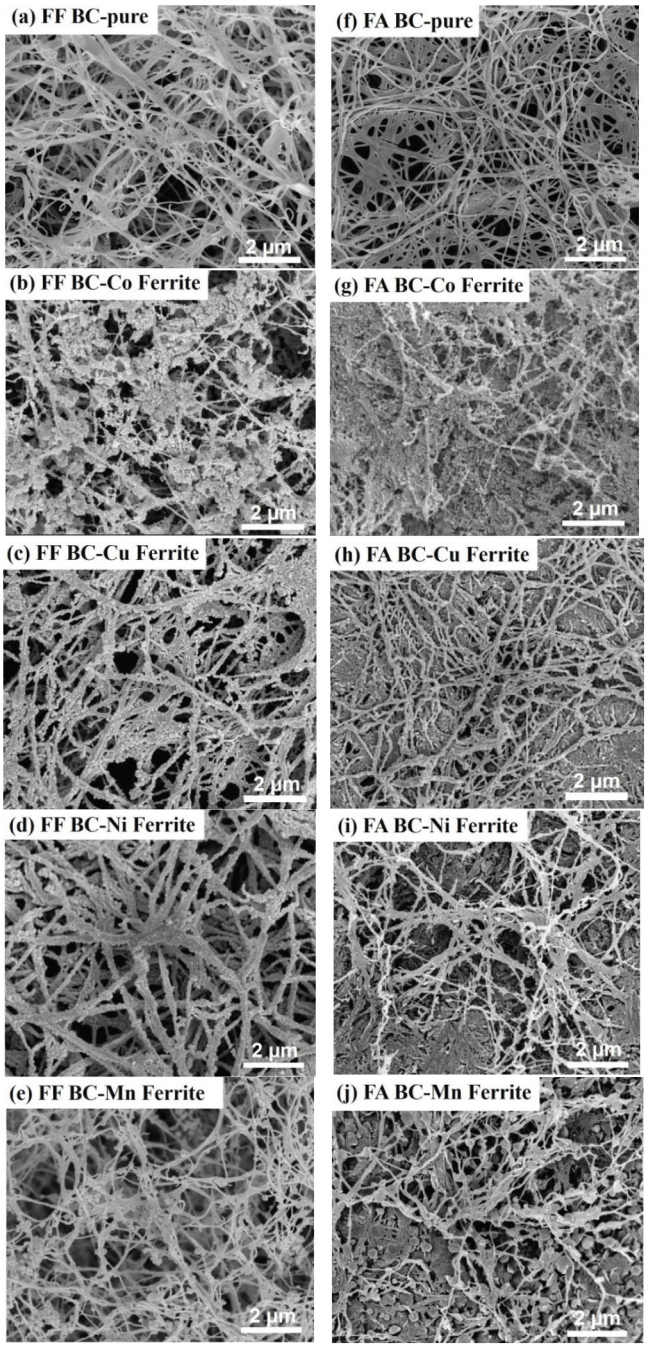

Figure 7. SEM images of the FF BC-ferrites nanocomposites ((a)–(e) in left column) and the FA BC-ferrites nanocomposites ((f)–(j) in right column).

stretching vibration and the hydroxyl group, respectively [26, 27]. Other small peaks related to C–H deformation vibration, C–H bending and stretching can be found at 810 cm^{-1}, 1325 cm^{-1} and 2880 cm^{-1}, which are the characteristic absorption peaks of BC [26, 27]. It should be noticed that the peak for –OH group was not decreased when the MFe_2O_4 NPs were impregnated in the BC templates. The –OH group on the BC surface was likely to attract the M^{2+} and Fe^{3+} ions in the first stage of co-precipitation process. The unreduced peak intensity of –OH group suggested that dipole-dipole interactions were the main force that anchor metallic ions onto the surface of the BC nanofibrils.

For the FA series, the Mn and Co ferrite samples showed very similar FTIR spectra to the pure BC and the FF series. The abnormality was found in the Ni and Cu ferrite samples. The strong absorption peak was found at 1425 cm^{-1} for the Ni and Cu ferrite samples which was attributed to the unreacted NaOH precipitating agent. As mentioned earlier that the kinetics of Ni and Cu ferrite phases transformation may require high temperature process, thus, in order to obtain the Ni and Cu ferrite NPs, subsequent annealing above 500 °C should be applied [24, 25].

For the NF and NA series (figure 4), the FTIR spectra of the pristine BC resembled the FF and FA series. All BC-ferrite composite samples showed very strong absorption peaks around 1400–1500 cm^{-1}, which corresponded to the unreacted NaOH molecules. The FTIR analysis confirmed once again that the synthesis of ferrite NPs in the presence of the never-dried BC was not achievable.

Magnetic property measurements are shown in figures 5 and 6. It is clearly seen that the magnetization values of all samples in the NF and NA series (figure 6) are much smaller than those in the FF and FA series (figure 5). The magnetic measurement supported the XRD and FTIR analysis that the ferrite NPs were not successfully formed in the never-dried BC templates, which led to low values of magnetization.

In the case of the FF and FA series (figure 5), the saturation magnetization (M_s) was maximized for the Co-ferrite samples, followed by the Mn-ferrite sample. Besides, the Co-ferrite nanocomposites exhibited a small hysteresis loops whereas the Mn-ferrite sample showed no loop, i.e. superparamagnetism. The M_s value of the BC-$CoFe_2O_4$ nanocomposites exceeded 30 emu g^{-1}, which was equivalent to approximately 1/3 of the M_s of the bulk cobalt ferrite [28]. It meaned the freeze-dried BC could uptake the $CoFe_2O_4$ NPs of roughly 30% of its volume. The FF BC-$CuFe_2O_4$ nanocomposites showed the superparamagnetic behavior but with relatively low M_s, whereas in the FA BC-$CuFe_2O_4$ and both FF and FA BC-$NiFe_2O_4$ samples, the ferromagnetism was almost completely diminished. These results, again, supported the XRD and FTIR analysis discussed in the previous section.

Since the magnetizations of the NF and NA series were much lower than those for the FF and FA series, the microstructural investigation was thus focused only for the FF and FA samples (figure 7). Compared between these two series, the FF samples consisted of 3D interconnected nanofibers (figures 7(a)–(e)) whereas the annealed samples (FA) resulted in some bundles of nanofibers (figures 7(f)–(j)). The FF samples also contained much higher porosity than the FA samples. The nanofiber structure of the FA BC samples appeared to be contracted and became more densely packed. The average fiber diameter of both series was less than 100 nm.

In figures 7(a)–(e), the BC-$CoFe_2O_4$ nanocomposites contained significant amount of NPs compared to the other samples. The NP loaded volume, approximated by eyes, could be up to 30–40 vol%. This was corresponded to the maximized M_s for the FF BC-cobalt ferrite sample in figure 5(a). The clustering of cobalt ferrite NPs could well explain the observed hysteresis loop of BC-$CoFe_2O_4$ nanocomposite. An isolated NPs exhibit superparamagnetic behavior because thermal

energy is larger than magnetic energy. A cluster of NPs has a larger volume which can sustain thermal fluctuation resulting in a hysteresis loop with finite coercivity values. Lower volume uptake of NPs was observed in the BC-$MnFe_2O_4$ sample. Well-separated NPs with small volume fraction were responsible for the superparamagnetic *M–H* curve with small M_s for the BC-$MnFe_2O_4$ nanocomposites in figure 5(a). For the BC-Ni and Cu ferrite nanocomposites, it was observed that the BC nanofibers were covered with the Ni and Cu precursors. However, the magnetic NPs were not precipitated on the surface of BC. These images showed the strong evident for the missing XRD peaks and the non-ferromagnetic properties of the BC-$NiFe_2O_4$ and BC-$CuFe_2O_4$ samples.

The SEM images of the BC-ferrite nanocomposites in the FA series showed the more compacted nanostructures (figures 7(f)–(j)). Pore volumes were significantly reduced in all samples due to the collapse of open-spaced nanofibrils when water was evaporated. For the BC–$MnFe_2O_4$ samples, the magnetic particle size was significantly larger due to the agglomeration of NPs during the annealing process. For the FA BC-$CoFe_2O_4$ sample, it is difficult to observe individual NPs due to the collapsed BC nanostructure. However, the volume fraction of the cobalt ferrite NPs was very high, in agreement with the high value of M_s. The magnetic NPs were not clearly seen in the case of BC-Ni and Cu ferrite nanocomposites. The morphologies of the FA BC-Ni and Cu ferrite samples looked similarly to the FF samples except that the nanostructure was densely compacted. The observed microstructure supported the magnetic measurement results.

4. Conclusion

In this work we have incorporated MFe_2O_4 ferrite NPs in the nanostructure of BC. The XRD and FTIR results showed that the synthesized NPs using the never-dried BC as a template were not successfully fabricated. This was interpreted that the significant amount of water in the never-dried BC inhibited the co-precipitation process of magnetic NPs on the surface of BC nanofibrils. On the other hand, using the freeze-dried BC as a template, the BC-Mn and Co ferrite nanocomposites could be produced successfully. The crystalline phases of Ni and Cu ferrites were not achieved probably due to the different transformation kinetics of these ferrite species. The magnetic property measurement showed that the BC-$CoFe_2O_4$ nanocomposites exhibited the strongest magnetic signals equivalent to about 1/3 of the $CoFe_2O_4$ bulk values. The M_s of $MnFe_2O_4$ is the second highest whereas the magnetization was nearly disappeared for the other samples. Microstructural analysis using SEM evidently supported the other measurements. The largest volume fraction of NPs was found in BC-$CoFe_2O_4$ nanocomposites. The SEM also showed the collapsed nanostructure in the annealed samples due to rapid evaporation of water. It is concluded that a simple co-precipitation method using the freeze-dried BC template is the best for synthesizing BC-$CoFe_2O_4$ nanocomposites. In addition, the samples should be freeze-dried in order to preserve the opened nanostructure.

Acknowledgment

This work is supported by the Thailand Research Fund (TRF) in cooperation with Khon Kaen University (RSA5980014), the Royal Golden Jubilee Ph D Programme (PHD/0063/2558), and the Nanotechnology Center (NANOTEC), NSTDA, Ministry of Science and Technology, Thailand, through its program of Center of Excellence Network.

References

[1] Hu W L, Chen S Y, Yang J X, Li Z and Wang H P 2014 *Carbohydrate Polym.* **101** 1043
[2] Huang Y, Zhu C L, Yang J Z, Nie Y, Chen C T and Sun D P 2014 *Cellulose* **21** 1
[3] Shah N, Ul-Islam M, Khattak W A and Park J K 2013 *Carbohydrate Polym.* **98** 1585
[4] Zhang W, Chen S Y, Hu W L, Zhou B H, Yang Z H, Yin N and Wang H P 2011 *Carbohydrate Polym.* **86** 1760
[5] Barud H S, Tercjak A, Gutierrez J, Viali W R, Nunes E S, Ribeiro S J L, Jafellici M, Nalin M and Marques R F C 2015 *J. Appl. Phys.* **117** 17B734
[6] Vitta S, Drillon M and Derory A 2010 *J. Appl. Phys.* **108** 053905
[7] Katepetch C and Rujiravanit R 2011 *Carbohydrate Polym.* **86** 162
[8] Marins J A, Soares B G, Barud H S and Ribeiro S J L 2013 *Mater. Sci. Eng.* C **33** 3994
[9] Park M, Cheng J, Choi J, Kim J and Hyun J 2013 *Colloids Surf.* B **102** 238
[10] Nata I F, Sureshkumar M and Lee C K 2011 *RSC Adv.* **1** 625
[11] Zhu H X, Jia S R, Wan T, Jia Y Y, Yang H J, Li J, Yan L and Zhong C 2011 *Carbohydrate Polym.* **86** 1558
[12] Chen N and Pan Q M 2013 *ACS Nano* **7** 6875
[13] Bonini M, Lenz S, Giorgi R and Baglioni P 2007 *Langmuir* **23** 8681
[14] Olsson R T, Samir M A S A, Salazar-Alvarez G, Belova L, Strom V, Berglund L A, Ikkala O, Nogues J and Gedde U W 2010 *Nat. Nanotechnol.* **5** 584
[15] Gich M *et al* 2003 *Appl. Phys. Lett.* **82** 4307
[16] Zeng M L, Laromaine A, Feng W Q, Levkin P A and Roig A 2014 *J. Mater. Chem.* C **2** 6312
[17] Lim G H, Lee J, Kwon N, Bok S, Sim H, Moon K S, Lee S E and Lim B 2016 *Electron. Mater. Lett.* **12** 574
[18] Menchaca-Nal S, Londono-Calderon C L, Cerrutti P, Foresti M L, Pampillo L, Bilovol V, Candal R and Martinez-Garcia R 2016 *Carbohydrate Polym.* **137** 726
[19] Thiruvengadam V and Vitta S 2013 *RSC Adv.* **3** 12765
[20] Sureshkumar M, Siswanto D Y and Lee C K 2010 *J. Mater. Chem.* **20** 6948
[21] Zheng Y, Yang J X, Zheng W L, Wang X, Xiang C, Tang L, Zhang W, Chen S Y and Wang H P 2013 *Mater. Sci. Eng.* C **33** 2407
[22] Klemm D, Kramer F, Moritz S, Lindstrom T, Ankerfors M, Gray D and Dorris A 2011 *Angew. Chem., Int. Ed.* **50** 5438
[23] Rajwade J M, Paknikar K M and Kumbhar J V 2015 *Appl. Microbiol. Biotechnol.* **99** 2491
[24] Sutka A, Millers M, Vanags M, Joost U, Maiorov M, Kisand V, Parna R and Juhnevica I 2015 *Res. Chem. Intermediates* **41** 9439
[25] Sun Z P, Liu L, Ha D Z and Pan W Y 2007 *Sensor Actuators* B **125** 144
[26] Alves L, Medronho B F, Antunes F E, Romano A, Miguel M G and Lindman B 2015 *Colloids Surf.* A **483** 257
[27] Mtibe A, Linganiso L Z, Mathew A P, Oksman K, John M J and Anandjiwala R D 2015 *Carbohydrate. Polym.* **118** 1
[28] Cullity B D and Graham C D 2009 *Introduction to Magnetic Materials* 2nd edn (Wiley Hoboken, NJ: IEEE Press)

Journal of Alloys and Compounds 739 (2018) 19–29

Contents lists available at ScienceDirect

Journal of Alloys and Compounds

journal homepage: http://www.elsevier.com/locate/jalcom

Magnetic behavior of novel alloyed $L1_0$-phase $Co_{1-x}Fe_xPt$ nanoparticles

Nipaporn Sriplai [a], Sireemas Koowattanasuchat [a], Pinit Kidkhunthod [b], Narong Chanlek [b], Stephen J. Eichhorn [c], Supree Pinitsoontorn [d, *]

[a] Materials Science and Nanotechnology Program, Faculty of Science, Khon Kaen University, Khon Kaen, 40002, Thailand
[b] Synchrotron Light Research Institute (Public Organization), Nakhon Ratchasima, Thailand
[c] Bristol Composites Institute (ACCIS), Queens Building, University of Bristol, Bristol, BS8 1TR, UK
[d] Integrated Nanotechnology Research Center, Department of Physics, Faculty of Science, Khon Kaen University, Khon Kaen, 40002, Thailand

ARTICLE INFO

Article history:
Received 18 September 2017
Received in revised form
9 December 2017
Accepted 19 December 2017
Available online 21 December 2017

Keywords:
Nanoparticle
Magnetic properties
FePt
CoPt

ABSTRACT

In this work, alloying of CoPt and FePt nanoparticles (NPs), i.e. the $Co_{1-x}Fe_xPt$ NPs ($x = 0, 0.25, 0.5, 0.75, 1$), were synthesized by the polyol process. These as-synthesized NPs show the A1 phase with a particle size less than 5 nm. After annealing at 700 °C, the A1 (cubic) phase was transformed to $L1_0$ (tetragonal) phase in all samples. The lattice parameters varied as a function of the composition. The particle size grew larger after annealing and the size distribution was wide ranging from <10 nm to >100 nm. The size and distribution was however independent of the Co(Fe) concentration. X-ray absorption spectroscopy indicated that there was a random distribution of Co and Fe atoms in the layered structure. Magnetic measurements of the annealed NPs showed that the magnetic hysteresis loop depends on the composition. The coercivity (H_c) was very high for the CoPt and FePt NPs, whereas the M_s value was maximized for the $Co_{0.5}Fe_{0.5}Pt$ NPs. The variation of H_c was attributed to the change in lattice parameters which could alter the exchange interaction, and thus the magnetocrystalline anisotropy. On the other hand, higher polarization and increased magnetic moments of Fe atoms were believed to be the reason for the enhanced M_s in the Co(Fe)Pt NPs. In addition, all NPs were magnetically stable against temperature variation with changes in M_s of less than 10%. The Curie temperature was expected to be as high as 800 −900 K. Given these properties, these new forms of magnetic nanoparticles may find use in advanced magnetic recording technology.

1. Introduction

Magnetic nanoparticles (NPs) research is currently one of the most exciting research areas in the field of materials science, applied physics, and nanotechnology [1–3]. When the scale size of the particles reaches the nanometer regime, the magnetic properties change significantly. Since the thermal energy can easily overcome the magnetic anisotropy energy, the NPs lose their ability to maintain the magnetic retention when an applied field is removed. A magnetization curve with no hysteresis loop is then generally observed; such NPs are termed superparamagnetic. These superparamagnetic NPs have a wide range of potential applications. For instance, magnetic NPs for medical applications is one of the most active research areas. These superparamagnetic NPs could be exploited as MRI contrast agents, hyperthermia, drug delivery etc. [4].

In the other field of applications, such as magnetic recording, the retentivity of magnetic properties as the particle size is scaled down is very important [5,6]. In magnetic recording media, data is stored in the magnetic bits consisting of a number of magnetic grains/particles. In order to store data over a long period of time, the magnetic energy of the magnetic grains, defined as K_uV (where K_u is magnetocrystalline anisotropy, and V is the NP volume), must be much larger than the thermal energy (k_BT) (where k_B = Boltzmann constant, T = absolute temperature) [7]. Failing to meet this criterion results in the superparmagnetic effect and thus the loss of data. As the recording areal density is increased, the size of the magnetic grains must also be reduced continuously. Conventional magnetic materials, such as Fe, Co, Ni alloys and ferrites, cannot sustain their magnetic properties when their size is lower than 100 nm because of the low values of the magnetic anisotropy [8,9]. Currently, the state-of-the-art materials for recording media are CoCrPt based alloys [5,6]. However, as the demand for higher recording density grows, even these state-of-the-art alloys cannot

* Corresponding author.
E-mail address: psupree@kku.ac.th (S. Pinitsoontorn).

https://doi.org/10.1016/j.jallcom.2017.12.202
0925-8388/

withstand thermal fluctuations as the particle size decreases. Therefore, alternative magnetic materials with a larger anisotropy constants are required in the near future.

Amongst the choice of magnetic materials with high K_u values, CoPt and FePt NPs have received a lot of attention from many research groups as candidates for extremely high data storage materials [9–16]. As-synthesized CoPt (FePt) NPs possess a face centered cubic structure (A1 phase). This phase is a disordered alloy, i.e. the distribution of Co(Fe) and Pt atoms is random, with low K_u. The high K_u phase, K_u ~10^7 erg/cm^3, ($L1_0$ phase) with a face-centered tetragonal (fct) structure can be achieved via a heat treatment process of the as-synthesized CoPt (FePt) NPs (Fig. 1). The $L1_0$ phase is also an ordered alloy, i.e. alternative arrangements of Co (Fe) layers and Pt layers along the *c*-axis.

A number of papers have been published covering several aspects of magnetic NPs including synthesis method, phase transitions, and morphology. For the synthesis method, a polyol process was developed as a common route for synthesizing CoPt (FePt) NPs with a size of a few nms [17–19]. A few different types of Co (Fe) and Pt sources as well as reducing agents have been experimented upon. For example, Yu et al. reported the synthesis of MPt (M = Fe, Co, Ni, Cu, Zn) NPs prepared from a facile oleylamine reduction of metal salts [10]. In their process, the co-reduction of $M(acac)_2$ and $Pt(acac)_2$ was performed at 300 °C using oleylamine as the reducing agent, surfactant, and solvent. Alternatively, the CoPt (FePt) has been synthesized by using a gas phase condensation method, for which the physical deposition apparatus for depositing thin films has been adapted [16]. However, either using chemical or physical methods the as-synthesized particles need to be subjected to post-synthesis annealing to obtain the $L1_0$ phase. Therefore, Bian et al. proposed a one-step solid-phase synthesis method for preparing $L1_0$ Co(Fe)Pt NPs [15]. In their method, after dissolving $Co(acac)_2$, or $Fe(acac)_2$, and $Pt(acac)_2$ in acetyl acetone by ultrasonication, the solution was dropped onto the carbon-coated Cu grid which was heated to 550 °C. The $L1_0$ CoPt (FePt) NPs core was then coated in a carbon shell with an average diameter of a particle of 14 nm.

The phase transition temperature is another important issue. To be of practical use for magnetic recording media, the temperature at which the A1 phase transforms into the $L1_0$ phase needs to be as low as possible since many components cannot tolerate high temperatures. A reduction in the transition temperature can be achieved via doping. For example, when Ag was added in the synthesis process, the transition temperatures were reduced from 700 to 600 °C for CoPt NPs [20], and from 550 to 400 °C for FePt NPs [11]. Other elemental doping, such as Sb [21,22], Cu [23,24]or B [25], also promoted the $L1_0$ phase transformation and thus reduced the phase transition temperature of the NPs. The underlying reason for the decrease in transition temperature was believed to be related to the ease of nucleation and growth of the $L1_0$ phase when CoPt (FePt) alloys were doped. On the other hand, the addition of sufficient Au in FePt NPs was found to promote the formation of the $L1_0$ phase without any need for a high temperature process, resulting in a very large coercivity [26]. Moreover, an alternative chemical synthesis route for FePt NPs has been proposed by controlling the co-reduction of $Fe(acac)_3$ and K_2PtCl_6 in the presence of olylamine at 350 °C [27]. The coercivity of 10.5 kOe was obtained without further annealing for this system.

The dependence of size and morphology of NPs on the chemical and magnetic ordering of CoPt and FePt NPs has also been investigated [13,14]. It was found that the particle size variation (4–15 nm) had an influence on the long-range ordering parameter, saturation magnetization (M_s), shape of hysteresis loops, and Curie temperature. The Curie temperature was also found to be sensitive to the shape of NPs when the size was <3 nm.

It can be seen from the above that many research groups have studied CoPt and FePt NPs extensively. Nevertheless, the alloying effect between CoPt and FePt has never been previously reported. It has long been known that Co-Fe alloys could generate higher M_s than either pure Co or Fe metals. The M_s of $Co_{35}Fe_{65}$ bulk alloy is as high as 240 emu/g, which is one of the highest M_s value substances ever known [28]. For magnetic recording media, materials with large M_s as well as large K_u values are desirable. In CoFe NPs, it has been reported that the ratio of Co:Fe showed an influential effect on the M_s values, with the highest M_s of 207 emu/g found for the $Co_{40}Fe_{60}$ composition [29]. Nevertheless, the CoFe NPs are soft magnetic materials with small K_u. Hence, a superparamagnetic hysteresis loop was observed.

In this work, we have synthesized the $Co_{1-x}Fe_xPt$ (x = 0, 0.25, 0.5, 0.75, 1) NPs and studied the effect of Co and Fe concentrations on phase, structure, morphology and magnetic properties.

2. Experimental procedure

$Co_{1-x}Fe_xPt$ nanoparticles (x = 0, 0.25, 0.50, 0.75, 1) were synthesized via a polyol process [25,30]. Cobalt (III) acetylacetonate ($Co(acac)_2$), iron acetylacetonate ($Fe(acac)_2$) and platinum acetylacetonate ($Pt(acac)_2$) were weighed in stoichiometric ratios and then dissolved in trimethylene glycol (TMEG) in a two-neck flask. An

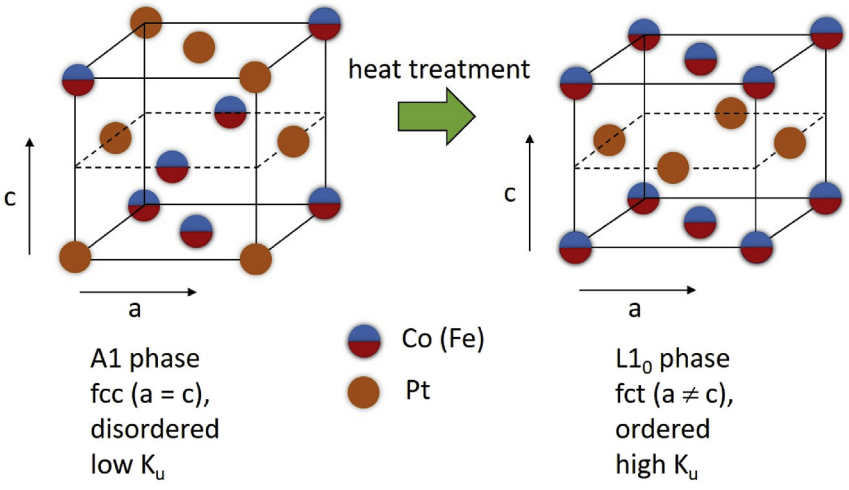

Fig. 1. Crystal structure of the Co(Fe)Pt NPs before and after heat treatment.

appropriate amount of NaOH was added into the solution which was then placed in an oil bath (glycerine) and heated to 230 °C. With constant mechanical stirring, the reflux process was allowed to continue for a maximum period of 3.5 h at this temperature. After the reflux, the suspension was cooled to room temperature. The black precipitated particles of $Co_{1-x}Fe_xPt$ alloy were isolated by centrifugation. The particles were washed with ethanol several times to remove the byproducts. The as-synthesized particles were then annealed in an Ar atmosphere at 700 °C for 2 h.

The phase formation and crystal structure of the as-synthesized and annealed samples were studied by using X-ray diffraction (XRD) with an X-ray diffractometer employing Cu-Kα radiation (PANalytical, Empyrean, Netherlands). The morphology and size of NPs before and after annealing were examined by using transmission electron microscopy (TEM) (FEI, Tecnai G2 20, USA). Thermal analysis of the as-synthesized NPs was studied by using a thermogravimetric (TGA) instrument (Hitachi, STA7200). The chemical composition of NPs was verified by using energy dispersive X-rays (EDX, Oxford) contained within the scanning electron microscope (SEM) (FEI, Helios, USA). The magnetic property measurement was carried out using a vibrating sample magnetometer (VSM) option in the VersaLab instrument (Quantum Design, USA) with the maximum applied field of 30 kOe.

To understand the local structure environment around Co and Fe ions, X-ray absorption spectroscopy (XAS) including X-ray absorption near edge structure (XANES) and extended X-ray absorption fine structure (EXAFS) spectra of Co and Fe K-edge were conducted at the SUT-NANOTEC-SLRI XAS beamline (BL5.2) [31] at the Synchrotron Light Research Institute (SLRI), Nakhon Ratchasima, Thailand. All spectra were collected in the fluorescence mode with a 4 element Si-drift detector. The normalized XAS data were processed and analyzed after background subtraction in the pre-edge and post-edge region using the ATHENA software which is included in the IFEFFIT package [32,33]. Additionally, the local-structure information around the Co and Fe atoms was obtained by fitting EXAFS data to the models based on the FEFF8.2 program [33,34].

3. Results and discussion

3.1. As-synthesized NPs

The structure and phase of the $Co_{1-x}Fe_xPt$ NPs can be observed from the XRD patterns as shown in Fig. 2. Every sample showed similar pattern with the broad peak at 2θ ~40° which is characteristic of the (111) plane of the A1 phase as previously reported [20,21,30,35]. The variation of Co and Fe ratios does not show an obvious effect of the phase change.

The NP size and morphology are observed by using TEM as shown in Fig. 3. Spherical NPs were observed in all samples with a size <5 nm, which is consistent with other similar NPs reported in the literature [10,11,17–21]. Most samples show homogeneous dispersion of NPs. Moreover, for different Co and Fe contents, the NP sizes and their shapes are not obviously different, indicating that the variation in Co(Fe) concentration has no effect on the NP morphology.

The magnetization (M-H) curves of the $Co_{1-x}Fe_xPt$ NPs are reported in Fig. 4. No hysteresis loop was observed for any sample, indicative of a superparamagnetic nature to the NPs. The observed superparamagnetism is thought to be as a result of a combination of effects. The very small particle size (< 5 nm) of all samples, as observed in Fig. 3, the low K_u value from the A1 phase, and the high portion of the amorphous phase (confirmed by from XRD), all contributed to this superparamagnetic property. However, a correlation between the M_s values and the Co:Fe ratios was not found.

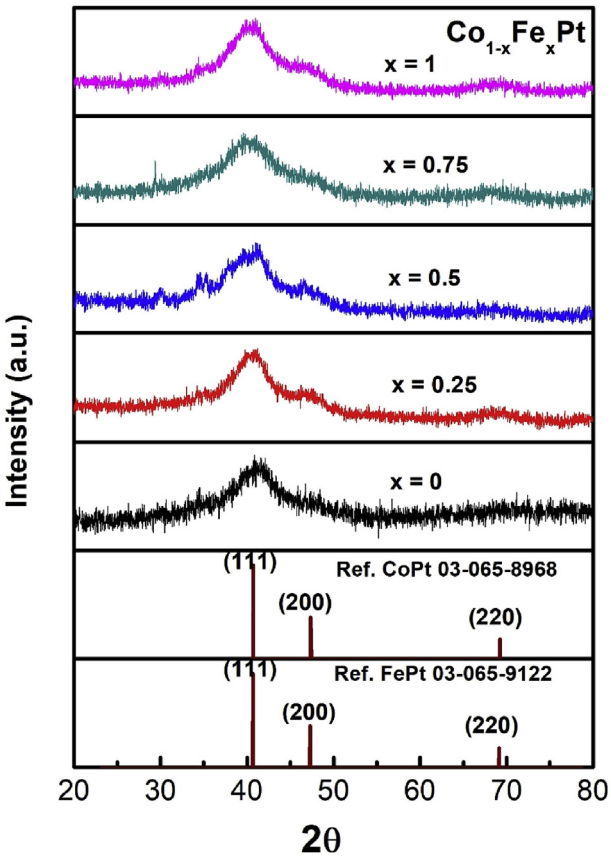

Fig. 2. XRD patterns of the as-synthesized $Co_{1-x}Fe_xPt$ NPs.

The thermogravimetry (TGA) analysis of the as-synthesized $Co_{1-x}Fe_xPt$ NPs is illustrated in Fig. 5a. The result from the TGA analysis and also from the differential thermal analysis (DTA) (not shown) did not indicate any evidence for a phase transformation temperature, which would normally occur around 500–700 °C [12,18,19,30,35]. The weight loss percentage at 700 °C as a function of Fe content is shown in Fig. 5b. The most stable NPs up to 700 °C were the CoPt NPs followed by the FePt NPs. $Co_{0.5}Fe_{0.5}Pt$ NPs underwent the highest weight loss at 700 °C, which could probably be due to the most random atomic arrangement from the equi-atomic ratio of Co:Fe.

3.2. Annealed NPs

XRD analysis of the NPs was carried out after annealing at 700 °C, and the results are shown in Fig. 6. Obviously, the XRD patterns of the NPs have changed significantly compared to Fig. 2. The NPs have clearly developed crystalline phases as can be seen from the sharp peaks in the XRD patterns. The XRD peaks in every sample can be matched with the ICDD references, 00-043-1359 for CoPt and 00-43-1358 for FePt, and also with previously published data [11,20–22]. This indicates that the phase of every sample was transformed from the A1 phase to the $L1_0$ phase after annealing at 700 °C. No obvious differences were observed between samples. The presence of small unidentified peaks around 30–40° are noted. These peaks are identified as the NaOH phases which are a residue from its use in the NPs synthesis process. Since these phases are clearly small in concentration, and are non-ferromagnetic, they ought to have little effect on the magnetic properties.

The lattice parameters (*a*, *b* and *c*) of the $Co_{1-x}Fe_xPt$ ($L1_0$ phase)

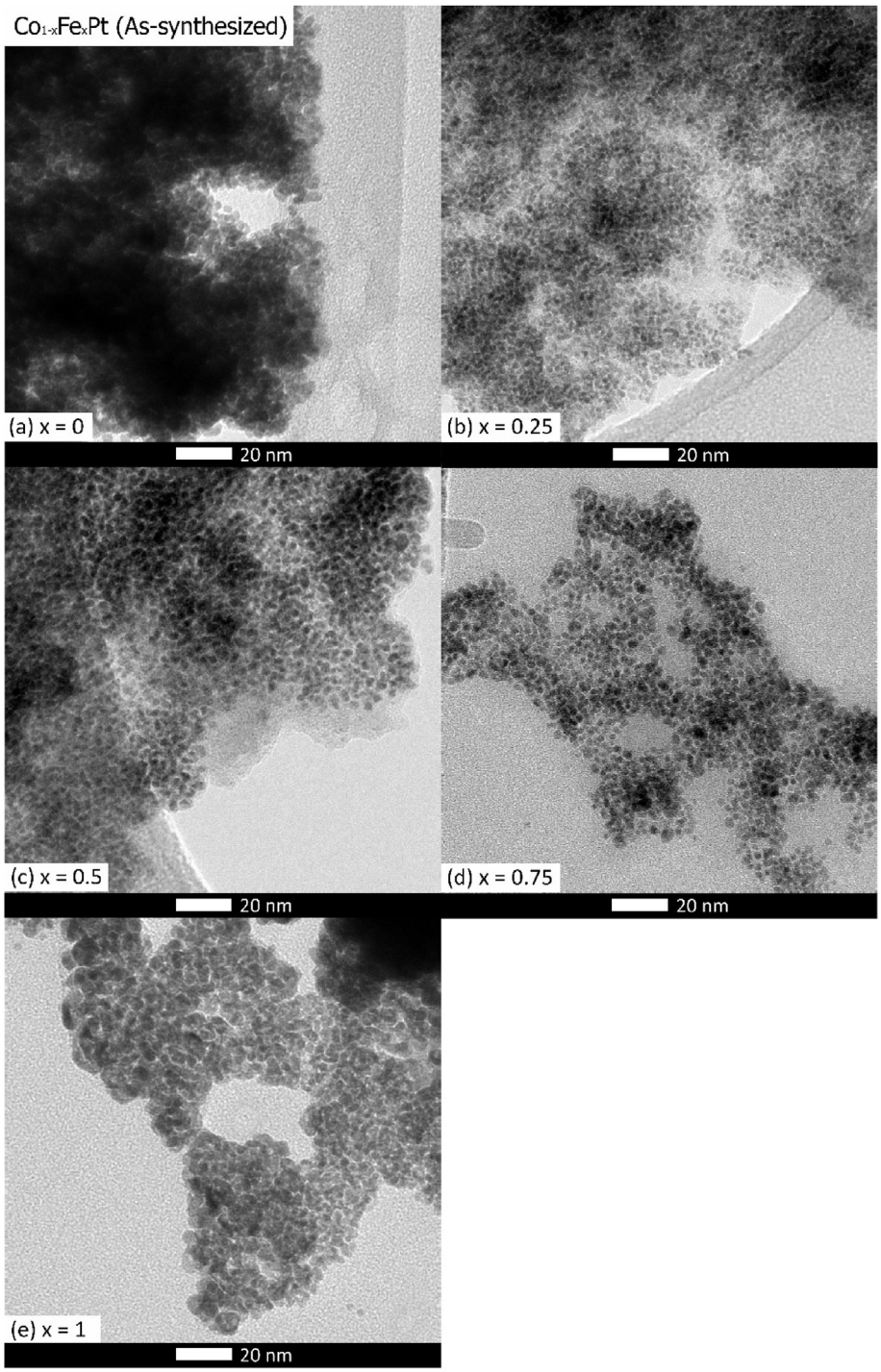

Fig. 3. TEM image of the as-synthesized $Co_{1-x}Fe_xPt$ NPs for different proportions (x) of the Co and Fe components of the elements (a–e).

NPs were extracted from the XRD patterns, using the equation $\frac{1}{d^2} = \frac{h^2+k^2}{a^2} + \frac{l^2}{c^2}$, as shown in Fig. 7a, where h,k and l are the Miller indices and d is the d-spacing from Bragg's law. There is an obvious variation in the lattice constants a and c, both of which decreased with an increasing Fe content up to $x = 0.5$, and then increased again. The minimum values of a and c for the $Co_{0.5}Fe_{0.5}Pt$ composition are somewhat unexpected. In the Co-Fe alloys with a cubic structure, the lattice parameter a increased almost monotonically as a function of Fe content [36]. This is understandable since the atomic radius of Fe is slightly larger than Co [37]. Therefore, the substitution of Co with Fe could lead to a lattice expansion, and hence an increase in the lattice parameters. For the $Co_{1-x}Fe_xPt$ NPs, the situation is more complicated since the Co(Fe) atoms are distributed in layers alternated with Pt layers. Moreover, the large surface of the NPs creates strain energy which affects the distances between neighboring atoms. These contributions could be one of the reasons for the variation of the lattice constants a and c with different Co and Fe ratios. The unit cell volumes are plotted against the composition $Co_{1-x}Fe_xPt$ as shown in Fig. 7b. Since the lattice parameters a and c show the minima at $x = 0.5$, the unit cell

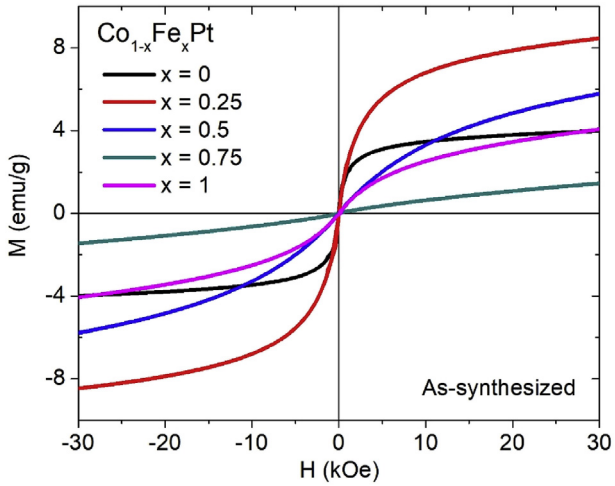

Fig. 4. Room temperature magnetization curve (M-H) of the as-synthesized $Co_{1-x}Fe_xPt$ NPs for different proportions (x) of the Co and Fe components of the elements.

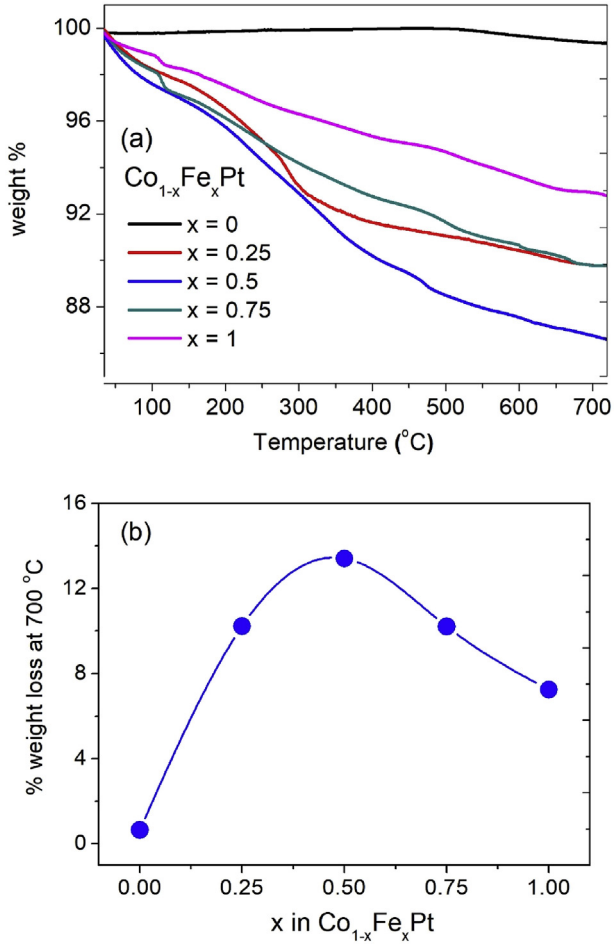

Fig. 5. (a) TGA wt.% and (b) %wt. loss at 700 °C of the as-synthesized $Co_{1-x}Fe_xPt$ NPs for different proportions (x) of the Co and Fe components of the elements.

volumes follow the same trend. The c/a ratio as a function of Fe content is also plotted in Fig. 7b. A c/a ratio of unity indicates a perfect cubic structure, whereas a deviation from this value implies the presence of a preferential tetragonal structure. As can be seen from Fig. 7b, the $Co_{0.5}Fe_{0.5}Pt$ sample shows the least deviation from

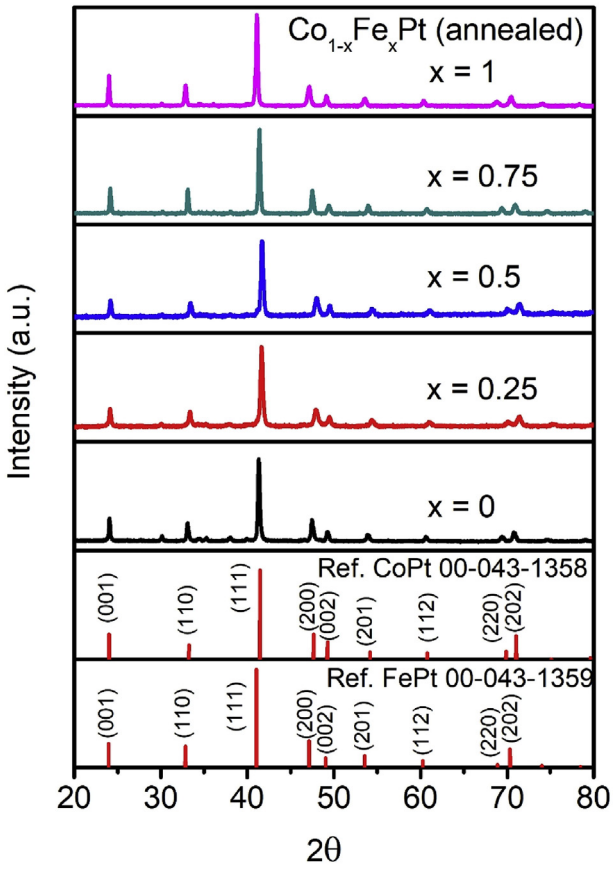

Fig. 6. XRD patterns of the annealed $Co_{1-x}Fe_xPt$ NPs for different proportions (x) of the Co and Fe components of the elements. The references of the $L1_0$ CoPt and FePt phase are also presented.

unity whereas larger distortions were found in the pure CoPt and FePt NPs. These results have a direct implication on the magnetic properties of the materials.

The TEM images for the $Co_{1-x}Fe_xPt$ NPs after annealing at 700 °C are shown in Fig. 8. For each sample, three images at different magnifications are presented. Obviously, the particle sizes of the annealed samples were larger than the as-synthesized NPs. The annealing process resulted in particle size growth for a minimization of the surface energy. Furthermore, Fig. 8 shows that the particle size distribution is very wide. The particle size could be as large as 100 nm, for instance, Fig. 8b ($x = 0.25$), or as small as < 10 nm (Fig. 8a and e). In general, every sample consists of a mixture of various sizes of NPs. Fig. 8 only presents some selected images. The average particle sizes from the TEM images are summarized in Fig. 9 which averaged from over 100 measurements for each composition. There is no indication that the particle size or size distribution has any correlation with the composition.

The morphology and chemical compositions of the annealed NPs were investigated by using SEM and EDX analysis as shown in Fig. 10. The SEM image of the FePt sample shows clusters of highly agglomerated NPs with an approximate size of individual particle of 30–50 nm which is slightly larger than the as-synthesized NPs; these values correspond well to the TEM micrographs. The larger NP size and their agglomeration could be attributed to crystal growth under a higher annealing temperature, the surface energy and their magnetic interactions. The size and morphology of the other samples look very similar to the FePt NPs. The ratios of Co:Fe verified by EDX are presented in Fig. 10b. In order to obtain the average value of the compositions, the EDX spectra were collected

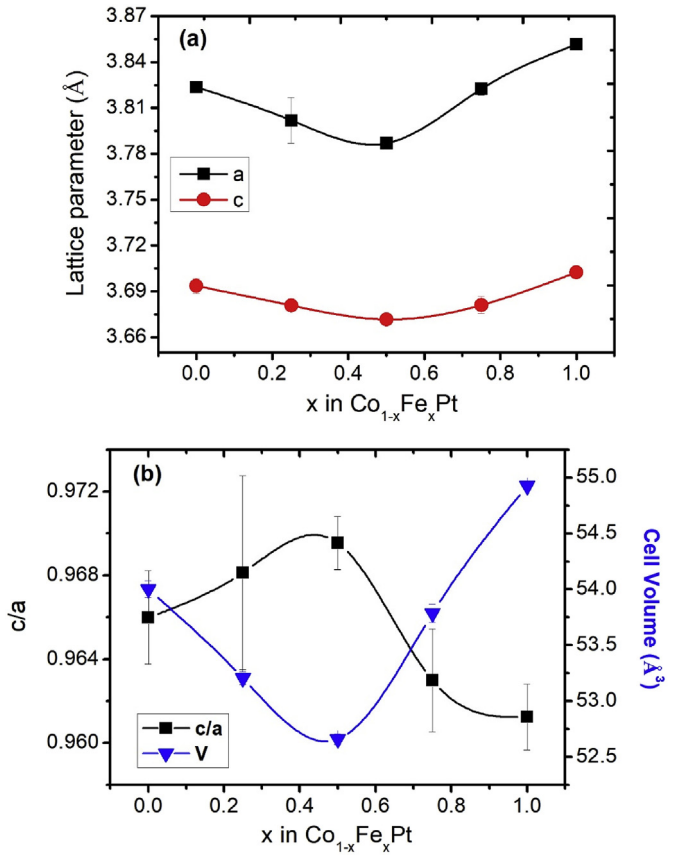

Fig. 7. *a* and *c* lattice parameters, and *c*/*a* ratio of $Co_{1-x}Fe_xPt$ NPs extracted from XRD patterns.

at a relatively low magnification (2000×) and large area (>100 × 100 μm^2). The compositions of Co and Fe were found to be very close to the $Co_{1-x}Fe_xPt$ nominal composition (±5%).

To investigate the local distribution of Co and Fe atoms in the $L1_0$ structure, the annealed samples were subjected to XAS measurement. The preferential local atomic site (random arrangement or clustering of Co and Fe atoms) can result in a critical difference in the magnetic anisotropy [8]. As shown in Fig. 11a, the XANES spectra at the Co K-edge in the $Co_{1-x}Fe_xPt$ NPs (x = 0, 0.25, 0.5, 0.75) are almost identical. It can be inferred to the first approximation that there is no distinct difference in the local distribution of Co atoms amongst the samples. Moreover, the shape of the XANES spectra of Co in this study is similar to previously published research [30,38]. The standard references for Co foil, CoO, and Co_3O_4 are also included in Fig. 11a. It is clearly seen that the samples show metallic characteristics. This is evident because the XANES spectra more closely match the Co foil (both absorption edge and peaks), with the except for the presence of Fe and Pt atoms. In addition, they are more clearly distinguished from the Co oxides spectra, and so this rules out the possibility of oxidation of the samples after annealing.

Similarly, the Fe XANES spectra in the $Co_{1-x}Fe_xPt$ NPs with x = 0.25, 0.5, 0.75, 1 are visibly similar (Fig. 11b). One noticeable difference is the increased intensity of the second peak (~7132 eV) as the Fe content increases, which could probably due to the characteristics of the metallic Fe XANES spectrum. Nevertheless, the characteristics of the Fe XANES spectra implied the indistinguishable arrangement of Fe atoms in the $Co_{1-x}Fe_xPt$ NPs. Again, the analysis of the Fe XANES spectra against the standard references (Fe foil, FeO, Fe_2O_3) in Fig. 11b indicate that these samples have more of a metallic characteristic, thereby excluding the presence of oxidative forms of Fe during the annealing process.

In order to gain more insight into the local structure of Co and Fe atoms in the $Co_{1-x}Fe_xPt$ system, the extended region (EXAFS spectra) of the selected data are plotted as shown in Fig. 12. The Co K-edge EXAFS spectra both in *k*- and *R*-space were plotted for CoPt whereas the Fe K-edge EXAFS spectra were plotted for $Co_{0.75}Fe_{0.25}Pt$ and FePt. Along with the experimental data, the fittings based on the model of a random distribution of Co and Fe atoms in the layered system are also presented. It can be seen that the fits match very well with the experimental results up to the 4th shell in *R*-space. In the same manner, the model fits the experimental data almost perfectly in the whole range of the *k*-space (3–10 Å^{-1}). The fitting parameters, the R-factor which measures the absolute misfit between data and models, are less than 0.05 in every data set, representing a good fit [32]. From the EXAFS analysis, it can be concluded that the effect of Co(Fe) concentration in $Co_{1-x}Fe_xPt$ NPs does not have a strong influence on the local distribution of Co or Fe atoms, i.e. they are randomly distributed in the alternate layers with Pt layers.

The magnetic properties of the annealed $Co_{1-x}Fe_xPt$ NPs are shown in Figs. 13–15. Fig. 13 represents the M-H curves which show the hysteresis loop for every sample. Magnetic remanence (M_r) and coercivity (H_c) are clearly observed. The change from superparamagnetic to ferromagnetic behavior for the annealed NPs could be due to several factors such as the larger particle size, higher crystallinity or an increased exchange interaction between particles. The most likely reason however would be the formation of the $L1_0$ phase as evidenced from the XRD analysis. This phase possesses the large K_u, a very hard ferromagnetic phase, making it magnetically stable against temperature fluctuations. It should be noted that the double shoulder characteristic of the M-H loop near H = 0 was observed, particularly for the CoPt and FePt samples. This is an indication of the mixed phases between the soft and hard ferromagnetic phases as a result of an incomplete phase transformation. The residual A1 phase in those samples implied that the kinetics for the $L1_0$ phase transformation in the pure CoPt and pure FePt was more difficult than the alloying samples. This finding is supported by the TGA result (Fig. 5b) from which it was observed that the CoPt and FePt NPs were more stable than the other samples. The other possible explanation for the double shoulder characteristics is the small particle size and size distribution, especially for x = 0. As demonstrated in Fig. 9, the CoPt sample (x = 0) shows the smallest average particle size and the narrowest distribution, indicating that a significant population of small particles exists in this sample. These small particles could contribute to the superparamagnetc phase and thus the observance of the multicomponent hysteresis in Fig. 13. The coercivity (H_c) and saturation magnetization (M_s) extracted from the hysteresis loop are presented in Fig. 14. An inverse proportion between H_c and M_s as a function of Co:Fe ratio is clearly observed. For the H_c variation, the largest values were observed in the CoPt and FePt NPs whereas for the other $Co_{1-x}Fe_xPt$ (x = 0.25, 0.5, 0.75), a smaller H_c was observed. The measured values of H_c of CoPt and FePt NPs are of the same order of magnitude as reported in the literature [10,14,15,18,35]. The drop in the H_c value for x = 0.25, 0.5, 0.75 could be related to the change in the lattice parameter *c*/*a* ratio as the composition changed (Fig. 7). The smallest H_c value was found for the $Co_{0.5}Fe_{0.5}Pt$ sample which has the largest *c*/*a* value. It has been reported that the exchange interaction of the CoPt (and FePt) system was altered as the *c*/*a* ratio was adjusted [39]. Thus, in the $Co_{1-x}Fe_xPt$ system, it is possible that the large *c*/*a* value changes the exchange interaction between the adjacent Co(Fe) layers and deteriorates the magnetocrystalline anisotropy (K_u). This argument is consistent with the first principle calculation of the $Fe_{1-y}Co_yPt$-$L1_0$

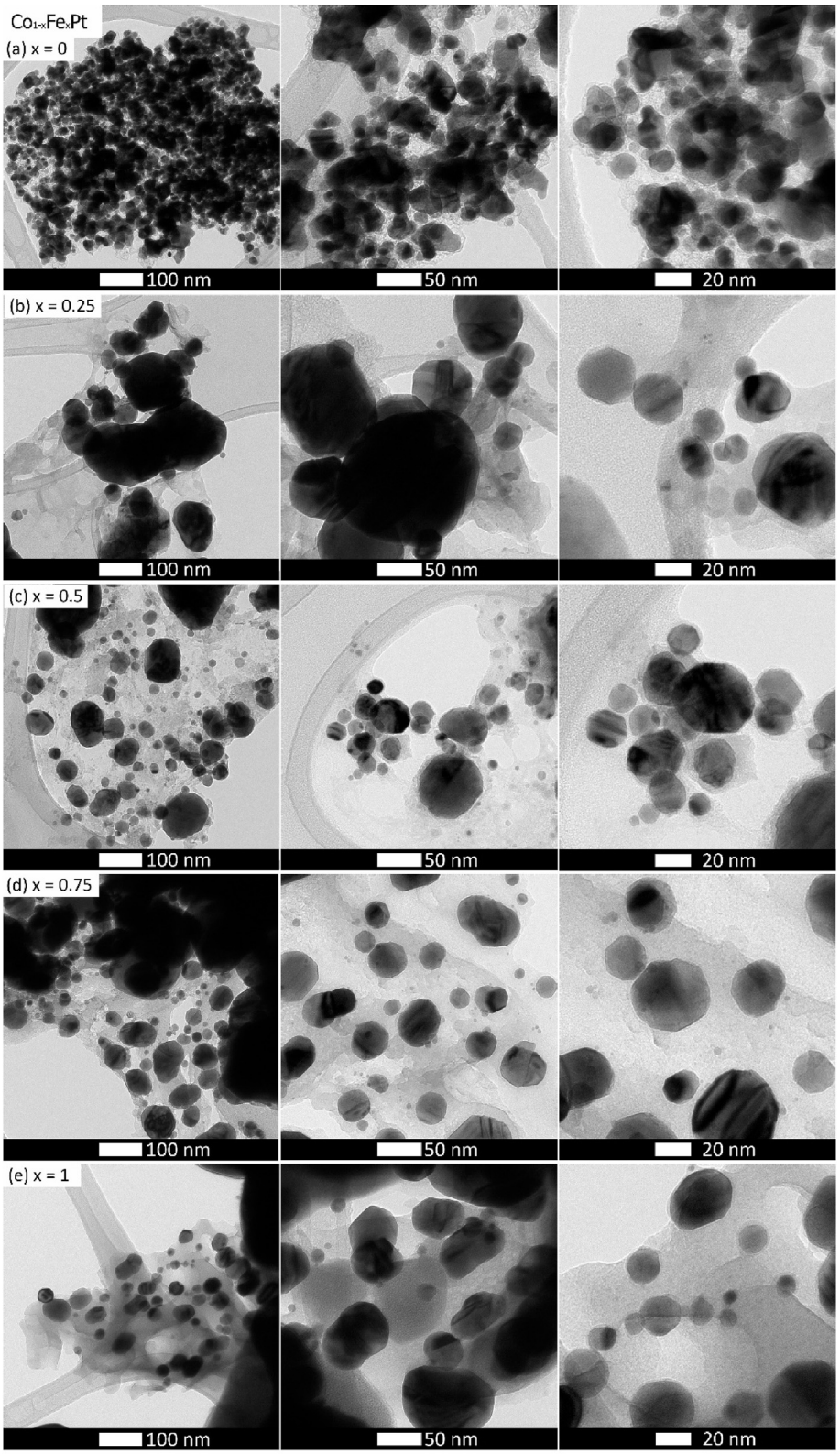

Fig. 8. TEM images of the annealed $Co_{1-x}Fe_xPt$ NPs. For each sample, the images at 3 different magnifications were shown for different proportions (x) of the Co and Fe components of the elements.

bulk alloys where the magnetocrystalline anisotropy falls rapidly as Co atoms were substituted for the Fe sites, as a result of the change in the effective number of valence electrons in the unit cell [40]. The reduced K_u would then result in a lower H_c value, since H_c is related to K_u as $H_c = 2K_u/M_s$ [41]. Based on this argument, it could explain the change in H_c as a function of Co(Fe) content. Our result is in agreement with the report for the $Fe_{1-x}Co_xPt$ thin film system which also showed the variation of H_c with the Fe:Co ratio [42].

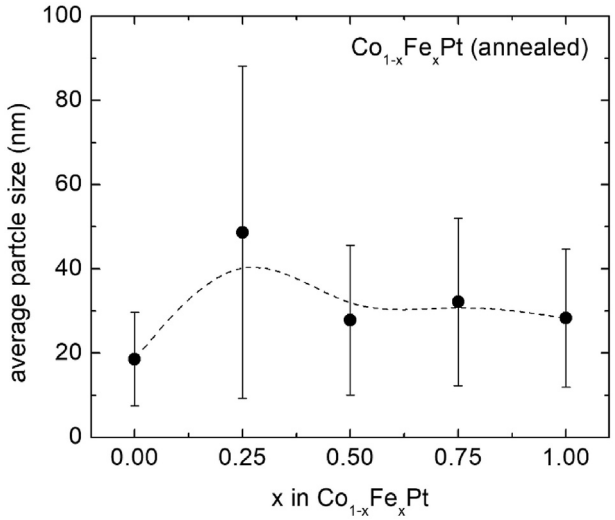

Fig. 9. Average particle size of the annealed $Co_{1-x}Fe_xPt$ NPs measured from TEM images.

On the other hand, the M_s was found to increase in the Co-Fe alloy samples with a maximum of ~44.5 emu/g for the $Co_{50}Fe_{50}Pt$ NPs. In this case, it has been reported that the addition of Co in pure Fe increased the M_s by 13% compared to pure Fe with a composition of $Co_{35}Fe_{65}$ [28]. The increase in magnetization of Fe-Co alloys with Co content is attributed to an increase in the polarization of Fe atoms with Co addition [28,43,44]. Furthermore, the band structure calculation of Fe-Co alloys based on the Korringa-Kohn-Rostoker layer method showed that the magnetic moment of Fe atoms exhibited a maximum near the equi-atomic composition whereas the magnetic moment of Co atoms remained almost the same [44]. Based on these previous studies, although for different systems, the enhancement in M_s of the $Co_{1-x}Fe_xPt$ NPs could possibly be due the same underlying physics as in the Fe-Co system. However, to gain a more insightful explanation, the calculation of the band structure of the $Co_{1-x}Fe_xPt$ $L1_0$ alloy is required.

Lastly, the M_s at 30 kOe of the $Co_{1-x}Fe_xPt$ NPs were plotted versus the temperature range of 50–390 K as presented in Fig. 15. In every sample, the M_s increased as the measurement temperature was lowered as a result of thermal fluctuation suppression. It can also be seen that all samples were magnetically stable against the temperature variation with changes in M_s of less than 10% for every sample. The $Co_{0.5}Fe_{0.5}$ NP still possessed the highest M_s throughout

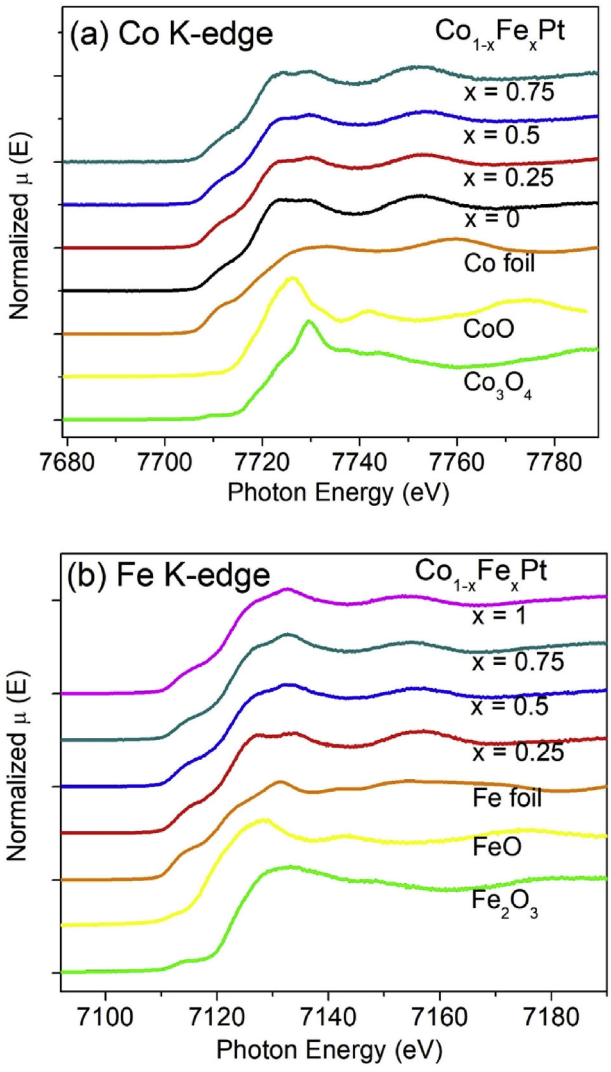

Fig. 11. (a) Co K-edge and (b) Fe K-edge XANES spectra of the annealed $Co_{1-x}Fe_xPt$ NPs for different proportions (x) of the Co and Fe components of the elements.

the temperature range with a value of 46.8 emu/g at 50 K. The Curie temperature (T_c) can be estimated by extrapolating the data in Fig. 15 to its intercept with the abscissa was reached. For a rough

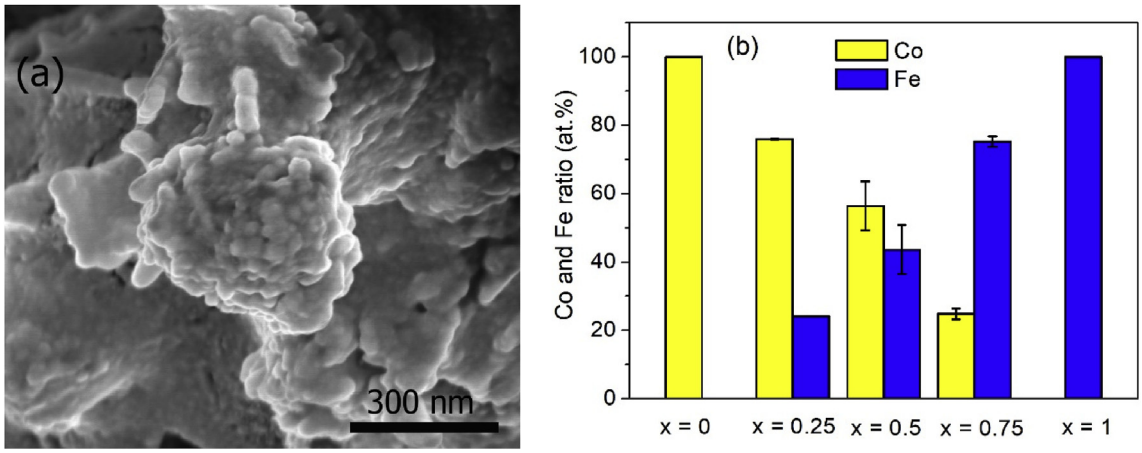

Fig. 10. (a) SEM image of the annealed FePt NP, (b) Co and Fe ratio (at.%) of $Co_{1-x}Fe_xPt$ NPs.

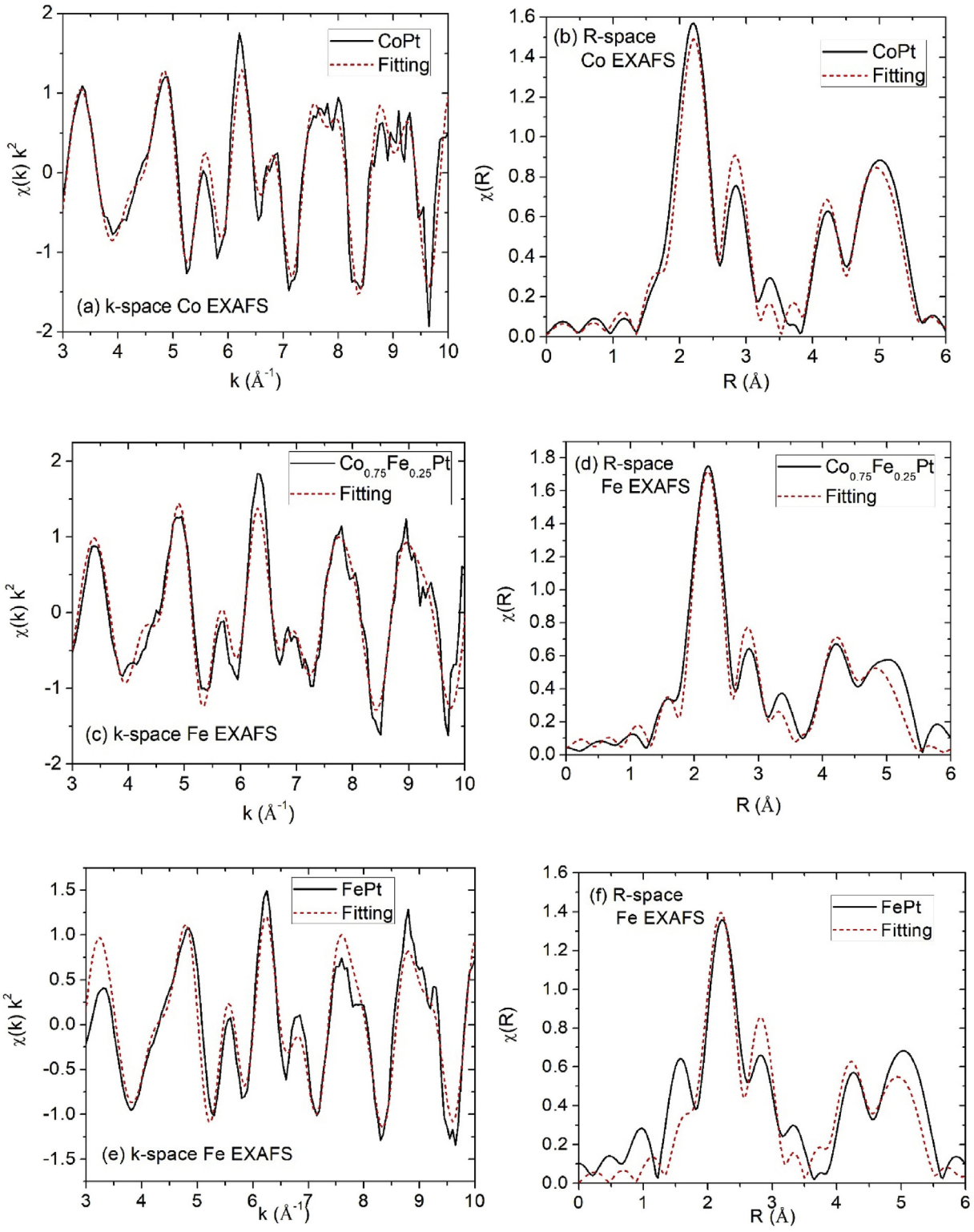

Fig. 12. (a,b) Co K-edge EXAFS data and fitting of CoPt NP, (c,d) Fe K-edge EXAFS data and fitting of $Co_{0.75}Fe_{0.25}Pt$ NP, (e,f) Fe K-edge EXAFS data and fitting of FePt NP. The data and fitting are shown in k-space (a,c,e) and R-space (b,d,f). Data are for different proportions (x) of the Co and Fe components of the elements.

approximation, the T_c should be in the range of 800–900 K depending on samples. These values are in agreement with the T_c values reported for CoPt and FePt NPs [39,45,46]. The implication is that even using the solid solution of CoPt and FePt alloys, these $Co_{1-x}Fe_xPt$ NPs could still be exploited in any high temperature application.

4. Conclusion

In this work, we have fabricated $Co_{1-x}Fe_xPt$ alloyed NPs. After synthesis via the polyol process, an A1-phase $Co_{1-x}Fe_xPt$ NPs with a size of less than 5 nm was formed. The effect of Co(Fe) substitution did not change the phase formation or particle size and its

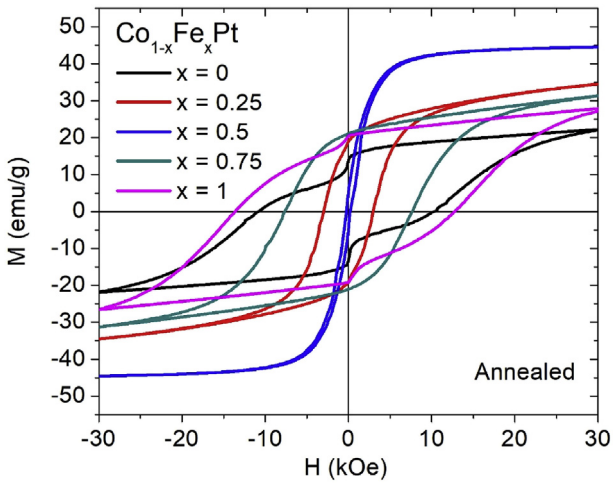

Fig. 13. Room temperature magnetization curve (M-H) of the annealed $Co_{1-x}Fe_xPt$ NPs for different proportions (x) of the Co and Fe components of the elements.

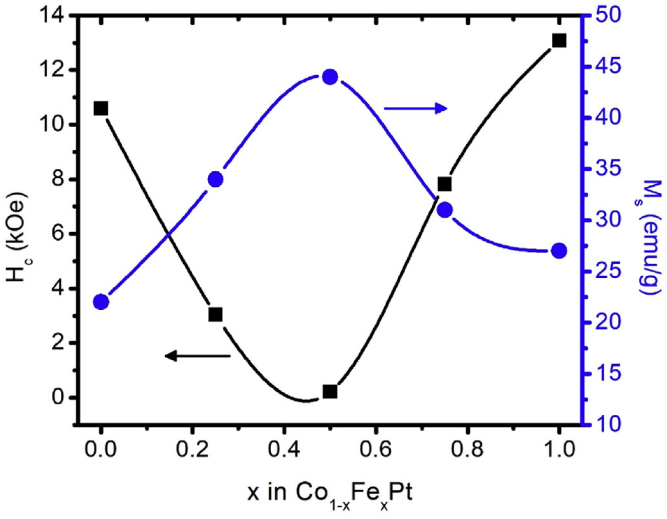

Fig. 14. Dependence of Co(Fe) in $Co_{1-x}Fe_xPt$ NPs on coercivity (H_c) and saturation magnetization (M_s) for different proportions (x) of the Co and Fe components of the elements.

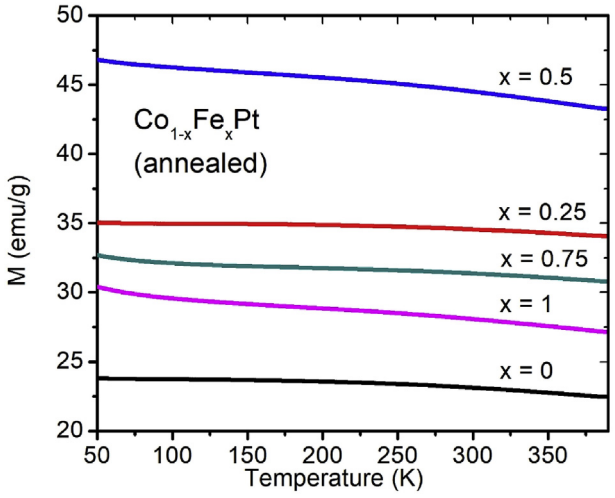

Fig. 15. Temperature dependence of saturation magnetization (M_s) for different proportions (x) of the Co and Fe components of the elements.

distribution. The magnetic measurement of the as-synthesized NPs showed superparamagnetic behavior as a result of the low K_u values and the small particle sizes. After annealing under an inert atmosphere, the $L1_0$ phase was clearly formed for all samples. The effect of Co (Fe) composition in the $L1_0$ phase led to the variation of the lattice parameters. The maximum c/a ratio was found in the $Co_{0.5}Fe_{0.5}Pt$ composition. The NPs were enlarged after annealing as a result of particle agglomeration and sintering to reduce surface energy. The size distribution is relatively wide ranging from less than 10 nm to more than 100 nm, and no obvious correlation between particle size and composition was observed. The concentration of Co and Fe from EDX measurements was found to be close to the nominal composition. For the local structure of Co and Fe atoms, the XANES and EXAFS analyses showed no preferential atomic sites or any sign of clustering of Co and Fe atoms; these were randomly distributed in the layered structure of the $L1_0$ phase. The magnetic hysteresis loops were observed in every annealed sample but the H_c varied with composition which could be related to the lattice parameters. The M_s was maximized for the $Co_{0.5}Fe_{0.5}Pt$ equiatomic composition which could be due to the enhancement of magnetic moments of Fe atoms as in the case of the Co-Fe alloys. The $Co_xFe_{1-x}Pt$ NPs were magnetically stable with less than 10% variation in M_s throughout the measurement temperature range.

Acknowledgment

This work is supported by the Thailand Research Fund (TRF) in cooperation with Khon Kaen University (RSA5980014), the Royal Society-Newton Advanced Fellowship (NA160147) in partnership with the Thailand Research Fund (TRF) (DBG6080002), the Royal Golden Jubilee PhD Programme (PHD/0063/2558), and the National Research Council of Thailand through Khon Kaen University (600015). Also, thanks to the Synchrotron Light Research Institute (public organization) (BL5.2) for awarding XAS beamtime.

References

[1] R. Hao, R.J. Xing, Z.C. Xu, Y.L. Hou, S. Gao, S.H. Sun, Adv. Mater. 22 (2010) 2729–2742.
[2] A.H. Lu, E.L. Salabas, F. Schuth, Angew. Chem. Int. Ed. 46 (2007) 1222–1244.
[3] N.A. Frey, S. Peng, K. Cheng, S.H. Sun, Chem. Soc. Rev. 38 (2009) 2532–2542.
[4] A.K. Gupta, M. Gupta, Biomaterials 26 (2005) 3995–4021.
[5] S.N. Piramanayagam, J. Appl. Phys. 102 (2007).
[6] S.N. Piramanayagam, K. Srinivasan, J. Magn. Magn Mater. 321 (2009) 485–494.
[7] J.-G. Zhu, Mater. Today 6 (2003) 22–31.
[8] N.A. Spaldin, Magnetic Materials : Fundamentals and Device Applications, Cambridge University Press, Cambridge, 2003.
[9] D. Weller, A. Moser, L. Folks, M.E. Best, W. Lee, M.F. Toney, M. Schiwickert, J.-U. Thiele, M.F. Doerner, IEEE Trans. Magn. 23 (2000) 10–15.
[10] Y.S. Yu, W.W. Yang, X.L. Sun, W.L. Zhu, X.Z. Li, D.J. Sellmyer, S.H. Sun, Nano Lett. 14 (2014) 2778–2782.
[11] S. Kang, J.W. Harrell, D.E. Nikles, Nano Lett. 2 (2002) 1033–1036.
[12] S. Sun, C.B. Murrya, D. Weller, L. Folks, A. Moser, Science 287 (2000) 1989–1992.
[13] D. Alloyeau, C. Ricolleau, C. Mottet, T. Oikawa, C. Langlois, Y. Le Bouar, N. Braidy, A. Loiseau, Nat. Mater. 8 (2009) 940–946.
[14] C.B. Rong, D.R. Li, V. Nandwana, N. Poudyal, Y. Ding, Z.L. Wang, H. Zeng, J.P. Liu, Adv. Mater. 18 (2006) 2984–2988.
[15] B.R. Bian, J.H. He, J. Du, W.X. Xia, J. Zhang, J.P. Liu, W. Li, C.F. Hu, A. Yan, Nanoscale 7 (2015) 975–980.
[16] J.P. Wang, Proc. IEEE 96 (2008) 1847–1863.
[17] B.H. An, J.H. Wu, H.L. Liu, S.P. Ko, J.S. Ju, Y.K. Kim, Colloid. Surface. A 313 (2008) 250–253.
[18] C.N. Chinnasamy, B. Jeyadevan, K. Shinoda, K. Tohji, J. Appl. Phys. 93 (2003) 7583–7585.
[19] M. Takahashi, T. Ogawa, D. Hasegawa, B. Jeyadevan, J. Appl. Phys. 97 (2005).
[20] N. Sehdev, R. Medwal, S. Annapoorni, J. Appl. Phys. 110 (2011), 033901.
[21] A.S. Hussein, P. Murugaraj, C.J. Rix, D.E. Mainwaring, J. Mater. Res. 24 (2008) 499–505.
[22] Q.Y. Yan, T. Kim, A. Purkayastha, P.G. Ganesan, M. Shima, G. Ramanath, Adv. Mater. 17 (2005) 2233–2237.
[23] H.B. Wang, Y. Li, X. Chen, D. Shu, X. Liu, X.N. Wang, J. Zhang, H. Wang, Y. Wang, P. Ruterana, J. Magn. Magn Mater. 422 (2017) 470–474.

[24] Y.X. Wang, X.L. Zhang, Y. Liu, S.Q. Lv, Y.H. Jiang, Y.J. Zhang, H.L. Liu, Y.Q. Liu, J.H. Yang, J. Alloys Compd. 582 (2014) 511–514.
[25] Y. Khemjeen, S. Pinitsoontorn, A. Chompoosor, J. Appl. Phys. 117 (2015), 17D513.
[26] Y.S. Yu, P. Mukherjee, Y. Tian, X.Z. Li, J.E. Shield, D.J. Sellmyer, Nanoscale 6 (2014) 12050–12055.
[27] W.J. Lei, Y.S. Yu, W.W. Yang, M. Feng, H.B. Li, Nanoscale 9 (2017) 12855–12861.
[28] R.S. Sundar, S.C. Deevi, Int. Mater. Rev. 50 (2005) 157–192.
[29] G.S. Chaubey, C. Barcena, N. Poudyal, C.B. Rong, J.M. Gao, S.H. Sun, J.P. Liu, J. Am. Chem. Soc. 129 (2007) 7214–7215.
[30] Y. Khemjeen, S. Pinitsoontorn, A. Chompoosor, S. Maensiri, J. Appl. Phys. 116 (2014), 053910.
[31] W. Klysubun, P. Kidkhunthod, P. Tarawarakarn, P. Sombunchoo, C. Kongmark, S. Limpijumnong, S. Rujirawat, R. Yimnirun, G. Tumcharern, K. Faungnawakij, J. Synchrotron Radiat. 24 (2017) 707–716.
[32] B. Ravel, M. Newville, J. Synchrotron Radiat. 12 (2005) 537–541.
[33] A.L. Ankudinov, B. Ravel, J.J. Rehr, S.D. Conradson, Phys. Rev. B 58 (1998) 7565–7576.
[34] A.K. Gupta, D.K. Paliwal, P. Bajaj, J. Macromol. Sci. Rev. Macromol. Chem. Phys. 31 (1991) 1–89.
[35] X.C. Sun, Z.Y. Jia, Y.H. Huang, J.W. Harrell, D.E. Nikles, K. Sun, L.M. Wang, J. Appl. Phys. 95 (2004) 6747–6749.
[36] R.M. Bozorth, D. Ferromagnetism, Van Nostrand Co, 1968. New York.
[37] J.C. Slater, J. Chem. Phys. 41 (1964) 3199.
[38] G. Krylova, L.J. Giovanetti, F.G. Requejo, N.M. Dimitrijevic, A. Prakapenka, E.V. Shevchenko, J. Am. Ceram. Soc. 134 (2012) 4384–4392.
[39] X.B. Liu, Z. Altounian, J. Appl. Phys. 109 (2011).
[40] R. Cuadrado, T.J. Klemmer, R.W. Chantrell, Appl. Phys. Lett. 105 (2014).
[41] B.D. Cullity, C.D. Graham, Introduction to Magnetic Materials, second ed., IEEE Press, Wiley, Hoboken, N.J., 2009.
[42] S.K. Chen, S.N. Hsiao, F.T. Yuan, W.C. Chang, IEEE Trans. Magn. 41 (2005) 3784–3786.
[43] M.S. Lataifeh, J. Phys. Soc. Jpn. 69 (2000) 248–250.
[44] J.M. MacLaren, J. Appl. Phys. 85 (1999) 4833–4835.
[45] J.M. Sanchez, J.L. Moran-Lopez, C. Leroux, M.C. Cadeville, J. Phys. Condens. Matter 1 (1989) 491–496.
[46] H. Zeng, R. Sabirianov, O. Mryasov, M.L. Yan, K. Cho, D.J. Sellmyer, Phys. Rev. B 66 (2002).

Carbohydrate Polymers 192 (2018) 251–262

Contents lists available at ScienceDirect

Carbohydrate Polymers

journal homepage: www.elsevier.com/locate/carbpol

Magnetically responsive and flexible bacterial cellulose membranes

Nipaporn Sriplai[a], Wiyada Mongkolthanaruk[b], Stephen J. Eichhorn[c], Supree Pinitsoontorn[a,d,*]

[a] Materials Science and Nanotechnology Program, Department of Physics, Faculty of Science, Khon Kaen University, Khon Kaen, 40002, Thailand
[b] Department of Microbiology, Faculty of Science, Khon Kaen University, Khon Kaen, 40002, Thailand
[c] Bristol Composites Institute (ACCIS), University of Bristol, Queen's Building, University Walk, Bristol, BS8 1TR, UK
[d] Integrated Nanotechnology Research Center, Department of Physics, Faculty of Science, Khon Kaen University, Khon Kaen, 40002, Thailand

ARTICLE INFO

Keywords:
Bacterial cellulose
Nanoparticles
Characteristics
Magnetic properties

ABSTRACT

Magnetically responsive and flexible bacterial cellulose (BC) membranes were successfully fabricated using a simple diffusion of a ferrofluid solution. BC hydrogels were either water-substituted by alcohol (BC-N) or freeze dried (BC-F) prior to their immersion in the ferrofluid. The presence of both crystalline BC and Fe_3O_4 phases, and the homogeneous distribution of nanoparticles (NPs) in BC nanofibrils were observed. Higher concentrations of Fe_3O_4 NPs were found in the BC-N samples than for the BC-F samples. Higher magnetization in the BC-N samples was observed compared to the BC-F samples. Mechanical properties tests showed the higher strength and Young's modulus for the BC-F samples was possibly due to their more compacted nanostructure compared to BC-N. Using this simple process, the magnetic BC membranes show elastic properties upon deformation, returning to their original shape without damage. Also, they were highly sensitive to external magnetic forces giving them potential for many applications.

1. Introduction

Cellulose is one of the most important and abundant natural polymers. It is an inexhaustible raw material, and a key source of sustainable materials on an industrial scale (Klemm, Heublein, Fink, & Bohn, 2005). Cellulose-based composite materials show improved performance from the combination of two or more properties. Magnetic cellulose composites combining the magnetic responsive properties of ferromagnetic particles with the excellent mechanical properties of cellulose could find use in several technological applications, such as flexible information storage (Behrens, 2011; Dai & Nelson, 2010), loudspeaker membranes (Galland et al., 2013), anti-counterfeiting papers (Barud et al., 2015; Mashkour, Tajvidi, Kimura, Kimura, & Ebrahimi, 2011), magneto-responsive actuators (Olsson et al., 2010; Zhang et al., 2011), electromagnetic shielding (Marins, Soares, Barud, & Ribeiro, 2013; Park, Cheng, Choi, Kim, & Hyun, 2013), and heavy metal removal (Nata, Sureshkumar, & Lee, 2011; Stoica-Guzun et al., 2016; Zhu et al., 2011).

There have been a few approaches proposed for the fabrication of magnetic cellulose composites. These approaches have been confined to lumen-loading and *in situ* synthesis methods (Wu, Jing, Gong, Zhou, & Dai, 2011). In the lumen-loading method, magnetic cellulosic fibers are prepared by mixing of the aqueous mixture containing pulp fibers and magnetic particles, such as magnetite or maghemite. After a mild washing step to remove all unbound-magnetic particles, all the fillers are confined in the lumens of the fibers. This leaves most of the external surfaces of the fibers free from the particles (Wu et al., 2011; Zakaria, Ong, Ahmad, Abdullah, & Yamauchi, 2005). For the *in situ* synthesis method, or *in situ* co-precipitation method, cellulosic fibers are immersed in a solution containing iron ions. The iron ions are adsorbed to the surface of the cellulose matrix and are chemically converted to iron oxide particles by the addition of NaOH or NH_4OH solutions (Small & Johnston, 2009; Sourty, Ryan, & Marchessault, 1998). Compared with lumen loading, the *in situ* synthesis method allows better dispersion, greater uniformity and a better control of magnetic properties (Shen, Song, Qian, & Ni, 2011). However, it cannot eliminate some intrinsic disadvantages such as rigorous reaction conditions, poor control of deposition location, and unstable composition of magnetic nanoparticles (MNPs) (Wu et al., 2011).

Apart from plant celluloses, bacterial cellulose (BC) produced from the cultivation of a particular type of bacteria, such as *Gluconacetobacter xylinum*, has received increasing attention from many researchers. This is due to the unique and superior properties of BC fibrils over plant cellulose fibers. In their pristine forms, BC possesses a 3D porous network of highly crystalline cellulose nanofibers (or nanofibrils) with high purity (free of lignin and hemicellulose) and a high degree of polymerization. It also possesses remarkable mechanical properties, high water absorbency, high moldability, biodegradability and

* Corresponding author at: Integrated Nanotechnology Research Center, Department of Physics, Faculty of Science, Khon Kaen University, Khon Kaen, 40002, Thailand.
E-mail address: psupree@kku.ac.th (S. Pinitsoontorn).

https://doi.org/10.1016/j.carbpol.2018.03.072
Received 21 November 2017; Received in revised form 19 March 2018; Accepted 21 March 2018
Available online 23 March 2018
0144-8617/

excellent biological affinity (Foresti, Vazquez, & Boury, 2017; Hu, Chen, Yang, Li, & Wang, 2014; Shah, Ul-Islam, Khattak, & Park, 2013). BC can be applied to a variety of applications, such as wound dressing materials. Recent research has shown that by using a dextran-modified BC hydrogel, accelerated cutaneous wound healing can occur compared to unmodified BC (Lin et al., 2017). Another example is the use of BC as strong, thermal-stable, flexible and transparent films for flexible devices, such as solar cells and displays (Wu & Cheng, 2017).

Several types of MNPs have been incorporated in BC nanofibrillar networks; for instance magnetite (Fe_3O_4) (Barud et al., 2015; Katepetch & Rujiravanit, 2011; Park et al., 2013; Stoica-Guzun et al., 2016; Sureshkumar et al., 2010; Zeng, Laromaine, Feng, Levkin, & Roig, 2014; Zhang et al., 2011; Zheng et al., 2013), maghemite (Fe_2O_3) (Marins et al., 2013; Mashkour, Moradabadi, & Khazaeian, 2017; Nata et al., 2011; Wan et al., 2015), cubic ferrites ($CoFe_2O_4$, $MnFe_2O_4$) (Liu, Yan, Cao, Zhou, & Yang, 2016; Menchaca-Nal et al., 2016; Olsson et al., 2010), barium hexferrite (Lim et al., 2016), Ni (Thiruvengadam & Vitta, 2013, 2017a), and permalloy (NiFe) (Thiruvengadam & Vitta, 2017b). Nevertheless, the most used MNPs for fabricating magnetic BC are iron oxides (magnetite and maghemite) due to their high magnetization values, stability, low cost, low toxicity and ease of fabrication.

Due to the very small size of the BC nanofibrils and the lack of a lumen structure, the lumen-loading method is not applicable for the fabrication of magnetic BC. Instead, a very widely used process for the impregnation of iron oxide MNPs into BC nanofibrils is the *in situ* co-precipitation method (Marins et al., 2013; Mashkour et al., 2017; Stoica-Guzun et al., 2016; Sureshkumar et al., 2010; Zhang et al., 2011). Although this method can produce iron oxide MNPs relatively easily, it has several drawbacks such as agglomeration of nanoparticles, broad particle size distributions, predominant precipitation of MNPs at the surface of BC pellicles, and the occurrence of unwanted phases (*e.g.* α-Fe_2O_3, α-FeOOH). Effectively controlling the dispersion of MNPs in nanocomposite materials is crucially important to obtain excellent magnetic properties since the collective behavior of MNPs is a strong function of their concentration as well as their spatial arrangement (Thiruvengadam & Vitta, 2016). Therefore, several modified *in situ* synthesis techniques have been explored for minimizing such disadvantages, including hydrothermal (Wan et al., 2015), solvothermal (Nata et al., 2011), ultrasonic irradiation (Zheng et al., 2013), microwave-assisted thermal decomposition (Zeng et al., 2014), ammonia M. gas-enhancing (Katepetch & Rujiravanit, 2011), or using amphiphilic comb-like polymer stabilizers to disperse the MNPs (Park et al., 2013). Although some improvements by such methods have been achieved, agglomeration of MNPs is still observed. Furthermore, the process become more complex with these approaches, and several processing parameters need to be more precisely controlled. In addition, the magnetization of the BC composites was found to be very low, indicating a low uptake volume of the iron oxide MNPs, or the formation of non-magnetic phase NPs. The use of an energy-assisted process can also deteriorate other properties of the BC itself. For example, flexible magnetic BC hybrids synthesized under ultrasonic irradiation exhibited poor mechanical behavior (Zheng et al., 2013). This occurs because the ultrasonic treatment impacts the crystallinity, surface modification and the roughness of the BC nanostructure (Foresti et al., 2017).

In this work, we present the fabrication of magnetic BC nanocomposites by using a simple immersion of BC pellicles in a commercially available ferrofluid. With this method, water-based Fe_3O_4 NPs in the ferrofluid solution simply diffuse and anchor to the 3D nanofiber network of the BC fibrils. Homogenization was used to produce an aqueous dispersion of MNPs. This process also has the advantage of reducing complications, such as controlling nitrogen flow to prevent oxidation, has low energy requirements and minimizes the use of chemical treatments which can cause structural and morphological changes (Foresti et al., 2017; Mashkour, Tajvidi, Kimura, Yousefi, & Kimura, 2014). Moreover, the magnetization saturation of the magnetic BC hybrid produced by our method was much higher than previous reports, and the mechanical properties appeared, from preliminary studies, to be maintained or even improved under certain conditions.

2. Materials and methods

2.1. Production of BC membranes

BC pellicles were produced by cultivating the bacteria *Gluconacetobacter xylinum* (strain TISTR 975), which was supplied from the Microbiological Resources Centre, Thailand Institute of Scientific and Technological Research (TISTR). The culture was grown in a medium consisting of D-Glucose (10 g) (anhydrous AR, Ajax Finechem) plus 1 g of yeast in 1 L of de-ionized (DI) water. After incubating for 8 days under static conditions at 30 °C, BC pellicles with a diameter and thickness of 5.5 cm and 1 cm were harvested (Gayathry & Gopalaswamy, 2014; Lee et al., 2017). These pellicles were purified by boiling in DI water then soaking in 0.5 M and 5 wt% NaOH for 15 min and 24 h respectively. They were then rinsed with DI water several times until they reached a pH of 7. Finally, BC hydrogels obtained from this step were separated into two groups to investigate the effect of the Fe_3O_4 MNP diffusion process into the BC nanostructure. In the first group, the DI water in the BC hydrogels was replaced with ethyl alcohol. This was done by immersing the BC hydrogels in diluted ethyl alcohol solution (25 vol.%) and then transferring them to more concentrated alcohol solutions (50, 75, 100 vol.%). In each step, the BC hydrogels were soaked for at least 1 h. This ethanol substituting process was used to stimulate the diffusion rate of the ferrofluid in the BC nanostructure during the next step. The hydrogels were kept in the ethanol solution prior to the synthesis of the BC/Fe_3O_4 nanocomposites. This group is referred to as the never-dried BC or denoted as BC-N (ethanol gel). In the second group, BC hydrogels were freeze-dried to obtain a BC aerogel prior to the incorporation of MNPs. The samples in this group are denoted as BC-F. Both groups were used as a template for preparing BC/Fe_3O_4 nanocomposites.

2.2. Synthesis of BC/Fe_3O_4 nanocomposites

The fabrication of magnetic BC composites was carried out by the simple immersion of both BC-N and BC-F samples in a commercial water-based ferrofluid supplied by Weistron Co. Ltd., Taiwan. The characteristics of the ferrofluid and the distribution of MNPs used in this experiment are shown in Table S1 and Fig. S1. Five different concentrations of the ferrofluid were prepared (1, 3, 5, 10 and 20 vol.%) in 40 mL of water. The immersion was carried out at 80 °C with continuous stirring for 1 h to accelerate the diffusion of Fe_3O_4 NPs into the BC nanostructure. It should be noted that the process can be done at room temperature without stirring but over an extended time-period. After the process was completed, the pristine BC pellicles were converted to BC/Fe_3O_4 nanocomposites, with their color changing to dark brown. Finally, the obtained samples were freeze-dried, and kept in a dry place before characterization. The samples from the BC-N and BC-F groups were designated as BC-N-x% and BC-F-x%, respectively, with x denoting the concentration of the ferrofluid (x = 1, 3, 5, 10, and 20). Fig. 1 summarizes the preparation process of the samples in this study.

2.3. Characterization methods

Information on the phases and crystalline structures of the samples was collected using X-ray diffraction (XRD) with a diffractometer employing Cu-Kα radiation (PANalytical, Empyrean, USA) in the 2θ range of 10–80°. The surface morphology of the samples and the distribution of Fe_3O_4 NPs were observed using a field emission scanning electron microscope (FESEM) (FEI, Helios, USA) at an acceleration voltage of 10 kV. Prior to imaging with the SEM, the samples were gold coated to improve conductivity. The functional groups of BC and the deposition of MNPs in the BC nanostructure were investigated using Fourier

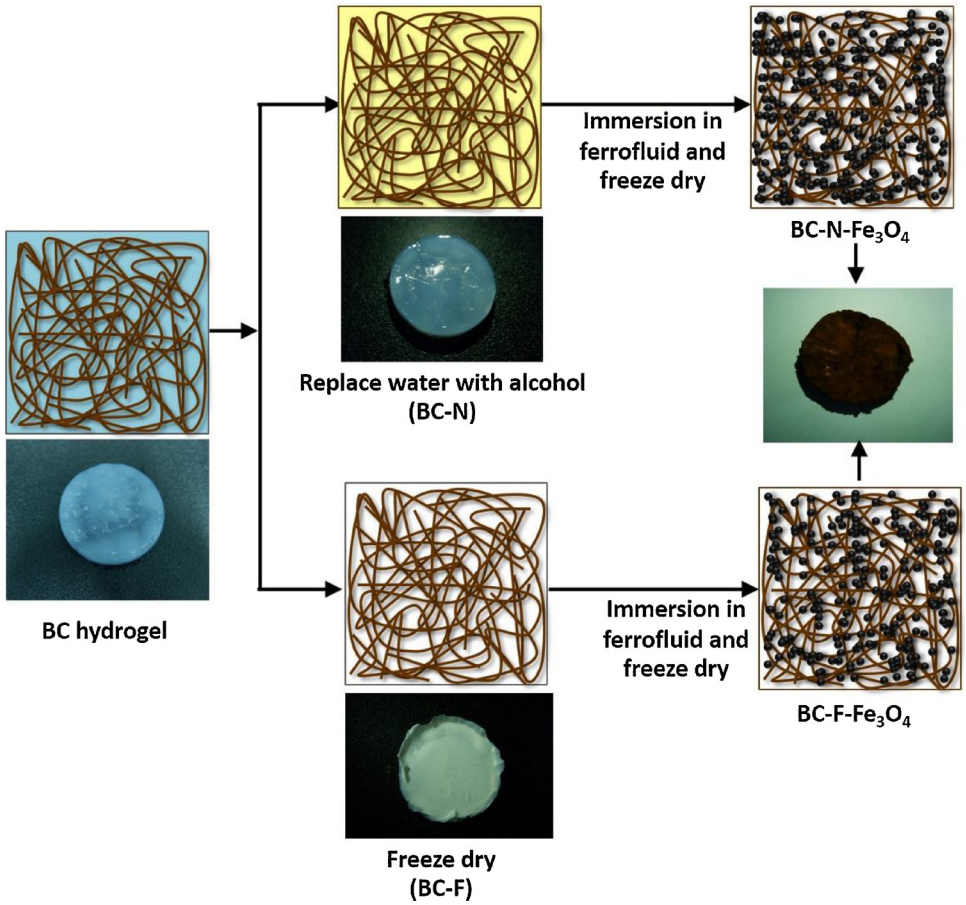

Fig. 1. Schematic summary of the sample preparation processes.

transform infrared (FTIR) spectroscopy (Bruker, TENSOR27, Germany) within a wavenumber range of 4000–600 cm^{-1}. Thermal stability of the pristine BC and BC/Fe_3O_4 nanocomposites was studied using a thermogravimetric analysis (TGA) technique (Hitachi, STA7200, Japan) by heating the samples from 30 to 800 °C under a nitrogen atmosphere, at a heating rate of 10 °C/min. Preliminary mechanical properties of the materials were obtained using a universal testing machine (UTM, Instron 5567A) with a 20 mm sample gauge length and a 10 mm/min testing speed. The samples used for tensile testing were cut into a rectangular membrane with dimensions of 15 mm width, 40 mm length and 0.3 mm thickness. For each sample condition, between 4 and 6 replicates were used and the mechanical tests were carried out under ambient temperature and humidity. The magnetic properties were investigated by measuring magnetization (*M*) *versus* magnetic field (*H*) using a vibrating sample magnetometer (VSM) option in the VersaLab instrument (Quantum Design, USA) under a maximum field of 30 kOe. The M-H curves were carried out at room temperature and at 50 K. In addition, the zero-field cooled (ZFC) and field cooled (FC) magnetic behaviors of all samples were measured and analyzed.

3. Results and discussion

3.1. Phase and morphology

Fig. 2 shows the XRD patterns of pristine BC and BC/Fe_3O_4 nanocomposites samples. The pristine BC samples (both drying conditions) consist of mostly crystalline phases, which was identified as cellulose I_α. Three main diffraction peaks were observed at 14.0°, 16.5° and 22.3° which were indexed as the ($1\bar{1}0$), (110) and (200) reflections according to according to (Czaja, Romanovicz, & Brown, 2004). In the composites, as the Fe_3O_4 NPs were introduced into the system, the characteristic peak at 35.4° corresponding to the (311) plane of the magnetite phase (ICCD 01-089-0950) was observed even at the lowest concentration of 1% ferrofluid. The intensities of Bragg peaks from the BCN-Fe_3O_4-1 are significantly stronger than for BCF-Fe_3O_4-1. At higher concentrations of ferrofluid, almost all the characteristic peaks of Fe_3O_4 gradually appeared; peaks located at 2θ = 30.0°, 35.4°, 43.1°, 57.2° and 62.6° corresponding to (220), (311), (400), (511) and (440) reflections of the face-centered cubic (FCC) magnetite structure (Katepetch & Rujiravanit, 2011; Ren et al., 2015; Zhao et al., 2016). On the other hand, the peak intensities coming from the BC gradually decrease with increased Fe_3O_4 concentrations. This is partly due to the presence of the intense XRD peaks from the crystalline Fe_3O_4 phase. It could also be a result of deterioration of the BC crystallinity as the Fe_3O_4 was introduced. These two effects are difficult to distinguish. The observed reduction of the BC diffracted peaks is commonly found in the BC/MNPs composites in literatures (Marins et al., 2013; Mashkour et al., 2017; Stoica-Guzun et al., 2016; Sureshkumar et al., 2010; Zhang et al., 2011; Zheng et al., 2013). However, our results still show distinct BC peaks even for the high MNP concentration, suggesting the preservation of the crystal structure of BC, which could be due to the present synthesis method. This indicates that the simple diffusion method can produce BC/Fe_3O_4 composites without any secondary phase. An advantage of this method is that the other poorer magnetic phases, such as maghemite, hematite, or FeOOH are not formed, comparing favorably to other *in situ* synthesis approaches (Nata et al., 2011; Sourty et al., 1998; Wan et al., 2015; Zeng et al., 2014).

The other feature that is noted from Fig. 2 is the difference in the peak intensities between the two sets of samples (BC-N and BC-F). The Fe_3O_4 phase in BC-N seems to exhibit more intense Bragg peaks than

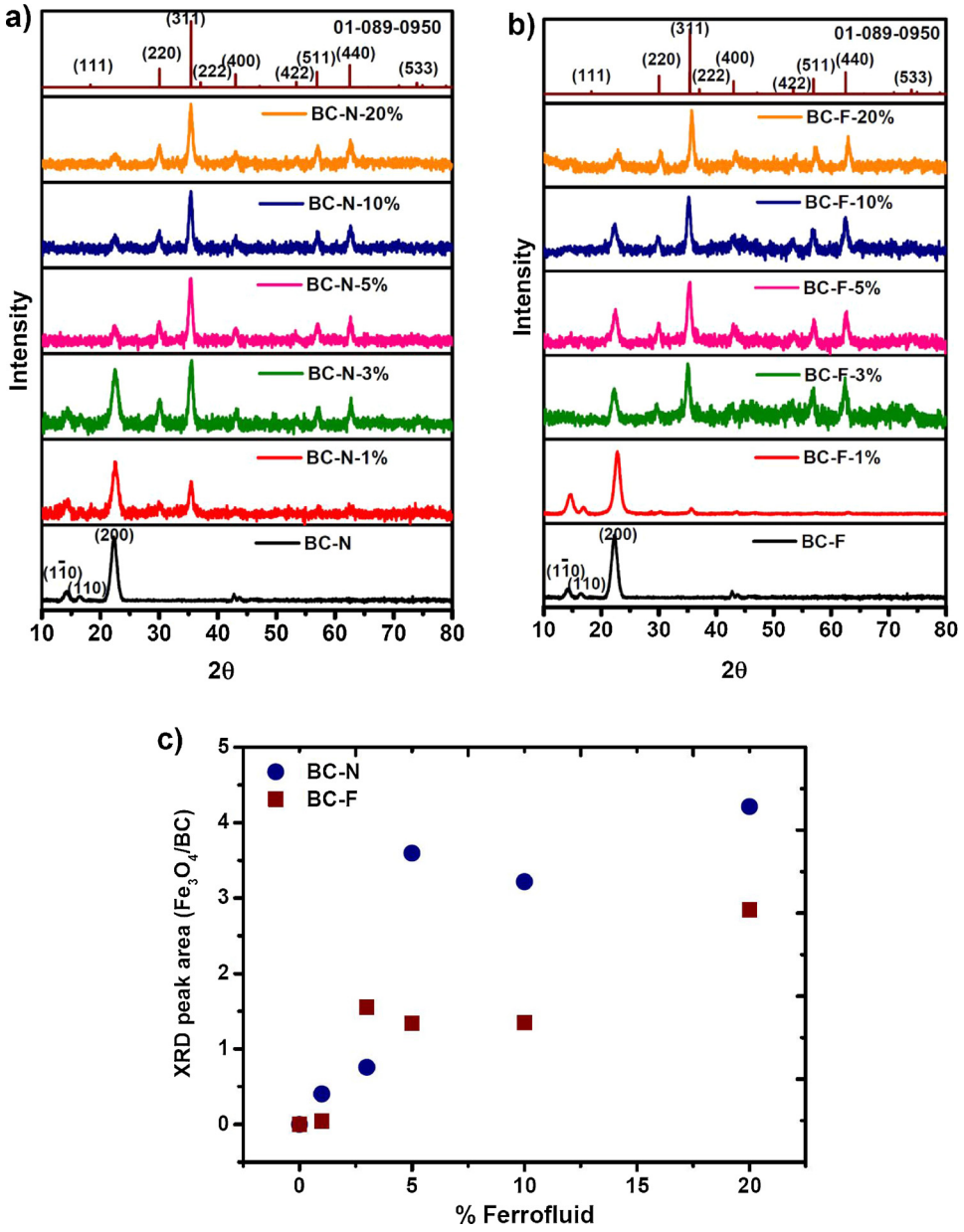

Fig. 2. Typical XRD patterns of the pristine BC and BC-Fe_3O_4 nanocomposites for (a) BC-N and (b) BC-F. (c) The ratio of the Fe_3O_4(311)/BC(200) peak area as a function of ferrofluid concentration.

the BC-F samples. To quantify this, we calculated the areas under the main peaks of BC and Fe_3O_4, and plotted the areal ratio of Fe_3O_4(311)/BC(200) as shown in Fig. 2c. The BC-N samples tend to have the larger peak areas for the Fe_3O_4 phase corresponding to the higher loaded volume of the Fe_3O_4 NPs. The underlying reasons will be subsequently discussed.

The morphologies of pristine BC and BC/Fe_3O_4 composites were investigated using SEM as shown in Fig. 3. Pristine BC nanofibers (Fig. 3a&b) consist of an ultrafine three-dimensional network structure. The average diameter of the BC-N nanofibrils (87.9 ± 21.0 nm) is smaller than that for the BC-F sample (109.6 ± 25.0 nm), due to the different preparation method. Water in the BC-N hydrogel was replaced by alcohol with a lower surface tension (Haynes, 2016) prior to freeze-drying. Alcohol was then easily removed resulting in the preservation of a nanostructure with relatively lower fiber diameters. For the BC-F sample, the removal of water in the freeze-drying process could cause aggregation of BC nanofibers resulting in larger diameters. Consequently, the porous structure looks slightly different between the two sample sets. The BC-F nanofibrils with a larger average diameter are likely to have larger mean pore sizes, according to a theoretical modelling of nanofibrous networks (Eichhorn & Sampson, 2005), compared to the BC-N samples.

From images of the composite samples (Fig. 3c–I), MNPs clearly attach to the surface of the BC nanofibers. As the concentration of the ferrofluid was increased, more Fe_3O_4 NPs were observed. Aggregation of the MNPs was still observed but the degree of agglomeration was much lower than previous reports (Marins et al., 2013; Nata et al., 2011; Park et al., 2013; Stoica-Guzun et al., 2016; Zheng et al., 2013). Another noticeable feature in Fig. 3 is the difference in the loaded volume of the MNPs between the BC-N and the BC-F samples. Significantly more Fe_3O_4 NPs were found to be anchored to the BC nanofibrils for the BC-N samples compared to BC-F. The higher concentration of MNPs in the BC-N samples, as observed from the SEM images, is consistent with the XRD analysis in Fig. 2c. The higher concentration in the BC-N samples is thought to be mainly due to the different preparation processes used. Since the impregnation of Fe_3O_4 NPs in the water-based

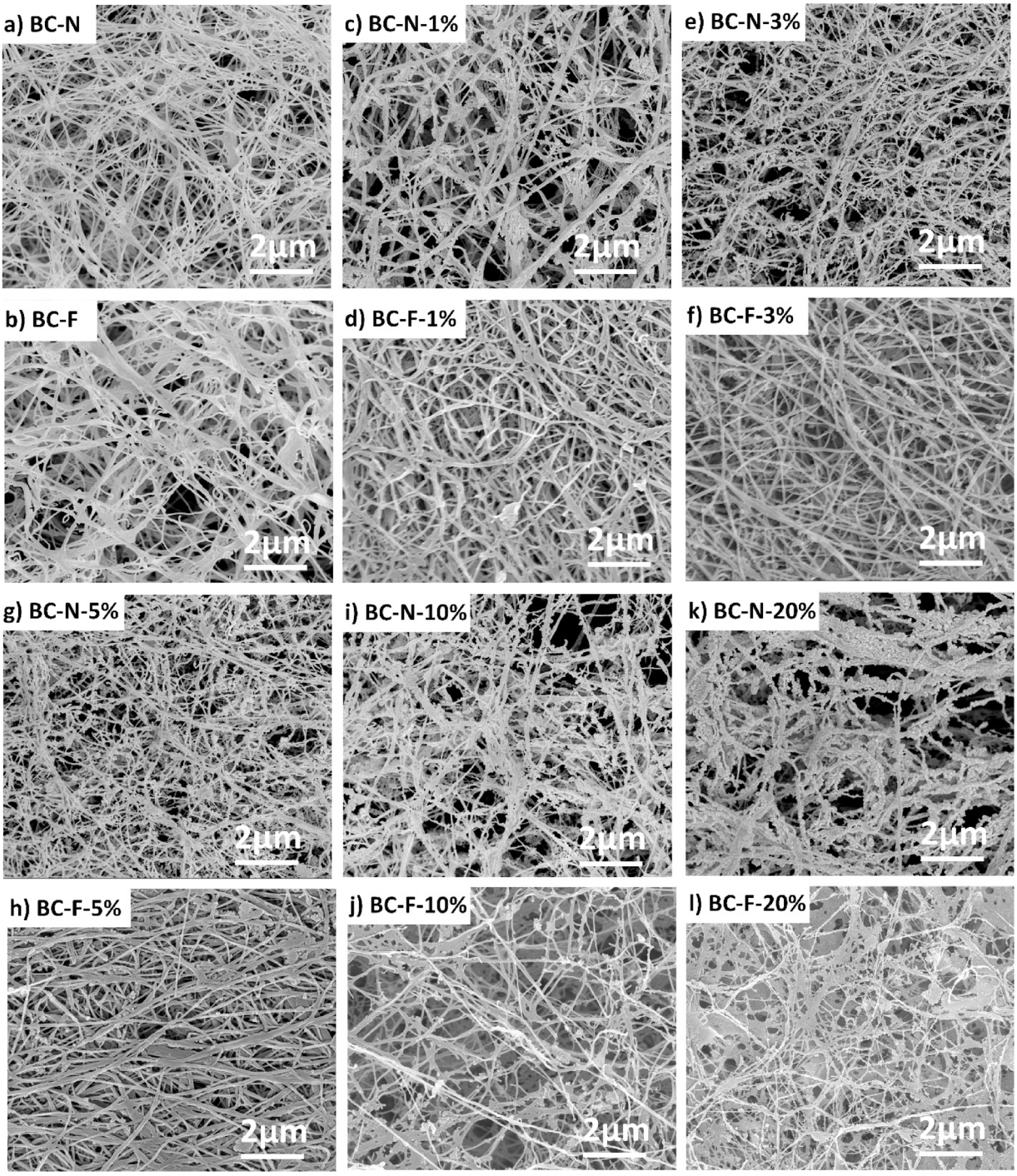

Fig. 3. Typical SEM images of the pristine BC and BC-Fe_3O_4 nanocomposites for BC-N (a,c,e,g,i,k) and BC-F (b,d,f,h,j,l).

ferrofluid solution depends on the diffusion process, the diffusion path of Fe_3O_4 between the BC-N and BC-F is thought to be different. The BC-N templates were in a hydrogel state (ethanol gel), and the immersion process of the ferrofluid was carried out at 80 °C which is higher than the boiling point of ethanol. Therefore, as the ethanol gradually evaporates, the water-based ferrofluid can more easily infiltrate through the liquid. The Fe_3O_4 NPs could then be more readily absorbed to the surface of BC nanofibers. On the other hand, the BC-F samples had larger mean pore sizes, and so the MNPs are thought to pass through the structure more easily without adsorption occurring. Also, there might be trapped air in the BC-F nanostructure. For the ferrofluid to diffuse within the BC-F structure, it must overcome the surface tension of the BC/air interface making it more difficult for infiltration of the Fe_3O_4 NPs.

3.2. FTIR analysis

The FTIR spectra of the pristine BC and BC/Fe_3O_4 composites are shown in Fig. 4. All samples have similar spectra regardless the drying process (BC-N and BC-F) or the concentration of MNPs. Higher resolution IR spectra in the wavenumber range of 3800–2600 cm^{-1} and 1800–600 cm^{-1} are shown in Fig. S2 (Supplementary Information). There are slight variations in the intensities of the peaks, but a clear trend is not found. Also, the positions of the peaks are not altered for all

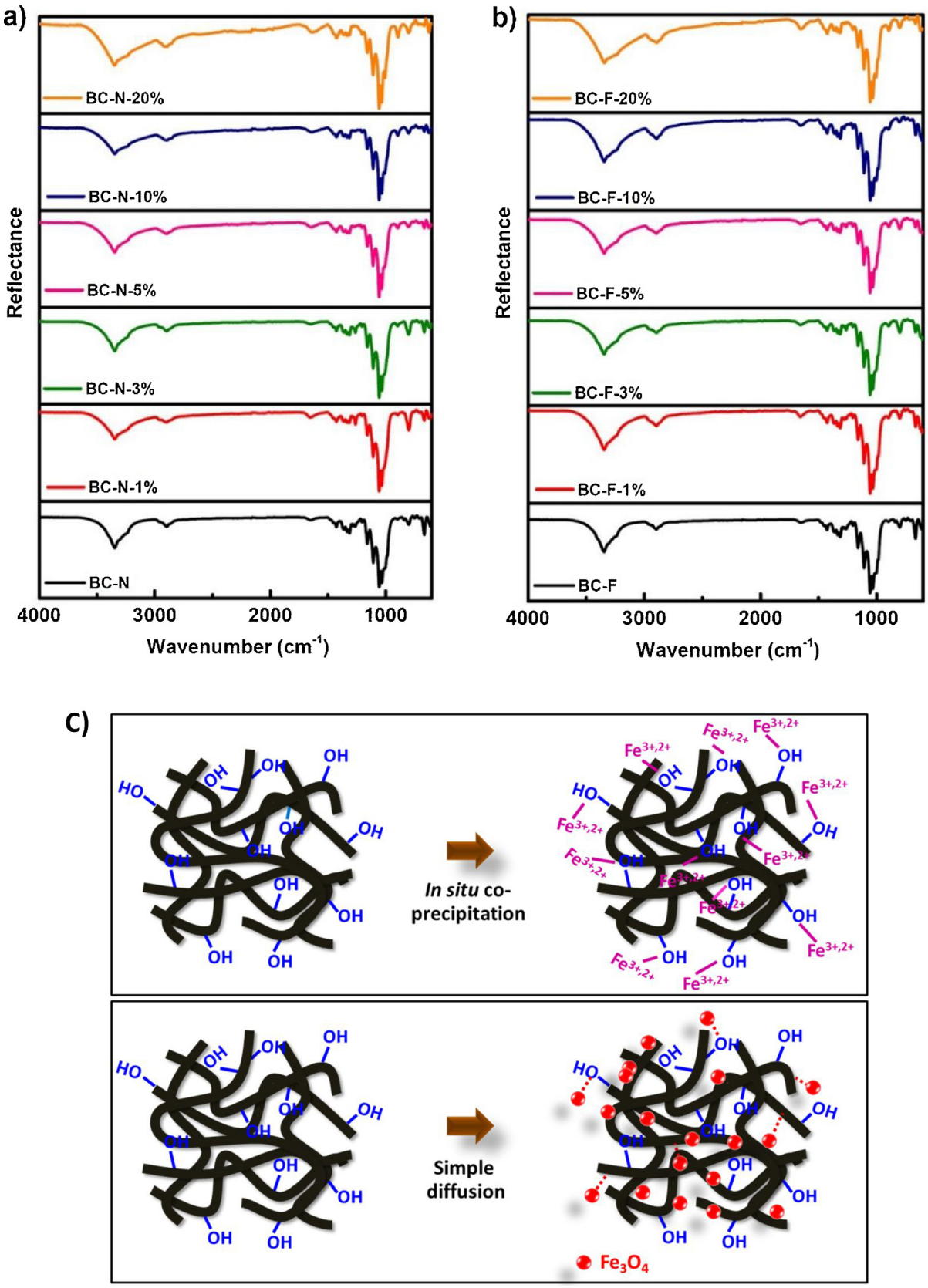

Fig. 4. Typical FTIR spectra of the pristine BC and BC-Fe_3O_4 nanocomposites for (a) BC-N and (b) BC-F. (c) Schematic illustration of the magnetic BC nanocomposite formation by *in situ* co-precipitation and simple diffusion.

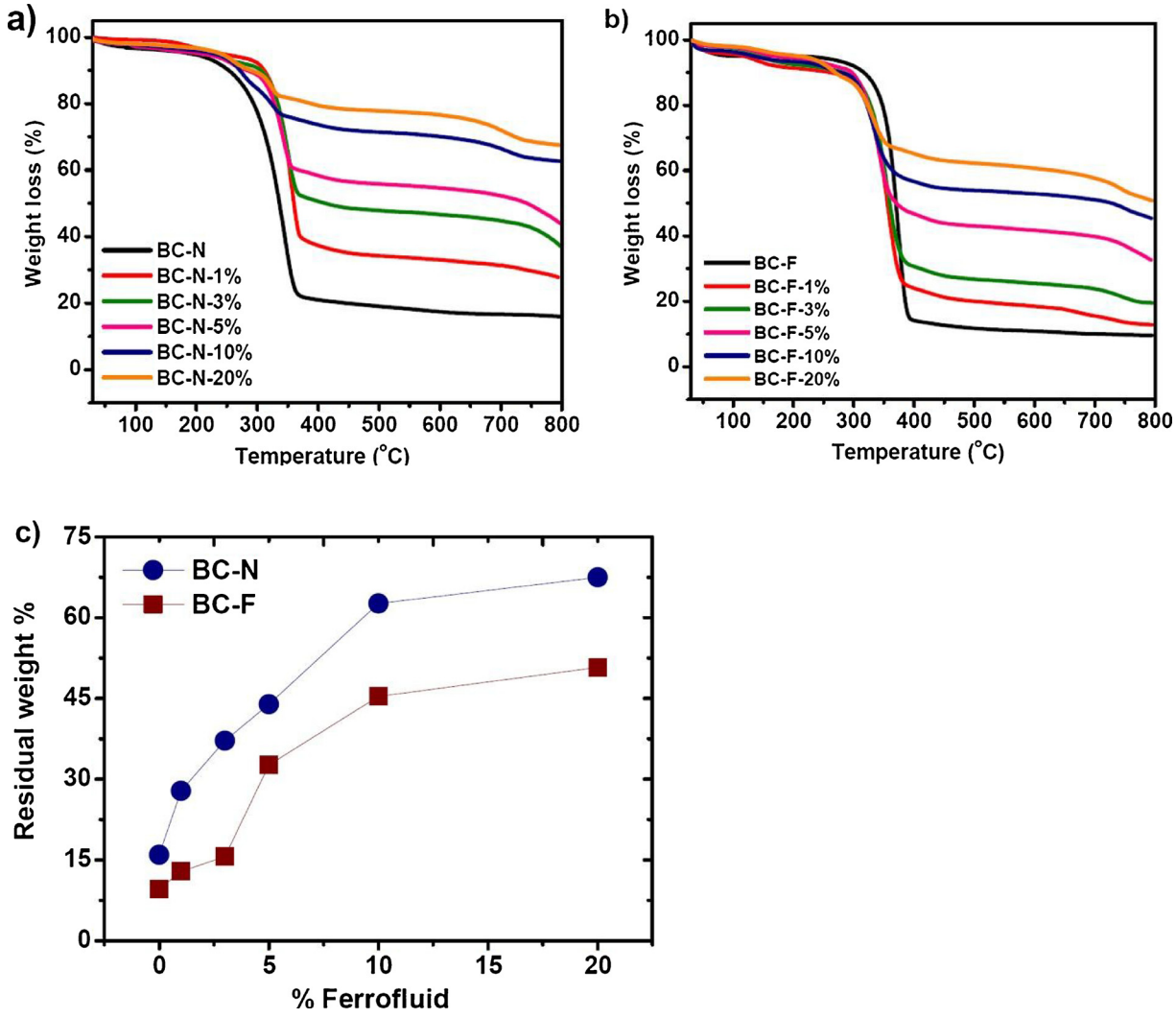

Fig. 5. Typical TGA curves of the pristine BC and BC-Fe_3O_4 nanocomposites for (a) BC-N and (b) BC-F. (c) The residual weight at 800 °C extracted from (a) and (b) as a function of ferrofluid.

samples. The incorporation of the MNPs did not affect the position of bands corresponding to the −OH groups. This finding is in contrast to previous studies which showed a shift in the position of the −OH group to a lower wavenumber position when MNPs were co-precipitated into BC networks (Marins et al., 2013; Park et al., 2013; Zhang et al., 2011; Zheng et al., 2013). The shift was thought to be due to the binding between the Fe^{2+}/Fe^{3+} precursor and the −OH functional groups due to an electrical dipole interaction. The −OH group is in turn acting as the anchoring sites for iron ions to deposit, but it also creates regions with a higher probability of agglomeration of MNPs. Since the shift of the −OH group was not found in the present study, an alternative explanation is required. Our method did not require the iron ion precursors but the nano-sphere of Fe_3O_4 in a water-based solution instead. These Fe_3O_4 NPs are neutral, and therefore they can easily adhere to many different parts of the BC nanofibers, not limited to the −OH groups. Moreover, with the simple diffusion process employed in this study, a more uniform distribution of the magnetite NPs can be achieved. As schematically illustrated in Fig. 4c, for the *in situ* co-precipitation methods, the positively charged iron ions are anchored predominantly at the −OH sites due to electrostatic forces (Hu et al., 2014), leading to an aggregation of the NPs. On the other hand, the Fe_3O_4 NPs in a ferrofluid, could be adsorbed all over the surface of BC nanofibers with no preferential sites, resulting in a more homogeneous distribution of MNPs in the composites.

3.3. Thermal analysis

TGA data from pristine BC and the BC/Fe_3O_4 composites are shown in Fig. 5. The main decomposition temperature ranges were found between 250–356 °C and 290–385 °C for the BC-N and BC-F samples, respectively. The samples are relatively stable against temperature, apart from within the decomposition temperature ranges, as can be seen from the derivative thermo-gravimetric (DTG) analysis in Fig. S3 (Supplementary Information). These temperature ranges are thought to be characteristic of a series of reactions related to the degradation of BC including decomposition, dehydration and depolymerization of the glycosidic units (Lv et al., 2016; Sureshkumar et al., 2010; Vasconcelos et al., 2017). During these events, molecular fragments such as CH_2−OH and −OH groups are thought to be removed (Wang et al., 2012). In the composite samples, as the concentration of ferrofluid increased, the residual weight at 800 °C also increased, corresponding to a higher amount of Fe_3O_4 NPs which was thermally stable up to 800 °C (Cao et al., 2014). Comparing the two processing conditions, the residual weights at 800 °C of the BC-N samples are significantly larger than those of the BC-F series (Fig. 5c). This represents a higher amount of MNP loading in the BC matrix which is consistent with the results in the previous sections. For a ferrofluid concentration of 20%, the residual weights were 65% and 48% for BC-N and BC-F samples, respectively. The results of the TGA analysis have a direct implication on

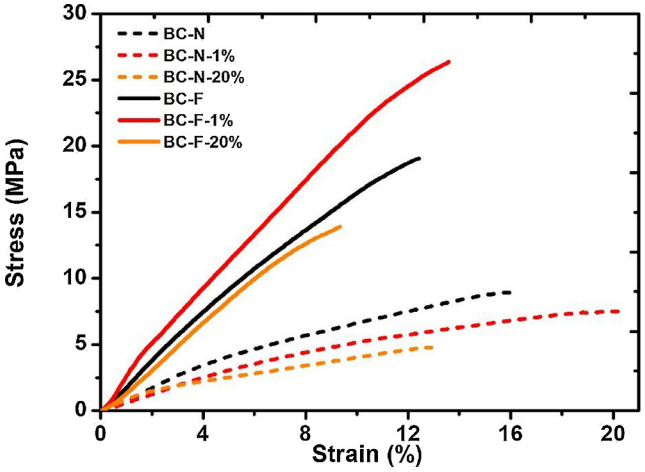

Sample	$Stress_{max}$ (MPa)	$Strain_{max}$ (%)	Young's Modulus (MPa)
BC-N	8.7±0.6	15.2±6.7	57.1±0.3
BC-N-1%	8.5±2.5	19.3±4.0	44.3±0.2
BC-N-20%	5.2±0.6	14.8±1.7	34.7±0.1
BC-F	13.7±5.1	9.4±3.4	144.6±1.1
BC-F-1%	25.8±4.6	14.1±0.9	183.6±0.4
BC-F-20%	9.6±4.4	8.1±2.1	118.9±0.9

Fig. 6. Representative stress-stain curves of the pristine BC and BC-Fe_3O_4 nanocomposites, with the average values of $Stress_{max}$, $Strain_{max}$ and Young's Modulus.

the magnetic properties of the materials.

Further analysis on the temperature at which maximum decomposition occurs (T_{max}) and the decomposition temperature intervals ($T_{interval}$) is presented in Fig. S3. (Supplementary Information). For the pristine BC membranes, the BC-N sample exhibits a lower T_{max}, but a higher $T_{interval}$ than found for BC-F. This could be due to the difference in the morphology of both samples. BC-N has more open structure with smaller fiber diameters and a larger surface area. Therefore, it can be thermally decomposed at a lower T_{max} compared to BC-F. On the other hand, the pristine BC-F has a more compacted structure with probably stronger inter-fibrillar bonding (Figs. 3b and 7b). Though the decomposition temperature (T_{max}) is higher, it can be decomposed over a shorter temperature range (smaller $T_{interval}$). Both BC-N and BC-F magnetic composites show similar results. The higher concentration of ferrofluid leads to a reduction in both T_{max} and $T_{interval}$. This could be due to a contribution of the interruption of inter-fibrillar interactions as the MNPs are impregnated in the BC nanofibrils. The results from the thermal analysis in this section also support the interpretation of the mechanical properties in the next section.

3.4. Mechanical properties

Fig. 6 shows the stress-strain curves for the pristine BC and BC/Fe_3O_4 nanocomposites. An almost linear relationship between the stress and strain is noted for the pristine BC-F samples. However, the BC-N samples exhibit strain hardening, whereby the slope of the curves increases after an initially "flat" region. The BC-N samples appear to exhibit much poorer mechanical properties (lower strength and Young's modulus) than the BC-F samples. For the BC-N series, incorporating higher concentrations of Fe_3O_4 NPs results in a reduction in both strength and Young's modulus. The reduction of the mechanical properties in BC/Fe_3O_4 nanocomposites has also been reported in the literature (Mashkour et al., 2017; Zheng et al., 2013). However, the strain to failure was increased as a small amount of MNPs was incorporated into the BC-N nanostructure (BC-N-1%). On the other hand, for the BC-F samples, impregnating a small amount of ferrofluid (BC-F-1%) causes an increase in strength, Young's modulus and strain to failure; adding an excess amount of ferrofluid (BC-F-20%) led to slightly reduced mechanical properties.

To better understand the changes in mechanical properties, and their relationship to the preparation conditions and nanocomposite effects, the cross-sectional morphology of the samples was observed using SEM (see Fig. 7). The large black arrows represent the stretching direction in Fig. 7. Firstly, comparing the BC-N and BC-F samples, particularly the pristine BC (Fig. 7a&b), the structure of the BC-N samples is observed to contain more uniformly open spaces. The BC-F samples had a more compacted layer-like structure. The uniform nanoporous structure was found to have collapsed in the BC-F samples. The underlying reason for this was probably due to the preparation process. In the BC-N samples, the water in the hydrogel was replaced by alcohol prior to the freeze-drying process. Due to the low boiling point

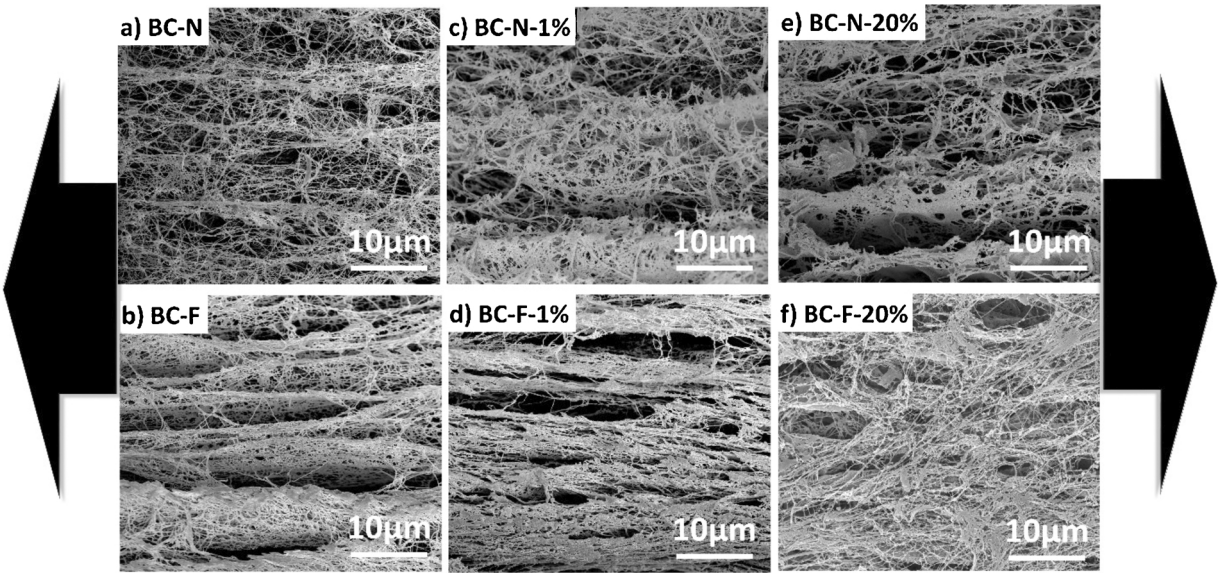

Fig. 7. Typical cross-sectional SEM images of (a) BC-N, (b) BC-F, (c) BC-N-1%, (d) BC-F-1%, (e) BC-N-20%, (f) BC-F-20%. The black arrows on both sides of the images show the direction of the tensile deformation.

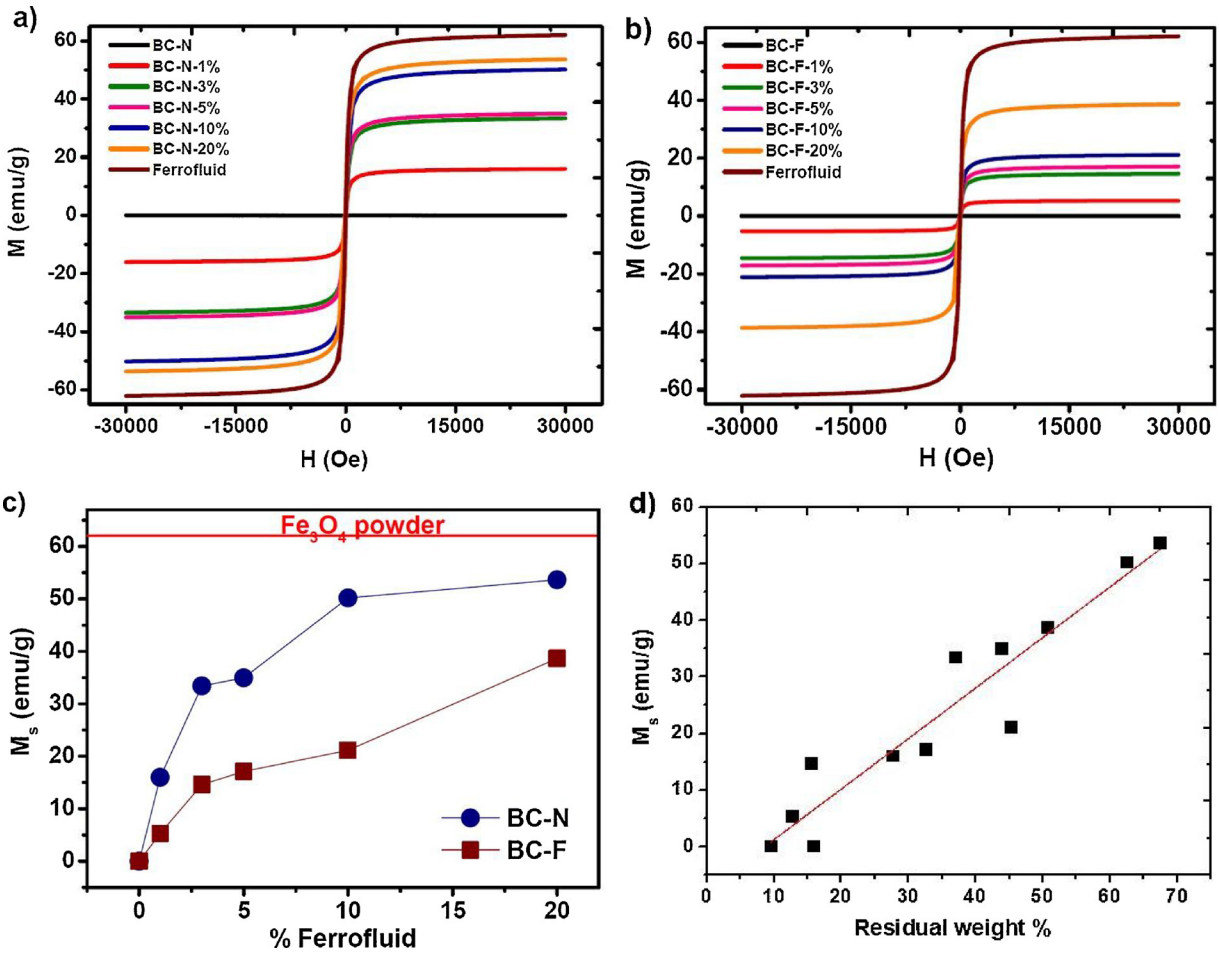

Fig. 8. Typical magnetization curves (M-H) of the pristine BC and BC/Fe_3O_4 nanocomposites for (a) BC-N samples and (b) BC-F samples. (c) M_s extracted from (a) and (b) plotted as a function of ferrofluid concentration. (d) The M_s value as a function of residual weight of BC/Fe_3O_4 nanocomposites at 800 °C.

and surface tension of ethyl alcohol (Haynes, 2016), it can be easily removed without affecting the nanostructure of the BC pellicle. Water in the BC-F samples needed to be freeze-dried out directly, and so it was not as easy to remove water without collapsing the structure. There is a higher interfacial energy between BC and water (Olsson et al., 2010; Sai et al., 2015; Zhang et al., 2011), leading to the distortion of the BC nanostructure. Some of the initially open pores collapsed during drying, and the nanofibers aggregated into a layered-like structure. However, these compacted and bundled nanofibers parallel to the stretching direction in the BC-F samples resulted in stronger materials due to the increased number of fibril-fibril interactions (see Fig. 6).

Fig. 7c&e shows the cross-sectional morphology of the BC-N/Fe_3O_4 composites. As the MNPs were introduced to the system, the 3D network of nanofibers of BC was still preserved. However, with Fe_3O_4 NPs covering the surfaces of the nanofibers, it is thought that they may have reduced the inter-fibrillar bonding, thereby possibly reducing the strength of the nanocomposites (Mashkour et al., 2017). The effect is more pronounced for higher Fe_3O_4 concentrations, as shown in Fig. 6. Nevertheless, the strain to failure was increased by the incorporation of a small amount of MNPs, presumably due to the interruption of inter-fibrillar interactions. This mechanism could be the reason why the materials display excellent flexibility. For the BC-F nanocomposites, as a small amount of MNPs were incorporated, the morphology of the sample consisted of an even more compacted layered-like structure parallel to the tensile stress direction (Fig. 7d). This more densely packed structure resulted in a stronger material (Fig. 6). Nevertheless, an excess of Fe_3O_4 NPs destroyed the layer-like structure (Fig. 7f), resulting in reduced mechanical properties.

The stiffness and flexibility of the magnetic BC membranes was demonstrated, as shown in Fig. S4 and Movie S1 in the Supplementary Information. The materials can be rolled into a cylindrical shape, or folded in both directions. Importantly they can be returned in their original shape without any noticeable damage. This elastic deformation can be repeated several times, showing the excellent mechanical durability of the BC magnetic nanocomposites.

3.5. Magnetic properties and responses

Magnetic M-H curves at room temperature are shown in Fig. 8. The pristine BC samples (both BC-N and BC-F) exhibited non-magnetic behavior as expected. Incorporating Fe_3O_4 NPs results in superparamagnetic properties, ferromagnetic behavior with a diminishing loop width, due to the nanosize of the magnetite particles. The saturation magnetization (M_s) of the nanocomposites increased monotonically as the concentration of ferrofluid increased. The highest M_s value of 53.6 emu/g was found for the BC-N-20% sample which is equivalent to 86.5% of the dried ferrofluid (M_s = 62.0 emu/g). The M_s value for the BC-N series was found to be considerably higher than that of the BC-F series for all ferrofluid concentrations (Fig. 8c). This is also related to the higher concentration of Fe_3O_4 NPs in the BC-N samples as previously discussed. Comparing Fig. 8c with Fig. 5c, there is a correlation between M_s and the residual weight which can be explicitly expressed as shown in Fig. 8d. A linear relationship between M_s and the residual weight is clearly observed, irrespective of the sample preparation method. It is therefore inferred that the magnetization of the BC nanocomposites only depends on the concentration of the magnetite

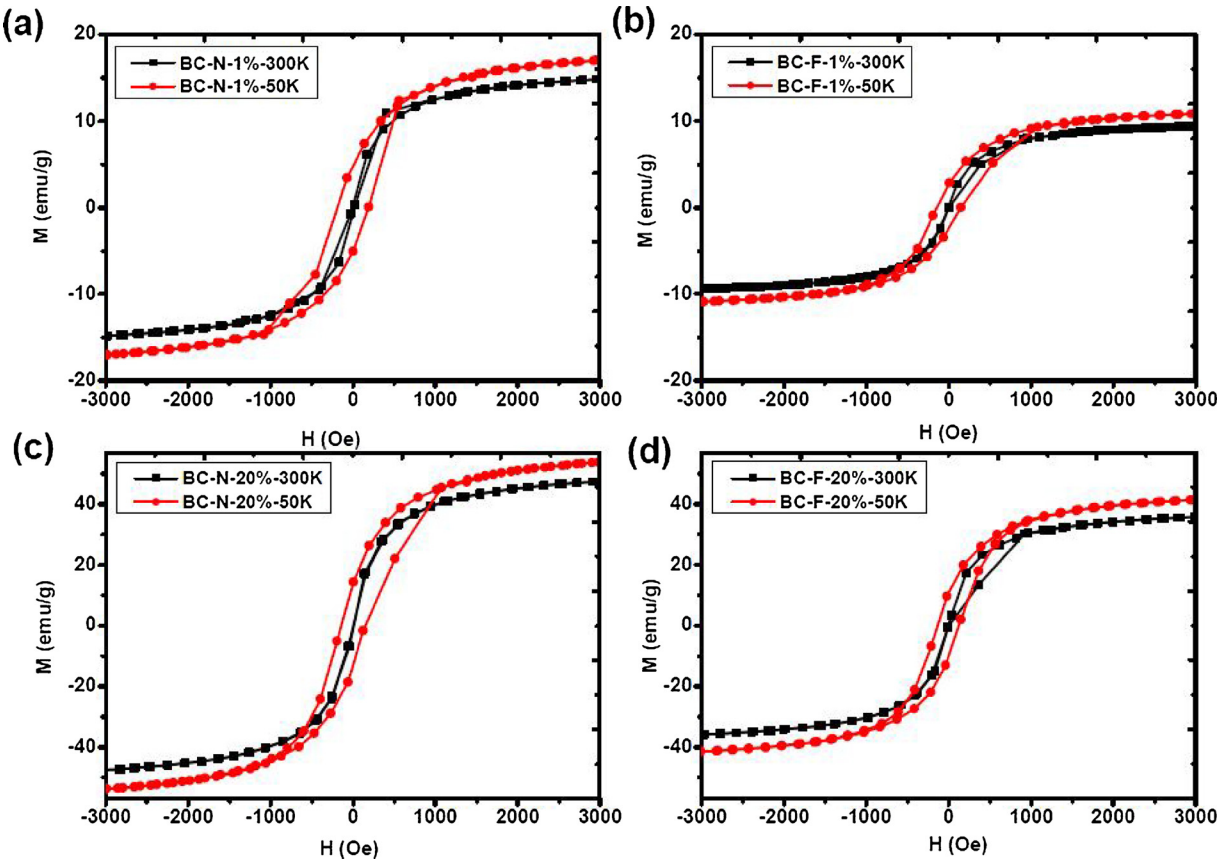

Fig. 9. Comparison between the magnetization curves at 300 K and 50 for (a) BC-N-1%, (b) BC-F-1%, (c) BC-N-20%, and (d) BC-F-20%.

NPs.

The M_s values of the magnetic BC composites in the present work are significantly higher than many other published values for magnetite NPs in BC. For instance, maximum magnetizations of only about 10 emu/g (Park et al., 2013), 14 emu/g (Zhang et al., 2011), 18 emu/g (Sureshkumar et al., 2010) M. and 28 emu/g (Katepetch & Rujiravanit, 2011) in BC/Fe_3O_4 nanocomposites prepared by the *in situ* co-precipitation have been previously reported. The higher M_s values provides advantages, such as greater sensitivity and response to external magnetic fields. These properties make the present magnetic BC membrane very useful for a variety of applications. The only higher Ms than the present work was reported by Marins et al.; an Ms of ~60 emu/g (Marins et al., 2013). In their work, a significantly large concentration of MNPs was incorporated into the composites. The concentration of NPs was so overwhelming that the BC nanofibrils were not visible under SEM investigation. Such a large quantity of NPs in the BC nanostructure could significantly deteriorate the mechanical properties of the magnetic BC nanocomposites. In addition, the BC/Fe_3O_4 nanocomposites in the present work exhibit magnetic stability over a very long period of time. As shown in Fig. S5 (Supplementary Information), the M_s values of all samples are retained even after a period of more than 6 months. The stability of these magnetic properties over a long-time period could be very useful for applications.

Magnetization curves at low temperature (50 K) were measured as shown in Fig. 9. The M_s value was enhanced at low temperature due to the suppression of thermal fluctuations. For example, the M_s of BC-N-20% was increased from 53.6 emu/g at 300 K to 61.8 emu/g at 50 K, equivalent to a 15% increase. Furthermore, hysteresis loops were found at 50 K. This is a characteristic of ferromagnetic properties which infers that the phase transition temperature (from superparamagnetic to ferromagnetic) must be somewhere between 300 and 50 K. To obtain that information, ZFC-FC experiments were carried out and the results are shown in Fig. S6 (Supplementary Information). Normally, from ZFC-FC curves of nanoparticle/nanocomposites, two temperature parameters can be extracted: the magnetic irreversibility temperature (T_{irr}) at which the ZFC and FC curves merge, and the blocking temperature (T_B) at the maxima of the ZFC curve. In the present study, the T_{irr} is out of the range of the experiment (> 400 K) but the T_B could be extracted as shown in Fig. S6 (Supplementary Information). T_B is the transition temperature above which the NPs are in the superparamagnetic phase, and below which the NPs are the ferromagnetic phase. In all nanocomposite samples, T_B was found to be in the range of 261–286 K. These values are consistent with the M-H curve measurements, where at 300 K (above T_B) the samples show superparamagnetic behavior (no loop) but at 50 K (below T_B) ferromagnetic hysteresis loops were observed. The blocking temperatures found this experiment are somewhat higher than the *in situ* synthesis system (50–100 K) (Zeng et al., 2014). This is understandable from the difference in the nanoparticle sizes since T_B is directly proportional to the volume (V) of the NPs according to the equation $K_uV/k_BT_B = 25$, where K_u is the magnetic anisotropy constant, and k_B is Boltzmann's constant (Spaldin, 2003). Using the measured value T_B of 280 K and particle diameter of 20 nm, K_u was found to be 2.31×10^5 erg/cm^3, which is in close agreement with a literature value for this constant (2.64×10^5 erg/cm^3) (Linh, Manh, Phong, Hong, & Phuc, 2014).

The response to external fields of magnetic BC membranes were demonstrated as shown in Fig. 10 (and Movie S2, Supplementary Information). The materials can be easily lifted up by or bent towards a magnet and returned to their original shape once it is removed. In addition, the magnetic BC membrane was demonstrated for a spontaneous response to an alternating magnetic field. As shown in Fig. 10 (and Movie S3, Supplementary Information) the magnetic membrane is shown to oscillate with an alternating magnetic field generated by a permanent magnet attached to a 100-Hz vibrator. This demonstrates

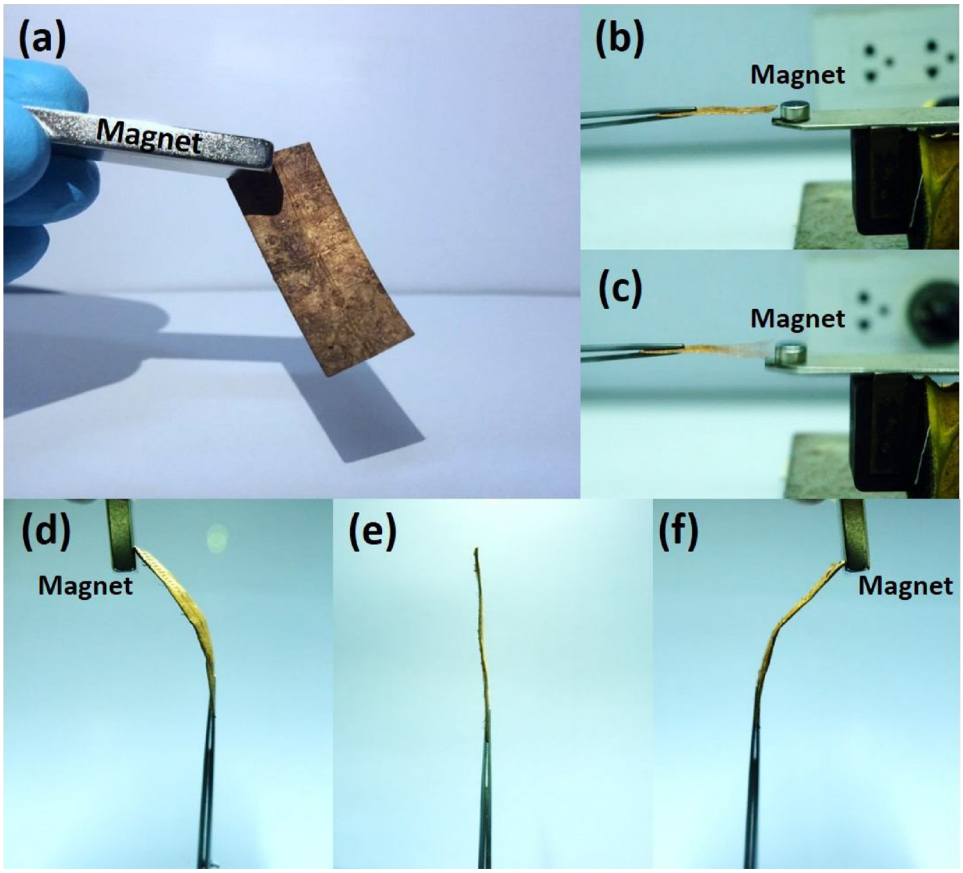

Fig. 10. Response of the magnetic BC membrane to external magnetic fields: (a) lift up by a magnet, (b)&(c) subjected to an alternating magnetic field, (d)–(f) bendability towards a magnet.

both the quick response to external magnetic fields and the high flexibility of the magnetic BC membrane which could have various potential applications, such as magnetic actuators, switches, sensors, or diaphragms.

4. Conclusions

In summary, a facile approach to fabricate BC/Fe_3O_4 nanocomposites by a simple diffusion process was successfully demonstrated. The existence of both the crystalline BC phase and the magnetite phase in the composites was confirmed. Increasing the concentration of ferrofluid resulted in a higher concentration of the Fe_3O_4 NPs. With the present method, the MNPs were uniformly dispersed on the BC nanofibrils' surfaces, and the degree of agglomeration was much less than previously published research. The diffusion process of Fe_3O_4 NPs enabled them to be adsorbed to the fibrils' surfaces, but this was not limited to the −OH functional groups. The preparation process prior to ferrofluid diffusion had a substantial effect on the characteristics of the nanocomposites. For the BC-N samples, higher concentrations of MNPs was achieved, due to the ease of diffusion of Fe_3O_4 NPs in the liquid solutions. This, in turn, led to a higher magnetization and therefore higher sensitivity to external magnetic fields. Our preliminary mechanical testing has shown that higher properties were obtained for the BC-F samples due to their more compacted structure. The magnetic membranes based on BC/Fe_3O_4 nanocomposites were demonstrated to show high flexibility and durability, and were also highly responsive to both static and alternating external magnetic fields. This enables the usage of the magnetic BC membranes for many applications such as actuators, switches, sensors, flexible data storages or diaphragms.

Acknowledgements

This work was supported by the Thailand Research Fund (TRF) in cooperation with Khon Kaen University (RSA5980014), the Royal Society-Newton Advanced Fellowship (NA160147) in partnership with the Thailand Research Fund (TRF) (DBG6080002), and the Royal Golden Jubilee PhD Programme (PHD/0063/2558).

Appendix A. Supplementary data

Supplementary data associated with this article can be found, in the online version, at https://doi.org/10.1016/j.carbpol.2018.03.072.

References

Barud, H. S., Tercjak, A., Gutierrez, J., Viali, W. R., Nunes, E. S., Ribeiro, S. J. L., & Marques, R. F. C. (2015). Biocellulose-based flexible magnetic paper. *Journal of Applied Physics, 117*(17), 17B734.

Behrens, S. (2011). Preparation of functional magnetic nanocomposites and hybrid materials: Recent progress and future directions. *Nanoscale, 3*(3), 877–892.

Cao, C. H., Xiao, L., Chen, C. H., Shi, X. W., Cao, Q. H., & Gao, L. (2014). In situ preparation of magnetic Fe3O4/chitosan nanoparticles via a novel reduction-precipitation method and their application in adsorption of reactive azo dye. *Powder Technology, 260*, 90–97.

Czaja, W., Romanovicz, D., & Brown, R. M. (2004). Structural investigations of microbial cellulose produced in stationary and agitated culture. *Cellulose, 11*(3–4), 403–411.

Dai, Q., & Nelson, A. (2010). Magnetically-responsive self assembled composites. *Chemical Society Reviews, 39*(11), 4057–4066.

Eichhorn, S. J., & Sampson, W. W. (2005). Statistical geometry of pores and statistics of porous nanofibrous assemblies. *Journal of the Royal Society Interface, 2*(4), 309–318.

Foresti, M. L., Vazquez, A., & Boury, B. (2017). Applications of bacterial cellulose as precursor of carbon and composites with metal oxide, metal sulfide and metal nanoparticles: A review of recent advances. *Carbohydrate Polymers, 157*, 447–467.

Galland, S., Andersson, R. L., Salajkova, M., Strom, V., Olsson, R. T., & Berglund, L. A. (2013). Cellulose nanofibers decorated with magnetic nanoparticles – synthesis, structure and use in magnetized high toughness membranes for a prototype

loudspeaker. *Journal of Materials Chemistry C, 1*(47), 7963–7972.
Gayathry, G., & Gopalaswamy, G. (2014). Production and characterisation of microbial cellulosic fibre from Acetobacter xylinum. *Indian Journal of Fibre & Textile Research, 39*(1), 93–96.
Haynes, W. M. (2016). *CRC handbook of chemistry and physics* (Ninety-seventh ed.). Boca Raton: CRC Press.
Hu, W. L., Chen, S. Y., Yang, J. X., Li, Z., & Wang, H. P. (2014). Functionalized bacterial cellulose derivatives and nanocomposites. *Carbohydrate Polymers, 101*, 1043–1060.
Katepetch, C., & Rujiravanit, R. (2011). Synthesis of magnetic nanoparticle into bacterial cellulose matrix by ammonia gas-enhancing in situ co-precipitation method. *Carbohydrate Polymers, 86*(1), 162–170.
Klemm, D., Heublein, B., Fink, H. P., & Bohn, A. (2005). Cellulose: Fascinating biopolymer and sustainable raw material. *Angewandte Chemie-International Edition, 44*(22), 3358–3393.
Lee, Y. J., An, S. J., Bae, E. B., Gwon, H. J., Park, J. S., Jeong, S. I., & Huh, J. B. (2017). The effect of thickness of resorbable bacterial cellulose membrane on guided bone regeneration. *Materials, 10*(3).
Lim, G. H., Lee, J., Kwon, N., Bok, S., Sim, H., Moon, K. S., & Lim, B. (2016). Fabrication of flexible magnetic papers based on bacterial cellulose and barium hexaferrite with improved mechanical properties. *Electronic Materials Letters, 12*(5), 574–579.
Lin, S. P., Kung, H. N., Tsai, Y. S., Tseng, T. N., Hsu, K. D., & Cheng, K. C. (2017). Novel dextran modified bacterial cellulose hydrogel accelerating cutaneous wound healing. *Cellulose, 24*(11), 4927–4937.
Linh, P. H., Manh, D. H., Phong, P. T., Hong, L. V., & Phuc, N. X. (2014). Magnetic properties of Fe3O4 nanoparticles synthesized by coprecipitation method. *Journal of Superconductivity and Novel Magnetism, 27*(9), 2111–2115.
Liu, S. S., Yan, W. N., Cao, X. C., Zhou, Z. F., & Yang, R. Z. (2016). Bacterial-cellulose-derived carbon nanofiber-supported CoFe2O4 as efficient electrocatalyst for oxygen reduction and evolution reactions. *International Journal of Hydrogen Energy, 41*(11), 5351–5360.
Lv, P., Xu, W., Li, D., Feng, Q., Yao, Y., Pang, Z., & Wei, Q. (2016). Metal-based bacterial cellulose of sandwich nanomaterials for anti-oxidation electromagnetic interference shielding. *Materials & Design, 112*, 374–382.
Marins, J. A., Soares, B. G., Barud, H. S., & Ribeiro, S. J. L. (2013). Flexible magnetic membranes based on bacterial cellulose and its evaluation as electromagnetic interference shielding material. *Materials Science & Engineering C-Materials for Biological Applications, 33*(7), 3994–4001.
Mashkour, M., Tajvidi, M., Kimura, T., Kimura, F., & Ebrahimi, G. (2011). Fabricating unidirectional magnetic papers using permanent magnets to align magnetic nanoparticle covered natural cellulose fibers. *Bioresources, 6*(4), 4731–4738.
Mashkour, M., Tajvidi, M., Kimura, F., Yousefi, H., & Kimura, T. (2014). Strong highly anisotropic magnetocellulose nanocomposite films made by chemical peeling and in situ welding at the interface using an ionic liquid. *Acs Applied Materials & Interfaces, 6*(11), 8165–8172.
Mashkour, M., Moradabadi, Z., & Khazaeian, A. (2017). Physical and tensile properties of epoxy laminated magnetic bacterial cellulose nanocomposite films. *Journal of Applied Polymer Science, 134*(30).
Menchaca-Nal, S., Londono-Calderon, C. L., Cerrutti, P., Foresti, M. L., Pampillo, L., Bilovol, V., & Martinez-Garcia, R. (2016). Facile synthesis of cobalt ferrite nanotubes using bacterial nanocellulose as template. *Carbohydrate Polymers, 137*, 726–731.
Nata, I. F., Sureshkumar, M., & Lee, C. K. (2011). One-pot preparation of amine-rich magnetite/bacterial cellulose nanocomposite and its application for arsenate removal. *Rsc Advances, 1*(4), 625–631.
Olsson, R. T., Samir, M. A. S. A., Salazar-Alvarez, G., Belova, L., Strom, V., Berglund, L. A., & Gedde, U. W. (2010). Making flexible magnetic aerogels and stiff magnetic nanopaper using cellulose nanofibrils as templates. *Nature Nanotechnology, 5*(8), 584–588.
Park, M., Cheng, J., Choi, J., Kim, J., & Hyun, J. (2013). Electromagnetic nanocomposite of bacterial cellulose using magnetite nanoclusters and polyaniline. *Colloids and Surfaces B-Biointerfaces, 102*, 238–242.
Ren, Y., Dai, B., Wang, G. H., Zhang, X. W., Zhu, P., & Li, S. R. (2015). Preparation and microwave absorption properties of novel carbon nanofiber/Fe3O4 composites. *Journal of Nanoscience and Nanotechnology, 15*(4), 2845–2849.
Sai, H. Z., Fu, R., Xing, L., Xiang, J. H., Li, Z. Y., Li, F., & Zhang, T. (2015). Surface modification of bacterial cellulose aerogels' web-like skeleton for oil/water separation. *Acs Applied Materials & Interfaces, 7*(13), 7373–7381.
Shah, N., Ul-Islam, M., Khattak, W. A., & Park, J. K. (2013). Overview of bacterial cellulose composites: A multipurpose advanced material. *Carbohydrate Polymers, 98*(2), 1585–1598.
Shen, J., Song, Z. Q., Qian, X. R., & Ni, Y. H. (2011). A review on use of fillers in cellulosic paper for functional applications. *Industrial & Engineering Chemistry Research, 50*(2), 661–666.
Small, A. C., & Johnston, J. H. (2009). Novel hybrid materials of magnetic nanoparticles and cellulose fibers. *Journal of Colloid and Interface Science, 331*(1), 122–126.
Sourty, E., Ryan, D. H., & Marchessault, R. H. (1998). Characterization of magnetic membranes based on bacterial and man-made cellulose. *Cellulose, 5*, 5–17.
Spaldin, N. A. (2003). *Magnetic materials: Fundamentals and device applications.* Cambridge: Cambridge University Press.
Stoica-Guzun, A., Stroescu, M., Jinga, S. I., Mihalache, N., Botez, A., Matei, C., & Ionita, V. (2016). Box-Behnken experimental design for chromium(VI) ions removal by bacterial cellulose-magnetite composites. *International Journal of Biological Macromolecules, 91*, 1062–1072.
Sureshkumar, M., Siswanto, D. Y., & Lee, C.-K. (2010). Magnetic antimicrobial nanocomposite based on bacterial cellulose and silver nanoparticles. *Journal of Materials Chemistry, 20*(33), 6948–6955.
Thiruvengadam, V., & Vitta, S. (2013). Ni-bacterial cellulose nanocomposite; a magnetically active inorganic-organic hybrid gel. *Rsc Advances, 3*(31), 12765–12773.
Thiruvengadam, V., & Vitta, S. (2016). Interparticle interactions mediated superspin glass to superferromagnetic transition in Ni-bacterial cellulose aerogel nanocomposites. *Journal of Applied Physics, 119*(24).
Thiruvengadam, V., & Vitta, S. (2017a). Bacterial cellulose based flexible multifunctional nanocomposite sheets. *Cellulose, 24*(8), 3341–3351.
Thiruvengadam, V., & Vitta, S. (2017b). Flexible bacterial cellulose/permalloy nanocomposite xerogel sheets—Size scalable magnetic actuator-cum-electrical conductor. *Aip Advances, 7*(3).
Vasconcelos, N. F., Feitosa, J. P. A., da Gama, F. M. P., Morais, J. P. S., Andrade, F. K., de Souza Filho, M.d. S. M., & Rosa, M.d. F. (2017). Bacterial cellulose nanocrystals produced under different hydrolysis conditions: Properties and morphological features. *Carbohydrate Polymers, 155*, 425–431.
Wan, Y. Z., Yang, Z. W., Xiong, G. Y., Guo, R. S., Liu, Z., & Luo, H. L. (2015). Anchoring Fe3O4 nanoparticles on three-dimensional carbon nanofibers toward flexible high-performance anodes for lithium-ion batteries. *Journal of Power Sources, 294*, 414–419.
Wang, H., Zhu, E., Yang, J., Zhou, P., Sun, D., & Tang, W. (2012). Bacterial cellulose nanofiber-supported polyaniline nanocomposites with flake-shaped morphology as supercapacitor electrodes. *The Journal of Physical Chemistry C, 116*(24), 13013–13019.
Wu, C. N., & Cheng, K. C. (2017). Strong, thermal-stable, flexible, and transparent films by self-assembled TEMPO-oxidized bacterial cellulose nanofibers. *Cellulose, 24*(1), 269–283.
Wu, W. B., Jing, Y., Gong, M. R., Zhou, X. F., & Dai, H. Q. (2011). Preparation and properties of magnetic cellulose fiber composites. *Bioresources, 6*(3), 3396–3409.
Zakaria, S., Ong, B. H., Ahmad, S. H., Abdullah, M., & Yamauchi, T. (2005). Preparation of lumen-loaded kenaf pulp with magnetite (Fe3O4). *Materials Chemistry and Physics, 89*(2–3), 216–220.
Zeng, M. L., Laromaine, A., Feng, W. Q., Levkin, P. A., & Roig, A. (2014). Origami magnetic cellulose: Controlled magnetic fraction and patterning of flexible bacterial cellulose. *Journal of Materials Chemistry C, 2*(31), 6312–6318.
Zhang, W., Chen, S. Y., Hu, W. L., Zhou, B. H., Yang, Z. H., Yin, N., & Wang, H. P. (2011). Facile fabrication of flexible magnetic nanohybrid membrane with amphiphobic surface based on bacterial cellulose. *Carbohydrate Polymers, 86*(4), 1760–1767.
Zhao, X., Li, H., Ding, A., Zhou, G., Sun, Y., & Zhang, D. (2016). Preparing and characterizing Fe3O4@cellulose nanocomposites for effective isolation of cellulose-decomposing microorganisms. *Materials Letters, 163*, 154–157.
Zheng, Y., Yang, J. X., Zheng, W. L., Wang, X., Xiang, C., Tang, L., & Wang, H. P. (2013). Synthesis of flexible magnetic nanohybrid based on bacterial cellulose under ultrasonic irradiation. *Materials Science & Engineering C-Materials for Biological Applications, 33*(4), 2407–2412.
Zhu, H. X., Jia, S. R., Wan, T., Jia, Y. Y., Yang, H. J., Li, J., & Zhong, C. (2011). Biosynthesis of spherical Fe3O4/bacterial cellulose nanocomposites as adsorbents for heavy metal ions. *Carbohydrate Polymers, 86*(4), 1558–1564.

Journal of Materials Chemistry C

PAPER

Cite this: J. Mater. Chem. C, 2018, 6, 11427

White magnetic paper based on a bacterial cellulose nanocomposite

Nipaporn Sriplai,[a] Pornkanok Sirima,[a] Dulayawit Palaporn,[a] Wiyada Mongkolthanaruk,[c] Stephen J. Eichhorn [d] and Supree Pinitsoontorn *[ab]

Received 16th August 2018, Accepted 7th October 2018

DOI: 10.1039/c8tc04103b

rsc.li/materials-c

A newly proposed idea for the fabrication of white magnetic paper is presented. These papers are fabricated from a layered composite of bacterial cellulose (BC) sheets. Magnetic BC sheets are prepared by the incorporation of $CoFe_2O_4$ nanoparticles (NPs) in the BC structure (MBC). White BC sheets were formed by the impregnation of ZnO NPs in the BC nanofibrils (ZBC), and then forming a ZBC/MBC/ZBC sandwich structure. This structure was then hot-pressed to obtain white magnetic paper. The fabricated magnetic BC paper exhibits a 'whiteness' of over 80%, with a high reflectance of over 70% in the visible spectral range. XRD and SEM analysis confirmed the presence of the BC, $CoFe_2O_4$ and ZnO phases in the white magnetic paper. The whiteness of the paper is improved further with a higher concentration of ZnO NPs, but at the cost of a reduction in the mechanical properties. Magnetic hysteresis was observed in the fabricated white magnetic paper with a saturation magnetization of $\sim$20 emu g^{-1}, comparable to the literature values for black magnetic papers. The white magnetic paper was demonstrated to exhibit flexibility and foldability just like regular paper sheets but can also be distinguished by subjecting it to an external magnetic field. This gives potential for its use as security paper or in anti-counterfeiting applications.

Introduction

Cellulose is an almost inexhaustible resource and a key source of sustainable materials on an industrial scale.[1] The use of fillers in a cellulosic paper network can deliver some unique functions which are not available in its pristine form.[2] In particular, magnetic cellulosic papers, in which magnetic particles are incorporated into the fibrous network structure, have attracted great attention from many research groups due to their potential uses in a wide range of technological applications, *e.g.* information storage, electromagnetic shielding, security paper, magnetographic printing, and magnetic filtering.[3–8]

Recently, several researchers have focused on magnetic papers or magnetic membranes based on a bacterial cellulose template. Bacterial cellulose (BC) is a form of the material with a microbial origin. It is commonly produced from the cultivation of a particular type of Gram negative bacteria *e.g. Gluconacetobacter xylinum*. The material typically consists of a network of nanofibers with large porosity. Bacterial cellulose has a number of advantages over plant celluloses, such as its high purity, high water absorbency, excellent biological affinity, and remarkable mechanical properties.[9–11] A number of studies on magnetic BC papers, films or membranes, synthesized by an *in situ* synthesis method, have been published.[12–20] For instance, Olsson *et al.* fabricated flexible magnetic aerogels and stiff magnetic nanopapers using BC nanofibrils as templates.[21] They *in situ* synthesized $CoFe_2O_4$ nanoparticles (NPs) in freeze-dried BC membranes, which exhibited both excellent mechanical and magnetic properties.[21] In other research, flexible BC/permalloy nanocomposite xerogel sheets were fabricated by *in situ* co-precipitation of $FeNi_3$ NPs.[22] Due to the metallic behavior of $FeNi_3$, the xerogel sheets showed both ferromagnetic and electrically conductive behavior. Lim *et al.* fabricated flexible magnetic papers by incorporating barium hexaferrite nanoplates in a BC matrix.[7] The resultant product exhibited strong ferromagnetic properties and improved mechanical properties.

One obvious disadvantage of magnetic paper, when using either a plant cellulose base or a BC base, is the diminishing whiteness of the sheet. The magnetic papers in all of the above mentioned publications had dark colours.[7,8,12–22] White papers are commonly used in various applications[23,24] but the introduction of magnetic particles typically destroys the whiteness, turning them black, or reddish-brown depending on the type of magnetic particles used. Non-magnetic papers, such as flexo and offset, also require a high degree of whiteness. Discolouration is inevitable, since in ferromagnetic transition metals or oxides the

[a] Department of Physics, Faculty of Science, Khon Kaen University, Khon Kaen 40002, Thailand. E-mail: psupree@kku.ac.th
[b] Institute of Nanomaterials Research and Innovation for Energy (IN-RIE), Khon Kaen University, Khon Kaen 40002, Thailand
[c] Department of Microbiology, Faculty of Science, Khon Kaen University, Khon Kaen 40002, Thailand
[d] Bristol Composites Institute (ACCIS), University of Bristol, Queens Building, University Walk, Bristol, BS8 1TR, UK

Fermi level lies in the spin-splitted spd hybridization band; whiteness is typically found in a material with a large band gap. The diminished white colour appearance limits the uses of the magnetic papers. Another downside to the introduction of inorganic fillers in paper is the loss of strength of the sheet, something which is avoided in common printing paper (*e.g.* newsprint).

Some research has been reported on attempts to produce white magnetic paper, or improve the whiteness of magnetic paper. For instance, Gao *et al.* prepared magnetic paper by mixing Tb-based magnetic glass particles with hardwood chemical pulp by a lumen loading process.[25] The whiteness of the magnetic papers was found to be greater than 80%, even with the addition of more than 50 wt% of magnetic particles. However, the papers in this work were paramagnetic, with very low magnetization ($\sim$0.1 emu g^{-1}), which cannot really be used in magnetic applications. Another example is the work carried out by Mo *et al.* who reported the addition of surface-modified graphene oxide (GO) coated magnetic particles incorporated into an oven-dried bamboo pulp.[26] The presence of GO improved the strength properties of the paper, but reduced the whiteness to below 70%, even for a small addition of GO (1.5 mg mL^{-1}). Again, paramagnetism was observed, when Tb-based magnetic glass particles were used in a similar approach to Gao *et al.*[25] Alternatively, Pacurariu *et al.* synthesized γ-Fe_2O_3/SiO_2 core shell NPs as possible candidates for magnetic paper pigments.[27] A SiO_2 shell coated on a γ-Fe_2O_3 core helped improve the whiteness of the particles, but at the cost of a reduction in the saturation magnetization (M_s = 0.8 emu g^{-1}). However, only magnetic NPs were studied in this work, and magnetic papers were not fabricated. For magnetic paper based on BC, Zeng *et al.* have reported the synthesis of Fe_2O_3 NP impregnated BC films with the aid of microwave-assisted thermal decomposition.[28] Ferromagnetism was observed in the synthesized papers, and the transparency was improved when a low concentration of NPs was used. The appearance of the paper was however far from white; the samples look reddish-brown or light-gold at best. Similarly, Barud *et al.* prepared flexible magnetic paper by the incorporation of well dispersed PEG–Fe_2O_3 in a BC matrix.[6] A light brown colour was obtained, with a low Fe_2O_3 concentration, but darker shades were observed as more Fe_2O_3 NPs were introduced.

In the present work, we propose a new concept for the fabrication of white magnetic paper based on BC templates, by using a composite approach to their production. A magnetic BC network is sandwiched between two white BC network layers, composed of BC plus ZnO NPs. Using this simple approach, ferromagnetic papers with preservation of the whiteness, can be fabricated. As far as we are aware, this is a novel approach and has not been previously reported.

Experimental

Materials

The chemicals used for fabricating magnetic BC papers were iron(III) chloride hexahydrate ($FeCl_3{\cdot}6H_2O$, reagent grade, Sigma-Aldrich), cobalt(II) chloride hexahydrate ($CoCl_2{\cdot}6H_2O$, reagent grade, Ajax Finechem), Zn(II) chloride ($ZnCl_2$, reagent grade, Rankem), sodium hydroxide (NaOH, 99%, RCI Labscan), yeast extract powder (Himedia) and D-glucose (anhydrous AR, Ajax Finechem).

Production of BC membranes

BC membranes were produced by cultivating the bacteria *Gluconacetobacter xylinum* (strain TISTR 975), supplied by the Microbiological Resources Center, Thailand Institute of Scientific and Technological Research (TISTR). The medium used in the bacteria culture consisted of 100 g of D-glucose and 10 g of yeast extract in 1 L of de-ionized (DI) water (GYE medium). After incubating in an incubator (Termaks, KBP-6395F) for 3 days under static conditions at 30 °C, BC pellicles with a thickness around 0.3 cm were harvested and purified in boiling DI water. They were then soaked in 0.5 M and 5 wt% NaOH for 15 min and 24 h, respectively. To ensure that no contamination occurred, the BC pellicles were rinsed further with DI water several times until a pH of 7 was reached. Finally, BC hydrogels obtained from this step were either kept under this condition (never-dried state) or in a freeze-dried (FD) state for the synthesis of nanocomposites in the next step.

Preparation of BC nanocomposites

Two nanocomposites were fabricated; namely BC + magnetic NPs, and BC + ZnO NPs. The former is labelled as MBC and the latter as ZBC. To synthesize MBC, co-precipitation between $CoCl_2{\cdot}6H_2O$ and $FeCl_3{\cdot}6H_2O$ in the presence of the FD-BC template was carried out using NaOH as a reducing agent. Firstly, 0.05 M of $CoCl_2{\cdot}6H_2O$ and 0.10 M of $FeCl_3{\cdot}6H_2O$ were dissolved in 50 ml of DI water. The FD-BC was soaked in the prepared solution which was then heated to 60 °C and held for 4 h. After that, 100 ml of 1.2 M NaOH was added to convert the metallic ions into cobalt ferrite ($CoFe_2O_4$) NPs according to the chemical reaction:

$$CoCl_2{\cdot}6H_2O + 2FeCl_3{\cdot}6H_2O + 8NaOH \rightarrow CoFe_2O_4 + 8NaCl + 22H_2O \quad (1)$$

The products were rinsed with water several times to remove unwanted materials until a pH of 7 was reached. The MBC was obtained in the form of a hydrogel.

For the synthesis of ZBC, $ZnCl_2$ was dissolved in 50 ml of DI water. The never-dried BC pellicles were then immersed in the zinc chloride solution for 24 h before soaking in NaOH solution at 55 °C for 1 h with continuous stirring. The BC + ZnO nanocomposites were formed according to the chemical reaction:

$$ZnCl_2 + 2NaOH \rightarrow ZnO + 2NaCl + H_2O \quad (2)$$

The effect of $ZnCl_2$ concentration on the whiteness of the samples was also explored. Two $ZnCl_2$ concentrations were used, 0.05 M and 0.10 M, for this purpose. The nanocomposite samples from these two concentrations were labeled as ZBC(1) and ZBC(2). The final products were then rinsed with water several times to obtain the ZBC hydrogels.

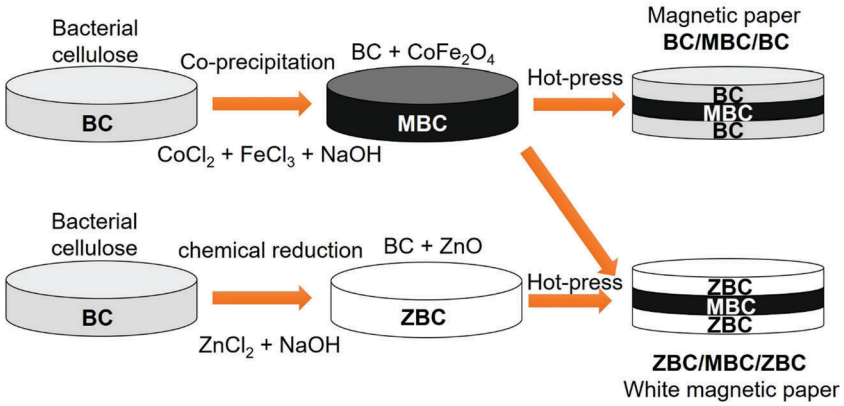

Fig. 1 Schematic of the synthesis process for white magnetic paper based on magnetic BC nanocomposites.

Fabrication of magnetic papers

Magnetic papers in this work were fabricated by hot-pressing BC hydrogels in an oven at 80 °C for 24 h. Four types of papers were prepared: BC/BC paper, MBC paper, BC/MBC/BC composite paper, and a ZBC/MBC/ZBC composite paper. For BC/BC and MBC paper, two layers of BC or a one-layer MBC sheet was compressed. In the case of BC/MBC/BC or ZBC/MBC/ZBC composite paper, an MBC sheet was sandwiched between BC or ZBC sheets before hot-pressing (0.2 MPa at 80 °C). The final thickness was approximately 0.03 mm per sheet. The amount of the retained mineral particles in the BC sheets was determined by thermogravimetric analysis (TGA) (Hitachi, STA7200). There are approximately 43 wt% of $CoFe_2O_4$ NPs in the MBC sheet, and 24 wt% and 39 wt% of ZnO NPs in the ZBC(1) and ZBC(2) sheets, respectively.

The fabrication process for these materials is summarized in Fig. 1.

Characterization of the samples

The whiteness of the papers was measured at the Department of Science Service, Ministry of Science and Technology, Thailand, according to the ISO 11476:2010 standard. A UV-visible spectrometer (Shimadzu, UV-3101PC) was used to collect the optical absorption spectra in the wavelength range 200–800 nm. X-ray diffraction (XRD) was carried out using a diffractometer employing Cu-Kα radiation (PANalytical, Empyrean) in a 2θ range of 5–80° to collect the information on the NPs' phases and crystalline structures. A field emission scanning electron microscope (FESEM) (FEI, Helios) was used to observe the surface morphologies and cross-sectional images of the samples. Prior to imaging with the SEM, the samples were gold coated to improve conductivity. For the mechanical properties tests, the tensile strength was measured using a universal testing machine (UTM, Instron 5567A) with a 20 mm sample gauge length, a sample width of 15 mm and a 20 mm min^{-1} testing speed. All tensile testing was conducted at 25 °C and 55% humidity. Tensile index was calculated according to the TAPPI T 494 standard. The tear index was tested at the Department of Science Service, Ministry of Science and Technology, Thailand, according to ISO 1974:2014. Magnetic properties were investigated by measuring magnetization (M) *versus* magnetic field (H) using a vibrating sample magnetometer (VSM) option in a VersaLab instrument (Quantum Design, USA) under a maximum field of 20 kOe.

Results and discussion

Fig. 2 shows photographic images, without any colour adjustment, of the fabricated BC paper samples. The BC/BC paper shows a faint white colour with some degree of opacity. As expected, the introduction of magnetic NPs turned the MBC sample black, on account of the colour of the $CoFe_2O_4$ powder. For the BC/MBC/BC composite, since the MBC was covered with a layer of a transparent BC, the dark colour of the interior layer can still be visible. Thus, the composite appears light gray, on account of the combined colour of both MBC and BC. Although the colour appearance of the BC/MBC/BC composite has improved significantly (much whiter than MBC), it is still far from the shade of normal white paper. Finally, the ZBC/MBC/ZBC sample exhibits a much whiter colour, due to the whiteness of ZnO NPs. This sample looks similar to normal white paper.

To quantify the level of whiteness, a test according to the ISO 11476:2010 standard was performed, the results of which are presented in Fig. 3a. The whiteness of the BC/BC paper is relatively low (~32%), and introducing the magnetic NPs resulted in decreased whiteness (~27%) for the MBC paper. On the other hand, the ZBC/MBC/ZBC composite papers exhibit whiteness greater than 75%. In particular, for a higher concentration of ZnO, the ZBC/MBC/ZBC(2) exhibits a whiteness of nearly 85%. This suggests that using a more concentrated ZnO content can improve the whiteness of the paper. This increase

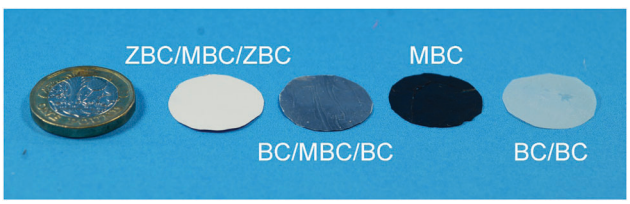

Fig. 2 Images of the synthesized samples. A one-pound coin is used as a scale bar (far left) and a colour indicator. This figure is shown without any colour adjustment.

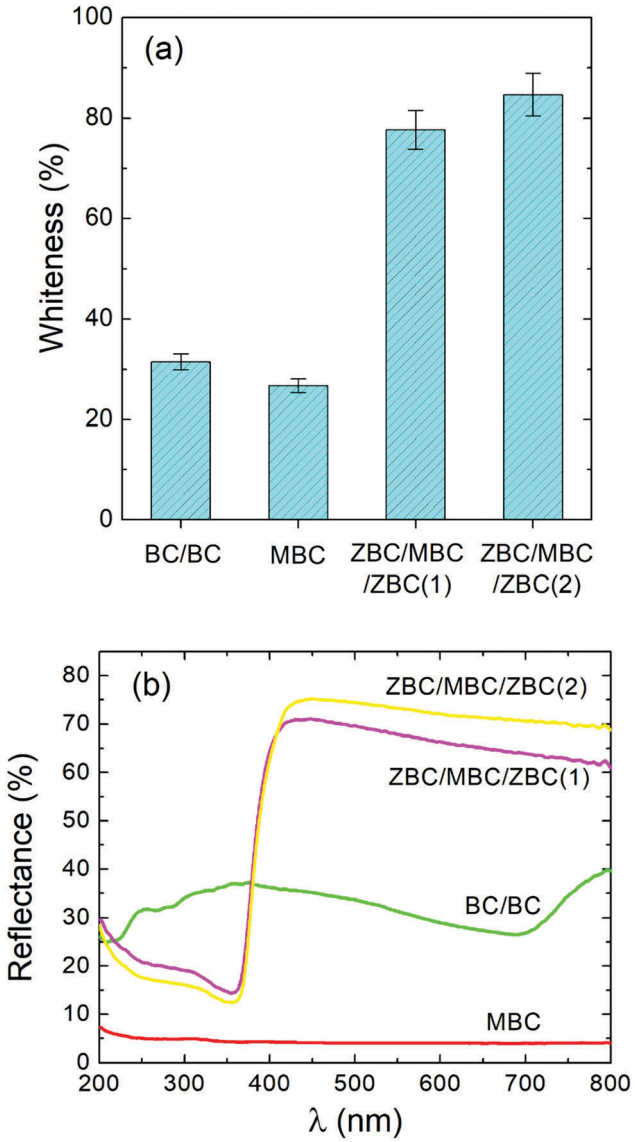

Fig. 3 Measurements of (a) the whiteness and (b) the UV-vis reflectance for the BC based papers.

in whiteness however comes at the cost of a reduction in the magnetization, and inferior mechanical properties. Compared to other published works, the whiteness of our magnetic paper is higher than the literature values for magnetic papers where Tb-based magnetic glass NPs were employed.[25,26] The UV-visible spectra in Fig. 3b also confirm the photographic images and whiteness tests. Within the visible spectral range (400–700 nm), the reflectance of the BC/BC paper is approximately 30–35% corresponding to an opaque white appearance, as seen in Fig. 2. The addition of $CoFe_2O_4$ significantly suppressed the reflectance in the visible (and UV) ranges, resulting in a black appearance to the MBC paper. This is due to the very low reflectance of $CoFe_2O_4$ NPs in the visible range, as has been previously reported.[29] However, incorporation of ZnO NPs in the ZBC/MBC/ZBC nanocomposites results in a substantial increase in the reflectance in the visible range, but a reduced reflectance in the UV range compared to the pristine BC paper. This is to be expected, since the ZnO nanostructures have been reported to exhibit very high reflectance in the visible range.[30,31] The observed high light absorption in the UV region (at wavelengths below 356 nm) is probably due to the ZnO band gap, which is a common characteristic of these NPs.[32] It is also known that the size of ZnO particles has an effect on the UV light absorption properties, this being one of the principles behind sunscreens. As previously reported, the UV absorbance of ZnO NPs (in the size range above the quantum limit) increases with increasing particle sizes.[33] Increasing the concentration of ZnO (ZBC/MBC/ZBC(2)) led to higher reflectance in the visible region, compared to ZBC/MBC/ZBC(1), corresponding to an increase in whiteness as shown in Fig. 3a. These results verify our proposed concept idea showing that we can successfully produce white magnetic paper based on BC nanocomposites.

To obtain information on the phase formation in the BC papers, XRD patterns were collected, the results of which are shown in Fig. 4 along with reference patterns for ZnO and

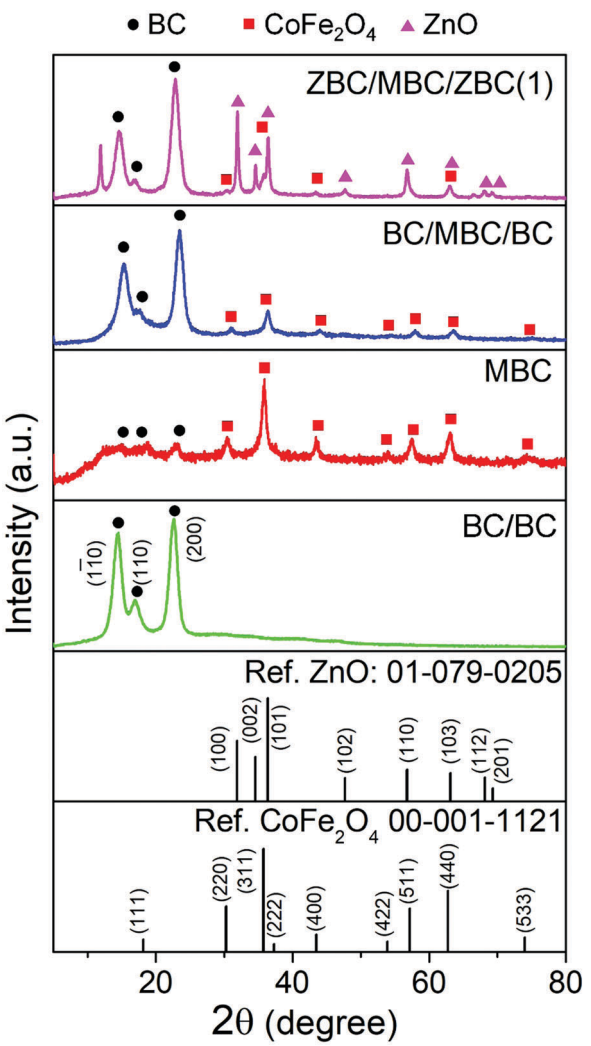

Fig. 4 Typical XRD patterns for the synthesized samples showing the mixed phases in the nanocomposite samples.

$CoFe_2O_4$. For the pristine BC paper, only three diffraction peaks corresponding to $(1\bar{1}0)$, (110) and (200) reflections of the BC crystalline structure were observed.[34] In the MBC sample, the combined XRD peaks from both BC and $CoFe_2O_4$ crystalline phases were observed, indicating a successful incorporation of cobalt ferrite NPs in the BC network structure. The reduction in the peak intensities from the BC was possibly caused by the intense reflection from the $CoFe_2O_4$ NPs, and even the deterioration of the BC's crystallinity, as the $CoFe_2O_4$ NPs were introduced. These observations have been previously reported.[8,13,14,16,18,19] For the composite papers, the BC/MBC/BC sample again shows the presence of both BC and $CoFe_2O_4$ phases, but the peaks for the BC phase are more intense than for the cobalt ferrite phase. The reason for this increase in intensity could be that it is a sandwich structure, and so there is a larger scattering volume from the top BC layer, resulting in more intense reflections from this material. The scattering volume of the $CoFe_2O_4$ phase is comparatively low compared to the BC layers, and so reduced intensity XRD peaks are observed for this material. For the white ZBC/MBC/ZBC paper, the mixed crystalline phases of BC, $CoFe_2O_4$, and ZnO can all be identified. Strong reflections from the BC as well as those from ZnO were observed; this indicates that the structure of the BC was not significantly affected by the incorporation of ZnO NPs. This result is similar to that obtained for BC-ZnO nanocomposites.[35,36]

Typical SEM micrographs of the plan-view images of the BC paper and MBC paper are shown in Fig. 5a and b, respectively. In order to image the inner structure of the fibrillar network, the top surface was peeled off before SEM imaging. The BC paper consists of numerous nanofibers woven randomly in the plane. The diameter of each fibril is of the order of ~100 nm. On the other hand, the SEM image of the MBC paper showed that $CoFe_2O_4$ NPs were coated on the surface of the BC nanofibrils. The NPs were distributed evenly all over the BC structure, indicating a homogeneous synthesis of the cobalt ferrite NPs in the BC network template. Unlike FD samples, where a porous structure is preserved,[8,15,21] the porous structure in BC is found to have collapsed due to the hot-pressing process to form the paper sheet. This resulted in very dense samples with few pores in the nanometer range. Fig. 5c shows an image of the cross section of the BC/MBC/BC composite paper. The thickness of each layer is ~20 μm. The composite sheets are not well attached to one another, and clear interfaces are visible between the layers. On the other hand, the cross-sectional image of the ZBC/MBC/ZBC paper (Fig. 5d) shows that the nanocomposite BC sheets are seamlessly joined, probably due to fibril–fibril bonding induced in the dried state. The difference between the cracked interfaces of the BC/MBC/BC paper and the seamless interfaces of ZBC/MBC/ZBC paper can possibly be explained as follows. It is well known that BC has a large number of labile –OH groups on its surface,[10] making it negatively charged. During the *in situ* synthesis process, either $CoFe_2O_4$ or ZnO NPs are thought to anchor to these –OH sites leading to the neutralization of the BC nanocomposite. The BC/MBC interface thus consists of one negatively charged BC sheet and another neutral MBC sheet, and hence cannot bond very well. On the other hand, the ZBC/MBC interface can be bonded better due to no charge difference.

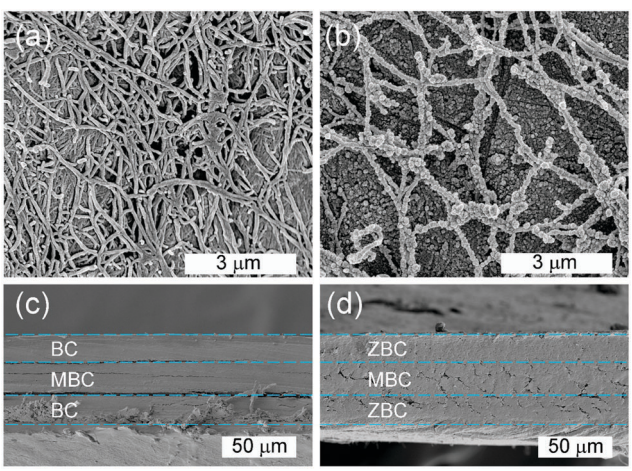

Fig. 5 Typical SEM images of the plan-view of (a) BC/BC and (b) MBC samples, and cross sections of (c) BC/MBC/BC and (d) ZBC/MBC/ZBC samples.

The mechanical properties of the BC papers are shown in Fig. 6. It is clear that both the tensile index and tearing index (Fig. 6a) of the BC/BC sample is the highest amongst the sample set. It is also very ductile and highly flexible (strain >20%, *cf.* Fig. 6b). This is due to the excellent mechanical properties of the pure BC membrane.[1,37] Fig. 6b shows the typical stress–strain curves of the BC-based papers. All curves exhibit typical non-linear stress–strain behavior. The MBC sample exhibited the lowest tensile and tearing indices. Incorporation of magnetic NPs in the BC structure generally deteriorates the BC network strength,[7,8,14,19] partly due to the modification of the BC functional groups,[8] but also due to the interruption of the inter-fibrillar bonding.[14] Furthermore, the MBC becomes very brittle with a very limited flexibility (strain <2%, *cf.* Fig. 6b). The mechanical properties of the sandwich-structure paper, BC/MBC/BC, were much enhanced compared to those of the MBC sample. This is understandable since in the sandwich structure, there are two sheets of pure BC which help to retain flexibilty. Introducing ZnO in the BC structure (ZBC/MBC/ZBC(1)) results in a decrease in the mechanical properties. Again, it is thought that the presence of ZnO NPs causes a reduction in inter-fibrillar bonding.[8,14] Using higher concentrations of ZnO NPs (ZBC/MBC/ZBC(2)) leads to a further reduction in mechanical properties. As mentioned previously, impregnation of ZnO improved the whiteness of the magnetic paper; the more concentrated the ZnO particles, the whiter the paper becomes, but at the cost of a reduction in mechanical properties.

Measurements of the magnetic properties of the BC based papers are presented in Fig. 7a. As expected, pristine BC does not exhibit ferromagnetic behavior. For other samples, magnetic hysteresis loops are observed. The inset to Fig. 7a shows the difference in the height and width of the loops. Therefore, we extracted the saturation magnetization (M_s), the magnetic remanence (M_r) and the coercvity (H_c) from the hysteresis loops, which are presented in Fig. 7b. The largest values of

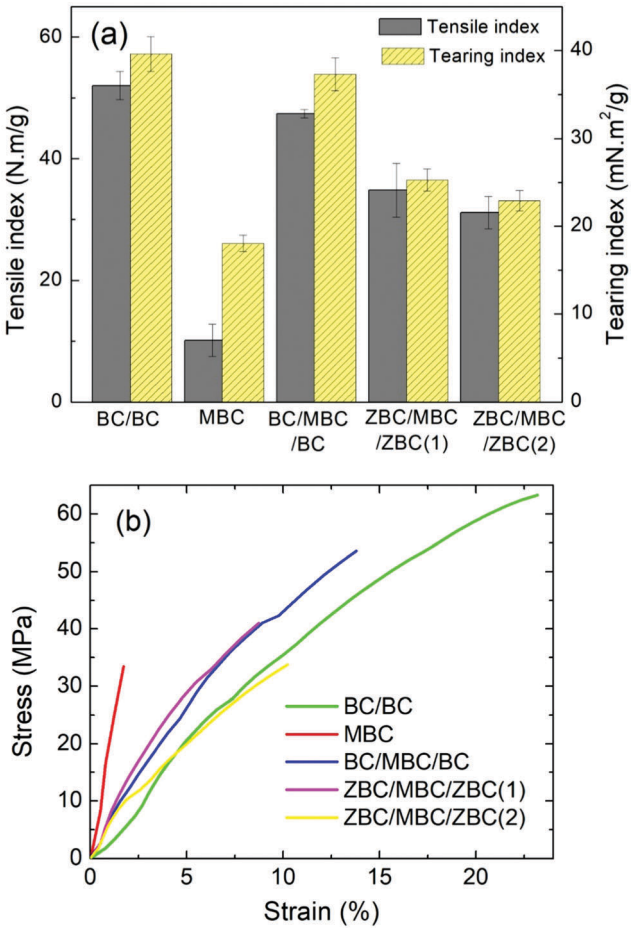

Fig. 6 (a) Tensile indices and tearing indices of the magnetic BC papers; (b) typical stress–strain curves for the samples.

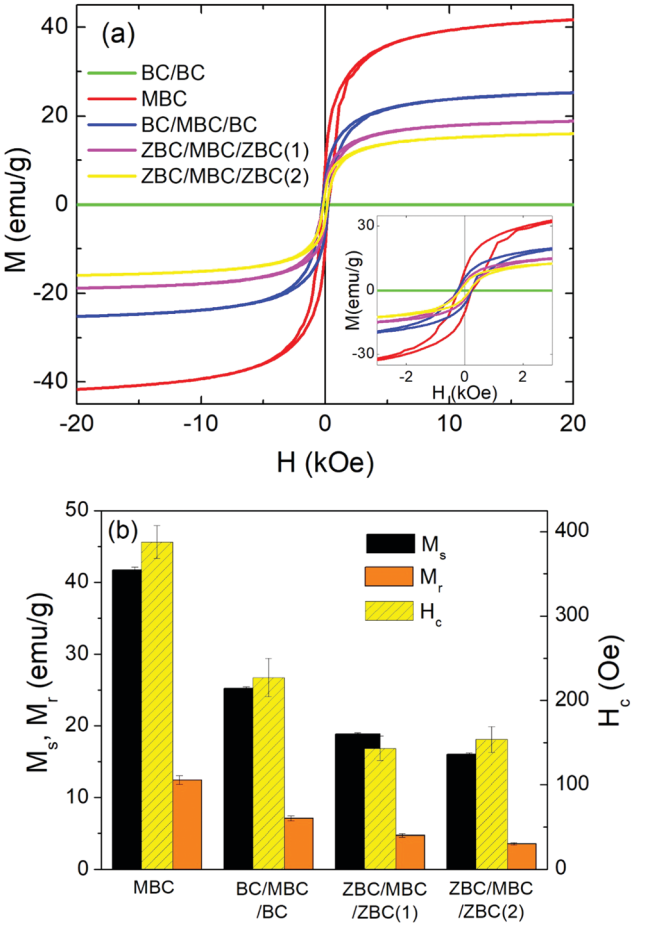

Fig. 7 (a) M–H curves of the synthesized samples, with a magnified view in the inset; (b) M_s, M_r and H_c parameters extracted from the M–H curves.

M_s, M_r and H_c belong to the MBC paper due to the highest portion of the magnetic NPs in these samples. These values are reduced in the BC/MBC/BC and ZBC/MBC/ZBC samples since the weight fraction of the magnetic cobalt ferrite was diluted with non-magnetic phases (BC and ZnO). Interestingly, the white magnetic paper (ZBC/MBC/ZBC(1)) in the present study shows a relatively large M_s value of $\sim$20 emu g^{-1}, comparable, if not higher than some literature values for the black magnetic BC membranes ($\sim$8–26 emu g^{-1}).[7,12,17,18,22] This shows that this sample has very favourable magnetic properties, and can be highly sensitive to an external magnetic field which could be exploited in several potential applications.

To demonstrate the magnetic responsive behavior of the white magnetic paper, the ZBC/MBC/ZBC(1) sample was tested with a permanent magnet. As shown in Fig. 8, it is easily bent towards or can be lifted by a magnet. The magnetic paper in our work is highly responsive to an external magnetic field similar to other reports[6,12,14,18,19,21,22] but most distinctly and importantly it retains its white appearance. Moreover, Fig. 9 illustrates the flexibility and foldability of the white magnetic paper. Fig. 9a shows that the fabricated paper in this work can be rolled just like normal paper. It can be also folded into an origami swan starting from the 3-cm-square sheet (Fig. 9b). As demonstrated in Fig. 9c and d, the origami swans made from our white magnetic paper are visually indistinguishable from the swans made from normal white paper, but can be identified by their magnetic properties. This experiment suggests a variety of applications for such white magnetic paper, for example, as security paper or in anti-counterfeiting applications.

Finally, a printing test was demonstrated using the fabricated white magnetic paper in this work as a substrate. As shown in Fig. 10, the image printed on the ZBC/MBC/ZBC(1) paper was almost indistinguishable from the same image printed on a standard A4 80 gsm paper. The printed white magnetic paper is however magnetic. This demonstrates the printability of the white magnetic papers in this work, while also maintaining their magnetic properties. These properties make them comparable to a one-sided white magnetic paper commercially available on the market (for example, the Quirkii® product). However, the commercial one-sided white magnetic paper is based on a bound system (embedded magnetic particles in a rubber sheet) adhesively attached to the sheet. Although it is very useful for printing or sticking notes on metallic surfaces, or for education, it is visually different to normal A4 paper. Our white magnetic paper,

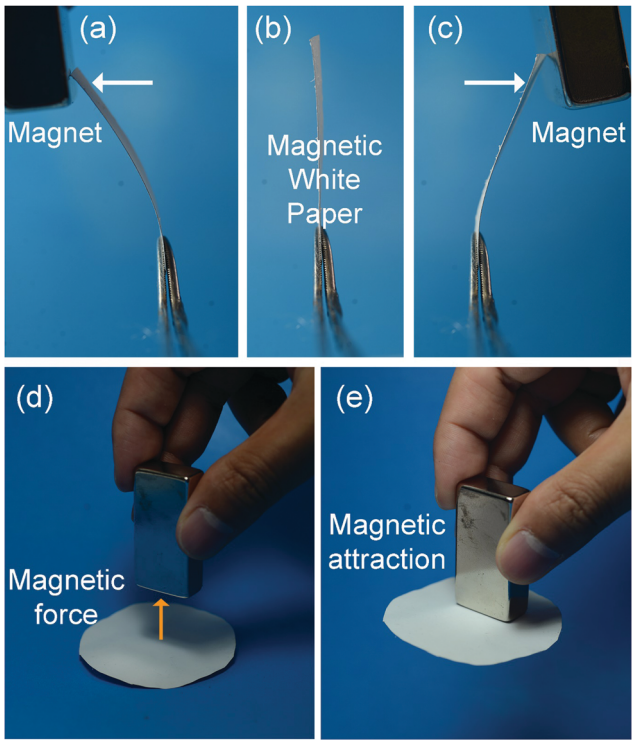

Fig. 8 Magnetic response of the white magnetic paper (ZBC/MBC/ZBC) to a permanent magnet: (a–c) bending towards the magnet, (d and e) magnetic lifting.

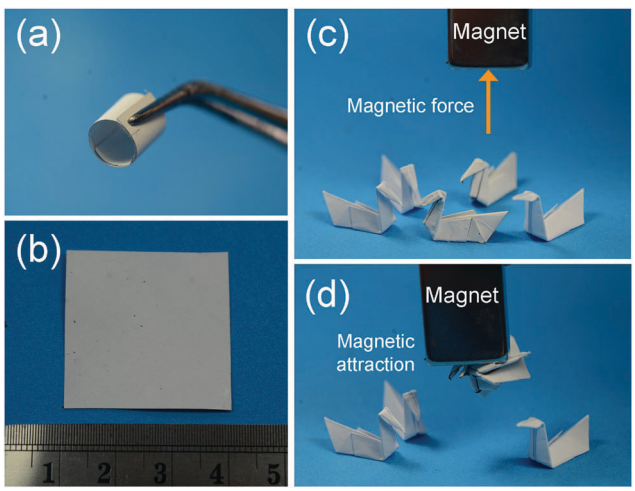

Fig. 9 (a) Demonstration of the flexibility of the white magnetic paper, and (b–d) foldability of the paper to form the white origami swan. The swan made from the BC magnetic paper looks just like those made from normal papers but can be separated by a magnet.

on the other hand, looks very similar to normal white paper, so that it can be used in many different applications. Moreover, the price of the commercial product is relatively high (~$4.8 per 1 A4 sheet). The cost for the fabricated sample in the present research is estimated to be less than $3 per A4 sheet, and this cost could be much lower when produced on an industrial scale.

Fig. 10 (upper) Demonstration of the printability of the white magnetic paper (right), compared to the same image printed on standard A4 80 gsm paper (left). (lower) The printed white magnetic paper can be lifted by a magnet.

Conclusions

White magnetic paper, based on a composite sandwich structure comprising a ZBC/MBC/ZBC sheet, has been fabricated using a nanocomposite approach and by hot-pressing. A white colour appearance was observed for these materials, just like normal paper, with a whiteness of 75–85% corresponding to high reflectance in the visible range. XRD analysis showed the formation of the ZnO and $CoFe_2O_4$ phases in the BC nanofibrillar network structure. SEM micrographs showed that there was a homogeneous distribution of $CoFe_2O_4$ NPs coated on the BC nanofibers' surfaces, and the seamless interfaces between ZBC and MBC layers. The mechanical properties were significantly reduced for the MBC single sheet but enhanced for the ZBC/MBC/ZBC composite papers. The white magnetic paper also exhibited flexibility, rollability and foldability, just like normal paper. Magnetic measurements showed a ferromagnetic property with a relatively large value of M_s (~20 emu g^{-1}). This value corresponded well with the magnetic responsive behavior of the fabricated paper to an external magnetic field. The combined characteristics of the white appearance, magnetic sensitivity and good mechanical properties make our newly proposed white magnetic paper potentially useful in a wide range of applications.

Conflicts of interest

There are no conflicts to declare.

Acknowledgements

This work was supported by the Thailand Research Fund (TRF) in cooperation with Khon Kaen University (RSA5980014), the Royal Society-Newton Advanced Fellowship (NA160147) in partnership with the Thailand Research Fund (TRF) (DBG6080002), and the Royal Golden Jubilee PhD Programme (PHD/0063/2558).

References

1 D. Klemm, B. Heublein, H. P. Fink and A. Bohn, Cellulose: Fascinating biopolymer and sustainable raw material, *Angew. Chem., Int. Ed.*, 2005, **44**(22), 3358–3393.
2 J. Shen, Z. Q. Song, X. R. Qian and Y. H. Ni, A Review on Use of Fillers in Cellulosic Paper for Functional Applications, *Ind. Eng. Chem. Res.*, 2011, **50**(2), 661–666.
3 C. H. Chia, S. Zakaria, K. L. Nguyen and M. Abdullah, Utilisation of unbleached kenaf fibers for the preparation of magnetic paper, *Ind. Crops Prod.*, 2008, **28**(3), 333–339.
4 D. Fragouli, I. S. Bayer, R. Di Corato, R. Brescia, G. Bertoni, C. Innocenti, D. Gatteschi, T. Pellegrino, R. Cingolani and A. Athanassiou, Superparamagnetic cellulose fiber networks via nanocomposite functionalization, *J. Mater. Chem.*, 2012, **22**(4), 1662–1666.
5 A. C. Small and J. H. Johnston, Novel hybrid materials of magnetic nanoparticles and cellulose fibers, *J. Colloid Interface Sci.*, 2009, **331**(1), 122–126.
6 H. S. Barud, A. Tercjak, J. Gutierrez, W. R. Viali, E. S. Nunes, S. J. L. Ribeiro, M. Jafellici, M. Nalin and R. F. C. Marques, Biocellulose-based flexible magnetic paper, *J. Appl. Physiol.*, 2015, **117**(17), 17B734.
7 G. H. Lim, J. Lee, N. Kwon, S. Bok, H. Sim, K. S. Moon, S. E. Lee and B. Lim, Fabrication of Flexible Magnetic Papers Based on Bacterial Cellulose and Barium Hexaferrite with Improved Mechanical Properties, *Electron. Mater. Lett.*, 2016, **12**(5), 574–579.
8 N. Sriplai, W. Mongkolthanaruk, S. J. Eichhorn and S. Pinitsoontorn, Magnetically responsive and flexible bacterial cellulose membranes, *Carbohydr. Polym.*, 2018, **192**, 251–262.
9 M. L. Foresti, A. Vazquez and B. Boury, Applications of bacterial cellulose as precursor of carbon and composites with metal oxide, metal sulfide and metal nanoparticles: A review of recent advances, *Carbohydr. Polym.*, 2017, **157**, 447–467.
10 W. L. Hu, S. Y. Chen, J. X. Yang, Z. Li and H. P. Wang, Functionalized bacterial cellulose derivatives and nanocomposites, *Carbohydr. Polym.*, 2014, **101**, 1043–1060.
11 N. Shah, M. Ul-Islam, W. A. Khattak and J. K. Park, Overview of bacterial cellulose composites: A multipurpose advanced material, *Carbohydr. Polym.*, 2013, **98**(2), 1585–1598.
12 C. Katepetch and R. Rujiravanit, Synthesis of magnetic nanoparticle into bacterial cellulose matrix by ammonia gas-enhancing *in situ* co-precipitation method, *Carbohydr. Polym.*, 2011, **86**(1), 162–170.
13 J. A. Marins, B. G. Soares, H. S. Barud and S. J. L. Ribeiro, Flexible magnetic membranes based on bacterial cellulose and its evaluation as electromagnetic interference shielding material, *Mater. Sci. Eng., C*, 2013, **33**(7), 3994–4001.
14 M. Mashkour, Z. Moradabadi and A. Khazaeian, Physical and tensile properties of epoxy laminated magnetic bacterial cellulose nanocomposite films, *J. Appl. Polym. Sci.*, 2017, **134**(30), 45118.
15 S. Menchaca-Nal, C. L. Londono-Calderon, P. Cerrutti, M. L. Foresti, L. Pampillo, V. Bilovol, R. Candal and R. Martinez-Garcia, Facile synthesis of cobalt ferrite nanotubes using bacterial nanocellulose as template, *Carbohydr. Polym.*, 2016, **137**, 726–731.
16 M. Sureshkumar, D. Y. Siswanto and C. K. Lee, Magnetic antimicrobial nanocomposite based on bacterial cellulose and silver nanoparticles, *J. Mater. Chem.*, 2010, **20**(33), 6948–6955.
17 V. Thiruvengadam and S. Vitta, Bacterial cellulose based flexible multifunctional nanocomposite sheets, *Cellulose*, 2017, **24**(8), 3341–3351.
18 W. Zhang, S. Y. Chen, W. L. Hu, B. H. Zhou, Z. H. Yang, N. Yin and H. P. Wang, Facile fabrication of flexible magnetic nanohybrid membrane with amphiphobic surface based on bacterial cellulose, *Carbohydr. Polym.*, 2011, **86**(4), 1760–1767.
19 Y. Zheng, J. X. Yang, W. L. Zheng, X. Wang, C. Xiang, L. Tang, W. Zhang, S. Y. Chen and H. P. Wang, Synthesis of flexible magnetic nanohybrid based on bacterial cellulose under ultrasonic irradiation, *Mater. Sci. Eng., C*, 2013, **33**(4), 2407–2412.
20 M. Park, J. Cheng, J. Choi, J. Kim and J. Hyun, Electromagnetic nanocomposite of bacterial cellulose using magnetite nanoclusters and polyaniline, *Colloids Surf., B*, 2013, **102**, 238–242.
21 R. T. Olsson, M. A. S. A. Samir, G. Salazar-Alvarez, L. Belova, V. Strom, L. A. Berglund, O. Ikkala, J. Nogues and U. W. Gedde, Making flexible magnetic aerogels and stiff magnetic nanopaper using cellulose nanofibrils as templates, *Nat. Nanotechnol.*, 2010, **5**(8), 584–588.
22 V. Thiruvengadam and S. Vitta, Flexible bacterial cellulose/permalloy nanocomposite xerogel sheets – Size scalable magnetic actuator-cum-electrical conductor, *AIP Adv.*, 2017, **7**(3), 035107.
23 G. C. Hu, S. Y. Fu, F. Q. Chu and M. H. Lin, Relationship between Paper Whiteness and Color Reproduction in Inkjet Printing, *BioResources*, 2017, **12**(3), 4854–4866.
24 M. A. Hubbe, J. J. Pawlak and A. A. Koukoulas, Paper's Appearance: A Review, *BioResources*, 2008, **3**(2), 627–665.
25 D. N. Gao, J. Z. Ma, Z. J. Li and J. L. Liu, Preparation and characterization of a new white magnetic paper, *Mater. Lett.*, 2014, **137**, 487–490.
26 Z. X. Mo, H. W. Guo, Y. F. Wang, H. R. Yin, C. Yang and J. B. Song, Surface modification of graphene oxide sheets on magnetic particles for magnetic paper, *J. Alloys Compd.*, 2017, **695**, 2525–2531.
27 C. Pacurariu, E. A. Taculescu, R. Ianos, O. Marinica, C. V. Mihali and V. Socoliuc, Synthesis and characterization of gamma-Fe_2O_3/SiO_2 composites as possible candidates for magnetic paper manufacture, *Ceram. Int.*, 2015, **41**(1), 1079–1085.
28 M. L. Zeng, A. Laromaine, W. Q. Feng, P. A. Levkin and A. Roig, Origami magnetic cellulose: controlled magnetic fraction and patterning of flexible bacterial cellulose, *J. Mater. Chem. C*, 2014, **2**(31), 6312–6318.

29 E. Girgis, M. M. S. Wahsh, A. G. M. Othman, L. Bandhu and K. V. Rao, Synthesis, magnetic and optical properties of core/shell $Co_{1-x}Zn_xFe_2O_4/SiO_2$ nanoparticles, *Nanoscale Res. Lett.*, 2011, **6**, 460.
30 N. Kiomarsipour, R. S. Razavi, K. Ghani and M. Kioumarsipour, Evaluation of shape and size effects on optical properties of ZnO pigment, *Appl. Surf. Sci.*, 2013, **270**, 33–38.
31 R. Zamiri, A. Rebelo, G. Zamiri, A. Adnani, A. Kuashal, M. S. Belsley and J. M. F. Ferreira, Far-infrared optical constants of ZnO and ZnO/Ag nanostructures, *RSC Adv.*, 2014, **4**(40), 20902–20908.
32 C. Wang, X. M. Wang, B. Q. Xu, J. C. Zhao, B. X. Mai, P. Peng, G. Y. Sheng and H. M. Fu, Enhanced photocatalytic performance of nanosized coupled ZnO/SnO_2 photocatalysts for methyl orange degradation, *J. Photochem. Photobiol., A*, 2004, **168**(1–2), 47–52.
33 E. G. Goh, X. Xu and P. G. McCormick, Effect of particle size on the UV absorbance of zinc oxide nanoparticles, *Scr. Mater.*, 2014, **78–79**, 49–52.
34 W. Czaja, D. Romanovicz and R. M. Brown, Structural investigations of microbial cellulose produced in stationary and agitated culture, *Cellulose*, 2004, **11**(3–4), 403–411.
35 A. Khalid, R. Khan, M. Ul-Islam, T. Khan and F. Wahid, Bacterial cellulose-zinc oxide nanocomposites as a novel dressing system for burn wounds, *Carbohydr. Polym.*, 2017, **164**, 214–221.
36 F. S. Jebel and H. Almasi, Morphological, physical, antimicrobial and release properties of ZnO nanoparticles-loaded bacterial cellulose films, *Carbohydr. Polym.*, 2016, **149**, 8–19.
37 J. M. Rajwade, K. M. Paknikar and J. V. Kumbhar, Applications of bacterial cellulose and its composites in biomedicine, *Appl. Microbiol. Biotechnol.*, 2015, **99**(6), 2491–2511.

Results in Physics 8 (2018) 1245–1249

Contents lists available at ScienceDirect

Results in Physics

journal homepage: www.journals.elsevier.com/results-in-physics

Investigation of the spin Seebeck effect and anomalous Nernst effect in a bulk carbon material

Poramed Wongjom [a,b], Supree Pinitsoontorn [a,b,*]

[a] Integrated Nanotechnology Research Center, Department of Physics, Faculty of Science, Khon Kaen University, Khon Kaen 40002, Thailand
[b] Nanotec-KKU Center of Excellence on Advanced Nanomaterials for Energy Production and Storage, Khon Kaen University, Khon Kaen 40002, Thailand

ARTICLE INFO

Article history:
Received 7 November 2017
Received in revised form 6 February 2018
Accepted 8 February 2018
Available online 14 February 2018

Keywords:
Spin Seebeck effect
Anomalous Nernst effect
Inverse spin Hall effect
Bulk carbon

ABSTRACT

Since the discovery of the spin Seebeck effect (SSE) in 2008, it has become one of the most active topics in the spin caloritronics research field. It opened up a new way to create the spin current by a combination of magnetic fields and heat. The SSE was observed in many kinds of materials including metallic, semiconductor, or insulating magnets, as well as non-magnetic materials. On the other hand, carbon-based materials have become one of the most exciting research areas recently due to its low cost, abundance and some exceptional functionalities. In this work, we have investigated the possibility of the SSE in bulk carbon materials for the first time. Thin platinum film (Pt), coated on the smoothened surface of the bulk carbon, was used as the spin detector via the inverse spin Hall effect (ISHE). The experiment for observing longitudinal SSE in the bulk carbon was set up by applying a magnetic field up to 30 kOe to the sample with the direction perpendicular to the applied temperature gradient. The induced voltage from the SSE was extracted. However, for conductive materials, e.g. carbon, the voltage signal under this set up could be a combination of the SSE and the anomalous Nernst effect (ANE). Therefore, two measurement configurations were carried out, i.e. the in-plane magnetization (IM), and the perpendicular-to-plane magnetization (PM). For the IM configuration, the SSE + ANE signals were detected where as the only ANE signal existed in the PM configuration. The results showed that there were the differences between the voltage signals from the IM and PM configurations implying the possibility of the SSE in the bulk carbon material. Moreover, it was found that the difference in the IM and PM signals was a function of the magnetic field strength, temperature difference, and measurement temperature. Although the magnitude of the possible SSE voltage in this experiment was rather low (less than 0.5 μV at 50 K), this research showed that potential of using low cost and abundant bulk carbon as spin current supplier or thermoelectric power generators.

Introduction

At present, thermal energy wastes from many sources are lost to environment. Thermoelectric technology which can directly convert heat to electricity can solve this problem. This technology employs the concept of the Seebeck effect which involves the interaction between charge and heat creating a voltage difference at a junction of two different metals [1–3]. On the other hand, the interaction between electron spin and heat creates a spin induced voltage where the spin voltage refers to the potentials which drive spin current, i.e., a flow of electron spin-angular momentum into an attached conductor [4–6]. The effect is known as "spin Seebeck effect (SSE)" firstly observed by K. Uchida in 2008 [5]. After its discovery, it has become one of the most active topics in the spin caloritronics research field. It opened up a new way to create the spin current by a combination of magnetic fields and heat. This effect can be observed via the inverse spin Hall effect (ISHE) [7–11] which can convert spin voltage to charge voltage.

The SSE was observed in many magnetic materials ranging from metals, semiconductors, or even insulators. The physical theories behind the SSE involve magnon and phonon drag mechanisms [12]. Moreover, the SSE was studied on many spin injector materials such as garnet ferrite, spinel ferrite, hexagonal ferrite, etc. [13]. On the other hand, carbon-based materials, which are currently one of the most exciting research areas due to its low cost, abundance and some exceptional functionality, have never been investigated for the SSE aspect. Therefore, in this work, the investigation

* Corresponding author at: Integrated Nanotechnology Research Center, Department of Physics, Faculty of Science, Khon Kaen University, Khon Kaen 40002, Thailand.
E-mail address: psupree@kku.ac.th (S. Pinitsoontorn).

https://doi.org/10.1016/j.rinp.2018.02.022
2211-3797/

of the possibility of the SSE in bulk carbon materials was carried out for the first time.

Materials and methods

The bulk carbon (C) disc with a density of 1.75 g/cm^3 was cut into a rectangular shape with the size of $2 \times 2 \times 6$ mm^3. To obtain the smooth surface, the sample was finely polished with 0.05 μm alumina powders. The surface roughness of the sample was investigated by scanning electron microscopy (SEM, FEI Helios). The cleaned samples were coated with a 10 nm thick platinum film using the SC 701H Quick Coater. The magnetic characteristics of the bulk carbon before and after Pt coating was investigated by using a vibrating sample magnetometer (VSM, Quantum Design VersaLab) with a maximum magnetic field of 30 kOe. The crystal structure of the bulk carbon was studied by X-ray diffraction (XRD) technique (PANalytical Emperean).

To observe the SSE, the measurement was set up as shown in Fig. 1(a), known as the in-plane magnetization (IM) configuration. The temperature gradient (∇T) in the z direction induces a spin current (J_s) flowing through an interface between the bulk carbon and Pt. According to ISHE, J_s in the sample is converted into the electric field (E_{ISHE}) by the spin orbit coupling between J_s and polarization vector (σ), parallel to **M**, as described in Eq. (1).

$$E_{ISHE} = \theta_{SH} \rho \cdot J_s \times \sigma \quad (1)$$

where θ_{SH}, ρ, J_s and σ are spin Hall angle, electrical resistivity of spin detector, spin current and spin polarization vector, respectively.

However, for the IM configuration, not only the SSE signal was created but the signal due to anomalous Nernst effect (ANE) was also occured in a conductive sample. To separate SSE from ANE, the measurement using the perpendicular magnetization (PM) configuration was carried out [14] (Fig. 1(b)). In the PM configuration, the sample was sandwiched between the heat source and drain. The temperature gradient was applied parallel to the surface of the Pt film (z), and the magnetic field was applied perpendicularly. The ANE signal was obtained from Eq. (2).

$$E_{ANE} = S_{ANE} \cdot \nabla T \times M \quad (2)$$

where E_{ANE}, S_{ANE}, ∇T and M are electric field of ANE, anomalouse Nersnt coefficient, temperature gradient and magnetic moment, respectively.

The SSE and ANE signals in the bulk carbon were measured using the IM and PM configurations as shown in Fig. 1. Three samples were investigated and yielded similar results. In every sample, the same sample was performed for the IM and PM configuration. To measure the voltage, very fine gold wire (diameter of 0.025 mm) was used and bonded on Pt film by silver paste. The contact spot size was less than 0.1 mm. For the voltage measurement, the voltages were read out by using a nanovoltmeter (Keithley 2182A). The system temperature was controlled by loading the samples in the vacuum chamber of the VersaLab instrument (Quantum Design). The base temperature and the magnetic field were controlled by the Versalab. The temperature gradient was generated by passing a current (using Keithley 2400 Source Meter) to a resistive heater embedded in a Cu blocks on the hot side. The temperature gradient was monitored by using the K-type thermocouples attached to the Cu blocks on both hot and cold sides. To avoid electrical short circuit, the sample was sandwiched between two AlN plate insulators but with large thermal conductivity. The magnetic field was varied the in range of 30 kOe. The temperature gradients were between 0 and 12 K. The measurement temperature was from 50 to 300 K.

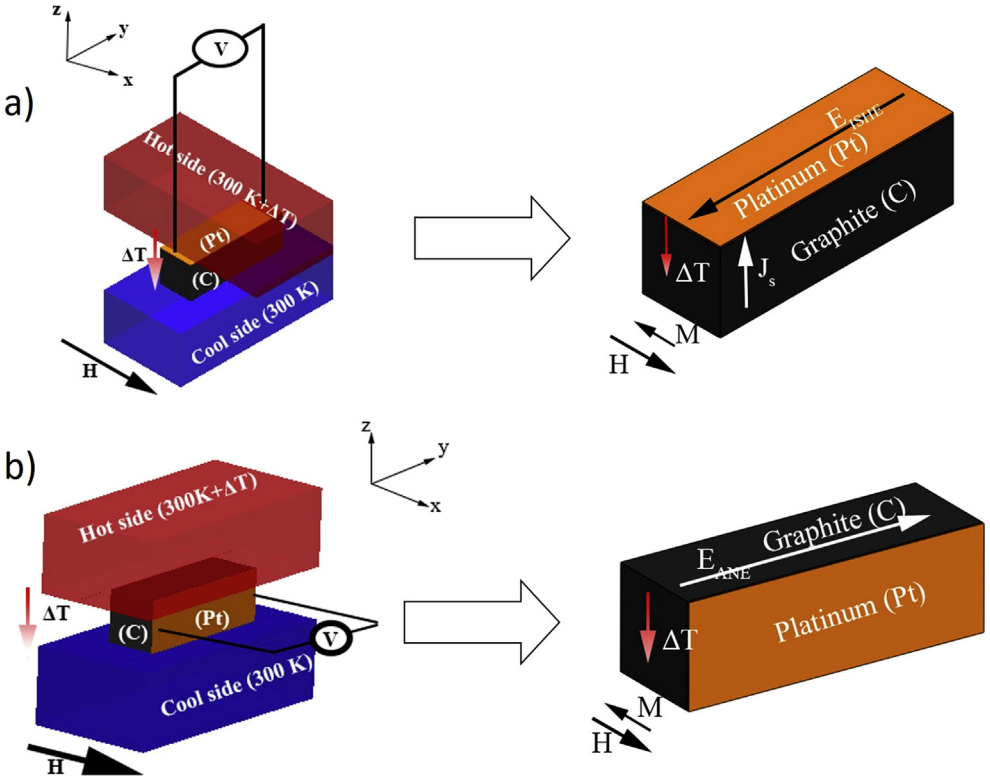

Fig. 1. a) In-plane magnetization (IM) configuration for SSE measurement, the temperature gradient was perpendicular to the magnetic field and the Pt detector surface. b) Perpendicular magnetization (PM) configuration for SSE measurement, the magnetic field was applied perpendicular to the temperature gradient but parallel to the Pt film.

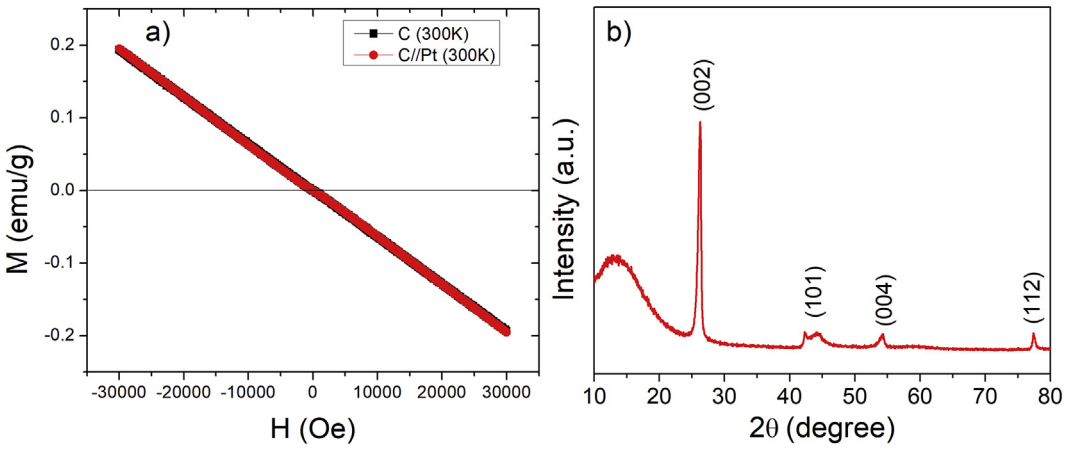

Fig. 2. a) M–H curve of the bulk carbon with Pt coating, b) XRD pattern of the bulk carbon.

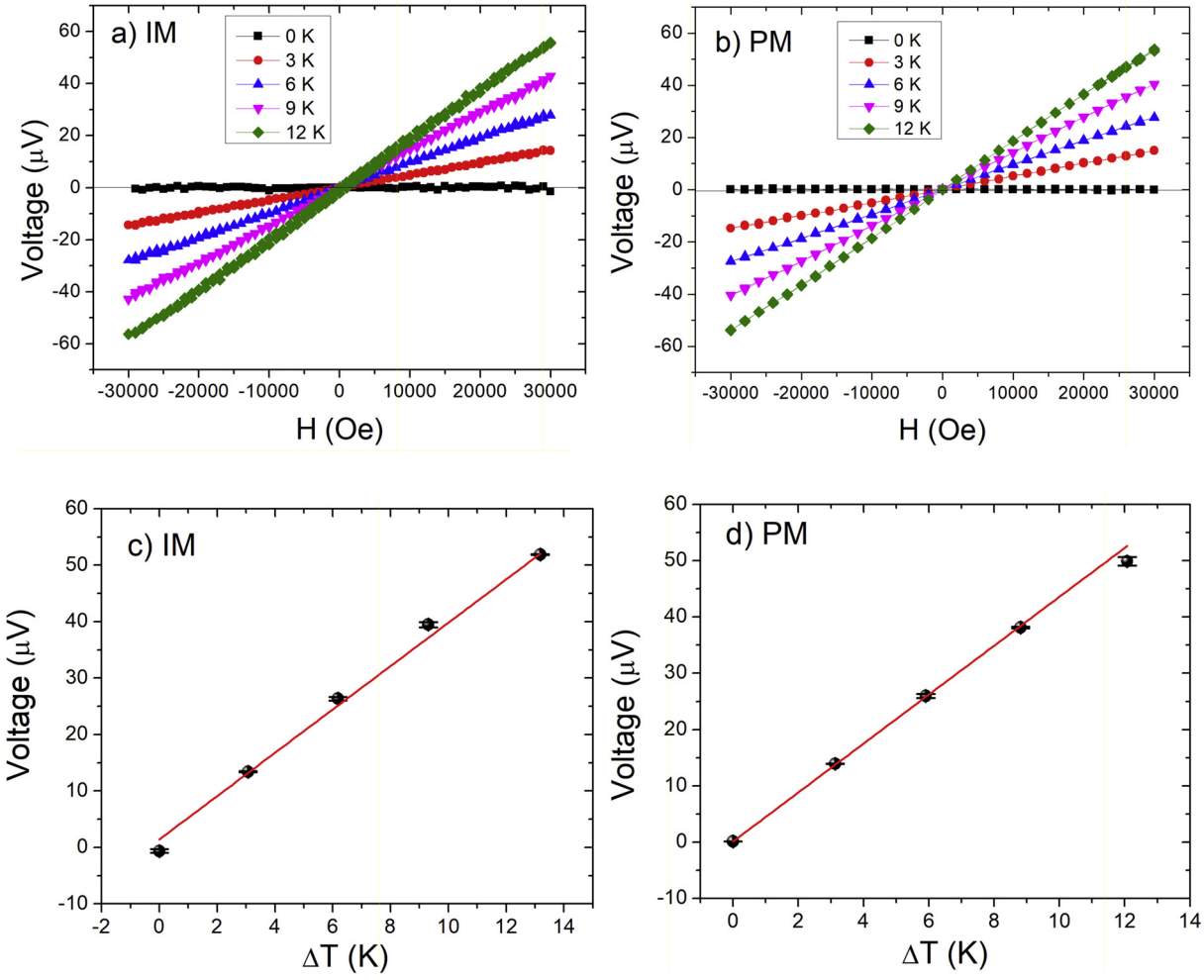

Fig. 3. The measured voltage at 300 K versus magnetic field as a function of temperature gradient for a) IM configuration (SSE + ANE), and b) PM configuration (ANE). Linear temperature gradient dependence of the measured signal for c) IM configuration and d) PM configuration.

Results and discussion

The magnetic properties of the bulk carbon with and without Pt film are shown in Fig. 2(a). It was found that there is no difference between the Pt coated and non-Pt coated sample. The diamagnetic characteristic is observed with the magnetic moment of −0.18 emu/g at +30 kOe. The XRD pattern of the bulk carbon is shown in Fig. 2(b). The main peaks are located at at 26.28°, 44.36°, 53.97° and 77.46° which are corresponded to the hexagonal structure of the graphite carbon according to the JCPDS 01-075-1621 reference.

Fig. 3 shows the relationship between the magnetic field and the voltage measurement of the C//Pt samples at 300 K. Moreover, the dependence of temperature difference (0–12 K) on the

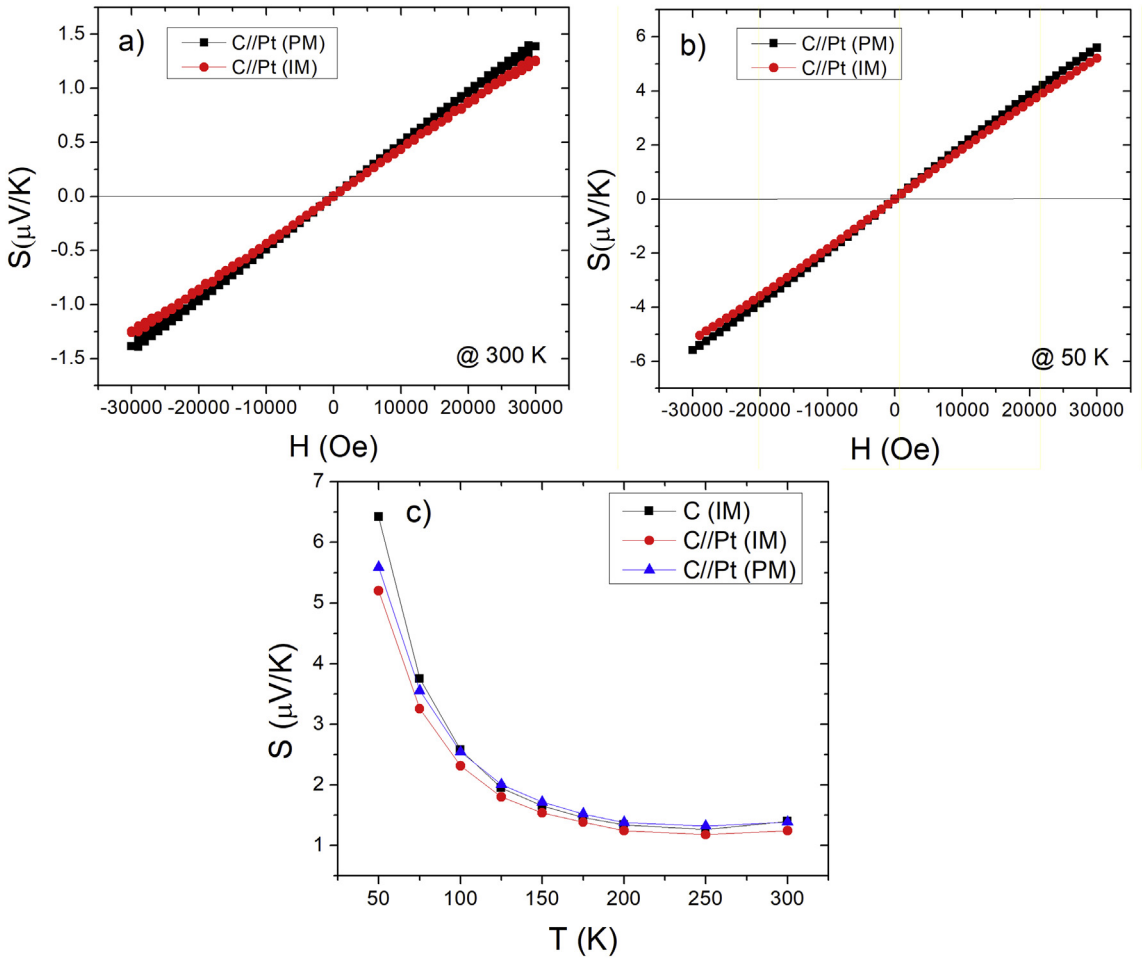

Fig. 4. The signal from the Pt coated bulk carbon measured in IM and PM configurations with ΔT = 12 K at a) 300 K and b) 50 K. c) The ANE and the combination of ANE and SSE of the C, C//Pt (PM) and C//Pt (IM) systems as a function of temperature at H = 30,000 Oe and ΔT = 12 K.

measured voltage was also presented. The measurements from the IM and PM configuration are shown in Fig. 3(a) and Fig. 3(b), respectively. The graphs show the linearly increased signals when the magnetic field increased. However, the mixing of SSE and ANE effect are shown only in Fig. 3(a). but the ANE effect only is illustrated in Fig. 3(b). Furthermore, as the temperature gradient was increased, the measured voltages were also increased for both IM and PM measurement, as summarized in Fig. 3(c) and (d). The linear relationship between the temperature difference and the measured voltage was found. The slopes between the voltage and temperature are directly relates to spin Seebeck coefficient which were estimated to be around 4.5 μV/K.

The SSE and ANE signals in the bulk carbon was measured by varying magnetic field and measurement temperature, using the IM and PM configuration as explained in the previous section. The temperature gradient was fixed at the maximum value of 12 K. The results are presented in Fig. 4. Fig. 4(a) shows the difference of the signal at room temperature between the measurements using PM and IM configurations. The PM configuration represents only the ANE signal but the IM configuration shows the combination of ANE and SSE signals. The spin Seebeck coefficient of the PM configuration was larger than that of the IM configuration about 0.142 μV/K at 30 kOe. The differences between the voltage signals from the IM and PM configurations implying the possibility of the SSE in the bulk carbon material.

Fig. 4(b) shows the same measurement as in Fig. 4(a) but measuring at the temperature of 50 K. It is clearly seen that the ANE and SSE signals were enhanced from about 1–1.5 μV/K at 300 K to about 5–6 μV/K at 50 K. The dependence of measurement temperature on the ANE and SSE signals are presented in Fig. 4(c) for the C, C//Pt (PM) and C//Pt (IM) systems. The graphs show the enhancement in the signal when the temperature was decreased from room temperature to 50 K. The spin Seebeck coefficient was dramatically enhanced at the temperature less than 125 K which correspond with phonon drag mechanism [12]. The signal from the PM configuration was still higher than that of the IM configuration about 0.39 μV/K at 50 K which meaned that the ANE signal was higher than the combination of ANE and SSE signal. It should be noted that the voltage signal wtihout Pt coating on the bulk carbon was slightly larger than with Pt coating. This is probably due to a difference in electron spin channel [15] and/or an effect between interface of C and Pt [16].

Conclusion

The SSE of the Pt coated bulk carbon was studied. The combination of the SSE and ANE signals was recorded. The signal voltage from the combined SSE + ANE contribution was lower than the signal from the ANE contribution alone. The reduced voltage was possibly due to the contribution of ISHE and/or interface interaction. This combination of SSE and ANE was also enhanced at the temperature less than 125 K which corresponded to phonon drag mechanism. The voltage from the possible SSE in this research was relatively low (less than 0.5 μV at 50 K). However, it is the first

study that shows the potential uses of low cost and abundant bulk carbon as spin current supplier for spintronic applications.

Acknowledgements

This work is supported by the Thailand Research Fund (TRF) in cooperation with Khon Kaen University (RSA5980014), and the Nanotechnology Center (NANOTEC), NSTDA, Ministry of Science and Technology, Thailand, through its program of Center of Excellence Network.

References

[1] Geballe T, Hull G. Seebeck effect in germanium. Phys Rev 1954;94:1134.
[2] S. Maekawa T. Tohyama S.E. Barnes S. Ishihara W. Koshibae G. Khaliullin Physics of transition metal oxides Springer Science & Business Media 2013
[3] Jimenez-Cavero P, Lucas I, Anadon A, Ramos R, Niizeki T, Aguirre MH, et al. Spin Seebeck effect in insulating epitaxial gamma-Fe_2O_3 thin films. Appl Mater 2017;5:2.
[4] Uchida K, Ota T, Adachi H, Xiao J, Nonaka T, Kajiwara Y, et al. Thermal spin pumping and magnon-phonon-mediated spin-Seebeck effect. J Appl Phys 2012;111:10.
[5] Uchida K, Takahashi S, Harii K, Ieda J, Koshibae W, Ando K, et al. Observation of the spin Seebeck effect. Nature 2008;455:778–81.
[6] Kikkawa T, Uchida K, Shiomi Y, Qiu Z, Hou D, Tian D, et al. Longitudinal spin seebeck effect free from the proximity nernst effect. Phys Rev Lett 2013;110:6.
[7] Uchida K, Ota T, Harii K, Ando K, Sasage K, Nakayama H, et al. Spin seebeck effect in $Ni_{81}Fe_{19}$/Pt thin films With different widths. IEEE T Magn 2009;45:2386–8.
[8] Ramos R, Kikkawa T, Uchida K, Adachi H, Lucas I, Aguirre MH, et al. Observation of the spin seebeck effect in epitaxial Fe_3O_4 thin films. Appl Phys Lett 2013;102:7.
[9] Niizeki T, Kikkawa T, Uchida K, Oka M, Suzuki KZ, Yanagihara H, et al. Observation of longitudinal spin-Seebeck effect in cobalt-ferrite epitaxial thin films. Aip Adv 2015;5:5.
[10] Qu D, Huang SY, Hu J, Wu RQ, Chien CL. Intrinsic Spin Seebeck Effect in Au/YIG. Phys Rev Lett 2013;110:6.
[11] Bauer GE, Saitoh E, Van Wees BJ. Spin caloritronics. Nat Mater 2012;11:391–9.
[12] Adachi H, Uchida K, Saitoh E, Ohe J, Takahashi S, Maekawa S. Gigantic enhancement of spin Seebeck effect by phonon drag. Appl Phys Lett 2010;97:25.
[13] Uchida K, Ishida M, Kikkawa T, Kirihara A, Murakami T, Saitoh E. Longitudinal spin seebeck effect: from fundamentals to application. J Phys-Condens Mat 2014;26:34.
[14] Kikkawa T, Uchida K, Daimon S, Shiomi Y, Adachi H, Qiu Z, et al. Separation of longitudinal spin Seebeck effect from anomalous Nernst effect: determination of origin of transverse thermoelectric voltage in metal/insulator junctions. Phys Rev B 2013;88:21.
[15] Sinova J, Valenzuela SO, Wunderlich J, Back C, Jungwirth T. Spin hall effects. Rev Mod Phys 2015;87:1213.
[16] Zhou L, Grigoryan VL, Maekawa S, Wang X, Xiao J. Spin Hall effect by surface roughness. Phys Rev B 2015;91:045407.

Phys. Status Solidi A **214**, No. 10, 1700235 (2017) / **DOI** 10.1002/pssa.201700235

physica status solidi a
www.pss-a.com
applications and materials science

The effect of YSi_2 nanoinclusion on the thermoelectric properties of p-type SiGe alloy

Suphagrid Wongprakarn[1], Supree Pinitsoontorn[*,2,3], Sora-at Tanusilp[4], and Ken Kurosaki[4,5]

[1] Materials Science and Nanotechnology Program, Faculty of Science, Khon Kaen University, Khon Kaen 40002, Thailand
[2] Integrated Nanotechnology Research Center, Department of Physics, Faculty of Science, Khon Kaen University, Khon Kaen 40002, Thailand
[3] Nanotec-KKU Center of Excellence on Advanced Nanomaterials for Energy Production and Storage, Khon Kaen University, Khon Kaen 40002, Thailand
[4] Graduate School of Engineering, Osaka University, 2-1 Yamadaoka, Suita, Osaka 565-0871, Japan
[5] JST, PRESTO, 4-1-8 Honcho, Kawaguchi, Saitama 332-0012, Japan

Received 18 April 2017, revised 23 June 2017, accepted 26 June 2017
Published online 20 July 2017

Keywords melt spinning, SiGe, thermoelectric, YSi_2

[*] Corresponding author: email psupree@kk.ac.th, Phone: +66 87 373 11 22, Fax: +66 43 203 359

In this research, the p-type $Si_{80}Ge_{20}B_3$ alloys composited with YSi_2 nanoinclusions were fabricated by melting spinning and then, spark plasma sintering. The metallic Y was chosen as the source of YSi_2 nanoparticles. It was found that the fully dense nanocomposites were formed with the homogeneous distribution of YSi_2 nanoinclusions in the SiGe matrix. The thermoelectric measurement showed that YSi_2 addition reduces the electrical conductivity but increases the Seebeck coefficient, which was attributed to the decrease in carrier concentration. The thermal conductivity was suppressed for the composite SiGe-1.4%Y, which made this composition to exhibit the largest thermoelectric figure-of-merit (ZT) of 0.52.

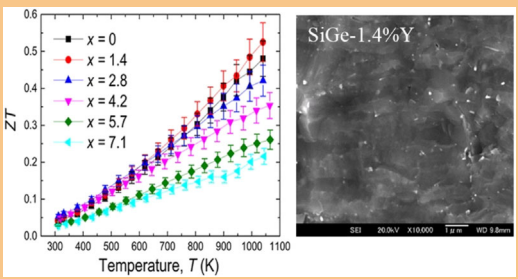

Figure-of-merit (ZT) and microstructure of the SiGe-*x*%Y SiGe-1.4%Y.

1 Introduction Thermoelectric (TE) materials can directly convert waste heat into electrical energy [1, 2]. The TE efficiency depends on the dimensionless figure-of-merit (ZT), defined as $ZT = (S^2\sigma/\kappa)T$, where S, σ, κ, and T are Seebeck coefficient, electrical conductivity, total thermal conductivity, and absolute temperature, respectively.

Materials with the maximized ZT in the working temperature ranges are good TE materials. At present the best of TE materials are bismuth telluride (Bi_2Te_3) and lead telluride (PbTe) for around room temperature (300–450 K) and midrange temperature (600−800 K) applications, receptively [1, 2]. For high temperature range, Si-based materials have been the best choice for several decades. In particular, the $Si_{80}Ge_{20}$ compound has been used in radioisotope TE generators (RTGs), with the ZT values of ∼0.5 (p-type) and ∼0.9 (n-type) at 1100 K, by NASA since 1976 [3].

In the last decade, the enhanced ZT values of SiGe alloys have been reported continuously exploiting a nanostructuring approach [4–10]. The idea of this approach is to reduce grain sizes of SiGe to a few ten nanometers. The SiGe nano-grains can scatter phonon effectively but show a minimum effect on the electrical transport since the phonon mean free path (MFP) is larger than charge carrier MFP. The ZT values were demonstrated to be as large as 1.84 [4] and 1.2 [5] for n- and p-type SiGe alloys, respectively.

Another approach for enhancing ZT of SiGe was by using nanocomposites. Nanoinclusions which were homogeneously distributed in SiGe matrix grains acted as phonon scattering sites whereas charge carrier transport was carried out through matrix grains. Among several types of nanoinclusions, silicides were very attractive. Theoretical calculations showed that silicide nanoparticles could suppress lattice thermal conductivity (κ_l) effectively and enhanced ZT by several folds [11]. Experimentally, a number TE studies of silicide nanoparticles in SiGe or Si matrix have been demonstrated, for example, $FeSi_2$ [12–14], $MgSi_2$ [12], WSi_2 [15–17], $CrSi_2$ [18, 19], $MoSi_2$ [20, 21], $NiSi_2$ [22, 23], and VSi_2 [24, 25]. However, some experiments showed that even though the thermal conductivity were decreased, the ZT of such systems were not enhanced [13, 14, 19, 21], which was due to the changes in S and σ when silicide nanoinclusions were introduced. On the other hand, incorporating silicides in SiGe could lead to increasing κ if the nanosize of the silicides were not maintained [15].

Recently, Ahmad et al. demonstrated the recorded value of ZT ~1.81 for the p-type SiGe alloys by incorporating YSi_2 nanoparticles in $Si_{80}Ge_{20}$ matrix [26]. With the optimized amount of YSi_2, κ was significantly reduced while the power factor was not affected which was attributed to the coherent interfaces between YSi_2 nanoparticles and SiGe grains. This work has shown that YSi_2 (not included in the calculation in Ref. [11]) may be the right choice of silicide nanoparticles in SiGe matrix. Interestingly, though obtaining the recorded ZT, this work has used Y_2O_3 as a source of Y. YiS_2 was produced through the reaction of Y_2O_3 and Si [27]. However, this might also produce SiO_2 by-products which should generally be avoided [28–30].

In this work, we attempted to improve ZT of the p-type SiGe by incorporating YSi_2 nanoinclusions but using metallic Y as starting materials to avoid the formation of oxides. Moreover, a melt spinning (MS) technique was employed for preparing the nanocomposite phases to minimize possibility of oxidation and contamination from a conventional ball milling method. The bulk nanocomposites were prepared by spark plasma sintering (SPS). The effect of YSi_2 nanoinclusions on the thermoelectric properties was studied and discussed.

2 Experimental P-type SiGe ingots with a nominal composition of $Si_{80}Ge_{20}B_3$ were prepared by arc melting under an Ar atmosphere, using high purity Si (11N), Ge (3N), and B (99.9%). The ingots were crushed and Y chips (99.9%) were added with the composition of SiGe-x wt.%Y ($x = 0$, 1.4, 2.8, 4.2, 5.7, and 7.1), before subjected to a melt spinning (MS) process for producing nanocrystalline composite ribbons. In this process, the mixtures were melted by induction coil under an Ar atmosphere. The molten liquid was ejected through a boron nitride nozzle using 0.02 MPa Ar gas onto a Cu roller with a rotating speed of 2000 rpm. The MS ribbon samples were crushed to fine powder and loaded into a high strength graphite die for fabricating bulk samples by using a spark plasma sintering (SPS) technique. The SPS was carried out at 1293 K in an Ar atmosphere under a uniaxial pressure of 100 MPa.

Characteristics, phase, and morphology of the samples (MS and SPS) were observed by using X-ray diffraction (XRD, Rigaku, Ultima IV) and a field emission scanning electron microscope (FE-SEM, JEOL, JSM-6500F). The chemical composition was investigated by using energy dispersive X-ray spectrometer (EDS) equipped in the FE-SEM. The bulk samples were polished and cut for thermoelectric and Hall measurements. The carrier concentration and mobility were measured at room temperature (RT) by using a Hall measurement system (Toyo, ResiTest 8300). Seebeck coefficient and electrical conductivity were measured from RT to 1073 K by using a commercial system (Ulvac-Riko, ZEM-3). Thermal conductivity was calculated from $\kappa = DC_pd$, where C_p is the heat capacity which was taken from the literature value [3], d is the bulk density, and D is the thermal diffusivity, measured from RT to 1073 K by using a laser flash technique (NETZSCH, LFA457).

3 Results and discussion XRD patterns of the SPS (MS) samples are shown in Fig. 1 (Supporting information Fig. S1). All peaks of $Si_{80}Ge_{20}$ match very well with the reference pattern (JCPDS no. 01-077-2650), whereas every peak related to the YSi_2 precipitate phase matches with the YSi_2 database (JCPDS no. 00-011-0324). The observed peaks indicate the formation of the $Si_{80}Ge_{20}$-YSi_2 composite phases. The small peak of SiB_4 at 2θ ~35° can also be observed for $x = 1.4$ and 2.8 but this phase does not exist in other samples. However, the amount of the SiB_4 phase is estimated to be very small and thus has limited effect on thermoelectric properties. The lattice parameters (a) of SiGe matrix calculated by using Bragg's law, from the main diffraction peaks ($2\theta = 28.42°$, 47.30°, and 56.10°), and the crystallite sizes of SiGe matrix calculated by using the Halder–Wagner method [31, 32] are presented in Table 1. The value of a is ~0.5469 nm for the SiGe-0%Y, and increased slightly with increasing amount of Y addition. The crystallite sizes of the SiGe matrix grains were in the range of 33–46 nm for the MS samples but increased to

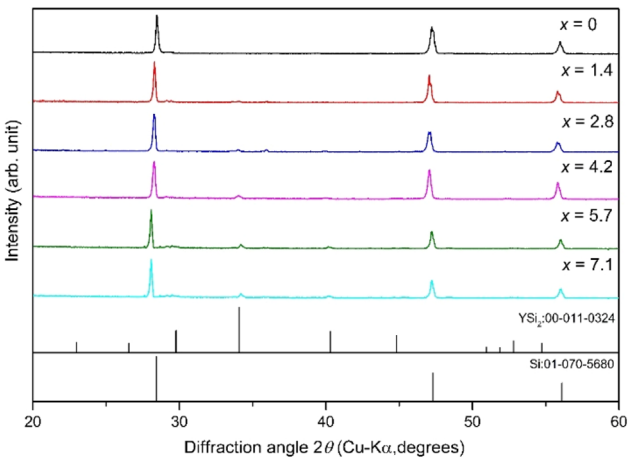

Figure 1 XRD patterns of the bulk SiGe-x wt.%Y after SPS.

Table 1 Summary of the characteristic parameters of the *p*-type SiGe-*x* wt.%Y.

composition (x)	lattice parameter, a (nm)	crystallite size, (nm) MS	crystallite size, (nm) SPS	d (g cm^{-3})	% density	EDS (wt.%Y)	n_H ($\times 10^{20}$cm^{-3})	μ_H (cm^2 V^{-1} s^{-1})
0	0.5469	36	100	2.87	96	0	6.2	16
1.4	0.5470	38	156	2.89	96	1.7	2.0	19
2.8	0.5473	46	156	2.90	96	2.0	2.2	23
4.2	0.5474	42	175	2.92	97	2.4	2.4	22
5.7	0.5477	40	164	2.94	97	2.7	2.1	18
7.1	0.5480	33	184	2.97	98	3.4	2.4	21

100–184 nm for the SPS samples due to grain growth during SPS process. It should be noted that the SPS temperature in our process is lower than many reports [10, 14, 19, 20, 24] so that the effect of grain growth should be minimized.

Fractured surfaces of the MS and SPS samples are presented in Fig. 2 which shows sub-micrometer size features comprising of SiGe grains and YSi_2 nanoinclusions (bright contrast). For $x = 0$, the grain growth of SiGe is clearly observed. It can be seen that with addition of Y ($x = 1.4$, 4.2, 7.1), the SiGe grain size tends to reduce probably due to the pinning effect from the YSi_2 nanoparticles which suppressed SiGe grain growth. The homogenous distribution of YSi_2 nanoinclusions can be observed and was confirmed by using EDS elemental mapping which showed uniformly distribution of YSi_2 over a large scale area (Supporting information Fig. S2). The chemical composition of all samples is closed to the nominal compositions for Si and Ge (Supporting information Table S1) but the concentration of Y is lower than expected (Table 1).

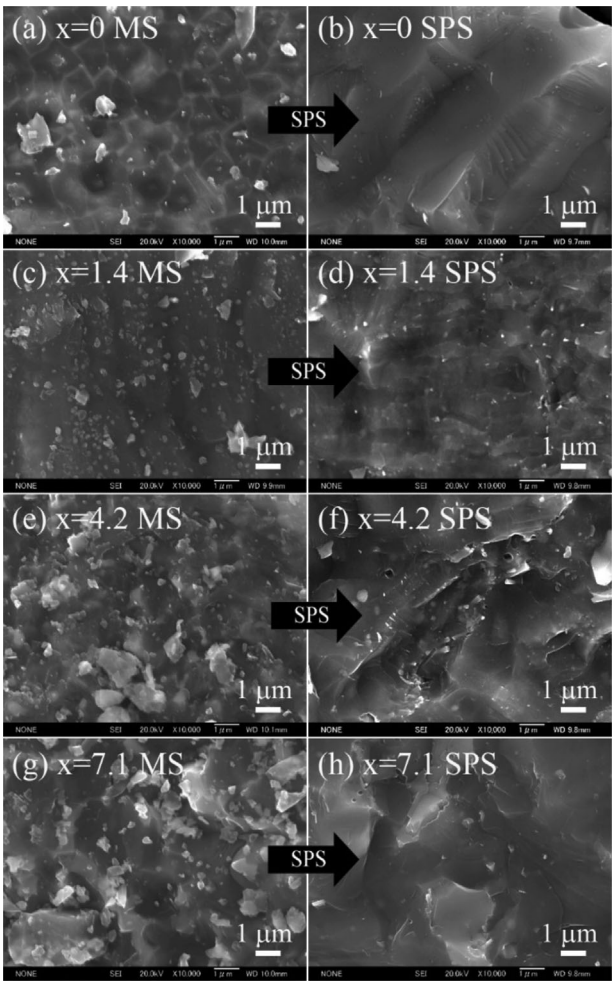

Figure 2 SEM micrographs of the fractured surfaces of the SiGe-*x* wt.%Y samples (a, b) $x = 0$, (c,d) $x = 1.4$, (e,f) $x = 4.2$, (g,h) $x = 7.1$.

The main difference between the MS and SPS samples in Fig. 2 is that in the MS samples a number of particulates can still be found whereas after SPS process the samples are fully dense which are generally good for thermoelectric performance [33, 34]. In fact, the density of every sample after SPS is above 95% of its theoretical value (Table 1) indicating that the SPS parameters were optimized.

Thermoelectric properties of the bulk SiGe-*x*%Y samples are summarized in Fig. 3. It is clearly seen that σ decreased monotonically with temperature (Fig. 3a), similar to other previous studies [5, 6]. Adding small

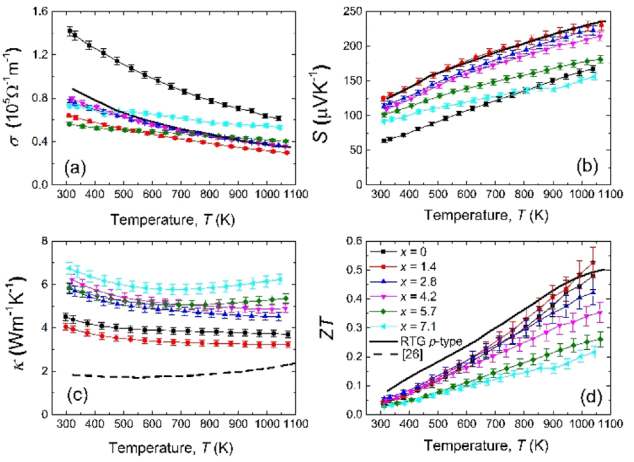

Figure 3 Thermoelectric properties of the SiGe-*x*%Y samples along with the reference data (a) electrical conductivity, (b) Seebeck, (c) thermal conductivity, (d) ZT.

amount of Y ($x = 1.4$) resulted in a minimum σ but adding more Y increased σ again. On the other hand, the positive value of S (Fig. 3b) was observed throughout the temperature range indicating the p-type behavior of the samples. The S was enhanced for the SiGe-1.4%Y, but subsequently decreased when higher content of Y was added. The changes in σ and S showed a similar trend to Ref. [26] but the values in our study were lower. A variation of σ and S with Y concentration was attributed to a change in carrier concentration (n_H) and mobility (μ_H) which were measured by the Hall measurement (Table 1). For degenerated semiconductors, σ is directly proportional to n_H whereas S is inversely proportional to n_H [2]. Thus, for SiGe-0%Y, the carrier concentration is the largest resulting in the highest σ. With 1.4%Y addition, n_H was reduced to less than one third of that without Y while the mobility only changed slightly. The smallest n_H is corresponding to the lowest σ and the highest S. For further addition of Y, n_H gradually increased, resulting in the slight increase in σ and the reduction in S.

The reason for the change in n_H with YSi_2 nanoinclusions could be related to the metallic nature of the silicides. Unlike other silicides, the knowledge on electric and thermal transport properties of YSi_2 is very limited. From our preliminary measurement of the TE properties (unpublished), YSi_2 showed metallic conducting behavior with $\sigma \sim 4$–$10 \times 10^5\ \Omega^{-1}\,m^{-1}$, nearly an order of magnitude larger than the SiGe matrix, and S ranging from -20 to $-30\ \mu m K^{-1}$. Thus, the charge carrier of YSi_2 is electron. Incorporating YSi_2 in the p-type SiGe matrix could result in the electron-hole pair recombination [35], leading to reduction in hole concentration.

Figure 3c shows temperature dependence of κ. It is obvious that the SiGe-1.4%Y showed a reduced κ in comparison to the SiGe-0%Y. However, when higher concentration of Y was introduced, κ increased. From this figure, it may suggest that with 1.4%Y, the YSi_2 nanoinclusions can suppress κ_l. The total thermal conductivity $\kappa = \kappa_l + \kappa_e$ and, from the Wiedemann–Franz law, the carrier thermal conductivity, $\kappa_e = L\sigma T$, where L is Lorenz number ($2.44 \times 10^{-8}\ W\,\Omega\,K^{-2}$). The reduction in the SiGe-1.4%Y sample is in fact a result of the suppression of κ_e, not κ_l, due to limited carrier concentration as evident from the Hall measurement. Actually, introducing Y in SiGe results in the enhanced κ_l in every sample. The reason for which the YSi_2 could not reduce κ_l could be attributed to the size of YSi_2. From the calculation in Ref. [11], the optimized size of silicide nanoparticles for κ_l suppression must be less than 10 nm. In our case, the YSi_2 nanopartilces are much larger than the optimized value so that κ_l could not be decreased. Also, the preliminary κ measurement of YSi_2 was found to be ~ 4–$6\ W m^{-1}\,K^{-1}$, slightly higher than that of SiGe matrix grains. Thus, using high concentration of YSi_2 nanoparticles could lead to the increase in κ as observed in Fig. 3c.

Compared to the SiGe-YiS_2 in Ref. [26], our measured κ was much higher. As mentioned earlier that in Ref. [26] Y_2O_3 was used as a source of Y. Therefore, oxides could reside in the matrix due to the $Y_2O_3 \rightarrow YSi_2$ conversion process. The small κ in Ref. [26] could in fact be the contribution of oxides, e.g., SiO_2. In a previous study, it was shown in the SiGe-$MoSi_2$ system that κ was significantly reduced in the presence of SiO_2 amorphous nanophase in the matrix [20]. Since the level of oxygen was not provided in Ref. [26], it is hard to draw a conclusion at this point.

Figure 3d shows the ZT of the SiGe-x%Y samples in this research, as well as the ZT of the RTG sample as a reference. A combination of high σ and relatively low κ resulting in a maximum ZT of 0.48 at 1073 K for the SiGe-0%Y sample. In the composite samples, the maximum ZT of 0.52 at 1073 K was realized for the SiGe-1.4%Y sample as a contribution of high S and low κ. For higher amount of YSi_2, due to relatively low σ and large κ from the reasons explained above, the ZT continuously dropped with increasing %Y. The maximum ZT for the SiGe-1.4%Y sample is slightly larger than the RTG sample but much lower than the recorded value obtained for the SiGe-YSi_2 nanocomposite in Ref. [26]. However, to be fair, TE properties of the p-type Si-silicide or SiGe-silicide systems were rarely reported. Besides [26], very few studies have shown an enhanced ZT in such system [16]. Moreover, a few reports found that the ZT was not improved when silicides were introduced to the SiGe matrix [15, 19, 21, 23]. Therefore, the TE performance for our SiGe-YSi_2 nanocomposites is similar to what found in the literatures.

4 Conclusions We successfully synthesized p-type SiGe-YSi_2 nanocomposite materials from MS and SPS methods. The fully dense materials consisted of YSi_2 nanoinclusions homogeneously distributed in the submicron SiGe grains. Introducing YSi_2 resulted in the reduction in carrier concentration due to the metallic nature of YSi_2 which in turn led to a reduction in σ and an increase in S. κ_l increased with YSi_2 because of the high κ of YSi_2 and the larger size of nanoinclusions than the optimized value. The maximum ZT of 0.52 was found for the SiGe-1.4%Y sample.

Supporting Information Additional supporting information may be found in the online version of this article at the publisher's web-site.

Acknowledgements This work is supported by the Thailand Research Fund (TRF) in cooperation with Khon Kaen University (RSA5980014), the Royal Golden Jubilee Ph.D. Program (PHD/0063/2558), and the Nanotechnology Center (NANOTEC), NSTDA, Ministry of Science and Technology, Thailand, through its program of Center of Excellence Network.

References

[1] K. Biswas, J. Q. He, I. D. Blum, C.-I. Wu, T. P. Hogan, D. N. Seidman, V. P. Dravid, and M. G. Kanatzidis, Nature **490**, 414–418 (2012).

[2] G. J. Snyder and E. S. Toberer, Nat. Mater. **7**, 105–114 (2008).

[3] D. M. Rowe, CRC Handbook of Thermoelectrics (CRC Press, Boca Raton, London, 1995).
[4] R. Basu, S. Bhattacharya, R. Bhatt, M. Roy, S. Ahmad, A. Singh, M. Navaneethan, Y. Hayakawa, D. K. Aswal, and S. K. Gupta, J. Mater. Chem. A **2**, 6922–6930 (2014).
[5] S. Bathula, M. Jayasimhadri, B. Gahtori, N. K. Singh, K. Tyagi, A. K. Srivastava, and A. Dhar, Nanoscale **7**, 12474–12483 (2015).
[6] G. Joshi, H. Lee, Y. C. Lan, X. W. Wang, G. H. Zhu, D. Z. Wang, R. W. Gould, D. C. Cuff, M. Y. Tang, M. S. Dresselhaus, G. Chen, and Z. F. Ren, Nano Lett. **8**, 4670–4674 (2008).
[7] X. W. Wang, H. Lee, Y. C. Lan, G. H. Zhu, G. Joshi, D. Z. Wang, J. Yang, A. J. Muto, M. Y. Tang, J. Klatsky, S. Song, M. S. Dresselhaus, G. Chen, and Z. F. Ren, Appl. Phys. Lett. **93**, 193121 (2008).
[8] B. Yu, M. Zebarjadi, H. Wang, K. Lukas, H. Z. Wang, D. Z. Wang, C. Opeil, M. Dresselhaus, G. Chen, and Z. F. Ren, Nano Lett. **12**, 2077–2082 (2012).
[9] M. Zebarjadi, G. Joshi, G. H. Zhu, B. Yu, A. Minnich, Y. C. Lan, X. W. Wang, M. Dresselhaus, Z. F. Ren, and G. Chen, Nano Lett. **11**, 2225–2230 (2011).
[10] S. Bathula, M. Jayasimhadri, N. Singh, A. K. Srivastava, J. Pulikkotil, A. Dhar, and R. C. Budhani, Appl. Phys. Lett. **101**, 213902 (2012).
[11] N. Mingo, D. Hauser, N. P. Kobayashi, M. Plissonnier, and A. Shakouri, Nano Lett. **9**, 711–715 (2009).
[12] A. Nozariasbmarz, P. Roy, Z. Zamanipour, J. H. Dycus, M. J. Cabral, J. M. LeBeau, J. S. Krasinski, and D. Vashaee, APL Mater. **4**, 104814 (2016).
[13] A. Nozariasbmarz, Z. Zamanipour, P. Norouzzadeh, J. S. Krasinski, and D. Vashaee, RSC Adv. **6**, 49643–49650 (2016).
[14] A. Usenko, D. Moskovskikh, A. Korotitskiy, M. Gorshenkov, A. Voronin, D. Arkhipov, M. Lyange, G. Isachenko, and V. Khovaylo, J. Electron. Mater. **45**, 3427–3432 (2016).
[15] F. W. Dynys, A. Sayir, J. Mackey, and A. Sehirlioglu, J. Alloy. Compd. **604**, 196–203 (2014).
[16] J. Mackey, F. Dynys, and A. Sehirliogiu, Acta. Mater. **98**, 263–274 (2015).
[17] N. Petermann, T. Schneider, J. Stotzel, N. Stein, C. Weise, I. Wlokas, G. Schierning, and H. Wiggers, J. Phys. D Appl. Phys. **48**, 314010 (2015).
[18] K. Kurosaki, A. Yusufu, Y. Miyazaki, Y. Ohishi, H. Muta, and S. Yamanaka, Mater. Trans. **57**, 1018–1021 (2016).
[19] Z. Zamanipour and D. Vashaee, J. Appl. Phys. **112**, 093714 (2012).
[20] K. Favier, G. Bernard-Granger, C. Navone, M. Soulier, M. Boidot, J. Leforestier, J. Simon, J. C. Tedenac, and D. Ravot, Acta. Mater. **64**, 429–442 (2014).
[21] Y. Ohishi, K. Kurosaki, T. Suzuki, H. Muta, S. Yamanaka, N. Uchida, T. Tada, and T. Kanayama, Thin Solid Films **534**, 238–241 (2013).
[22] N. Uchida, T. Tada, Y. Ohishi, Y. Miyazaki, K. Kurosaki, and S. Yamanaka, J. Appl. Phys. **114**, 134311 (2013).
[23] M. Zebarjadi, K. Esfarjani, M. S. Dresselhaus, Z. F. Ren, and G. Chen, Energ. Environ. Sci. **5**, 5147–5162 (2012).
[24] A. Yusufu, K. Kurosaki, Y. Ohishi, H. Muta, and S. Yamanaka, Jpn. J. Appl. Phys. **55**, 061301 (2016).
[25] S. Tanusilp, K. Kurosaki, A. Yusufu, Y. Ohishi, H. Muta, and S. Yamanaka, J. Electron. Mater. **46**, 3249–3255 (2017).
[26] S. Ahmad, A. Singh, A. Bohra, R. Basu, S. Bhattacharya, R. Bhatt, K. N. Meshram, M. Roy, S. K. Sarkar, Y. Hayakawa, A. K. Debnath, D. K. Aswal, and S. K. Gupta, Nano Energy **27**, 282–297 (2016).
[27] M. H. Cho, D. H. Ko, Y. G. Choi, I. W. Lyo, K. Jeong, and C. N. Whang, J. Appl. Phys. **92**, 5555–5559 (2002).
[28] H. Y. Li, H. Y. Jing, Y. D. Han, G. Q. Lu, and L. Y. Xu, Mater. Chem. Phys. **143**, 400–406 (2013).
[29] G. Schierning, R. Theissmann, N. Stein, N. Petermann, A. Becker, M. Engenhorst, V. Kessler, M. Geller, A. Beckel, H. Wiggers, and R. Schmechel, J. Appl. Phys. **110**, 113515 (2011).
[30] T. Claudio, G. Schierning, R. Theissmann, H. Wiggers, H. Schober, M. M. Koza, and R. P. Hermann, J. Mater. Sci. **48**, 2836–2845 (2013).
[31] N. C. Halder and C. N. J. Wagner, Acta. Crystallogr. **20**, 312–313 (1966).
[32] N. C. Halder and C. N. J. Wagner, Advances in X-Ray Analysis, Eds. G. R. Mallett, M. J. Fay, and W. M. Mueller (Springer US, 1966), chap. 8, pp. 91–102.
[33] M. Saleemi, M. S. Toprak, S. H. Li, M. Johnsson, and M. Muhammed, J. Mater. Chem. **22**, 725–730 (2012).
[34] L. D. Zhao, B. P. Zhang, J. F. Li, H. L. Zhang, and W. S. Liu, Solid State Sci. **10**, 651–658 (2008).
[35] G. Bakan, N. Khan, H. Silva, and A. Gokirmak, Sci. Rep. **3**, 2724 (2013).

physica status solidi a
www.pss-a.com

Thermoelectric Properties of Bulk Yttrium Silicide (YSi2) Fabricated by Arc Melting and Spark Plasma Sintering

Suphagrid Wongprakarn, Supree Pinitsoontorn, Sora-at Tanusilp, and Ken Kurosaki*

Yttrium silicide (YSi_2) nanoparticles in SiGe are reported to enhance the thermoelectric figure-of-merit (*ZT*) to the recorded value (≈1.81). However, the thermoelectric properties of bulk YSi_2 has never been reported. In this work, the thermoelectric properties of YSi_2 is studied for the first time. The bulk YSi_2 is fabricated by arc melting highly pure Si and Y raw materials. The ingot is crushed to powder and compacted to form a highly dense pellet by spark plasma sintering. By optimizing the processing parameters, the single phase with the AlB_2-type structure (*P6/mmm*) is formed. The Hall measurements show that YSi_2 exhibit a metallic-like behavior with a very high electron concentration. This result in the thermoelectric properties with a very large electrical conductivity ($\approx 18 \times 10^5\ \Omega^{-1}\ m^{-1}$) but a small Seebeck coefficient ($-26\ \mu V\ K^{-1}$) at room temperature, and decrease with temperature. The thermal conductivity is around 14–19 $W\ m^{-1}\ K^{-1}$ for all temperature range. The maximum *ZT* value is 0.026 at 423 K.

1. Introduction

Thermoelectric (TE) materials can directly convert wastes heat into electrical power.[1–3] The performance of TE materials is determined by the dimensionless figure-of-merit, $ZT = (S^2\sigma/\kappa)T$, where S, σ, κ, and T are Seebeck coefficient, electrical conductivity, thermal conductivity, and absolute temperature, respectively. The present state-of-the-art TE materials around room temperature and mid-range temperature are Bi_2Te_3 and PbTe.[1,2] However, these materials have a certain draw back from their thermal instability and consisting of toxic and rare elements.

Metal silicides are a class of materials which has been considered as candidates for TE materials. In recent review papers, several types of silicides for TE applications were summarized, including Mg_2Si, $MnSi_x$, $CrSi_2$, β-$FeSi_2$.[4–6] With proper doping, these silicides showed promising TE performances with a relatively large *ZT* (>0.5).

TE properties of silicide nanoparticles in Si or SiGe matrix was theoretically calculated by Mingo et al.[7] In their work, several types of silicide nanoparticles were incorporated in the matrix and a fivefold increase in the *ZT* values were observed as a consequence of a significant suppression in thermal conductivity. This work has stimulated many experimental works in exploiting silicide nanoparticles as phonon scattering sources. For instance, Mg_2Si and $FeSi_2$ nanoinclusions in SiGe matrix showed the reduced thermal conductivity compared to the single-phase SiGe alloy, and hence the maximum *ZT* of 1.3.[8] Furthermore, the Si/WSi_2 nanocomposites showed 40% reduction in lattice thermal conductivity and the *ZT* enhancement of 30%.[9]

The most promising experiment was demonstrated by Ahmad et al.[10] who incorporated yttrium silicide (YSi_2) nanoparticles in SiGe matrix and obtained the recorded *ZT* (≈1.81) for the *p*-type SiGe alloy. The enormous improvement in TE performance was attributed to the coherent interfaces between YSi_2 nanoparticles and SiGe grains which strongly scattered phonon but have a minimum effect on the power factor. This work has not only emphasized the nanoparticle-in-alloy concept but also shed the light on YSi_2 as a promising TE material. Nevertheless, YSi_2 was not included in the reviews on silicides,[4,5] or in the calculation by Mingo et al.[7] Moreover, research on bulk YSi_2 were rarely reported.

Consequently, in this work, the bulk YSi_2 was fabricated and the TE properties were investigated for the first time.

S. Wongprakarn
Materials Science and Nanotechnology Program
Faculty of Science
Khon Kaen University
Khon Kaen 40002, Thailand

Dr. S. Pinitsoontorn
Integrated Nanotechnology Research Center
Department of Physics
Faculty of Science
Khon Kaen University
Khon Kaen 40002, Thailand
E-mail: psupree@kku.ac.th

S. Tanusilp, Dr. K. Kurosaki
Graduate School of Engineering
Osaka University
2-1 Yamadaoka, Suita, Osaka 565-0871, Japan

Dr. K. Kurosaki
Research Institute of Nuclear Engineering
University of Fukui
1-2-4 Kanawa-cho, Tsuruga, Fukui 914-0055, Japan

Dr. K. Kurosaki
JST, PRESTO
4-1-8 Honcho, Kawaguchi, Saitama 332-0012, Japan

DOI: 10.1002/pssa.201700769

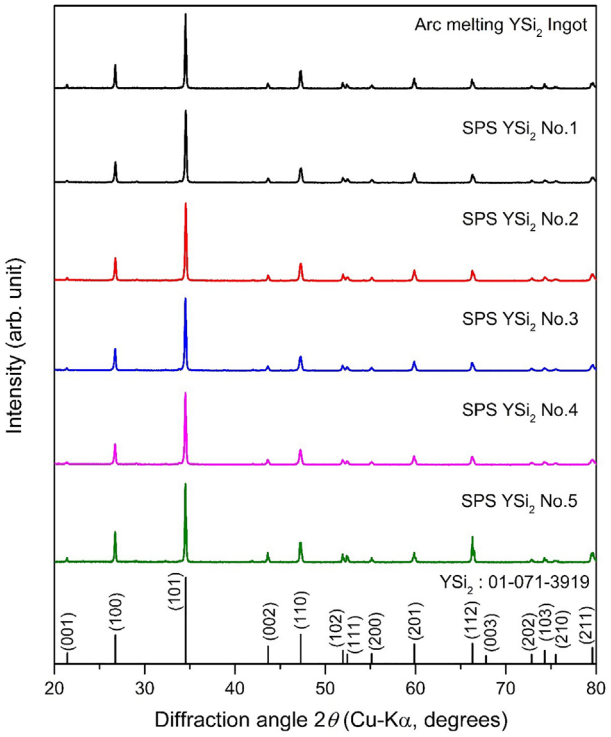

Figure 1. Powder XRD patterns of the YSi_2 samples after arc melting and after SPS.

2. Experimental Section

YSi_2 ingots were prepared by arc melting (AM) under Ar atmosphere, by melting highly pure Si (11N), and Y chunks (99.9%). The ingot was crushed to powder and then loaded into a graphite die for fabricating the bulk samples by using spark plasma sintering (SPS). The SPS was carried out at 1273 K for 5 min in Ar atmosphere under a pressure of 100 MPa. To test the reproducibility, five samples under the same synthesis conditions were prepared.

Crystallinity and morphology of the samples were observed using the X-ray diffraction analysis (XRD; Ultima IV, Rigaku) and scanning electron microscopy (SEM, JSM-6500F, JEOL). The chemical composition was confirmed by energy dispersive X-ray spectrometry (EDS) equipped in the SEM. Seebeck coefficient and electrical conductivity were measured by ZEM-3 (Ulvac-Riko) from room temperature to 773 K. The mobility and carrier concentration at room temperature were measured by Hall measurement system (Toyo ResiTest8300). Thermal conductivity (κ) was calculated from $\kappa = DC_pd$, where D, C_p, and d are thermal diffusivity, heat capacity, and density, respectively. D was measured by laser flash technique (NETZSCH, LFA457). $C_p = 3nR$, where n and R are the number of atoms per formula unit and gas constant. D was calculated from the measured weight and dimensions of the samples.

3. Results and Discussion

Figure 1 shows the powder XRD patterns of the YSi_2 ingot and the bulk samples after SPS. The main peaks of all samples agree well with the $YSi_{1.67}$ standard pattern (JCPDS 01-071-3919), representing the single phase of the AlB_2-type structure ($P6/mmm$), without any secondary phases observed. Samples 1–5 show the identical peaks indicating the reproducibility of the fabrication technique. The lattice parameters calculated from the XRD patterns are shown in **Table 1**, which are almost same with the literature values.[11] The densities of the bulk samples are also presented in Table 1. All samples possess very high density between 93.3 and 94.5% of theoretical values which are the fundamental requirements for good TE materials.

The SEM micrographs alongside with the EDS mappings of the pressed surface of the bulk YSi_2 sample are shown in **Figure 2**. It is obviously seen the fully dense sample with homogenous distribution of the elements. Quantitative analysis showed that the chemical compositions of Y and Si were 37.14 and 62.86 at.%, respectively, which is equivalent to Y:Si = 1:1.69. This result showed that the nominal composition YSi_2 was in fact $YSi_{1.69}$, which is closely agreed with the literature value of $YSi_{1.67}$.[11,12] The elemental analysis of all five samples show nearly identical compositions as summarized in Table 1.

The TE properties of the bulk YSi_2 samples are shown in **Figure 3**. All five samples show almost the same TE characteristics. The Seebeck coefficients were negative throughout the temperature range, indicating the n-type charge carrier, which was confirmed by the Hall measurement (Table 1). The absolute S values decreased with temperature from 26 $\mu V K^{-1}$ at room temperature to 14 $\mu V K^{-1}$ at 773 K. These values are very low compared to other silicide materials (100–300 $\mu V K^{-1}$).[4,5] The reason for the low S values is attributed to the very large carrier concentration ($n_H \approx 6–7 \times 10^{22}$ cm^{-3}), Table 1, much higher than

Table 1. Density (d), relative density (%T.D.), lattice parameter (a and c), Hall carrier concentration (n_H), and Hall mobility (μ_H) at room temperature.

Sample	d ($g\,cm^{-3}$)	%T.D.	Lattice parameter (nm)		EDS (at.%)		Carrier type	n_H ($\times 10^{20}$ cm^{-3})	μ_H ($cm^2 V^{-1} s^{-1}$)
			a	c	Y	Si			
No. 1	4.24	93.3	0.3843(4)	0.4143(2)	37.14	62.86	n	7.43 ± 0.7	17.9 ± 0.2
No. 2	4.29	94.5	0.3844(8)	0.4142(1)	37.11	62.89	n	6.11 ± 0.6	21.7 ± 0.2
No. 3	4.28	94.3	0.3845(4)	0.4147(5)	37.34	62.66	n	6.95 ± 0.7	19.1 ± 0.2
No. 4	4.25	93.6	0.3846(3)	0.4147(4)	37.26	62.74	n	6.84 ± 0.7	19.6 ± 0.2
No. 5	4.28	94.3	0.3844(9)	0.4143(2)	37.19	62.81	n	6.63 ± 0.7	18.7 ± 0.2
[11]	4.54	–	0.3843	0.4143	–	–	–	–	–

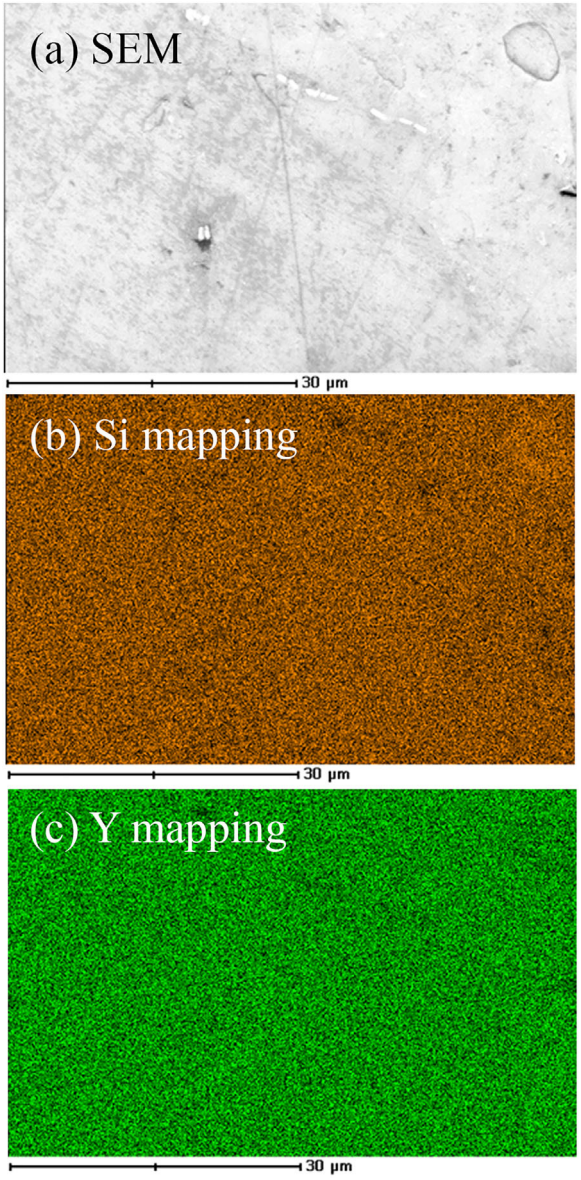

Figure 2. a) SEM images of the pressed surface of YiS_2 along with the elemental mapping (b) Y, (c) Si.

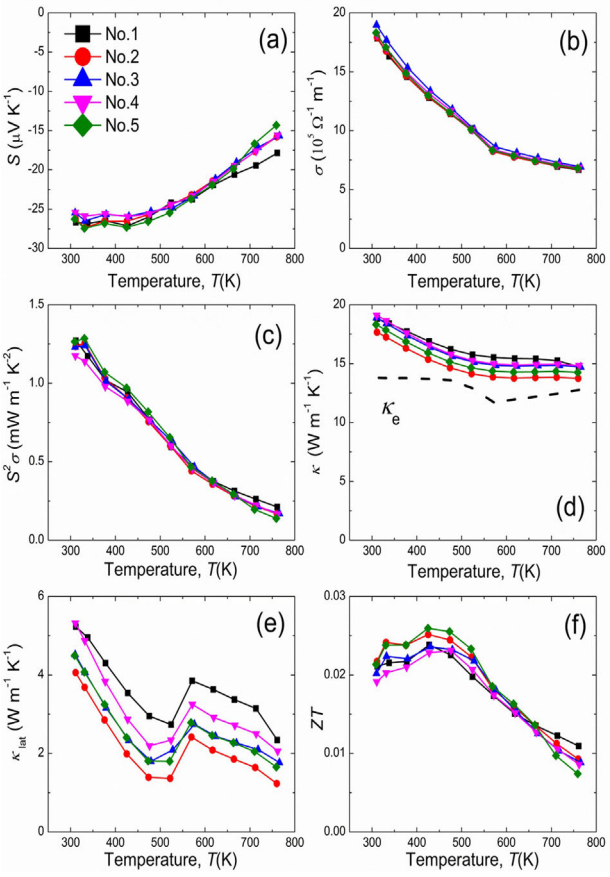

Figure 3. Temperature dependences of (a) S, (b) σ, (c) $S^2\sigma$, (d) κ, (e) κ_{lat}, and (f) ZT of YSi_2.

other silicide materials ($\approx 10^{20}$–$10^{21}\,cm^{-3}$).[4,5] Normally, for metals or degenerate semiconductors, the Seebeck coefficient is inversely proportional to the carrier concentration.[1,13] Therefore, the very large carrier concentration resulted in the reduced S values.

Figure 3b showed the decreasing electrical conductivity with increasing temperature, illustrating a metallic-like behavior. The observed σ values were very high throughout the measurement temperature ($18 \times 10^5\,\Omega^{-1}\,m^{-1}$ at RT), about an order of magnitude larger than other silicides ($\approx 10^4$–$10^{-5}\,\Omega^{-1}\,m^{-1}$).[4,5] The metallic-like behavior and large σ are consistent with the high n_H. The mobility of YSi_2 in the present study was nearly double of other silicides ($\approx 10\,cm^2\,V^{-1}\,s^{-1}$).[4,5] Though with very high σ, the small S led to relatively low power factor (1.28 mW $m^{-1}\,K^{-2}$ at RT), as shown in Figure 3c. It should be noted that the TE and Hall measurements in the present work are in consistence with the previous electronic structure calculations of which the Fermi energy was right in the middle of the conduction band,[14] representing the metallic characteristic of YSi_2.

Figure 3d shows the thermal conductivity of the bulk YSi_2 samples. The κ values slightly decreased with temperature and were approximately about $15\,Wm^{-1}\,K^{-1}$ above 500 K, several folds higher than other silicides.[4,5] Generally, $\kappa = \kappa_{lat} + \kappa_e$, where κ_{lat} is the lattice thermal conductivity and κ_e is the electronic thermal conductivity which can be estimated from Wiedemann–Franz's law, $\kappa_e = L\sigma T$, where L = Lorenze number $= 2.45 \times 10^{-8}\,V^2\,K^{-2}$.[1] The reason for the high thermal conductivity is due to the very large κ_e (dotted line). After subtracting κ_e, the κ_l is plotted as shown in Figure 3e. This implies that the thermal conductivity is mostly govern by the electronic part which could be justified from the very high carrier concentration. Figure 3f shows the temperature dependence of ZT which has the maximum of 0.026 at 423. This value is relatively low in comparison to other good TE silicides, i.e., Mg_2Si, $MnSi_x$, $CrSi_2$, $FeSi_2$, with $ZT > 0.5$. However, the ZT of YSi_2 in our case is comparable (or even better) to some inferior silicides, for example, URu_2Si_3, $Fe_{0.95}Cr_{0.05}Si_2$, $CeSi_2$, $SrSi_2$, $SrAl_2Si_2$, $BaSi_2$, $CaSi$.[5]

4. Conclusion

In this work, the single phase of fully dense bulk YSi_2 was successfully fabricated using a combination of arc melting and SPS. The TE and Hall measurements of the bulk YSi_2 sample were carried out for the first time. From the results it was concluded that the bulk YSi_2 possessed the metallic characteristics. A large concentration of electrons above the Fermi level acts as the charge carrier. As a result, the very high electrical conductivity was found with the relatively small Seebeck coefficient. The thermal conductivity, dominated by the electronic contribution, was also large. Consequently, the *ZT* of this material is relatively low in comparison to other good TE silicides. Since the carrier concentration of YSi_2 was an order of magnitude larger than the optimum value for TE applications, it would be difficult to tune the carrier concentration by doping or other means. Therefore, even though the YSi_2 nanoparticles were successfully added in SiGe matrix to enhance the overall *ZT*, the stand-alone bulk YSi_2 might not be a promising TE material.

Acknowledgments

This work is supported by Thailand Research Fund (TRF) in cooperation with Khon Kaen University (RSA5980014), Royal Golden Jubilee Ph.D. Program (PHD/0192/2556), and National Research Council of Thailand through Khon Kaen University (6100067).

Conflict of Interest

The authors declare no conflict of interest.

Keywords

silicides, spark plasma sintering, thermoelectric, YSi_2

Received: October 10, 2017
Published online: February 14, 2018

[1] G. J. Snyder, E. S. Toberer, *Nat. Mater.* **2008**, *7*, 105.
[2] K. Biswas, J. Q. He, I. D. Blum, C. I. Wu, T. P. Hogan, D. N. Seidman, V. P. Dravid, M. G. Kanatzidis, *Nature* **2012**, *490*, 414.
[3] A. Yusufu, K. Kurosaki, Y. Miyazaki, M. Ishimaru, A. Kosuga, Y. Ohishi, H. Muta, S. Yamanaka, *Nanoscale* **2014**, *6*, 13921.
[4] M. I. Fedorov, G. N. Isachenko, *Jpn. J. Appl. Phys.* **2015**, *54*, 07JA05.
[5] A. Nozariasbmarz, A. Agarwal, Z. A. Coutant, M. J. Hall, J. Liu, R. Liu, A. Malhotra, P. Norouzzadeh, M. C. Ozturk, V. P. Ramesh, Y. Sargolzaeiaval, F. Suarez, D. Vashaee, *Jpn. J. Appl. Phys.* **2017**, *56*, 05DA04.
[6] K. Kurosaki, A. Yusufu, Y. Miyazaki, Y. Ohishi, H. Muta, S. Yamanaka, *Mater. Trans.* **2016**, *57*, 1018.
[7] N. Mingo, D. Hauser, N. P. Kobayashi, M. Plissonnier, A. Shakouri, *Nano Lett.* **2009**, *9*, 711.
[8] A. Nozariasbmarz, P. Roy, Z. Zamanipour, J. H. Dycus, M. J. Cabral, J. M. LeBeau, J. S. Krasinski, D. Vashaee, *APL Mater.* **2016**, *4*, 104814.
[9] J. Mackey, F. Dynys, A. Sehirliogiu, *Acta. Mater.* **2015**, *98*, 263.
[10] S. Ahmad, A. Singh, A. Bohra, R. Basu, S. Bhattacharya, R. Bhatt, K. N. Meshram, M. Roy, S. K. Sarkar, Y. Hayakawa, A. K. Debnath, D. K. Aswal, S. K. Gupta, *Nano Energy* **2016**, *27*, 282.
[11] I. Mayer, I. Felner, *J. Less Common Met.* **1972**, *29*, 25.
[12] T. W. Button, I. J. Mccolm, J. M. Ward, *J. Less Common Met.* **1990**, *159*, 205.
[13] D. M. Rowe, *CRC Handbook of Thermoelectrics*. CRC Press, Boca Raton **1995**.
[14] L. Martinage, *J. Phys. Condens. Mattter* **1989**, *1*, 2593.

Materials Science in Semiconductor Processing 88 (2018) 239–249

Contents lists available at ScienceDirect

Materials Science in Semiconductor Processing

journal homepage: www.elsevier.com/locate/mssp

Enhancing thermoelectric properties of *p*-type SiGe alloy through optimization of carrier concentration and processing parameters

Suphagrid Wongprakarn[a], Supree Pinitsoontorn[b,c,*], Sora-at Tanusilp[d], Ken Kurosaki[d,e,f]

[a] Materials Science and Nanotechnology Program, Faculty of Science, Khon Kaen University, Khon Kaen 40002, Thailand
[b] Integrated Nanotechnology Research Center, Department of Physics, Faculty of Science, Khon Kaen University, Khon Kaen 40002, Thailand
[c] Thailand Center of Excellence in Physics, Commission on Higher Education, 328 Si Ayutthaya Road, Bangkok 10400, Thailand
[d] Graduate School of Engineering, Osaka University, 2-1 Yamadaoka, Suita, Osaka 565-0871, Japan
[e] JST, PRESTO, 4-1-8 Honcho, Kawaguchi, Saitama 332-0012, Japan
[f] Research Institute of Nuclear Engineering, University of Fukui, 1-2-4 Kanawa-cho, Tsuruga, Fukui 914-0055, Japan

ARTICLE INFO

Keywords:
Thermoelectric
SiGe
p-type
Boron concentration
Melt spinning
Spark plasma sintering

ABSTRACT

The enhancement in thermoelectric (TE) properties of *p*-type SiGe alloys through the optimization of carrier concentration and processing parameters was reported. The *p*-type $Si_{80}Ge_{20}B_x$ alloys were prepared by melt spinning (MS) followed by spark plasma sintering (SPS). The effect of B concentration and processing parameters (rotating speed of Cu wheel in MS and holding time in SPS) was investigated. By adjusting the B content, the carrier concentration was notably changed but the carrier mobility was not significantly different. Consequently, TE properties were varied with B concentration and showed the optimum value for $Si_{80}Ge_{20}B_{0.5}$ with the maximum *ZT* of 0.71 at 1073 K. Increasing the Cu wheel rotating speed resulted in the refined microstructure of the MS ribbons. The smaller grain sizes were maintained even after SPS. However, despite the refined grains, the TE properties were insignificantly different for any rotating speed. Reducing the SPS holding time resulted in bulk samples with lower density, presumably containing nano/micro porous structure. The presence of pores in the microstructure effectively reduced thermal conductivity due to a stronger phonon scattering, but also suppressed the electrical contribution making an obvious drop in the power factor. The optimized holding time for SPS was 5 min at 1323 K.

1. Introduction

Thermoelectric (TE) devices can directly convert heat into electricity. Typically, they consist of semiconducting materials (*n*-type and *p*-type) connected in series. A thermoelectric conversion efficiency of each material is determined by the dimensionless figure-of-merit, *ZT*, which is given by the equation $ZT = S^2\sigma T/\kappa$, where *S* is the Seebeck coefficient, σ is the electrical conductivity, *T* is the absolute temperature and κ is the thermal conductivity.

Although there is no theoretical upper limit for *ZT* values, the *ZT* of 1 is considered as the benchmark in the TE community [1,2], and is the value of the best TE materials used in present TE devices [3]. At present, the conventional TE materials around room temperature (RT) and mid-range temperature are Bi_2Te_3 and PbTe-related alloys, respectively [4–6]. For higher temperature range, SiGe alloys are one of the candidates due to their chemical stability and good TE properties at high temperature. In fact, the $Si_{80}Ge_{20}$ system has been used in Radioisotope TE Generators (RTGs) in NASA spaceships since 1970s (with $ZT \sim 0.5$ for *p*-type and ~ 0.9 for *n*-type at 1073 K) [7].

SiGe alloys are one of the most widely studied TE materials. Particularly in recent years, several studies have demonstrated the advanced improvement in *ZT* values of the SiGe system via nanostructuring approach. Nanostructures offer a material with complex crystal structures including high density of grain boundaries (nanostructured structure) [8–12], nanoparticles embedded in a matrix phase [13–17], modulation-doping in nanocomposites [18,19], and nanoscale defect features [20]. The main advantage of using SiGe nanostructure is the difference in the mean free path (MFP) between the electronic and phonon contributions (MFP of electron and phonon are $\sim$ 5 nm and $\sim$ 200–300 nm, respectively [11,21]). Therefore, nanostructuring approach in the scale range of 10–100 nm has a major influence to lattice thermal conductivity (κ_{lat}) but shows almost no effect on electrical transport. Such complex structures have been proven experimentally in which various effective phonon scattering mechanisms were introduced, leading to a drastic reduction of κ_{lat}. For instance, Basu et al. reported the improved TE performance of hot pressed nanostructured *n*-

* Corresponding author.
E-mail address: psupree@kku.ac.th (S. Pinitsoontorn).

https://doi.org/10.1016/j.mssp.2018.08.020
Received 3 May 2018; Received in revised form 3 July 2018; Accepted 19 August 2018

type SiGe bulk alloys with κ approaching 0.9 W m^{-1} K^{-1} and very high ZT of ~ 1.84 at 1073 K [8]. Bathula et al. dispersed SiC nanoparticles in the n-type SiGe matrix and observed the lowest κ of 1.9 W m^{-1} K^{-1} yielding a high value of ZT ~ 1.7 at 1173 K [13]. Ahmad et al. used the nanocomposite approach by introducing YSi_2 nanoinclusions in p-type SiGe alloys. With proper amount of YSi_2 nanoinclusions, the κ was reduced by 62%, resulting in 34% improvement of ZT (~ 1.81 at 1100 K) [14].

In the synthesis of SiGe nanostructured alloys, most experimental works employed a solid state ball milling method [8–16,18–20]. Although this method is simple and can provide powders in nanoparticle size, it also has several drawbacks, such as a long milling time (up to > 90 h) [8,9,20], contamination from the grinding media, or proneness to oxidation during the process. The contamination from the grinding media, e.g. yttria stabilized zirconia (YSZ), could lead to a significant reduction in electrical conductivity and hence lower ZT [22]. Similarly, oxidation of SiGe alloys or the formation of SiO_2 nanoinclusion could have a deteriorate effect on the TE properties [23–25]. On the other hand, melt spinning (MS) is a powerful technique for fabrication of homogeneous alloy. It is one of the rapid solidification techniques that play an important role in preparation of many advanced functional materials [26]. The process is much faster than ball milling and provide negligible contamination or oxidation. It has been demonstrated to fabricate many TE materials with improved TE properties, for example, Bi_2Te_3 [27], skutterudite $CoSb_3$ [28], and several Si-silicide systems [29–32].

In this work, we demonstrated the fabrication of *p*-type SiGe alloys (boron doped) by using the MS technique in combination with spark plasma sintering (SPS). Researching through literatures, it was hardly found reports on the variation of B concentration on the change in TE properties of SiGe alloys [24,33]. In addition, the processing parameters in the MS [30,31] and SPS processes [20,25] for the fabrication of SiGe alloy were rarely reported. Therefore, in the present research, the effect of boron concentration as well as processing parameters on the microstructure and TE properties were systematically investigated. Under the optimization condition, it was found that the TE properties of the *p*-type SiGe alloys were significantly improved.

2. Experimental procedure

Firstly, we investigated the effect of B concentration on the TE properties of SiGe alloys prepared by melt spinning (MS) and spark plasma sintering (SPS). A series of ingot samples with nominal compositions of $Si_{80}Ge_{20}B_x$ (x = 0.1, 0.23, 0.5, 1.0, 1.5, 3.0) were prepared by arc melting (AM) from high-purity Si chunk (11 N), Ge shot (3 N) and B chunk (99.9%) in a vacuum chamber under Ar atmosphere. Then, ribbon samples were prepared by melt spinning (MS) process. In this process, the obtained ingots were put into a boron nitride (BN) tube, with a 0.6 mm diameter nozzle, and melted by induction heating in Ar atmosphere. The 6-turn Cu coils in the space of 4 cm height and 3 cm width surrounds the BN tube. The inner diameter of the coil is 2 cm whereas the Cu wire diameter is 0.5 cm. The electrical power of 20 mA, 110 V, 60-Hz AC current was supplied to create induction heating. The molten alloys were ejected, with a pressure of 0.02 MPa, onto a Cu wheel (a radius of 10 cm) rotating at the speed of 2000 rpm. The gap between the nozzle and the wheel was 0.2 mm. The rapidly solidified ribbon samples were crushed manually into fine powders and placed into a high strength graphite die for fabricating bulk samples by SPS. The ramp rate for the SPS processing was 48 °C/min. The SPS process was controlled at 1323 K for 5 min in an Ar atmosphere under an axial pressure of 100 MPa. The $Si_{80}Ge_{20}B_x$ bulk samples in this stage were ready for microstructural and properties investigation.

Secondly, for the processing parameter optimization, the sample with the best TE properties from the first experiment was chosen. Two parameters were under investigation: the rotating speed of the Cu wheel, and the SPS holding time. The first parameter could change the crystallite size of the samples, and thus possibly improved TE properties. The rotating speed was adjusted between 2000 rpm and 6000 rpm. The SPS holding time also had an effect on the density and microstructure, and again, could enhance the TE properties. The SPS holding times used in this experiment were varied from 3 min to 7 min.

Phase and crystallographic structure were investigated using powder X-ray diffraction (XRD, Rigaku, Ultima IV) analysis using Cu K_α radiation. The microstructures of the ribbon surfaces and finely polished bulk sample surfaces were investigated under field emission scanning electron microscopy (FE-SEM; JEOL JSM-6500F). A carrier concentration (n) and carrier mobility (μ) were measured using the Hall coefficient measurement system (Toyo Resitest8340) at room temperature under a magnetic field of 0.5 T. The thermal conductivity (??) was calculated by using the equation $\kappa = DdC$, where d is the bulk density and C is the heat capacity of which the literature value was used [6]. The thermal diffusivity D was measured by a flash diffusivity method in the Netzsch LFA467 instrument from room temperature (RT) to 1073 K under an Ar atmosphere. Seebeck coefficient and electrical conductivity of the samples were measured by the commercial system (Ulvac-Riko, ZEM-3) from RT to 1073 K in a He atmosphere.

3. Results and discussion

3.1. Optimization of B concentration

Fig. 1 shows the powder XRD patterns of the *p*-type $Si_{80}Ge_{20}B_x$ (x = 0.1, 0.23, 0.5, 1.0, 1.5, 3.0) samples after SPS. All of the XRD peaks agree well with the literature data (JCPDS:00-005-0565) and [13,20,34], without any impurity phases, indicating the single phase of $Si_{80}Ge_{20}B_x$. However, the asymmetric XRD peaks were observed, particularly for x = 0.1 and 0.23. Usually, the asymmetric XRD peaks can occur from several causes, such as two phases, stacking fault, concentration gradient, dislocation, or strain. In our case, we believe that it could be due to strain contribution since the larger atoms of Ge were substituted for Si in these alloys. The addition of B with smaller size atoms can accommodate the strain. Thus the asymmetric peaks are reduced for increasing B content. The lattice parameters (a) calculated from these XRD patterns are summarized in Table 1, which shows that the a value is relatively the same for every sample (about

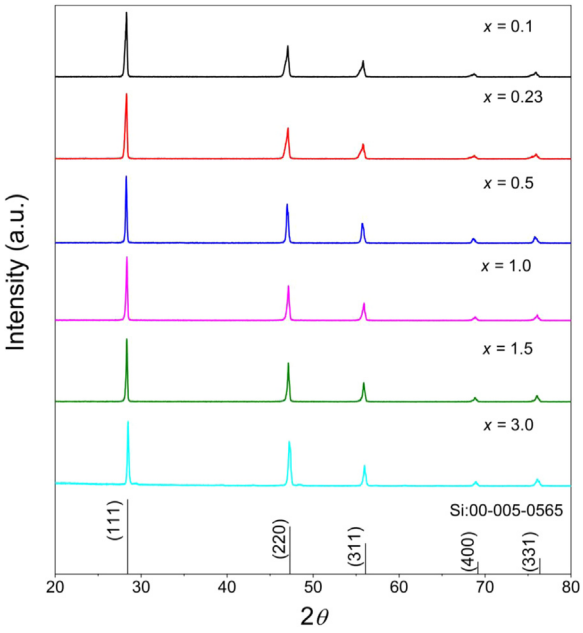

Fig. 1. Powder XRD patterns of the $Si_{80}Ge_{20}B_x$ (x = 0.1, 0.23, 0.5, 1.0, 1.5, 3.0) bulk samples.

Table 1
Summary of lattice parameter (a), grain size, density (d), % of theoretical density (%TD), Hall carrier concentration (n), and Hall mobility (μ) of $Si_{80}Ge_{20}B_x$.

Composition of B (x)	Lattice parameter, a (nm)	Grain size (μm)		d (g cm^{-3})	%TD	n ($\times$ 10^{20} cm^{-3})	μ (cm^2 V^{-1} s^{-1})
		MS	SPS				
0.1	0.5470	1.18	1.98	2.87	96	1.51	17.5
0.23	0.5468	1.11	1.86	2.87	96	2.25	19.7
0.5	0.5469	1.16	1.94	2.88	96	2.31	22.1
1	0.5470	1.27	1.97	2.87	96	2.54	20.8
1.5	0.5471	1.18	1.97	2.89	96	3.11	20.3
3	0.5469	1.32	1.95	2.87	96	6.22	15.7
0.23 [7]	–	–	–	2.96	–	1.54	29.2

0.5470 ± 0.0002 nm), independent of B concentration. Table 1 also summarizes other physical parameters of the samples at room temperature: grain size before and after SPS, density, percentage of theoretical density (%TD), Hall carrier concentration (n), and mobility (μ). The bulk densities of all samples are about 2.87–2.89 g cm^{-3} corresponding to 96%TD which is one of the important keys to achieve good TE properties [4,21].

The SEM images of $Si_{80}Ge_{20}B_x$ on the contact surface before SPS (MS ribbons) and the polished surface after SPS are shown in Fig. 2. It is clearly seen that all samples are very dense. The equiaxed grains were observed implying the isotropic properties of the samples. The grain growth was found after SPS as shown in Table 1 and in Fig. S1 (Supporting Information). However, the average grain size is independence of B concentration either for the MS ribbons or the SPS samples. The chemical composition of the bulk $Si_{80}Ge_{20}B_x$ samples were analyzed by using the EDS mapping technique, as shown in Fig. 3. The measured compositions were very close to the nominal ones for Si and Ge, as shown in Table 2, but the concentration of B could not be determined due to the limit of the instrument. The elemental maps showed that Si and Ge were distributed across the whole images at relative wide field of views. At closer look, the Si-rich (Ge-depleted) regions inside grains and the Si-depleted (Ge-rich) regions at grain boundaries can be observed. However, though different in composition for each region, the samples are still the single-phase solid solution alloys since the Si and Ge display complete solid solubility [35]. The single-phase formation was also confirmed by XRD in Fig. 1 which indicated the satisfaction of the fabrication technique.

Temperature dependence of the TE properties of the p-type $Si_{80}Ge_{20}B_x$ samples is shown in Fig. 4. The data from the RTG sample in reference [7] is also plotted. Fig. 4(a) shows the positive values of the Seebeck coefficient (S) for all samples in the whole temperature range. This shows the p-type conducting behavior of the B-doped SiGe. Furthermore, S increased with increasing temperature but decreased with increasing B concentration. Fig. 4(b) shows the electrical conductivity (σ) which decreased with temperature for all measurement temperatures, suggesting the electrical transport behavior for degenerated semiconductors [36]. The σ of $Si_{80}Ge_{20}B_x$ varied with B concentration such that the higher B the larger σ.

The variation of S and σ with B concentration for $Si_{80}Ge_{20}B_x$ is due to the difference in carrier concentrations. As larger amount of B is doped in SiGe, it generated higher hole concentration. The Hall measurement summarized the values of carrier concentration (n) and mobility (μ) as shown in Table 3. It is shown that n increased with the amount of B but no clear trend was found for μ. Generally, for metals or degenerated semiconductors, the Seebeck coefficient is inversely proportional to n according to the equation [6]:

$$S = \frac{8\pi^2 k_B^2}{3eh^2} m^* T \left(\frac{\pi}{3n}\right)^{2/3} \quad (1)$$

where k_B, e, h are Boltzman's constant, elementary charge, and Planck's constant, respectively. Therefore, with increasing n due to higher B concentration, the S dropped monotonically. On the other hand, the electrical conductivity is directly proportional to n according to the relation:

$$\sigma = ne\mu \quad (2)$$

Since μ is almost independent of B concentration (Table 1), σ increase linearly with the added amount of B.

The power factor ($S^2\sigma$) of $Si_{80}Ge_{20}B_x$ is illustrated in Fig. 4(c) which shows a variation of the power factor with B concentration. Compared to the RTG reference data, the power factors of most samples show relative lower values, with exception for x = 0.5 and 1.0 which show the larger power factors at high temperature range. The maximum power factor of 2.3 mW m^{-1} K^{-2} was obtained at 1073 K for x = 1.0.

Fig. 4(d) shows the decrease of thermal conductivity (κ) with increasing temperature for all samples. The measured κ for x = 1.0, 1.5, 3.0 are very similar to the RTG reference data for the whole temperature range. On contrary, for the lower B concentration (x = 0.1, 0.23, 0.5), κ were significantly lower than the RTG data. The total thermal conductivity (κ) is contributed from two components: the electronic thermal conductivity (κ_e) and the lattice thermal conductivity (κ_{lat}). The electronic thermal conductivity can be estimated from the Wiedemann-Franz law [37]:

$$\kappa_e = L\sigma T \quad (3)$$

where L is the Lorenz number ~ 2.44 × 10^{-8} W Ω K^{-2}. Therefore, κ_{lat} can be calculated and are represented in Fig. 4(e). The κ_{lat} of all samples decreased with increasing temperature implying that the phonon-phonon scattering is the main scattering mechanisms for κ_{lat} [37]. Furthermore, the values of κ_{lat} are nearly the same for every $Si_{80}Ge_{20}B_x$ sample throughout the measurement temperature. Therefore, the reason for the increasing total κ with higher B concentration in Fig. 4(d) is attributed to the κ_e contribution since σ increase with the amount of B. The addition of B in SiGe has almost no effect on the phonon transport. This implication is in fact supported by the XRD analysis where the lattice constant is insignificantly changed with B concentration. Therefore, the phonon transport is not interrupted by B addition.

The dimensionless figure-of-merit, ZT as a function of temperature is shown in Fig. 4(f). It can be seen that the ZT of every sample increases with temperature. The maximum of 0.71 at 1073 K is found for x = 0.5, which is about 40% higher than that of the RTG reference (ZT ~ 0.5 at 1073 K). However, our peak value of ZT is still lower than some of the literature values reported recently for the p-type SiGe, for example, Zebarjadi et al. with ZT of 0.92 at 1173 K [19], Joshi et al. with ZT of 0.95 at 1073 K [10], or Bathula et al. with ZT of 1.2 at 1173 K [20]. To investigate the effect of B concentration on the maximum ZT, we plotted ZT_{max} against B concentration as shown in Fig. 5. There exists a peak value around the B concentration of 0.5. This is justified since adjusting B concentration leads to a change in carrier concentration which certainly affects the TE properties. Only the optimized carrier concentration results in the peak ZT. Furthermore, the variation of the data follows a log-normal distribution (red curve), which is typically observed in any kind of TE materials [6,33,38].

From this part of the experiments, the composition $Si_{80}Ge_{20}B_{0.5}$

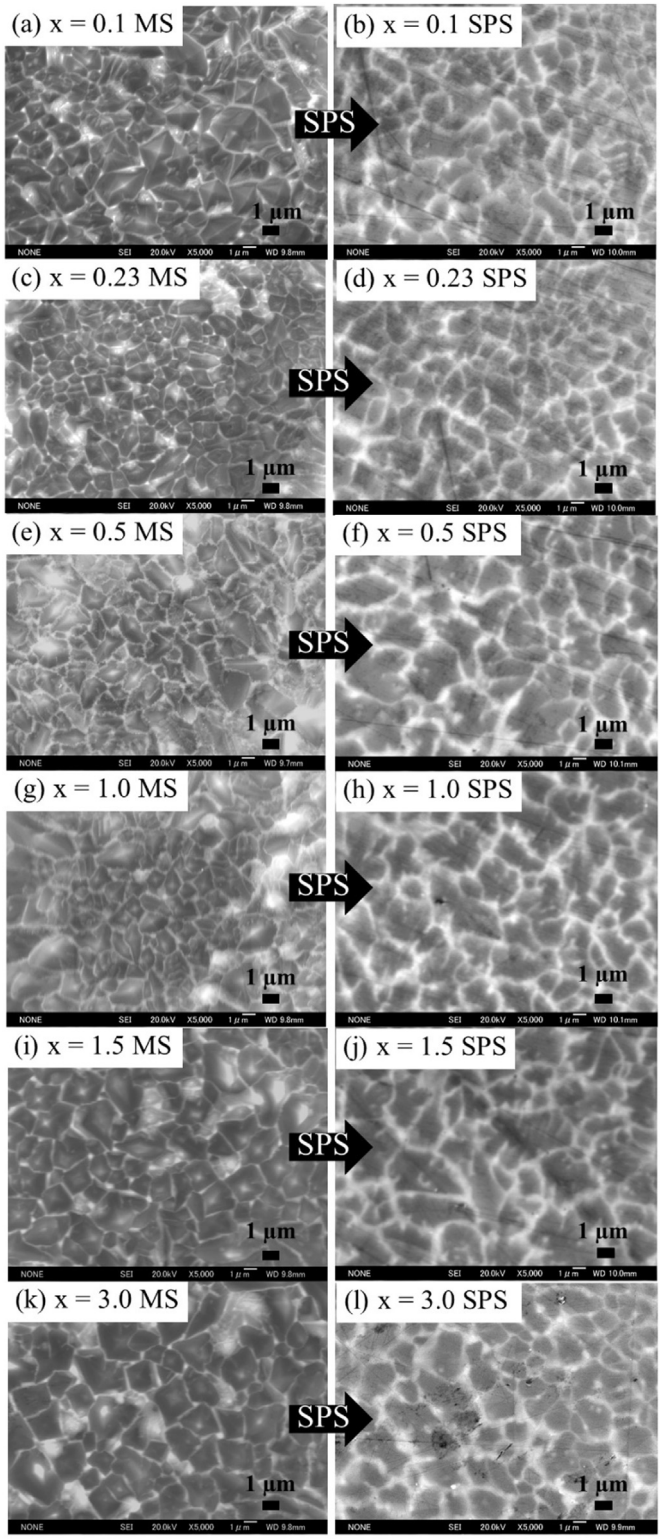

Fig. 2. SEM images of the $Si_{80}Ge_{20}B_x$ alloys (x = 0.1, 0.23, 0.5, 1.0, 1.5, 3.0) on the contact surface before SPS (left) and the polished surface after SPS (right).

shows the largest *ZT* for most of the temperature range. This composition was then subjected to the investigation of the processing parameter optimization.

3.2. Optimization of processing parameters

The processing parameters of interest in the present study are the rotating speed of the Cu wheel in the melt spinning (MS) process, and the holding time in the SPS process. Firstly, the rotating speed of the Cu roller was adjusted from 2000 rpm 6000 rpm (equivalent to ~ 21 – 63 m/s). In the previous experiment, the speed of 2000 rpm was exploited. By increasing the rotating speed, it is assumed that the molten alloys would be solidified more rapidly and would result in more refined microstructure of the ribbon samples which in turn could improve thermoelectric characteristics of the bulk samples.

The photographs of the $Si_{80}Ge_{20}B_{0.5}$ ribbon samples produced at different rotating speed are shown in Fig. 6. It is clearly seen that increasing the rotating speed resulted in smaller ribbons. The ribbon melt spun at 2000 rpm could be several centimeters long but at 6000 rpm the samples are at millimeters or sub-millimeters length scale. After crushing and compressing under SPS, the investigation for the phase and crystal structures of the samples was carried out using powder XRD, as shown in Fig. 7. The main peaks of all samples agreed well with standard Si peaks (JCPDS Card No. 00-005-0565), indicating that the rotating speed did not affect the crystal structure. The lattice parameters of the bulk samples were analyzed and summarized in Table 3. Similar to what found the Section 3.1, the lattice parameters did not change significantly with the Cu wheel rotating speed. The *a* value was still relatively about 0.5470 ± 0.0002 nm for every processing condition. Also presented in Table 3 are the densities after SPS which are very high (~ 96% of theoretical density) for every sample.

The SEM image of the $Si_{80}Ge_{20}B_{0.5}$ samples after MS (contact surface) and after SPS (polished surface) under different rotating speed are shown in Fig. 8. It can be seen that increasing the rotating speed of the Cu wheel resulted in the smaller grain sizes for both the ribbon samples (Fig. 8 left) and the bulk samples after SPS (Fig. 8 right). Quantitative analysis of the grain sizes is shown in Fig. S2 (Supporting Information). Obviously, one can see that though the rotating speed did not affect much for the grain size of the melt spun (MS) ribbon samples, it did have a significant effect on the SPS bulk samples. The grain size of the SPS sample at the speed of 2000 rpm was found to be around 2.0 μm but substantially reduced to ~ 1.1 μm at the speed of 6000 rpm, with very small grain growth compared to the grain size of the ribbon at the same speed (~ 0.9 μm). The reduction in the grain size was expected to have an influence on thermoelectric properties.

Temperature dependence of the thermoelectric properties of the $Si_{80}Ge_{20}B_{0.5}$ bulk samples is shown in Fig. 9. Interestingly, all the TE properties (S, σ, κ) for different rotating speed are insignificantly different throughout the measurement temperature. For all samples, the S values were positive for the whole temperature range (Fig. 9a) indicating the *p*-type semiconducting behavior with hole as charge carrier, which was supported by the Hall measurement. The σ values decreased with increasing measurement temperature (Fig. 9b), implying the degenerated semiconducting behavior. The similarity of the TE properties for the samples with different rotating speed is totally unexpected. However, plausible explanations can be found. Firstly, it can be explained regarding the carrier concentration (n) and mobility (μ) from the Hall measurement as summarized in Table 3. Increasing rotating speed did not result in the obvious changing trend of n and μ. This is understandable since the level of dopants in the samples did not change, the carrier concentration level was expected to be invariant (n ~ 2×10^{20} cm^{-3}). Furthermore, the mean free path of holes in Si-based materials is much shorter than the microstructural length scale of the present samples [11,21]. Therefore, such reduction of grain size (down to 1.0 μm) has no contribution to the scattering rate of hole transport. As a result, the power factor is nearly the same for the samples subjected to different rotating speed in MS process (Fig. 9c).

It should be mentioned that in the previous works, the melt spinning technique was employed in refining the microstructure of Si/silicides systems. For instance, in the Si ribbon dispersed with VSi_2 particles, the size of the VSi_2 particles were significantly reduced to a few nanometers when the Cu wheel was rotated at high speed [31]. Also, in the Si-$CrSi_2$ alloys, using the melt spinning technique created the nanostructures

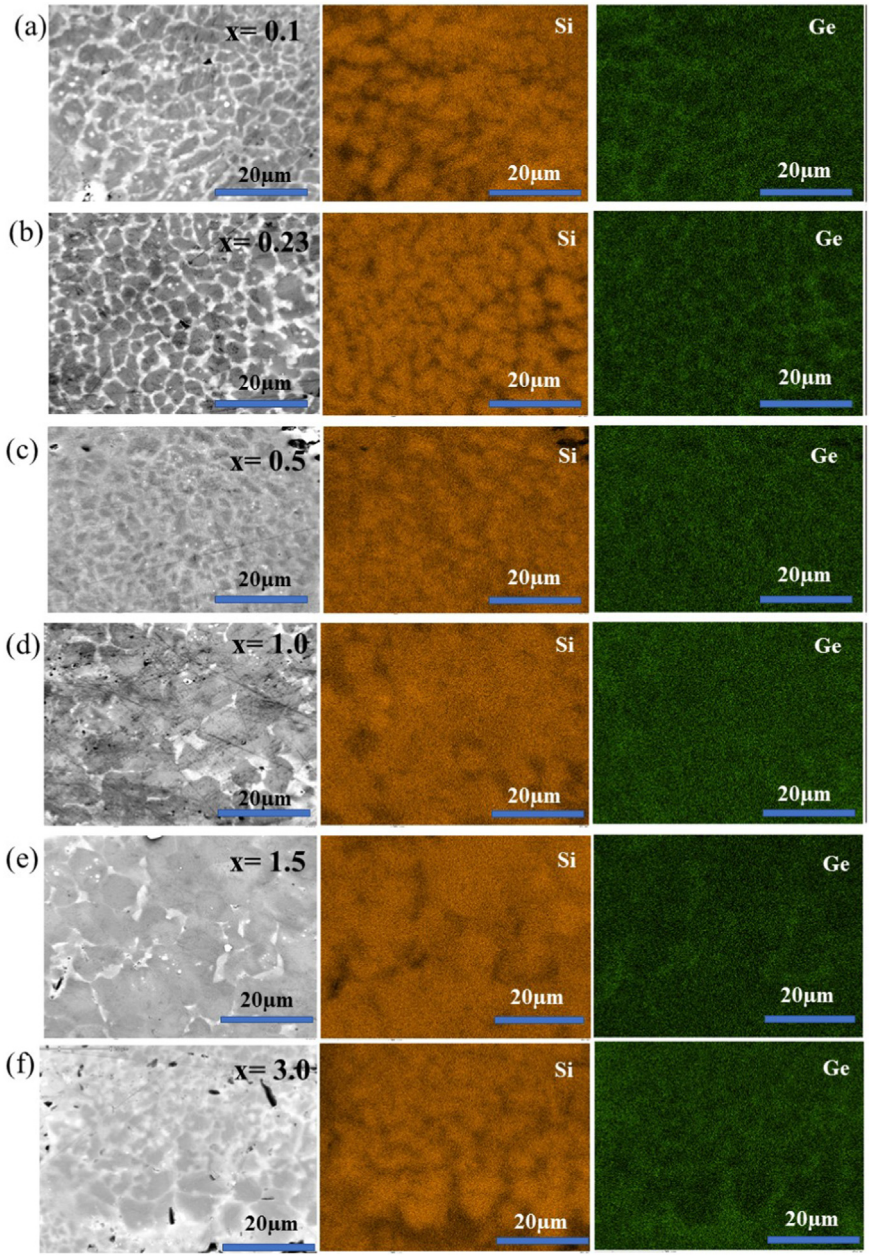

Fig. 3. EDS mapping images of the $Si_{80}Ge_{20}B_x$ bulk samples: (a) x = 0.1, (b) x = 0.23, (c) x = 0.5, (d) x = 1.0, (e) x = 1.5, and (f) x = 3.0.

Table 2
Chemical composition of $SiGeB_x$ (x = 0.1, 0.23, 0.5, 1.0, 1.5 and 3.0) determined through the EDS analysis (at%).

Samples $Si_{80}Ge_{20}B_x$	Composition (at%)		
	Si	Ge	B
0.1	80.87	19.13	–
0.23	81.17	18.83	–
0.5	80.49	19.51	–
1.0	79.76	20.24	–
1.5	80.01	19.99	–
3.0	80.10	19.90	–

with the scale of 20–40 nm at the eutectic composition ($Cr_{14.9}Si_{85.1}$) [30]. However, in these two examples, the grain sizes of the bulk Si were in a range of a few microns. Therefore, the results in the present study were supported by the previous studies.

Fig. 9d shows the temperature dependence of κ which is nearly the same for all samples. After subtracting κ_e, κ_{lat} as a function of temperature was plotted as shown in Fig. 9e. Again, no distinct difference was found amongst any sample. The implication is that the grain size reduction by increasing rotating speed did not further contribute to phonon scattering. According to previous reports, in order to reduce phonon transport, all-scale hierarchical architectures needs to be introduced to the material bulk structure [4,38]. The solid solution and nanoparticles can effectively scatter a significant portion of phonon with shorter mean free path (MFP) whereas the phonon with longer MFP can be controlled by the mesoscale architecture, such as grain boundaries with the grain size of sub-micrometer scale. The grain size reduction in the present work was still in the micrometer regime whereas the average phonon MFP in SiGe alloys was about 200 – 300 nm [11,21]. Therefore, only minority portion of phonon was scattered at grain boundaries, and κ_{lat}, hence was not effectively reduced.

Combining the TE measurement in Fig. 9a–d, the *ZT* values were

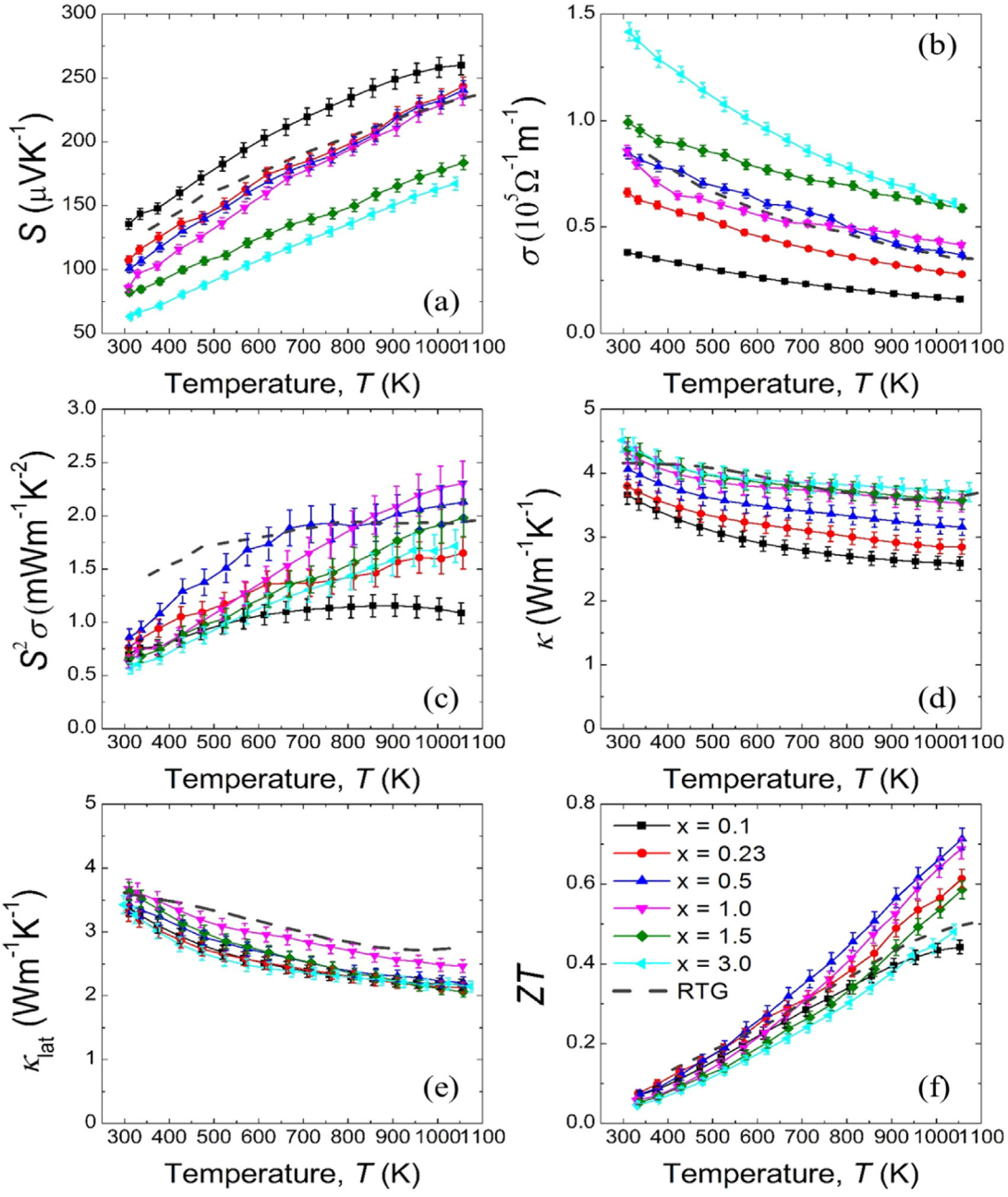

Fig. 4. Temperature dependence of (a) Seebeck coefficient (S), (b) electrical conductivity (σ), (c) power factor ($S^2\sigma$), (d) thermal conductivity (κ), (e) lattice thermal conductivity (κ_{lat}), and (f) the dimensionless figure-of-merit (ZT) for the $Si_{80}Ge_{20}B_x$ bulk samples (x = 0.1, 0.23, 0.5, 1.0, 1.5 and 3.0).

Table 3
Summary of lattice parameter (a), grain size, density (d), % of theoretical density (%TD), Hall carrier concentration (n), and Hall mobility (μ) of $Si_{80}Ge_{20}B_{0.5}$ with changing rotating speed of Cu wheel in the melt spinning (MS) process.

Cu wheel rotating speed (rpm)	Lattice parameter, a (nm)	Grain size (μm)		d (g cm^{-3})	%TD	n (× 10^{20} cm^{-3})	μ (cm^2 V^{-1} s^{-1})
		MS	SPS				
2000	0.5469	1.16	1.94	2.88	96	2.31	22.1
3000	0.5470	1.10	1.88	2.87	96	2.09	27.2
4000	0.5470	1.05	1.47	2.88	96	1.89	29.5
5000	0.5471	0.95	1.18	2.87	96	2.44	22.4
6000	0.5470	0.87	1.06	2.89	97	1.98	27.6

plotted as shown in Fig. 9f. It is obvious that ZT of the $Si_{80}Ge_{20}B_{0.5}$ bulk sample is independent of the Cu wheel rotating speed in the MS process. However, at high temperature regime the ZT values of every sample are significantly larger than the RTG reference.

Next, the holding time in the SPS process was investigated. The idea of this experiment was to introduce voids or pores into the microstructure of $Si_{80}Ge_{20}B_{0.5}$ bulk materials. It was previously investigated that the introduction of nanopores in $Si_{80}Ge_{20}$ alloys could significantly enhance the ZT by mainly suppressing the κ_{lat} contribution by several folds [20]. Therefore, in our experiment, it was aimed to create such pores by varying the holding time in the SPS process. The $Si_{80}Ge_{20}B_{0.5}$ melt spun ribbons (at the speed of 2000 rpm) were compressed to the bulk form by SPS at 1323 K using the holding time of 3, 4, 5, 6 and 7 min.

The effect of holding time on the density of the bulk $Si_{80}Ge_{20}B_{0.5}$ samples was investigated and shown in Fig. 10. It is clearly seen that the

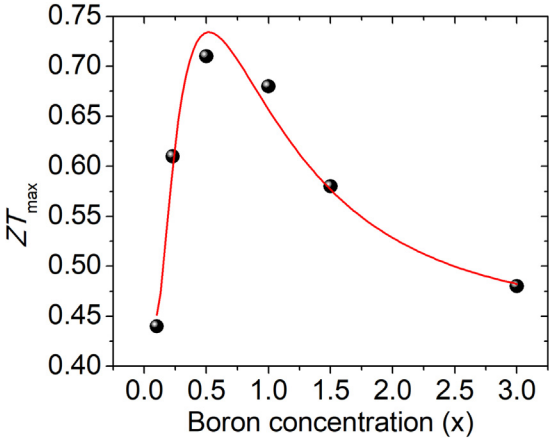

Fig. 5. ZT_{max} of $Si_{80}Ge_{20}B_x$ as a function of boron concentration.

density was significantly reduced when the SPS holding time was below 5 min, but was relatively stable (with approximately 96% of theoretical value) for the holding time of 5 min and above. Thus, there exists the threshold of the SPS holding time of at least 5 min to obtain the highest density. Below 5 min, the density decreased with increasing porosity within the structure, which may have an effect on TE characteristics.

To test the hypothesis, the TE properties of the bulk sample with different SPS holding time was studied as shown in Fig. 11. It is clearly seen in Fig. 11a that shortening the holding time suppressed the thermal conductivity as the κ for 3 and 4 min are significantly lower

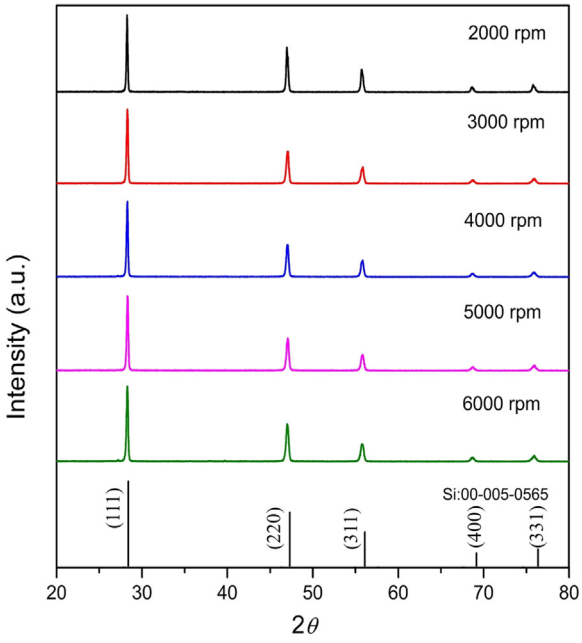

Fig. 7. Powder XRD patterns of the $Si_{80}Ge_{20}B_{0.5}$ bulk samples produced from the difference in the Cu wheel rotating speed (2000–6000 rpm).

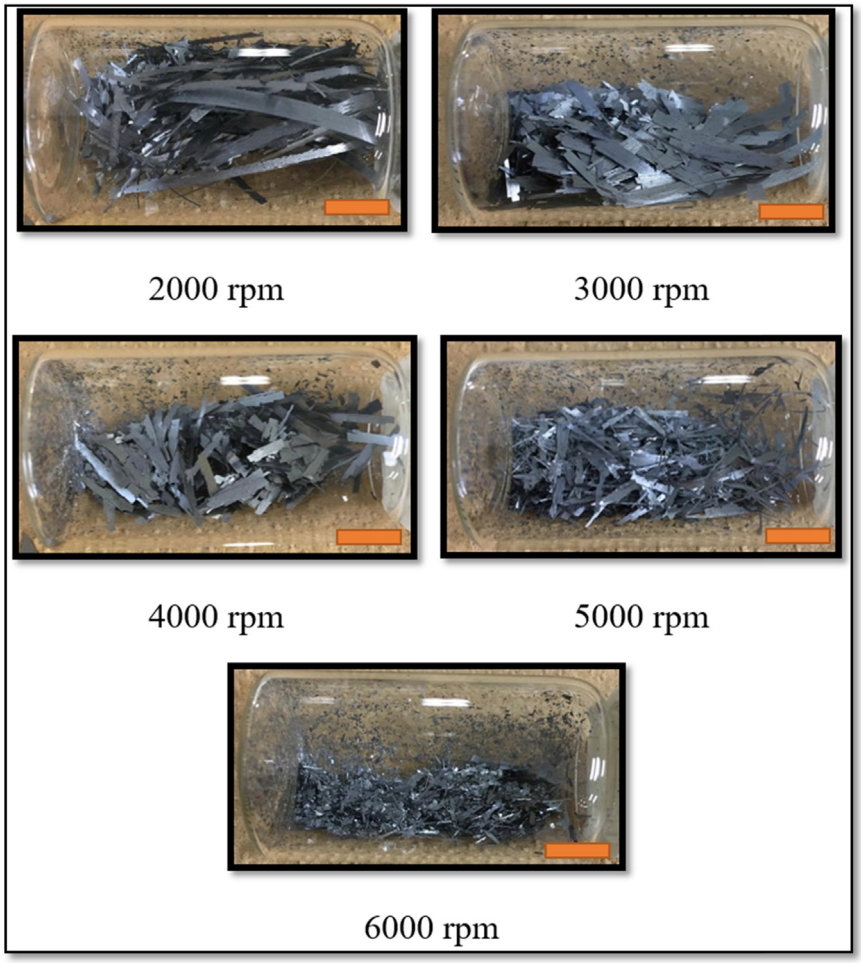

Fig. 6. Photographs of the melt spun $Si_{80}Ge_{20}B_{0.5}$ ribbon samples produced from the Cu wheel rotating speed of 2000–6000 rpm. The scale bars are 1 cm.

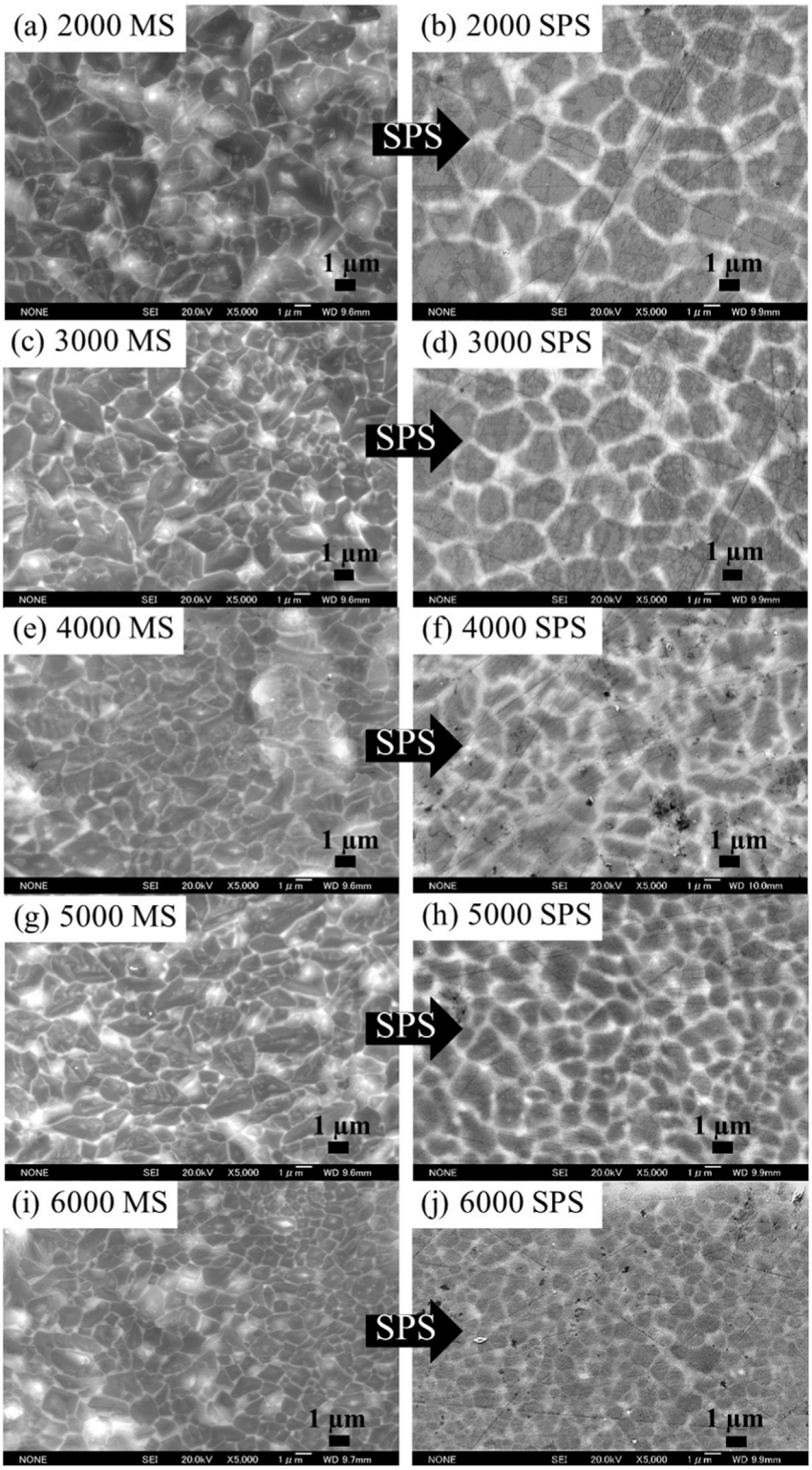

Fig. 8. SEM images of the $Si_{80}Ge_{20}B_{0.5}$ alloys produced from the difference in the Cu wheel rotating speed (2000–6000 rpm) on the contact surface before SPS (left) and the polished surface after SPS (right).

than other samples. Further analysis shows that the effect of shortening SPS holding time suppress the phonon contribution as the κ_{lat} are very low for the samples with 3 and 4 min holding time (Fig. 11b). The other samples exhibited insignificantly different values of κ_{lat}. It can be inferred that as the holding time was shortened, the SiGe grains of the bulk samples were not well connected fused and the micro/nano pores were created which acted as phonon scattering sites [39,40]. These factors effectively scatter phonon and suppress the κ and κ_{lat} as observed in Fig. 11a and b.

Although thermal transport of the bulk samples was successfully reduced by lowering the holding time in the SPS process, unfortunately, it had a direct impact on the electrical contribution. As shown in Fig. 11c, the power factors are not different for the holding of 5 min and above, but the power factor significantly dropped for the samples with

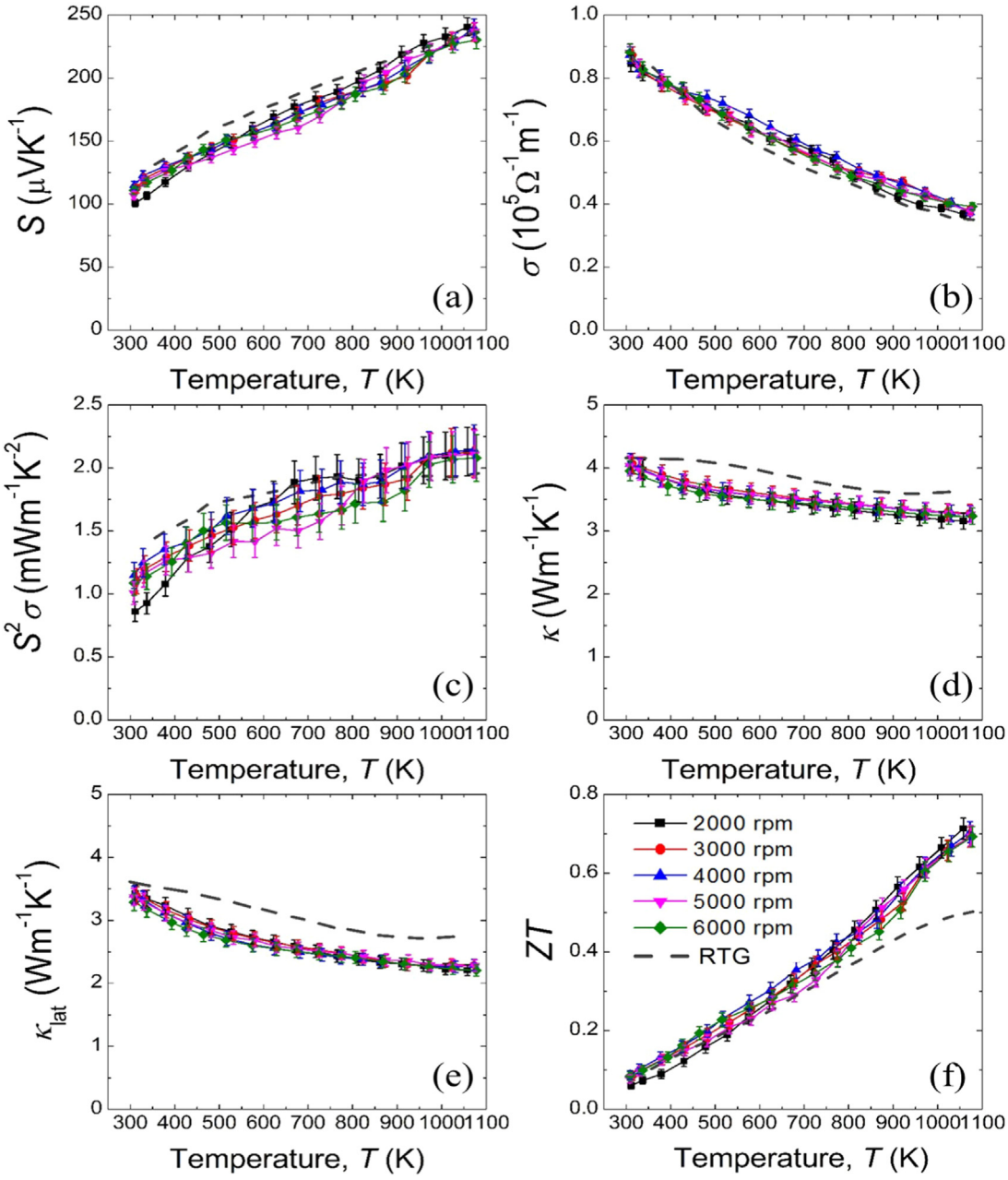

Fig. 9. Temperature dependence of (a) S, (b) σ, (c) $S^2\sigma$, (d) κ, (e) κ_{lat}, and (f) ZT for the $Si_{80}Ge_{20}B_{0.5}$ bulk samples produced from the difference in the Cu wheel rotating speed (2000–6000 rpm).

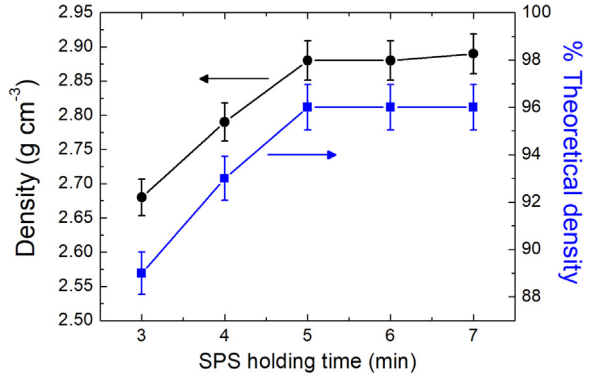

Fig. 10. Measured density and %theoretical density of the $Si_{80}Ge_{20}B_{0.5}$ bulk samples as a function of SPS holding time.

the SPS holding time of 3 and 4 min. The substantial decrease in the power factor was also due to the increase of porous structures in the samples which did not only suppress phonon but also scattered electron strongly [39–41]. It was previously shown that the power factor in several thermoelectric materials was maximized in highly dense bulk material [38,42,43]. Therefore, acquiring highly dense bulk sample with the density of > 95% of the theoretical value is very critical to achieve large power factors.

Lastly, by combining the measured TE properties, the ZT were calculated and shown in Fig. 11d. One can see that no significant difference in ZT can be found in any sample throughout the whole temperature range. The ZT could not be improved further by adjusting the holding time in the SPS process. In fact, through literatures, the effect of SPS holding time was found to be less influential to the TE properties compared to the other SPS parameters, e.g. temperature, heating rate, applied pressure [42,44]. However, though the ZT was not enhanced,

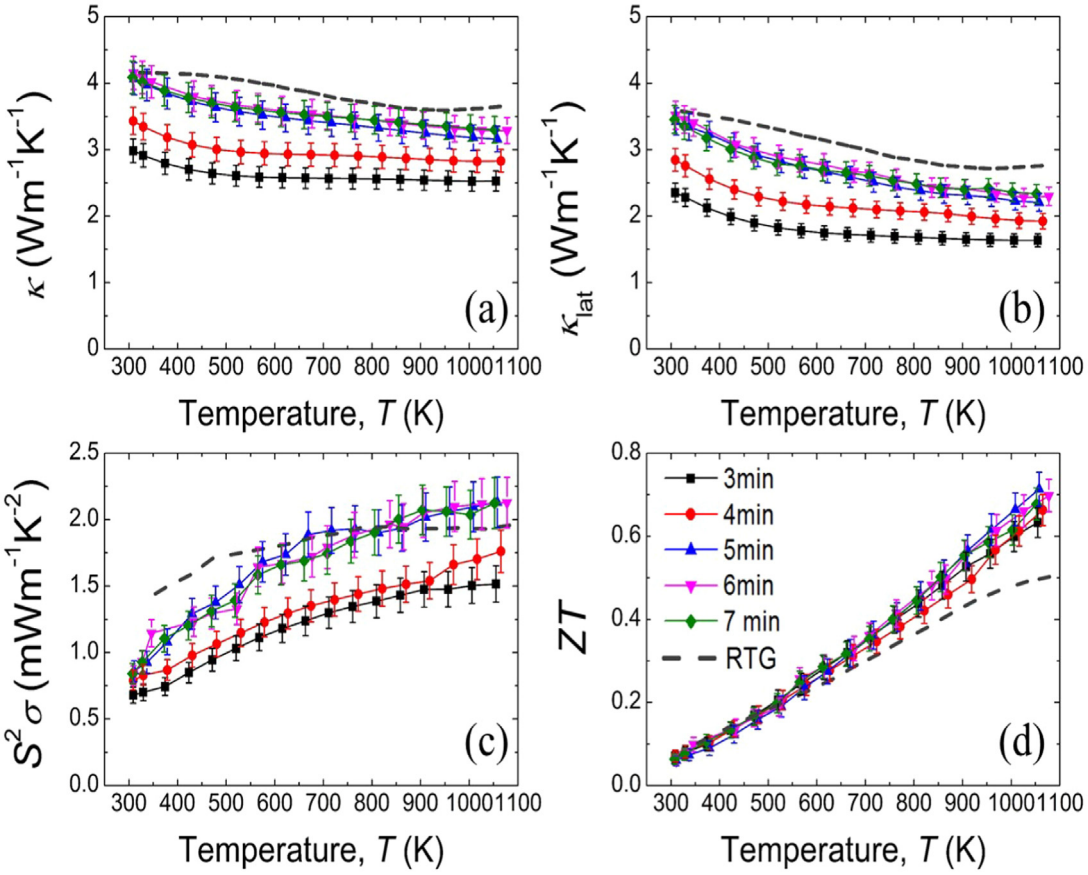

Fig. 11. Temperature dependence of (a) κ, (b) κ_{lat}, (c) $S^2\sigma$, and (d) ZT for the $Si_{80}Ge_{20}B_{0.5}$ bulk samples produced from the difference in SPS holding time (3–7 min).

the ZT in all samples were much larger than the RTG reference, especially at high temperature. It should be noted that the minimum holding time of 5 min was recommended since it provided the minimum time to achieve > 95% theoretical density. Highly dense sample also had a benefit for exhibiting good mechanical properties, reliability and durability [34,45,46].

4. Conclusions

The p-type $Si_{80}Ge_{20}B_x$ alloys were successfully fabricated by a combination of arc melting, melt spinning and spark plasma sintering. The effect of B concentration was investigated and was found that the carrier concentration varied proportionally with B content. Thus, S decreased and σ increased with B concentration with the optimum values around x = 0.5 – 1.0. κ increased with the amount of B but κ_{lat} was mostly unchanged. The best nominal composition of was found to be $Si_{80}Ge_{20}B_{0.5}$ with the maximum ZT of 0.71 at 1073 K, approximately 40% higher than the RTG reference. Moreover, the dependence of the Cu wheel speed in the MS process on the microstructure and TE properties was examined. The grain sizes of the ribbon samples and the bulk samples were evidently reduced with the faster Cu wheel. Nevertheless, the TE properties were indifferent for any rotating speed, probably due to the insufficient reduction of the grain sizes to nanometer regime. SPS holding time was another factor studied in the present work. It was found that the shorter SPS holding time resulted in the samples with lower densities. The porosity might have formed in the less compacted samples which led to the suppressed κ when the holding time was shorter than 5 min. However, the porous structures also interrupted electrical transport causing the decrease in the power factor. Consequently, the optimized holding time was about 5 min to assure the fully dense sample which possess both excellent TE and mechanical properties.

Acknowledgements

This work is supported by the Thailand Research Fund (TRF) in cooperation with Khon Kaen University (RSA5980014), the Royal Golden Jubilee Ph.D. Program (PHD/0192/2556), and the National Research Council of Thailand through Khon Kaen University.

Appendix A. Supplementary material

Supplementary data associated with this article can be found in the online version at doi:10.1016/j.mssp.2018.08.020.

References

[1] J. He, Y.F. Liu, R. Funahashi, J. Mater. Res. 26 (2011) 1762–1772.
[2] W.S. Liu, X. Yan, G. Chen, Z.F. Ren, Nano Energy 1 (2012) 42–56.
[3] T.M. Tritt, M.A. Subramanian, MRS Bull. 31 (2006) 188–194.
[4] K. Biswas, J.Q. He, I.D. Blum, C.I. Wu, T.P. Hogan, D.N. Seidman, V.P. Dravid, M.G. Kanatzidis, Nature 490 (2012) 414–418.
[5] B. Poudel, Q. Hao, Y. Ma, Y.C. Lan, A. Minnich, B. Yu, X.A. Yan, D.Z. Wang, A. Muto, D. Vashaee, X.Y. Chen, J.M. Liu, M.S. Dresselhaus, G. Chen, Z.F. Ren, Science 320 (2008) 634–638.
[6] G.J. Snyder, E.S. Toberer, Nat. Mater. 7 (2008) 105–114.
[7] D.M. Rowe, CRC Handbook of Thermoelectrics, CRC Press, Boca Raton; London, 1995.
[8] R. Basu, S. Bhattacharya, R. Bhatt, M. Roy, S. Ahmad, A. Singh, M. Navaneethan, Y. Hayakawa, D.K. Aswal, S.K. Gupta, J. Mater. Chem. A 2 (2014) 6922–6930.
[9] S. Bathula, M. Jayasimhadri, N. Singh, A.K. Srivastava, J. Pulikkotil, A. Dhar, R.C. Budhani, Appl. Phys. Lett. 101 (2012) 213902.
[10] G. Joshi, H. Lee, Y.C. Lan, X.W. Wang, G.H. Zhu, D.Z. Wang, R.W. Gould, D.C. Cuff, M.Y. Tang, M.S. Dresselhaus, G. Chen, Z.F. Ren, Nano Lett. 8 (2008) 4670–4674.
[11] X.W. Wang, H. Lee, Y.C. Lan, G.H. Zhu, G. Joshi, D.Z. Wang, J. Yang, A.J. Muto, M.Y. Tang, J. Klatsky, S. Song, M.S. Dresselhaus, G. Chen, Z.F. Ren, Appl. Phys. Lett. 93 (2008) 193121.

[12] G.H. Zhu, H. Lee, Y.C. Lan, X.W. Wang, G. Joshi, D.Z. Wang, J. Yang, D. Vashaee, H. Guilbert, A. Pillitteri, M.S. Dresselhaus, G. Chen, Z.F. Ren, Phys. Rev. Lett. 102 (2009) 196803.
[13] S. Bathula, M. Jayasimhadri, B. Gahtori, A. Kumar, A.K. Srivastava, A. Dhar, Phys. Chem. Chem. Phys. 19 (2017) 25180–25185.
[14] S. Ahmad, A. Singh, A. Bohra, R. Basu, S. Bhattacharya, R. Bhatt, K.N. Meshram, M. Roy, S.K. Sarkar, Y. Hayakawa, A.K. Debnath, D.K. Aswal, S.K. Gupta, Nano Energy 27 (2016) 282–297.
[15] J. Mackey, F. Dynys, A. Sehirliogiu, Acta Mater. 98 (2015) 263–274.
[16] A. Nozariasbmarz, P. Roy, Z. Zamanipour, J.H. Dycus, M.J. Cabral, J.M. LeBeau, J.S. Krasinski, D. Vashaee, APL Mater. 4 (2016) 104814.
[17] A. Yusufu, K. Kurosaki, Y. Miyazaki, M. Ishimaru, A. Kosuga, Y. Ohishi, H. Muta, S. Yamanaka, Nanoscale 6 (2014) 13921–13927.
[18] B. Yu, M. Zebarjadi, H. Wang, K. Lukas, H.Z. Wang, D.Z. Wang, C. Opeil, M. Dresselhaus, G. Chen, Z.F. Ren, Nano Lett. 12 (2012) 2077–2082.
[19] M. Zebarjadi, G. Joshi, G.H. Zhu, B. Yu, A. Minnich, Y.C. Lan, X.W. Wang, M. Dresselhaus, Z.F. Ren, G. Chen, Nano Lett. 11 (2011) 2225–2230.
[20] S. Bathula, M. Jayasimhadri, B. Gahtori, N.K. Singh, K. Tyagi, A.K. Srivastava, A. Dhar, Nanoscale 7 (2015) 12474–12483.
[21] Y.C. Lan, A.J. Minnich, G. Chen, Z.F. Ren, Adv. Funct. Mater. 20 (2010) 357–376.
[22] A. Lahwal, S. Bhattacharya, J. He, D. Wu, A. Peterson, S.J. Poon, L. Williams, A.M. Dehkordi, T.M. Tritt, J. Appl. Phys. 117 (2015) 145101.
[23] G. Schierning, R. Theissmann, N. Stein, N. Petermann, A. Becker, M. Engenhorst, V. Kessler, M. Geller, A. Beckel, H. Wiggers, R. Schmechel, J. Appl. Phys. 110 (2011) 113515.
[24] M.L. Snedaker, Y.C. Zhang, C.S. Birkel, H. Wang, T. Day, Y.F. Shi, X.L. Ji, S. Kraemer, C.E. Mills, A. Moosazadeh, M. Moskovits, G.J. Snyder, G.D. Stucky, Chem. Mater. 25 (2013) 4867–4873.
[25] A. Usenko, D. Moskovskikh, M. Gorshenkov, A. Voronin, A. Stepashkin, S. Kaloshkin, D. Arkhipov, V. Khovaylo, Scr. Mater. 127 (2017) 63–67.
[26] C. Suryanarayana, A. Inoue, Bulk Metallic Glasses, 2nd ed., CRC Press, 2017.
[27] M.G. Kanatzidis, Chem. Mater. 22 (2010) 648–659.
[28] X.F. Meng, Z.H. Liu, B. Cui, D.D. Qin, H.Y. Geng, W. Cai, L.W. Fu, J.Q. He, Z. Ren, J.H. Sui, Adv. Energy Mater. 7 (2017) 1602582.
[29] P. Eaksuwanchai, K. Kurosaki, S. Tanusilp, Y. Ohishi, H. Muta, S. Yamanaka, J. Appl. Phys. 121 (2017) 225110.
[30] K. Kurosaki, A. Yusufu, Y. Miyazaki, Y. Ohishi, H. Muta, S. Yamanaka, Mater. Trans. 57 (2016) 1018–1021.
[31] S. Tanusilp, K. Kurosaki, A. Yusufu, Y. Ohishi, H. Muta, S. Yamanaka, J. Electron. Mater. 46 (2017) 3249–3255.
[32] S. Wongprakarn, S. Pinitsoontorn, S. Tanusilp, K. Kurosaki, Phys. Stat. Solidi A 214 (2017) 1700235.
[33] Y. Ohishi, J. Xie, Y. Miyazaki, Y. Aikebaier, H. Muta, K. Kurosaki, S. Yamanaka, N. Uchida, T. Tada, Jpn. J. Appl. Phys. 54 (2015) 071301.
[34] S. Bathula, M. Jayasimhadri, A. Dhar, Mater. Des. 87 (2015) 414–420.
[35] R.W. Olesinski, G.J. Abbaschian, Bull. Alloy Phase Diagr. 5 (1984) 180–184.
[36] D. Jiles, Introduction to the Electronic Properties of Materials, 2nd ed., Nelson Thornes, Cheltenham, 2001.
[37] E.M. Barber, Thermoelectric Materials: Advances and Applications, Pan Stanford Publishing, Singapore, 2015.
[38] A.J. Minnich, M.S. Dresselhaus, Z.F. Ren, G. Chen, Energy Environ. Sci. 2 (2009) 466–479.
[39] M. Gunes, M. Ozenbas, J. Alloy Compd. 626 (2015) 360–367.
[40] H. Lee, D. Vashaee, D.Z. Wang, M.S. Dresselhaus, Z.F. Ren, G. Chen, J. Appl. Phys. 107 (2010).
[41] Q.H. Zhang, L.L. Xu, Z.X. Zhou, L.J. Wang, W. Jiang, L.D. Chen, J. Appl. Phys. 121 (2017) 055104.
[42] L. Han, S.H. Spangsdorf, N.V. Nong, L.T. Hung, Y.B. Zhang, H.N. Pham, Y.Z. Chen, A. Roch, L. Stepien, N. Pryds, RSC Adv. 6 (2016) 59565–59573.
[43] A. Usenko, D. Moskovskikh, A. Korotitskiy, M. Gorshenkov, E. Zakharova, A. Fedorov, Y. Parkhomenko, V. Khovaylo, Scr. Mater. 146 (2018) 295–299.
[44] M. Saleemi, M.S. Toprak, S. Fiameni, S. Boldrini, S. Battiston, A. Famengo, M. Stingaciu, M. Johnsson, M. Muhammed, J. Mater. Sci. 48 (2013) 1940–1946.
[45] R. Murugasami, P. Vivekanandhan, S. Kumaran, R.S. Kumar, T.J. Tharakan, Adv. Powder Technol. 28 (2017) 506–513.
[46] W.S. Liu, Q. Jie, H.S. Kim, Z.F. Ren, Acta Mater. 87 (2015) 357–376.

Magnetic Cement (Cementitious Magnet)

Nattapong Chuewangkam[1], Supree Pinitsoontorn[1, 2,*], Prinya Chindaprasirt[3,4]

[1]*Department of Physics, Faculty of Science, Khon Kaen University, Khon Kaen 40002, THAILAND*
[2]*Institute of Nanomaterials Research and Innovation for Energy (IN-RIE), Research Network of NANOTEC-KKU (RNN), Khon Kaen University, Khon Kaen 40002, THAILAND*
[3]*Sustainable Infrastructure Research and Development Center, Department of Civil Engineering, Faculty of Engineering, Khon Kaen University, Khon Kaen 40002, THAILAND*
[4]*The Academy of Science, The Royal Society of Thailand, Dusit, Bangkok, Thailand*

ABSTRACT

Enhanced functional properties of cement pastes were achieved by introducing hard magnetic powders (NdFeB) in the mixture. The magnetic cement (cementitious magnet) employed a simple and cheap cementitious process to form complex shapes of NdFeB magnets. The NdFeB particles were distributed uniformly in the cement matrix. The density and compressive strength of the magnetic cement composites increased with NdFeB concentration. The magnetization (stable up to one year) also increased with NdFeB powder but the coercivity did not change. The saturation magnetization (~85 emu/g) and coercivity (~7000 Oe) of the magnetic cement composites were larger than a pure Ni, cubic or hard ferrites. The energy product $(BH)_{max}$ was found to be ~1.0 MGOe, comparable to ferrite bonded magnets. The permanent magnetic ability was demonstrated by using the magnetic cement for lifting metallic pieces or other magnetic cements. The endurance of the samples was also tested in two artificial environments.

KEYWORDS: cement; magnetic; NdFeB; composite;
* Corresponding author's e-mail address: psupree@kku.ac.th.

1. Introduction

Cement is one of the most consumed materials for construction [1]. Due to the more demand for the functions of a structure, the functional properties of construction materials have received more attentions [2]. The functional properties of cement can be utilized by the addition of appropriate fillers in cement-matrix composites. The applications of functionalized cement composites may include sensing (strain, damage, temperature), thermal control, vibration reduction, electromagnetic shielding, and energy harvesting [2, 3]. A recent trend is to exploit many types of nano-materials, such as nano-SiO_2, nano-Al_2O_3, nano-TiO_2, nano-clay, and nano-carbon based materials, to improve mechanical properties as well as multi-functionality of cements [4]. For example, Han et al. reported the assembly of carbon nanotube (CNT) and nano carbon black into cement matrix to fabricate smart cement [5]. The flexural strength and electrical conductivity were effectively improved. Their smart cement composites also showed the stable and sensitive piezoelectric properties which could be employed as stress-strain monitoring sensors. In another work, the electrochemical impedance spectroscopy (EIS) was used as a non-destructive test for determining the fracture toughness of cement composites [6]. CNT was added into cement matrix to decrease electrical resistance which was linearly dependent with the fracture toughness of the samples. Liu et al. mixed carbon nanofiber in the cement-based composite to improve electrical conductivity [7]. The alternating current was then applied to the sample to generate Ohmic heating which was necessary to accelerate the hydration reaction and delay the frost damage of cement-based materials under very cold weather. Cement-based composites were also studied for energy storage devices. As an example, Zhang et al. fabricated a structural supercapacitor based on graphene and hardened cement paste [8]. Abundant pores inside hardened cement paste store ionic liquid for energy storage in supercapacitor which led to relatively large specific capacitance with reasonable compressive strength. Electromagnetic wave absorption is another interesting functional property of cement-based composites. Xie et al. introduced helical carbon fibers and expanded glass beads into the cement matrix which showed the high electromagnetic absorbing capacity with wide effective bandwidth [9].

In recent years, an introduction of magnetic particles into cement matrix is also another interesting choice to improve mechanical and other properties of cement-based materials. Iron oxide (Fe_2O_3, Fe_3O_4) nanoparticles (IONs) are amongst the most favorite fillers for mixing in cement. Not only that the cement composites mixed with IONs showed the improvement in their compressive strength [10-13], the other functionalities are also enhanced. For instance, electromagnetic wave absorption of cement-based composite was significantly enhanced when 5% of nano-Fe_3O_4 magnetic fluid was added, which showed a potential application for electromagnetic interference shielding buildings [10]. IONs mixed with cement pastes were also used as an embedded small resonator antenna [14]. The micro-sized IONs were the most effective to improve the performance (a small resonance frequency shift and an increased bandwidth) of the antenna. Moreover, the cement composited with IONs was reported to show an enhancement in the piezoresistive behavior [13]. In another work, ordinary Portland cement (OPC) concrete containing nano-Fe_3O_4 was tested in chloride and sulfate environments [15]. The results showed that the magnetic cement composite was less susceptible to corrosion relative to the reference material. The enhanced electrochemical stability was due to the absence of passive film breakdown and an enhanced electrical resistance to charge transfer. In the research by Seifan et al., magnetic IONs were employed as the protective vehicle for immobilized Bacillus bacteria, which were then loaded

in the OPC mixture [16]. They found that the incorporation of the bacteria in the cement matrix improved a crack healing behavior compared to a control specimen.

Apart from IONs, the mixture of cement matrix with other species of magnetic particles have been studied. Carbon encapsulated Co, Ni, Fe nanoparticles were mixed with cement-based matrix [17, 18]. The cement composites showed the improvement of mechanical properties in the case of Co and Ni nanoparticles but the opposite effect was observed for Fe nanoparticles. Ferromagnetic resonance-electron paramagnetic resonance (FMR/EPR) methods were successfully employed to identify the characteristics of the cement composites containing metallic magnetic nanoparticles [17-19]. Also, Ni fiber was dispersed in cement matrix and the electromagnetic shielding effectiveness of the cement/Ni fiber composites was substantially enhanced for the optimized volume of Ni fiber [20]. From the research so far, only soft magnetic particles have been incorporated into cement composite, but the addition of hard magnetic materials, such as $Nd_2Fe_{14}B$, has never been reported.

$Nd_2Fe_{14}B$ (NdFeB), discovered in 1982 by two research groups independently, is one class of hard magnetic materials with remarkable performance (magnetic remanence (B_r) above 1 T, coercivity (H_c) higher than 1,000 kAm^{-1}, and energy product $(BH)_{max}$ as high as 400 kJm^{-3}) [21, 22]. It has been used in many components, e.g. motors, wind turbine generators, cell phones, hard disk drives, cameras, sensors [23, 24]. Production of NdFeB is more than 80,000 tonnes and it occupies two-thirds of permanent magnets in the worldwide markets [21, 25]. Due to an increasing demand for high performance permanent magnets, such as in highly efficient motors for electric vehicles and robots, a substantial effort to improve the properties of NdFeB magnets has been provided from both industrial and scientific sides. One of obstacles for the development of NdFeB magnet is the capability to produce complex and net shaped magnets [25]. NdFeB is generally classified into two groups: sintered and bonded magnets. Sintered magnets retain nearly full density and maximize the energy product but the formation of complex geometrical shape is difficult due to the limitation of the conventional manufacturing techniques. The advanced technique, such as a direct metal 3D printing by selective laser melting [24], can overcome this difficulty but with the much higher manufacturing cost. On the other hand, bonded magnets are typically fabricated by blending NdFeB powders with polymeric binders, and casted into a mold with the final net shape. This makes the bonded NdFeB have a higher degree of net-shape formability but with a sacrifice of lower energy product. Conventional process in fabrication of bonded magnets include compression molding or powder injection molding. Recently, an additive manufacturing (AM) technique, also known as 3D printing, has been applied to fabricate near-net-shape bonded NdFeB with magnetic and mechanical properties comparable to traditional methods [26-28]. However, a special tool with computer-aided design (CAD) models is required and several processing parameters need to be properly adjusted.

In the present research, we propose a novel idea for fabrication of NdFeB magnets using a cementitious route. NdFeB powders were thoroughly mixed with cement and water, and casted using a simple cementitious process. The complex and net shaped NdFeB magnets were easily obtained. Conversely, this cementitious formed magnet can be considered as a magnetic cement, i.e. a cement-based composite with hard magnetic properties. The magnetic particles provide the enhancement in both mechanical and magnetic properties of the cement/NdFeB composites.

2. Experimental

2.1 Materials

Ordinary Portland cement type I was used in the whole experiment. For magnetic particles, $Nd_2Fe_{14}B$ powders (NdFeB crushed ribbon) were kindly supplied from Magnequench (Korat) Co., Ltd., Thailand. The density of the NdFeB powders was 7.63±0.20 g/cm^3. Particle size distribution was 216±5.8 μm, measured from the particle analyzer equipment (Malvern, Mastersize). The maximum energy product $(BH)_{max}$ was 15.4 MGOe.

2.2 Sample Preparation

To prepare magnetic cement paste, cement, magnetic powders and water were mixed according to the ASTM C305-06, and casted into 25×25×25 mm^3 acrylic molds. After 24 h, the samples were de-molded. The amount of NdFeB powders was varied from 0 to 80 wt.% of the total powder mass. The water-to-cement (W/C) ratio was adjusted between 0.5 and 0.7. The process for forming a magnetic cement sample is very simple and cheap. The movie clip (VDO1) in supplementary section summarize the manufacturing process. As the mass of NdFeB was increased, the mixed paste became more viscous and was difficult for molding. Therefore, the rheology of the magnetic cement paste was tested using a miniature slump (mini-slump) cone test [29, 30]. According to ASTM C143, the paste was poured into a truncated conical mold, which was then lifted in a vertical position. The paste was left to spread, and the diameters of paste were measured. The workability (%W) was calculated from the equation:

$$\%W = \left(\frac{d - d_0}{d_0}\right) \times 100$$

where d is the spread-out diameter of magnetic cement paste, and d_0 is the diameter of the original diameter.

2.3 Characterization techniques

The mechanical properties of the magnetic cement composites were tested by using a universal testing machine (UTM, Chun Yen testing machine Co., Ltd., CY-6040A12). The maximum load of 50 tons was applied at a rate of 50 kN/min until the samples fractured. According to ASTM C109, a 50 mm sample cube is normally used for measuring compressive strength of pastes, but a smaller 25 mm specimen cube has also been successfully used [31-33]. It should be noted that this could result in higher compressive strength values due to the smaller geometry of samples. However, the results can be compared amongst the same sample size.

Magnetic properties were investigated by measuring magnetization (M) versus magnetic field (H) using a vibrating sample magnetometer (VSM) option in the VersaLab instrument (Quantum Design, USA) under a maximum field of 30 kOe.

The distribution of magnetic NdFeB particles in the composite samples was observed under an optical microscope. The microstructure of the samples (fractured surface) was determined using a scanning electron microscope (SEM, LEO 1450VP). Prior to imaging with the SEM, the samples were gold coated to improve conductivity. The chemical composition was analyzed by an energy dispersive X-ray spectroscopy (EDS, Oxford INCA) equipped with the SEM. The information on

phases and crystallinity were collected by X-ray diffraction (XRD) using a diffractometer employing Cu-Kα radiation (PANalytical, Empyrean) in a 2θ range of 10 - 80°.

2.4 Tests under artificial environments

To explore the stability and durability of the magnetic cement composites, the samples were subjected to two artificial environmental conditions. In the first experiment, after the samples were casted for 3 days, they were put in an oven adjusting temperature to 80 °C, and soaked in that temperature for up to 28 days. For the second environmental conditions, the 3-day age pastes were immersed in an artificial sea water for up to 28 days. The properties of samples after both experiments were determined.

3. Results and discussion

Fig. 1 shows the workability of the magnetic cement pastes as a function of NdFeB concentration. For NdFeB of lower than 40 wt.%, the workability is not significantly varied, but at higher than 50 wt.% NdFeB the workability decreased rapidly. Fig. 1b-d show the pictures of the pastes during the workability test. Without magnetic powder, the paste spread out easily representing good rheological flow. For 70 wt.% NdFeB, the paste is so viscous that it holds the shape of the conical mold. At higher NdFeB of 80 wt.%, the paste cannot be formed, due to the excessive amount of magnetic powders and insufficient amount of cement and water, and the samples cannot be molded into the desired shape. With this reason, we thus limit the amount of the NdFeB powder to 70 wt.% for the rest of the experiments.

The picture of a hardened magnetic cement paste is shown in Fig. 2a. The shiny bits of NdFeB flakes can be observed on the surface of the sample. Investigation under an optical microscope (Fig. 2b-e) shows that the magnetic particles are dispersed uniformly. No obvious clusters of the NdFeB powders can be observed. The visualized NdFeB particles increase with increasing amount of the added powders. The particle size falls in the range of a few hundred microns, which are in a good agreement with the measurement by the particle analyzer equipment (Malvern, Mastersize) (216±5.8 μm).

One obvious advantage in mixing magnetic powders into cement is the ease of forming a complex shape. For a demonstration, a cementitious magnet was molded in a variety of shapes, as shown in Fig. 3a. The process is very cheap and simple, compared to other commercialized (e.g. injection molding) or developing (e.g. 3D printing) processes at present [26, 27]. After demolding, a magnetic cement (cementitious magnet) in any shape can be obtained (Fig. 3b), and the homogeneous dispersion of magnetic particles can still be found on the surface of the sample (Fig. 3c). The whole mixing, molding and demolding processes can be seen in movie clip (VDO1) in supplementary section.

The density and compressive strengths of the magnetic cement composites are illustrated in Fig. 4. The density increased with %NdFeB powder since the density of the magnetic powder (7.63±0.20 g/cm^3) is much higher than that of the pure cement paste. The density decreased slightly at the cement age of 28 days (compared to 7-day age), possibly due to the evaporation of water. The compressive strength (Fig. 4b) shows an increasing trend with higher concentration of NdFeB powder. This could be due to a large compressive strength of NdFeB (1,100 MPa) [34]. However,

the increasing trend is not so obvious for the 7-day age of cement pastes since the hydration reaction of the cement is still not matured. For the cement pastes of 28 days, the hydration reaction is more advanced leading to significantly higher compressive strength. Also, the increasing trend of the compressive strength with NdFeB is more obvious. Fig. 4 summarizes that the addition of NdFeB magnetic particles does not only increase the density of the composites but also improves the mechanical property of the samples. This finding proves that the cementitious process (wet process) did not have an effect on NdFeB, which is in fact well-known for its poor corrosion resistance in humid environments [35, 36]. The cementitious route can be applied as a simple and cheap process in fabricating NdFeB composite magnets.

The fractured samples after compression test at 28 days were investigated under SEM and the results are presented in Fig. 5. For the control cement paste without NdFeB powder (Fig. 5a), a smooth and dense surface of calcium silicate hydrate (C-S-H) gel was observed, indicating the mostly complete hydration process of cement and water [37]. For the magnetic cement samples, the magnetic particles are readily visualized with the size around a few hundred microns. The NdFeB particles are homogeneously embedded in the C-S-H gel, without any obvious agglomeration. At the 50% of NdFeB powders (Fig. 5b), the morphology of the C-S-H surface is still smooth and compact as in the case of the pure cement paste. For the lower amount of NdFeB powders, the morphology of every composite surface looks very similar. However, once the amount of the NdFeB increases to 60% and 70%, a significant change in the microstructure is observed (Fig. 5c, d). Although the smooth surface of C-S-H with embedded NdFeB flakes can still be observed, a substantial amount of the unreacted cement powders is found. This is due to insufficient water for a complete hydration reaction with raw cement powders [38]. It is understandable since in these experiments, the W/C ratio was fixed, and as the higher amount of NdFeB powders were loaded into the mixture, the amount of cement was substantially reduced. Consequently, the water was also decreased, leading to insufficient water for complete hydration reaction as observed in Fig. 5c,d. EDX point analysis was used to study the chemical composition of the cement matrix (green square) and the magnetic powder (yellow circle). The results, as tabulated in Table S1 and S2 (supplementary), show that the major elements in the matrix phase include Ca, Si and O, as expected, with some of Al and Fe. In the magnetic powder area, the concentration of Fe was significantly higher, and Nd was presented. The ratio of Fe:Nd is close to the nominal formula, $Nd_2Fe_{14}B$. In addition, the formation of the composite phases was confirmed by the XRD patterns, as shown in Fig. S1 (supplementary).

The magnetization (M-H) curves of the magnetic cement composites are shown in Fig. 6a. As expected, a nearly flat straight line was found for the cement paste without NdFeB, since a pure cement paste is non-magnetic. With the addition of NdFeB powders, the hysteresis loops were observed for the magnetic cement composites. The height of the loops is varied with the amount of NdFeB but the width of the loop is almost the same. For comparison, the M-H curve of the NdFeB powder was also plotted. From Fig. 6a, the values of saturation magnetization (M_s), remanence (M_r), and coercivity (H_c) are extracted and plotted, as shown in Fig. 6b. M_s and M_r increase linearly with NdFeB concentration, which is understandable from the linear combination of the composite phases. The M_s and M_r of the magnetic cement at 70% NdFeB are as high as 85 and 55 emu/g, respectively. As for comparison, the M_s value of the magnetic cement sample is higher than a pure Ni and some cubic ferrites whereas the M_r value is comparable to hard ferrites [23, 39]. The more interesting point is that the magnetization (M_s and M_r) values are very stable in ambient environment up to 300 days (Fig. 7). Typically, the cement hydration is a continuous process for a very long period, meaning that there is a humid environment in the cement paste

sample, which may cause oxidation or corrosion of the NdFeB powders [35, 36]. However, it is not the case for the present work since the magnetization is invariant for up to nearly one year. This finding is quite unexpected but it proves the durability of the magnetic cement composites which make them functional and operational enduringly. On the other hand, the H_c values (~7,000 Oe) are independent of magnetic powder concentration (Fig. 6b), and the same as H_c of raw NdFeB powders. Their values make the magnetic cement composites magnetically 'harder' than some of the commercialized permanent magnets, such as alnico or hard ferrites [39, 40].

One important quantity for a permanent magnet, its figure-of-merit, is defined as the energy product (BH) which can be found from the demagnetizing curve in the second quadrant of the hysteresis curve. Fig. 8a shows the plot of the demagnetizing curve (MH and BH) of the magnetic cement composites with several NdFeB concentrations. The areas under the curves are proportional to the amount of added NdFeB powders. The BH curves are plotted in Fig. 8b, and the maximum energy product $(BH)_{max}$ can be extracted from the peak of the curves as shown in Fig. 8c. As one can see that for a small amount of NdFeB powders, the $(BH)_{max}$ values are negligibly small, but raising the concentration of NdFeB powders leads to an exponential increase of $(BH)_{max}$. However, even for the highest $(BH)_{max}$ for the 70%NdFeB cement composite, its value (~1.0 MGOe) is an order of magnitude lower in comparison to a fully dense NdFeB sintered magnet, and still a few folds lower than other types of permanent magnets, such as hard ferrite or alnico [39, 40]. Even if we compared the $(BH)_{max}$ of the magnetic cement with typical NdFeB bonded magnets [41, 42] or the recently developed additive manufacturing NdFeB bonded magnets [26, 27], it is still several folds lower. The $(BH)_{max}$ of the cementitious magnet in this work is only comparable ferrite bonded magnets [42]. Nevertheless, from Fig. 8c, it is obviously seen that the energy product is increasing exponentially with the addition of NdFeB powder in the cement composite. Hence, increasing the amount of NdFeB powders could substantially boost the $(BH)_{max}$ for several folds. Although as mentioned earlier that the amount of NdFeB was limited due to the formability and moldability of the magnetic cement paste, the issue could possibly be solved by the addition of more water (using higher W/C ratio), or the exploitation of a superplasticizer. Several types of superplasticizers have been employed in preparing cement composites, for example, cement nanocomposites with graphene oxide [43] or nanosilica [44]. The presence of superplasticizer can reduce the amount of water required in mixing the cement pastes and better control the rheological behavior. Alternatively, a higher grade of NdFeB powders with higher $(BH)_{max}$ could be used [22, 41]. Therefore, a way to improve the energy product for a cementitious magnet is certainly possible.

The fabricated magnetic cement samples have been demonstrated for their permanent magnetic ability. As shown in Fig. 9 and the movie clip VDO2 in the supplementary section, the samples could be used to attract and lift metallic paper clips and nails, or other pieces of the magnetic cement samples. They can also stick upside down vertically to a steel bar by their magnetic force (Fig. 9). These demonstrations open up the potential application of the magnetic cement composites as they can be used in magnetic lifting, advanced construction, novel architecture design, decoration, toys etc., apart from the electromagnetic shielding applications [10, 20]. In fact, though in their infancy, magnetic cement composites have been commercialized for inductive applications by a few companies [45-47]. They claimed that their magnetic cement and concrete products, with soft magnetic properties, could be used to enable static and dynamic wireless charging of electric vehicles. These are still the ongoing projects with a very bright future. Therefore, the magnetic cement composite in the present work, with the hard properties, could

easily find a new market. Moreover, one can imagine the use of hard magnetic particles in cement matrix as a mean for resisting crack propagation. Unlike a concept of self-healing concrete where cracks are self-healed by a combination of complicated chemical and physical processes [48], the magnetic force between magnetic particles in cement composites could help resisting the initiation of micro-crack even before it was formed. Nonetheless, a lot more research is required to explore this idea.

In field applications, the samples may be subjected to a variety of environments. Here, we simulate two artificial environments to test the stability and durability of the samples. The magnetic cement composite and also the control sample were either baked at 80 °C for 28 days or soaked in sea water for 28 days. After that, the mechanical and magnetic properties were determined as shown in Fig. 10. Without any treatment, the compressive strength of the magnetic cement composite is higher than the control cement paste. For the treated samples, the compressive strengths decreased compared to the non-treated sample for both the control and magnetic samples. By baking, the cementitious products lost water, and thus the mechanical property was deteriorated. For sea water treatment, the cement matrix was attacked by chlorides and sulfates leading to a decrease in strength [15]. However, the sample with NdFeB powder showed a slightly higher strength for the 80 °C baked sample. This is understandable since some parts of cement were substituted with a stronger NdFeB powders, which was also oxidation resistive at 80 °C [49]. The magnetic composite sample shows a decrease in strength after submerged in sea water but the strength is not significantly different from the control cement paste under the same treatment. The chloride and sulfate components in the sea water do not only have a negative effect on cement matrix but also on corrosion of NdFeB materials as previously reported [50, 51]. Nonetheless, from Fig. 10a it is obvious that the addition of NdFeB powders in the cement composites do not worsen the mechanical property of cement paste under extreme conditions. It implies that the magnetic cement composite can be exploited in a field application as same as a pure cement paste.

The magnetic hysteresis loops of the control and tested samples are shown in Fig. 10b. The sample baked at 80 °C shows an enhanced magnetization compared to the control sample. The loss of water during the annealing process could be the main reason for the higher M_s and M_r. On the other hand, the sample immersed under sea water shows an obvious reduction in magnetization. This is due to the corrosion of NdFeB from chloride and sulfate attacks [50, 51]. The corrosion resistance could be improved by using NdFeB doped with some elements [36] or coated with oxide films [35]. It should be noted that though the magnetization changed by treating the magnetic cement composite in the artificial environments, the coercivity remained relatively unchanged.

Lastly, we have applied the cementitious process in making magnetic cement composites to another binding material: geopolymer. The NdFeB powders have been successfully incorporated into fly ash geopolymer matrix. However, unlike cement, the distribution of NdFeB particles was not very uniform. Magnetic measurement from different parts in the same batch resulted in significant variation of M_s and M_r (Fig. S2 in supplementary). Moreover, the H_c of the composites were substantially reduced compared to the raw magnetic powders. It is probably due to the use alkaline media, such as NaOH and Na_2SiO_3, for geopolymerization process, which could have a negative effect on NdFeB [52].

4. Conclusions

In this work, we have demonstrated that a cementitious route can be used to fabricate NdFeB permanent magnets. The process is very simple and cheap, and can form the cementitious magnets in various shapes. The magnetic particles are found to be homogeneously distributed in the cement matrix. The rheological flow of the magnetic cement paste becomes more difficult for NdFeB powders higher than 50%. The density and strength of the magnetic cement composites increase with higher content of NdFeB, due to the higher density and strength of NdFeB. Magnetic measurement shows that M_s and M_r increase linearly with NdFeB concentration but H_c remains quite stable. The magnetizations of the magnetic cements are higher than for pure Ni or cubic ferrites whereas the coercivity is larger than hard ferrites. The magnetic properties are very stable up to 300 days which proves the durability of the magnetic cement composites. The $(BH)_{max}$ products are still lower than commercial permanent magnets but could be certainly improved. The permanent magnetic ability of magnetic cement was demonstrated for lifting/moving metallic pieces or other magnetic cement pieces. This could open up many novel applications, for instance, electromagnetic shielding, magnetic lifting, advanced construction, novel architecture design, decoration, and toys.

Acknowledgements

This work was supported by the Thailand Research Fund (TRF) in cooperation with Khon Kaen University (RSA5980014), and the Institute of Nanomaterials Research and Innovation for Energy (IN-RIE), Khon Kaen University and the National Nanotechnology Center (NANOTEC), NSTDA, Ministry of Science and Technology, Thailand, through its program of Research Network NANOTEC (RNN). The third author would like to acknowledge the support of the Thailand Research Fund (TRF) under the TRF Distinguished Research Professor Grant No. DPG6180002.

References

[1] Schneider M, Romer M, Tschudin M, Bolio H. Sustainable cement production-present and future. Cement Concrete Res. 2011;41(7):642-50.
[2] Chung DDL. Functional properties of cement-matrix composites. J Mater Sci. 2001;36(6):1315-24.
[3] Lu SN, Xie N, Feng LC, Zhong J. Applications of Nanostructured Carbon Materials in Constructions: The State of the Art. Journal of Nanomaterials. 2015:807416.
[4] Norhasri MSM, Hamidah MS, Fadzil AM. Applications of using nano material in concrete: A review. Constr Build Mater. 2017;133:91-7.
[5] Han BG, Zhang LQ, Sun SW, Yu X, Dong XF, Wu TJ, et al. Electrostatic self-assembled carbon nanotube/nano carbon black composite fillers reinforced cement-based materials with multifunctionality. Compos Part a-Appl S. 2015;79:103-15.
[6] Li WW, Ji WM, Fang GH, Liu YQ, Xing F, Liu YK, et al. Electrochemical impedance interpretation for the fracture toughness of carbon nanotube/cement composites. Constr Build Mater. 2016;114:499-505.
[7] Liu YS, Wang MZ, Wang W. Ohmic heating curing of electrically conductive carbon nanofiber/cement-based composites to avoid frost damage under severely low temperature. Compos Part a-Appl S. 2018;115:236-46.

[8] Zhang JJ, Xu JM, Zhang D. A Structural Supercapacitor Based on Graphene and Hardened Cement Paste. J Electrochem Soc. 2016;163(3):E83-E7.
[9] Xie S, Ji ZJ, Li B, Zhu LC, Wang J. Electromagnetic wave absorption properties of helical carbon fibers and expanded glass beads filled cement-based composites. Compos Part a-Appl S. 2018;114:360-7.
[10] He YJ, Lu LN, Sun KK, Wang FZ, Hu SG. Electromagnetic wave absorbing cement-based composite using Nano-Fe3O4 magnetic fluid as absorber. Cement Concrete Comp. 2018;92:1-6.
[11] Oltulu M, Sahin R. Single and combined effects of nano-SiO2, nano-Al2O3 and nano-Fe2O3 powders on compressive strength and capillary permeability of cement mortar containing silica fume. Mat Sci Eng a-Struct. 2011;528(22-23):7012-9.
[12] Li H, Xiao HG, Yuan J, Ou JP. Microstructure of cement mortar with nano-particles. Composites Part B-Engineering. 2004;35(2):185-9.
[13] Vipulanandan C, Mohammed A. Smart cement modified with iron oxide nanoparticles to enhance the piezoresistive behavior and compressive strength for oil well applications. Smart Mater Struct. 2015;24(12):125020.
[14] Sum YL, Rheinheimer V, Soong BH, Monteiro PJM. Effects of Cement Paste Enhanced with Iron-Based Magnetic Particles on an Embedded Small Resonator Antenna. Sci Rep. 2017;7:15185.
[15] Braganca MOGP, Portella KF, Bonato MM, Alberti E, Marino CEB. Performance of Portland cement concretes with 1% nano-Fe3O4 addition: Electrochemical stability under chloride and sulfate environments. Constr Build Mater. 2016;117:152-62.
[16] Seifan M, Sarmah AK, Ebrahiminezhad A, Ghasemi Y, Samani AK, Berenjian A. Bio-reinforced self-healing concrete using magnetic iron oxide nanoparticles. Appl Microbiol Biot. 2018;102(5):2167-78.
[17] Blyszko J, Kiernozycki W, Guskos N, Zolnierkiewicz G, Typek J, Narkiewicz U, et al. Study of mechanical properties of concrete with low concentration of magnetic nanoparticles. J Non-Cryst Solids. 2008;354(35-39):4515-8.
[18] Guskos N, Zolnierkiewicz G, Typek J, Blyszko J, Kiernozycki W, Narkiewicz U. Ferromagnetic Resonance and Compressive Strength Study of Cement Mortars Containing Carbon Encapsulated Nickel and Iron Nanoparticles. Rev Adv Mater Sci. 2010;23(1):113-7.
[19] Guskos N, Zolnierkiewicz G, Guskos A, Typek J, Blyszko J, Kiernozycki W, et al. Magnetic properties of the micro-silica/cement matrix with carbon-coated cobalt nanoparticles and free radical DPPH. J Non-Cryst Solids. 2008;354(35-39):4510-4.
[20] Luo L, Xiong G, Zheng S, Deng M. Electromagnetic Shielding Effectiveness of Cement-matrix Composite Containing Nickel Fiber. Advanced Materials Research. 2011;177:570-3.
[21] Coey JMD. Permanent magnets: Plugging the gap. Scripta Mater. 2012;67(6):524-9.
[22] Sugimoto S. Current status and recent topics of rare-earth permanent magnets. J Phys D. 2011;44(6):064001.
[23] Coey JMD. Hard Magnetic Materials: A Perspective. IEEE Trans Magn. 2011;47(12):4671-81.
[24] Jacimovic J, Binda F, Herrmann LG, Greuter F, Genta J, Calvo M, et al. Net Shape 3D Printed NdFeB Permanent Magnet. Adv Eng Mater. 2017;19(8):1700098.
[25] Gutfleisch O, Willard MA, Bruck E, Chen CH, Sankar SG, Liu JP. Magnetic Materials and Devices for the 21st Century: Stronger, Lighter, and More Energy Efficient. Adv Mater. 2011;23(7):821-42.
[26] Li L, Post B, Kunc V, Elliott AM, Paranthaman MP. Additive manufacturing of near-net-shape and challenges. Scripta Mater. 2017;135:100-4.

[27] Li L, Tirado A, Nlebedim IC, Rios O, Post B, Kunc V, et al. Big Area Additive Manufacturing of High Performance Bonded NdFeB Magnets. Sci Rep. 2016;6:36212.
[28] Baldissera AB, Pavez P, Wendhausen PAP, Ahrens CH, Mascheroni JM. Additive Manufacturing of Bonded Nd-Fe-B-Effect of Process Parameters on Magnetic Properties. IEEE Trans Magn. 2017;53(11):2101704.
[29] Mebrouki A, Belas N, Bendani K, Bouhamou N. A Self-Compacting Cement Paste Formulation using Mixture Design. Journal of Applied Sciences. 2009;9(23):4127-36.
[30] Kantro DL. Influence of Water-Reducing Admixtures on Properties of Cement Paste - A Miniature Slump Test. Cement Concrete And Aggregates CCAGDP. 1980;2(2):95-102.
[31] Kong DL, Sanjayan JG, Sagoe-Crentsil K. Comparative performance of geopolymers made with metakaolin and fly ash after exposure to elevated temperatures. Cement Concrete Res. 2007;37(12):1583-9.
[32] Ogundiran MB, Kumar S. Synthesis of fly ash-calcined clay geopolymers: Reactivity, mechanical strength, structural and microstructural characteristics. Constr Build Mater. 2016;125:450-7.
[33] Sarkar M, Dana K, Das S. Microstructural and phase evolution in metakaolin geopolymers with different activators and added aluminosilicate fillers. Journal of Molecular Structure. 2015;1098:110-8.
[34] Pyrhonen J, Jokinen T, Hrabovcová V. Design of rotating electrical machines. Chichester, West Sussex, United Kingdom ; Hoboken, NJ: Wiley; 2008.
[35] Li Q, Yang XK, Zhang L, Wang JP, Chen B. Corrosion resistance and mechanical properties of pulse electrodeposited Ni-TiO2 composite coating for sintered NdFeB magnet. J Alloy Compd. 2009;482(1-2):339-44.
[36] Yu LQ, Wen YH, Yan M. Effects of Dy and Nb on the magnetic properties and corrosion resistance of sintered NdFeB. J Magn Magn Mater. 2004;283(2-3):353-6.
[37] Rostami V, Shao YX, Boyd AJ, He Z. Microstructure of cement paste subject to early carbonation curing. Cement Concrete Res. 2012;42(1):186-93.
[38] Ylmen R, Jaglid U, Steenari BM, Panas I. Early hydration and setting of Portland cement monitored by IR, SEM and Vicat techniques. Cement Concrete Res. 2009;39(5):433-9.
[39] Cullity BD, Graham CD. Introduction to magnetic materials. 2nd ed. Hoboken, N.J.: IEEE Press : Wiley; 2009.
[40] ASM International. Handbook Committee. ASM handbook. 10th editon. ed. Materials Park, Ohio: ASM International; 1990.
[41] Ma BM, Herchenroeder JW, Smith B, Suda M, Brown DN, Chen Z. Recent development in bonded NdFeB magnets. J Magn Magn Mater. 2002;239(1-3):418-23.
[42] Ormerod J, Constantinides S. Bonded permanent magnets: Current status and future opportunities (invited). J Appl Phys. 1997;81(8):4816-20.
[43] Birenboim M, Nadiv R, Alatawna A, Buzaglo M, Schahar G, Lee J, et al. Reinforcement and workability aspects of graphene-oxide-reinforced cement nanocomposites. Composites Part B-Engineering. 2019;161:68-76.
[44] Rostami MR, Abbassi-Sourki F, Bouhendi H. Synergistic effect of branched polymer/nano silica on the microstructures of cement paste and their rheological behavior. Constr Build Mater. 2019;201:159-70.
[45] https://www.apexmagnets.com/news-how-tos/2938-2/.
[46] https://www.electrive.com/2018/04/25/magnetic-cement-enables-dynamic-wireless-charging/.

[47] https://www.magment.de/en-magnetic-concrete-mc/.
[48] Wu M, Johannesson B, Geiker M. A review: Self-healing in cementitious materials and engineered cementitious composite as a self-healing material. Constr Build Mater. 2012;28(1):571-83.
[49] Cygan DF, McNallan MJ. Corrosion of NdFeB permanent magnets in humid environments at temperatures up to 150 C. J Magn Magn Mater. 1995;139:131-8.
[50] Rampin I, Bisaglia F, Dabala M. Corrosion Properties of NdFeB Magnets Coated by a Ni/Cu/Ni Layer in Chloride and Sulfide Environments. J Mater Eng Perform. 2010;19(7):970-5.
[51] Chitrada K, Raja KS, Pesic B, Chant I. Corrosion Behavior of Surface Modified NdFeB Permanent Magnet in Dilute Chloride Environments. Electrochim Acta. 2014;123:23-32.
[52] Bi MX, Xu C, Wattoo AG, Bagheri R, Chen YX, Mao SD, et al. Corrosion behavior of sintered CeNdFeB magnets in different solutions. J Alloy Compd. 2017;703:232-41.

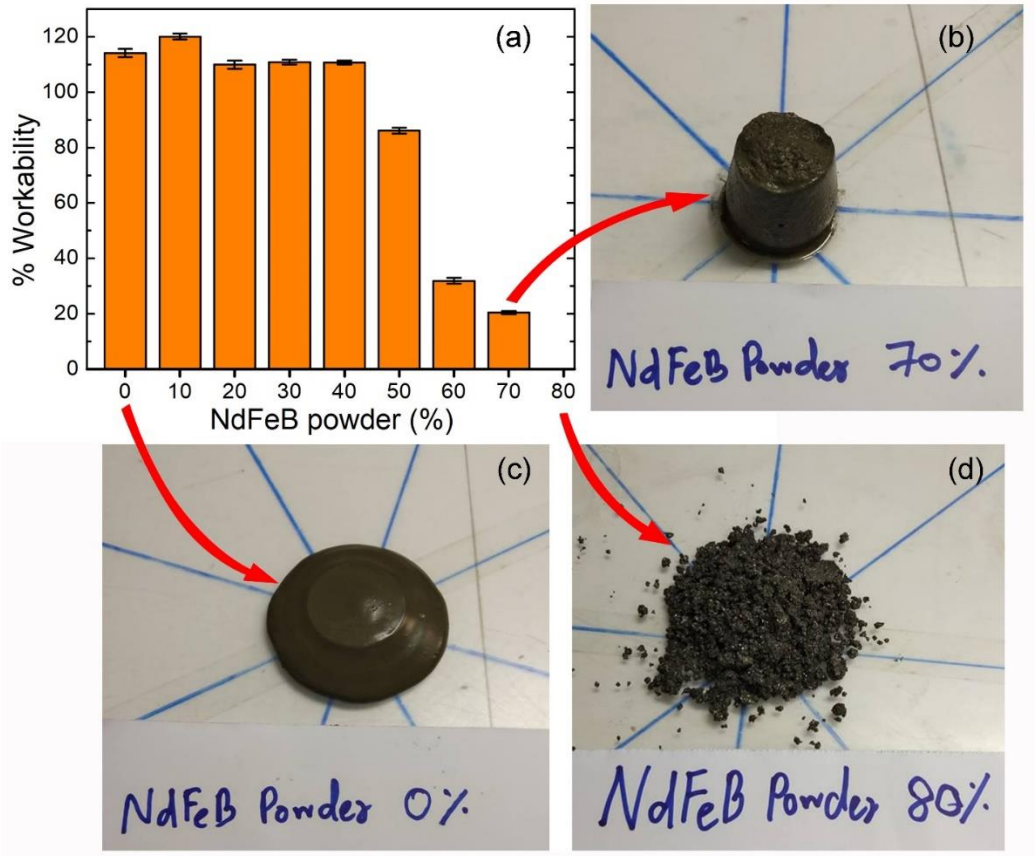

Fig. 1. (a) the workability of the cement and magnetic cement pastes, (b)-(d) the spread of the pastes during the workability test.

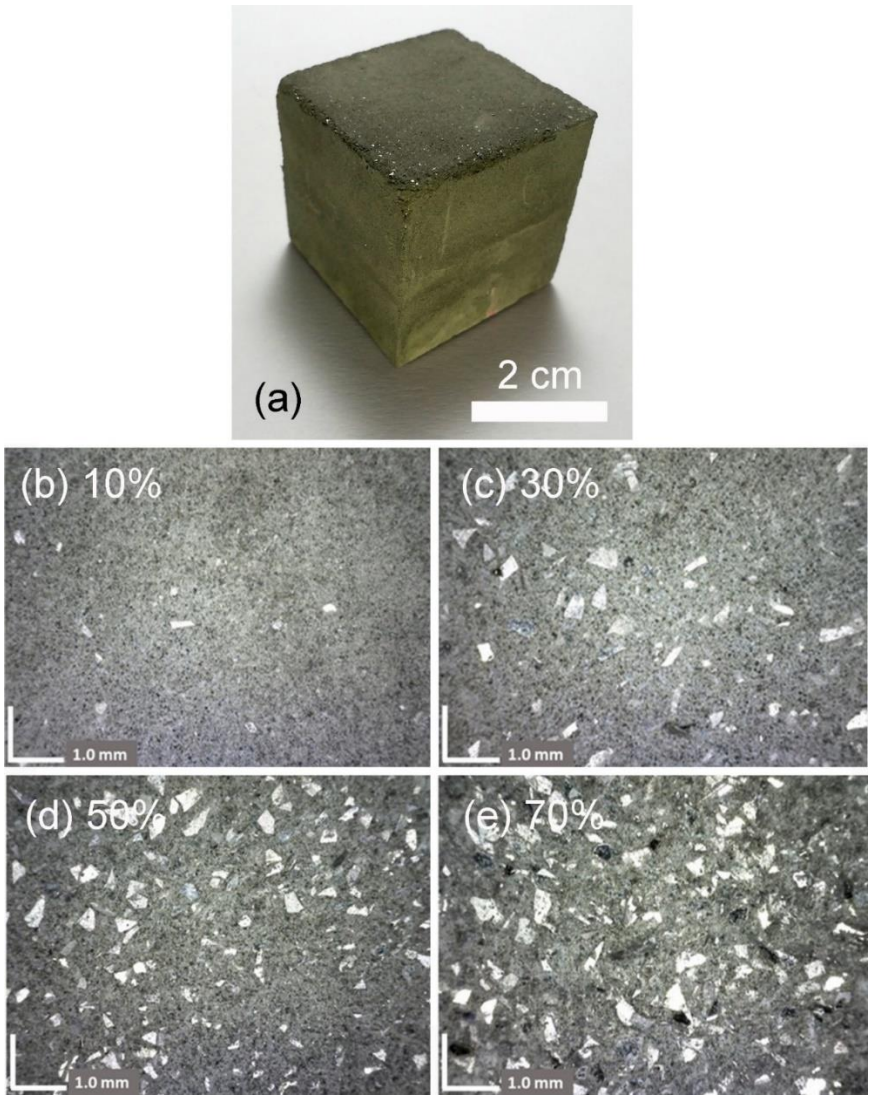

Fig. 2. (a) a magnetic cement (cementitious magnet) sample, (b)-(e) optical micrographs of the magnetic cement composite surface showing the uniform distribution of NdFeB particles.

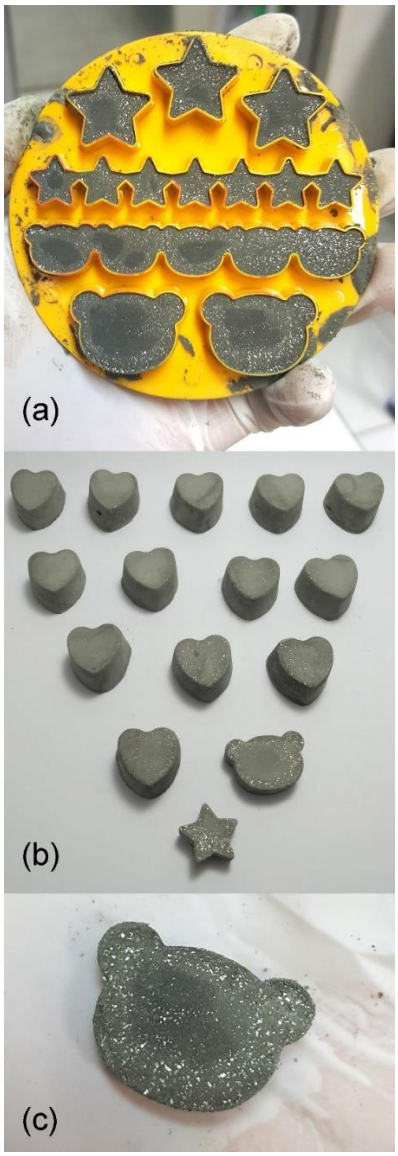

Fig. 3. Demonstrative formation of magnetic cement into any desired shape by a simple cementitious molding process.

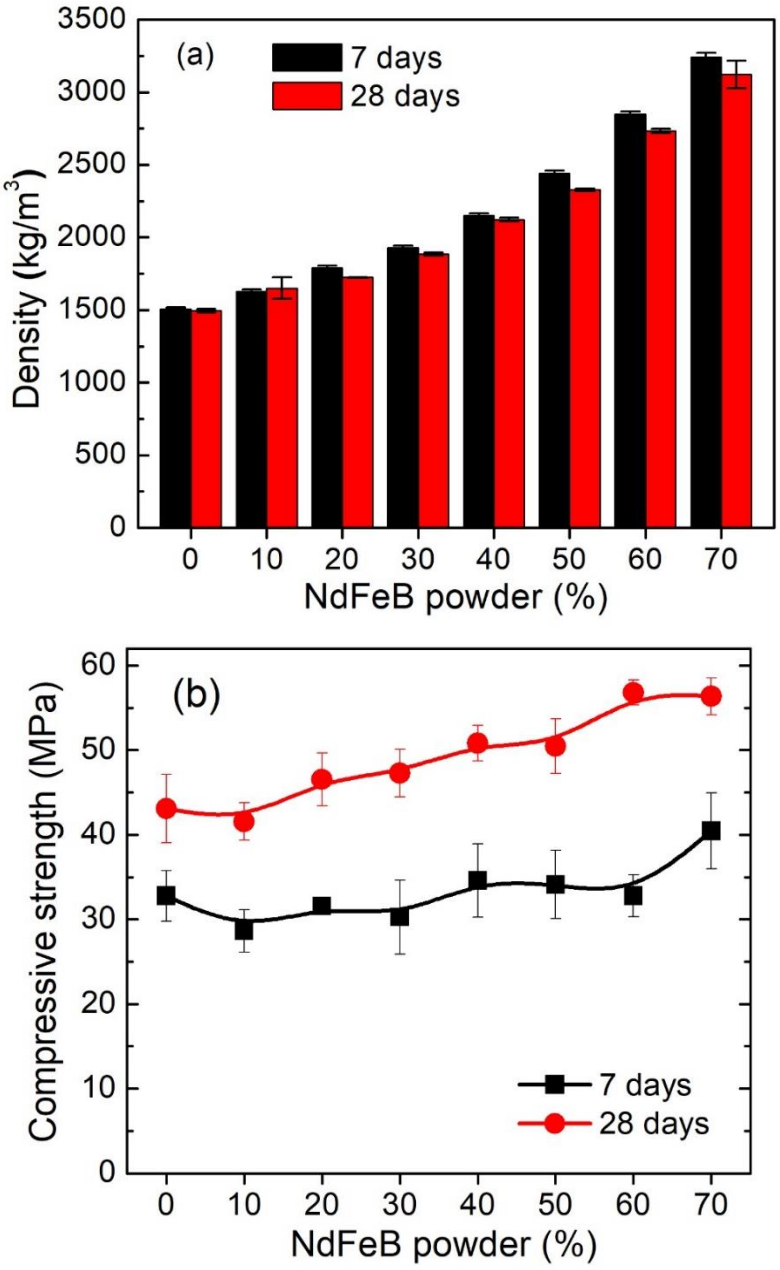

Fig. 4. (a) Density and (b) Compressive strength of the cement paste and magnetic cement composites.

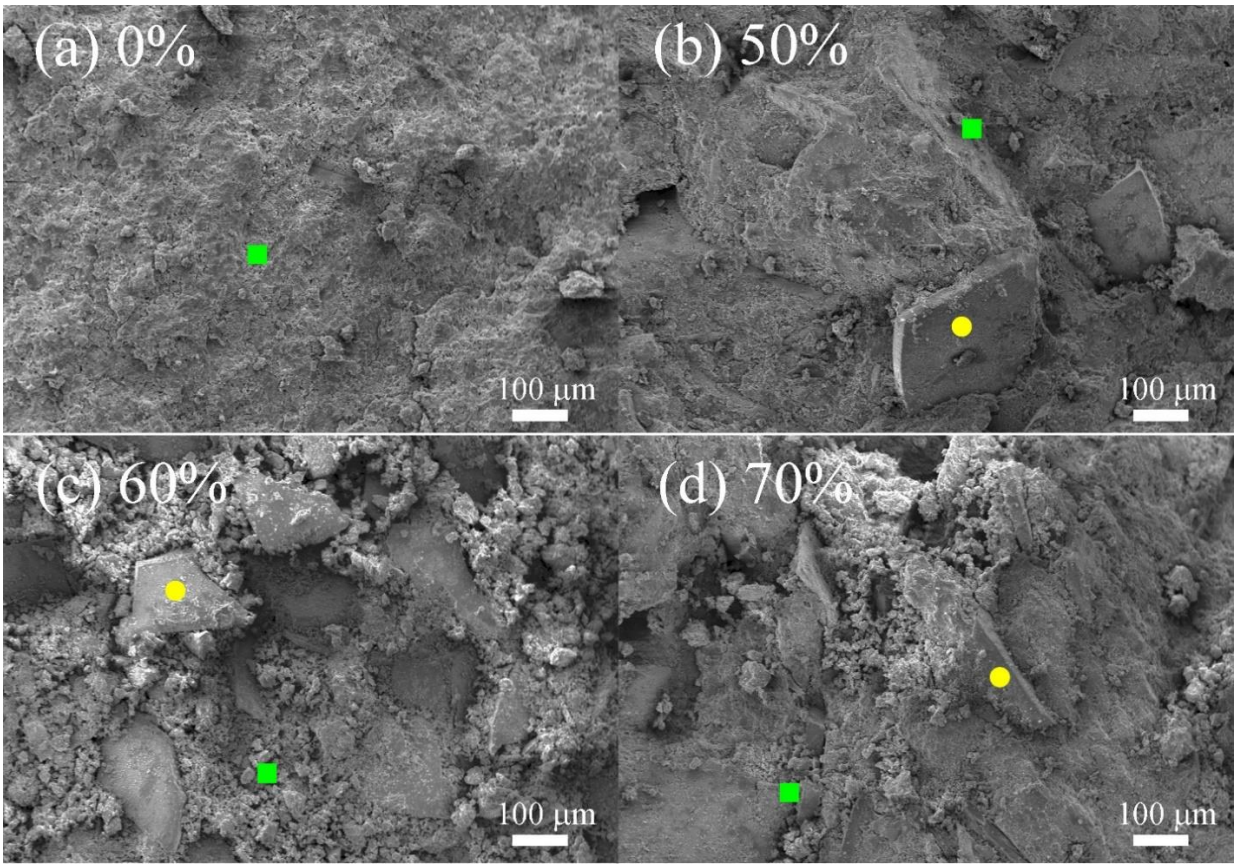

Fig. 5. Fractured surface SEM micrographs of the magnetic cement composites with NdFeB (a) 0%, (b) 50%, (c) 60%, (d) 70%. The green squares and yellow circles are the position for EDX spot analyses.

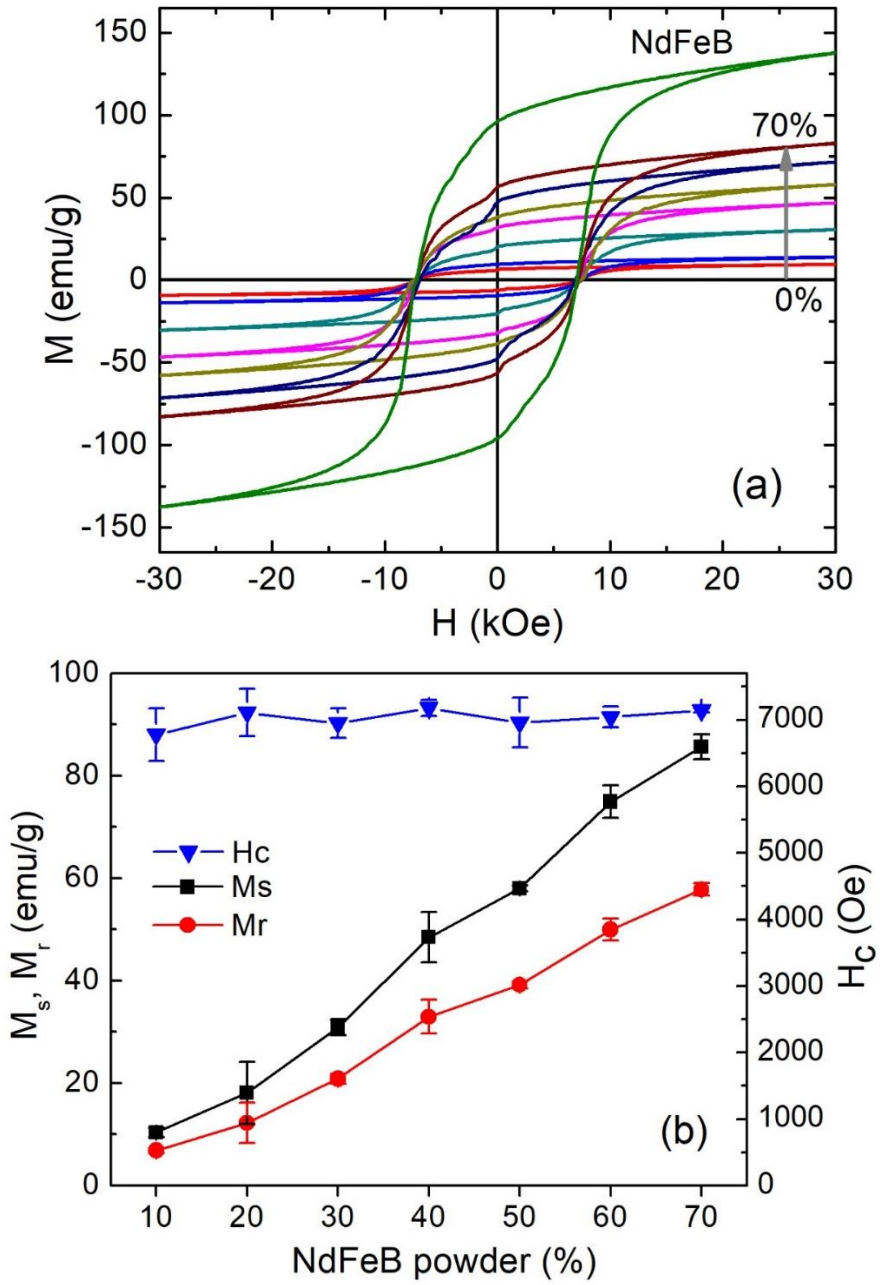

Fig. 6. (a) Magnetization curve (MH) of magnetic cement composites. The MH curve of raw NdFeB powder is plotted as a reference. (b) Magnetic properties (M_s, M_r, H_c) as a function of NdFeB concentration.

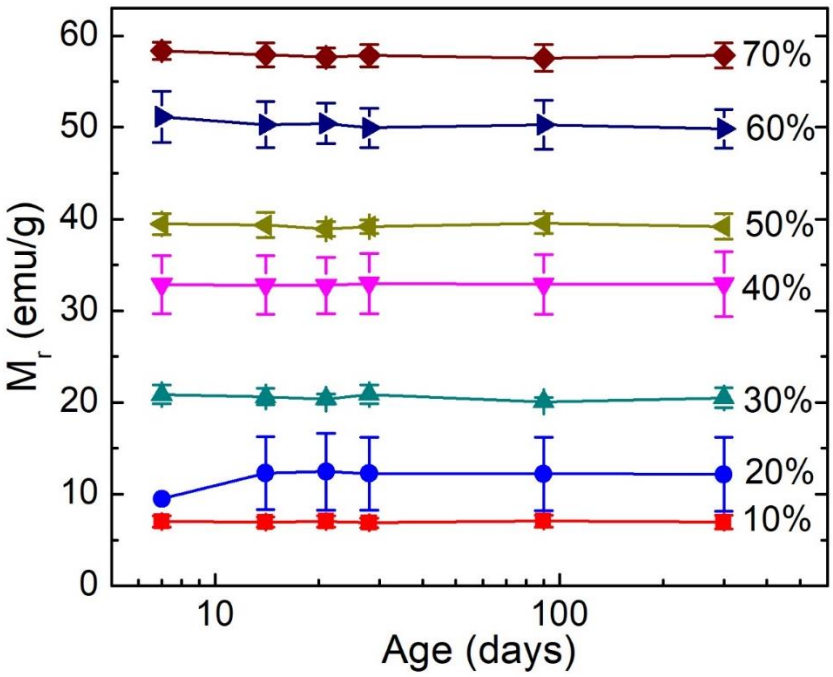

Fig. 7. Magnetic remanence (M_r) of the magnetic cement composites with different NdFeB concentration as a function of aging time.

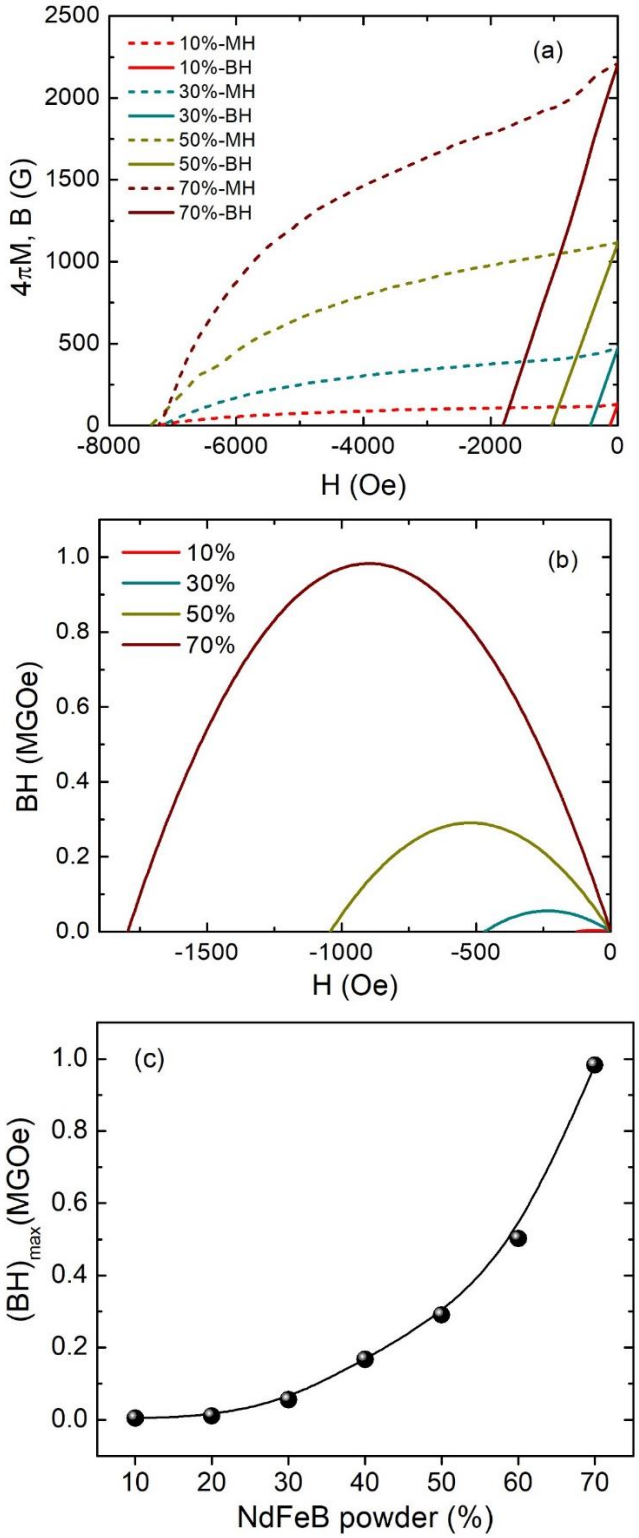

Fig. 8. (a) Demagnetization curves, (b) BH versus field and (c) $(BH)_{max}$ as a function of NdFeB concentration

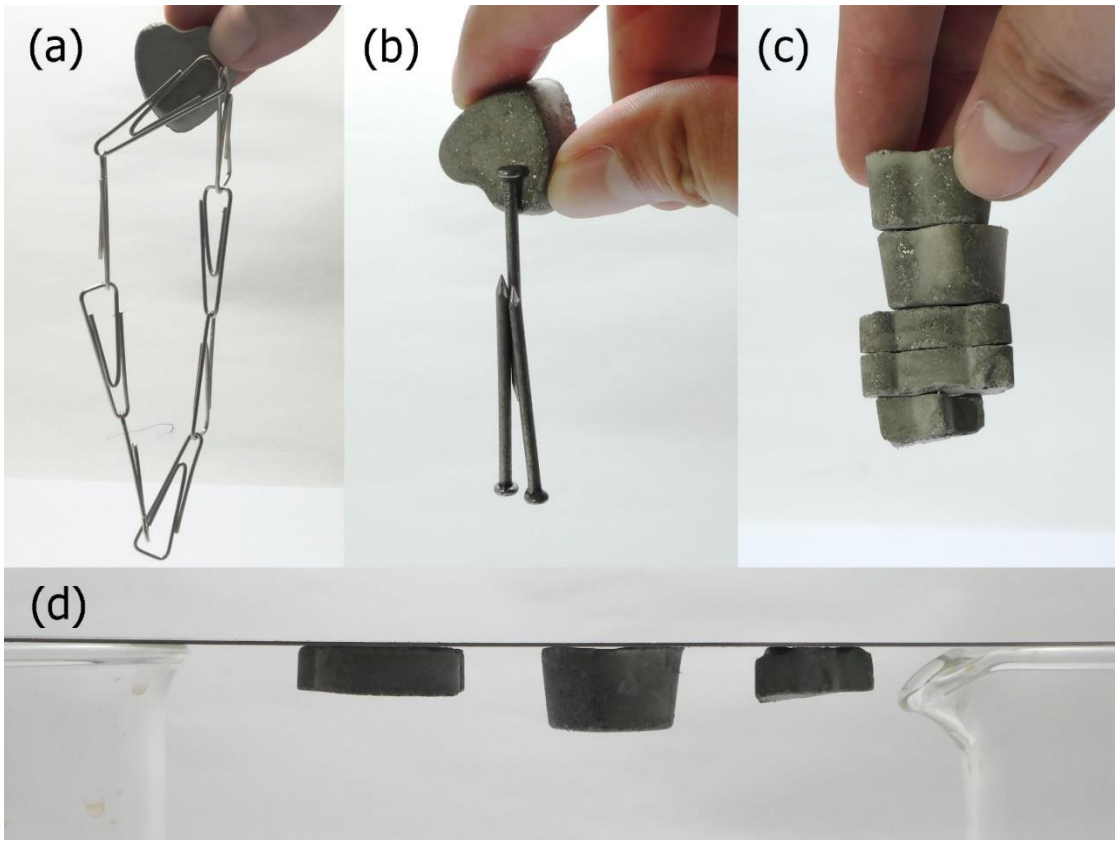

Fig. 9. Demonstration of permanent magnetic ability of the magnetic cement composites which can be used to lift metallic pieces or other magnetic cements (a)-(c), or attached upside down vertically to a steel bar by their magnetic force (d).

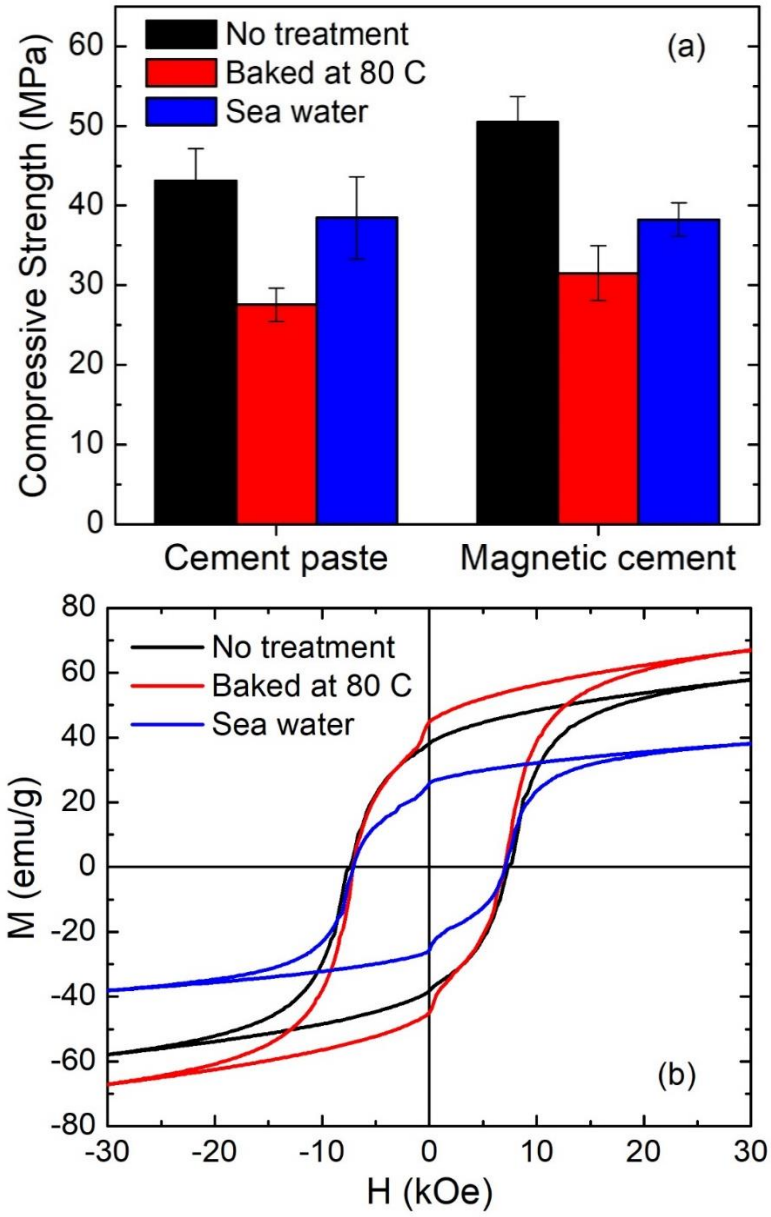

Fig. 10. (a) Compressive strength and (b) magnetization curves of the control cement paste and magnetic cement composites subjected to two artificial environmental conditions.

Supplementary Information:
Magnetic Cement (Cementitious Magnet)

Nattapong Chuewangkam[1], Supree Pinitsoontorn[1, 2,*], Prinya Chindaprasirt[3,4]

[1]*Department of Physics, Faculty of Science, Khon Kaen University, Khon Kaen 40002, THAILAND*
[2]*Institute of Nanomaterials Research and Innovation for Energy (IN-RIE), Research Network of NANOTEC-KKU (RNN), Khon Kaen University, Khon Kaen 40002, THAILAND*
[3]*Sustainable Infrastructure Research and Development Center, Department of Civil Engineering, Faculty of Engineering, Khon Kaen University, Khon Kaen 40002, THAILAND*
[4]*The Academy of Science, The Royal Society of Thailand, Dusit, Bangkok, Thailand*

Table S1. Chemical composition of cement paste and magnetic cement composite from the EDX spot analysis at the cement matrix (corresponding to the green squares in Fig. 5).

NdFeB (%)	Composition (at.%)						
	Ca	O	Si	Fe	Al	Nd	C
0	13.09±0.65	53.88±2.69	4.99±0.25	0.68±0.03	1.48±0.07	-	25.87±1.29
10	76.47±3.82	18.94±0.95	2.30±0.12	0.89±0.04	1.39±0.07	-	0
20	17.62±0.88	41.42±0.95	10.57±0.53	-	2.00±0.10	-	28.38±1.42
30	16.99±0.85	40.17±2.01	9.75±0.49	-	-	-	33.09±1.65
40	16.97±0.85	48.06±2.40	6.75±0.34	-	1.27±0.06	-	26.96±1.35
50	19.49±0.97	46.91±2.35	6.61±0.33	1.76±0.09	2.07±0.10	-	23.17±1.16
60	15.34±0.77	60.60±3.03	5.00±0.25	1.39±0.07	2.06±0.10	-	15.61±0.78
70	13.40±0.67	60.27±3.01	4.15±0.21	-	3.49±0.17	-	18.68±0.93

Table S2. Chemical composition of magnetic cement composite from the EDX spot analysis at the magnetic particle (corresponding to the yellow circles in Fig. 5).

NdFeB (%)	Composition (at%)						
	Ca	O	Si	Fe	Al	Nd	C
10	17.07±0.85	32.85±1.64	11.19±0.56	31.38±1.57	2.57±0.13	4.94±0.25	-
20	4.31±0.22	10.92±0.55	4.37±0.22	56.52±2.83	2.68±0.13	7.19±0.36	14.00±0.70
30	6.14±0.31	37.71±1.89	4.76±0.24	14.42±0.72	-	2.36±0.12	34.61±1.73
40	6.69±0.33	32.68±1.63	4.99±0.25	25.35±1.27	1.10±0.06	4.02±0.20	25.16±1.26
50	2.64±0.13	19.85±0.99	4.20±0.21	26.53±1.33	3.22±0.16	4.10±0.20	39.45±1.97
60	11.89±0.59	30.29±1.51	7.05±0.35	30.40±1.52	1.55±0.08	3.98±0.20	14.84±0.74
70	4.53±0.23	29.55±1.48	3.90±0.19	24.50±1.22	0.90±0.04	4.09±0.20	32.54±1.63

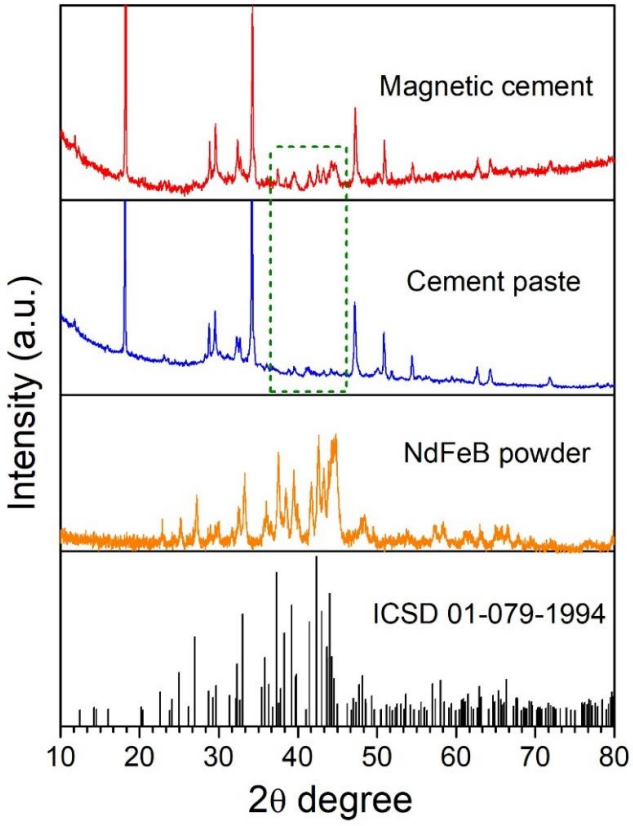

Fig. S1. XRD patterns of NdFeB powder (along with the reference pattern), pure cement paste, and magnetic cement composite. The difference of XRD patterns in the green box indicates the mixture of the composite phases between cement and NdFeB.

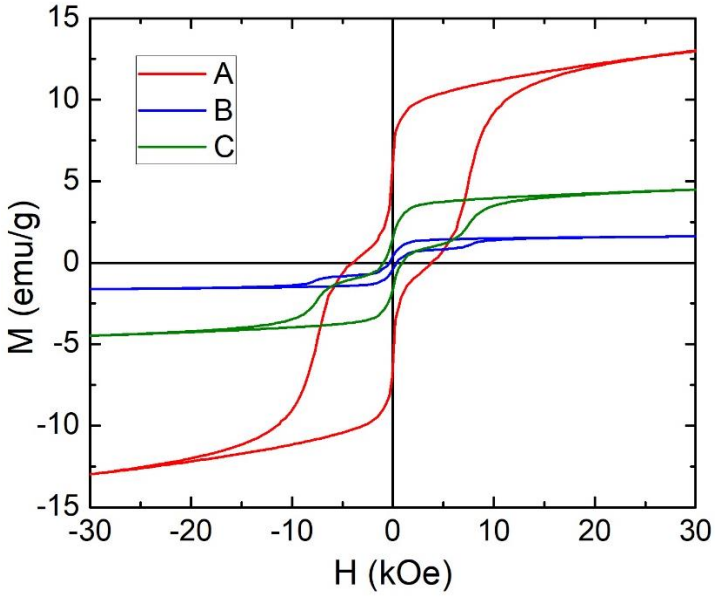

Fig. S2. Magnetization curves of magnetic geopolymer composites. The curves A, B, and C are from different parts of the same batch.